Karlsruhe Institute of Technology

Abschlussbericht ThermAc

Untersuchungen zur aquatischen Chemie und Thermodynamik von Actiniden bei erhöhten Temperaturen

M. Altmaier (ed.), E. Colas, F. Endrizzi, D. Fellhauer, X. Gaona, S. Hagemann, Ch. Kiefer, D. A. Kulik, J.-Y. Lee, G. D. Miron, T. Thoenen

INE SCIENTIFIC WORKING DOCUMENTS 04

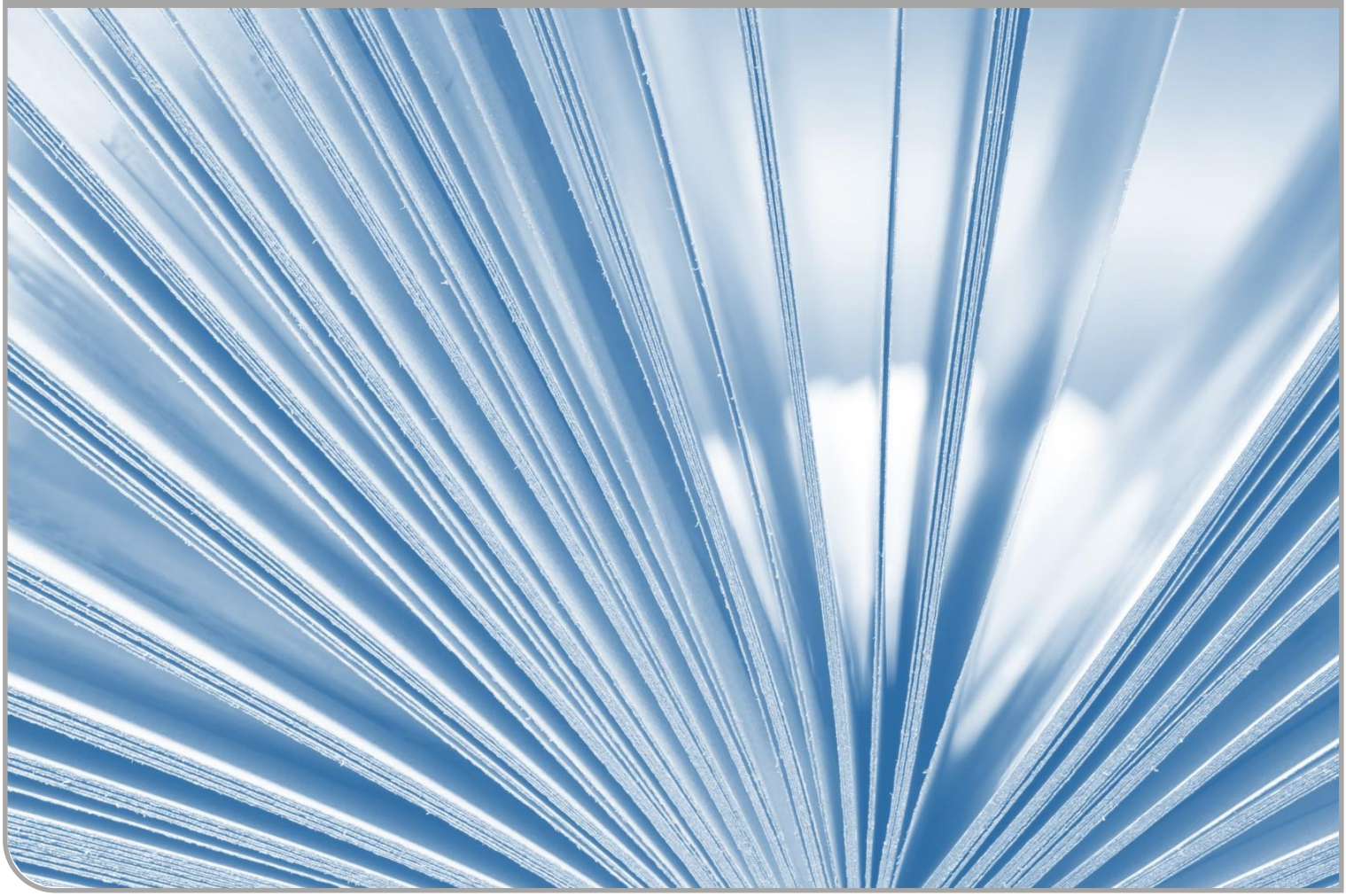

Institut für Nuklear Entsorgung (INE)

Das diesem Bericht zugrundliegende Vorhaben wurde mit Mitteln des Bundesministeriums für Bildung und Forschung (BMBF) unter dem Förderkennzeichen 02NUK039A gefördert. Die Verantwortung für den Inhalt dieser Veröffentlichung liegt bei den Autoren.

gefördert von

Bundesministerium
für Bildung
und Forschung

Institut für Nukleare Entsorgung (INE)

Hermann-von-Helmholtz-Platz 1
76344 Eggenstein-Leopoldshafen
www.ine.kit.edu

Impressum

Karlsruher Institut für Technologie (KIT)
www.kit.edu

2021

URL: http://www.ine.kit.edu/53.php
ISSN: 2701-262X
DOI: 10.5445/IR/1000135274

Karlsruher Institut für Technologie

Abschlussbericht

“ Aufklärung von Thermodynamik und Speziation von Actiniden bei höheren Temperaturen in Kombination von Schätzmethoden, spektroskopischen und quantenchemischen Methoden“
Akronym: ThermAc3

Teilprojekt: Untersuchungen zur aquatischen Chemie und Thermodynamik von Actiniden bei erhöhten Temperaturen

Projektpartner:

Institut für Nukleare Entsorgung, Karlsruher Institut für Technologie

Unterauftragnehmer von KIT-INE:

- *GRS (Gesellschaft für Anlagen- und Reaktorsicherheit), Deutschland*
- *PSI-LES, Schweiz*
- *Amphos^{21}, Spanien*

Förderkennzeichen: **02NUK039A**

Bewilligungszeitraum: **01.03.2015 bis 30.04.2020**

Teilvorhabenskoordination: Dr. Marcus Altmaier (KIT-INE)

Im Rahmen dieses Abschlussberichts werden die Arbeiten zusammengefasst, die von KIT-INE und Unterauftragnehmern unter dem Förderkennzeichen* 02NUK039A *innerhalb des BMBF geförderten Verbundprojekts ThermAc durchgeführt wurden.

ThermAc wurde gefördert vom:

Inhaltsverzeichnis und Einleitung

Mit diesem Dokument werden die im Rahmen von ThermAc von KIT-INE und Unterauftragnehmern durchgeführten Arbeiten dokumentiert und kommuniziert. Nach einer allgemeinen deutschsprachigen Zusammenfassung der wesentlichen Projektergebnisse werden die jeweiligen Arbeiten einzeln und in englischer Sprache dargestellt sind. Die von den Unterauftragnehmern von KIT-INE separat erstellten eigenständigen Teilberichte werden ebenfalls dargestellt.

Die Arbeiten in ThermAc wurden in einer ersten Projektphase mit dem Akronym „ThermAc3“ und einer folgenden zweijährigen Verlängerungsphase durchgeführt. In diesem Dokument werden die beiden Projektphasen zusammenfassend mit *ThermAc* bezeichnet.

Das Gesamtziel des Projekts ThermAc war die Erweiterung des Kenntnisstands und der thermodynamischen Datenbasis für Actiniden, langlebige Spaltprodukte und Matrixelemente mit Relevanz für Langzeitsicherheitsanalysen zur Endlagerung hochradioaktiver wärmeproduzierender nuklearer Abfälle. Die Arbeiten von KIT-INE beinhalten neue umfassende experimentelle Arbeiten sowie die Anwendung von Schätzmethoden für thermodynamische Daten. Die Arbeiten werden von KIT-INE selbst, sowie den Unterauftragnehmern von KIT-INE (GRS, Amphos[21] und PSI-LES) durchgeführt. Aufgrund der starken Beteiligung junger Wissenschaftler/innen stellen die Arbeiten einen relevanten Beitrag zum Kompetenzerhalt und -erwerb auf dem Gebiet der Nuklearen Sicherheits- und Entsorgungsforschung, bzw. auf dem Gebiet der Actiniden- und Radionuklidchemie dar. KIT-INE hat als Koordinator von ThermAc, verschiedene Beiträge zur Dissemination des Verbundprojekts geleistet, z.B. im Rahmen der Organisation des internationalen „*Workshop on High Temperature Aqueous Chemistry HiTAC (III)*“ (27.6.2019, Karlsruhe) welcher zugleich den Abschlussworkshop des Verbundprojekts ThermAc darstellte.

Kurzzusammenfassung der gesamten Arbeiten und Ergebnisse

Die Arbeiten von KIT-INE und Unterauftragnehmern innerhalb von ThermAc ermöglichten eine signifikante Verbesserung des Kenntnisstandes zur Actinidenchemie bei höheren Temperaturen. Es wurden neue umfassende experimentelle Studien zur Löslichkeit und Speziation von Radionukliden durchgeführt, aus denen neue chemische Modelle (für wässrige und feste Phasen) und thermodynamische Daten abgeleitet werden konnten. Die experimentellen Arbeiten wurden mit Arbeiten zur systematischen Abschätzung thermodynamischer Daten kombiniert. Hierdurch wird für die untersuchten Systeme erstmalig die spezifische Anwendung von Schätzmethoden für höhere Temperaturen und deren gezielte Validierung ermöglicht. Zudem wurden unterschiedliche Arbeiten durchgeführt um ein verbessertes Prozessverständnis, etwa zu Redoxprozessen und Festphasentransformationen als Funktion der Temperatur, zu erhalten. Die experimentellen Arbeiten mit Radionukliden wurden im Kontrollbericht des KIT-INE durchgeführt, die experimentellen Arbeiten zu den Fe-Systemen wurden in den Laboren der GRS Braunschweig durchgeführt. Die Entwicklung und Anwendung von Schätzmethoden für thermodynamische Daten fokussierte auf die isocoulombische Methode bzw. Entropie/Enthalpie Schätzungen und wurde in Zusammenarbeit mit erfahrenen internationalen Partnern, PSI-LES (Schweiz) und Amphos[21] (Spanien) ermöglicht.

Das Hauptergebnis der Arbeiten von KIT-INE und Unterauftragnehmern innerhalb von ThermAc liegt in der kritischen Analyse, Bewertung und Quantifizierung von grundlegenden Prozessen der wässrigen Chemie für Actinidensysteme. Es existiert eine generelle Tendenz zu zunehmender Komplexbildung in Lösung mit höheren Temperaturen. Des Weiteren tritt mit steigenden Temperaturen die Tendenz zur Ausbildung thermodynamisch stabilerer, d.h. weniger löslicher, Festphasen zutage. Für viele Systeme wird dementsprechend die Löslichkeit, also die Summe aus Festphasenstabilität und Komplexbildung in Lösung, bei Raumtemperatur und höheren Temperaturen zumindest in erster Näherung vergleichbar sein. In Einzelfällen kann jedoch auch ein unterschiedliches Verhalten nachgewiesen werden. Die im Rahmen von ThermAc angewendeten Schätzmethoden haben sich als wertvolle Werkzeuge für die Vorhersage von Temperatureinflüssen auf die betrachteten Gleichgewichts-prozesse erwiesen. Allerdings können sie nicht allgemein im Sinne eines „generellen vereinfachten Ansatzes“ für die Abschätzung von thermodynamischen Daten

verwendet werden, da in vielen Systemen spezifische Effekte die Prozesse steuern. Die Anwendung der Schätzmethoden kann lediglich für einzelne Systeme nach detaillierter Analyse der Eingangsparameter empfohlen werden und sollte auch dann zumindest stichpunktartig durch experimentelle Befunde validiert werden. Generell besteht auch nach Ende des Verbundprojekts ThermAc die Notwendigkeit, neue experimentelle Studien zu ausgewählten Systemen bei höheren Temperaturen durchzuführen, z.B. zur Generierung von Daten bei höheren Temperaturen als Basis für Schätzmethoden oder zur Identifizierung von bisher nicht bekannten Festphasentransformationen bzw. Lösungsspezies. Der verbesserte Kenntnisstand zu Löslichkeit und Speziation von ausgewählten Radionukliden bei höheren Temperaturen gibt einen wesentlichen Input für mögliche nachfolgende Forschungsaktivitäten mit dem Fokus auf Redoxprozesse und Radionuklidrückhaltung durch Sorption bei erhöhten Temperaturen.

Das übergeordnete Ziel der Nachwuchsförderung auf dem Gebiet der Actinidenchemie und der Endlagersicherheitsforschung konnte durch die Beteiligung von vier Nachwuchswissenschaftler/innen am KIT-INE erreicht werden.

Nachfolgend werden die im Rahmen der Arbeiten von KIT-INE und Unterauftragnehmern gewonnenen Ergebnisse innerhalb von ThermAc zusammengefasst.

Institut für Nukleare Entsorgung, Karlsruhe Institut für Technologie (KIT-INE)

Von KIT-INE wurde der Einfluss von Temperatur auf die Löslichkeit und Hydrolyse von U(VI) in verdünnten bis konzentrierten NaCl-Lösungen untersucht. Die Arbeit ermöglicht eine systematische Charakterisierung der Festphasen, welche die U(VI)-Löslichkeit bei erhöhten Temperaturen bestimmen. Für die Systeme wurden umfassende chemische und thermodynamische Modelle entwickelt, welche das Verhalten von wässrigen U(VI)-Spezies und der relevanten U(VI)-Festphasen quantitativ beschreiben. Es wurden Publikationen zu den Arbeiten von Endrizzi et al. „*Solubility and hydrolysis of U(VI) in 0.5 mol/kg NaCl solutions at T = 22 and 80 °C”* bzw. “*Thermodynamic description of U(VI) solubility and hydrolysis in dilute to concentrated NaCl solutions at T = 25, 55 and 80 °C”* erstellt.

Die Löslichkeit von ternären Festphasen des Typs Ca-U(VI)-CO_3 wurde bei T = 22°C und 80°C untersucht. Es wurden Festphasentransformationen in diesem System bei höheren Temperaturen analysiert und thermodynamische Löslichkeitskonstanten für die Festphasen abgeleitet. Eine Publikation von Lee et al. „*Solubility and stability of liebigite, $Ca_2UO_2(CO_3)_3 \cdot 10H_2O$(cr), in dilute to concentrated NaCl and $NaClO_4$ solutions at T = 22–80 °C"* wurde publiziert.

Ein weiterer Schwerpunkt der Arbeiten von KIT-INE war die Analyse des Einflusses von Temperatur auf die Festphasenstabilität und Löslichkeit von Np(V) in alkalischen Lösungen. Insbesondere wurden detaillierte Charakterisierungen von relevanten löslichkeitsbestimmenden Festphasen durchgeführt und deren Stabilität untersucht. Die Arbeiten sollen im Rahmen eines weiteren Manuskripts von Fellhauer et al. „*Transformation of Np(V) solid phase at elevated temperature"* publiziert werden. Im Neptuniumsystem wurden in weiteren Arbeiten von KIT-INE der Einfluss der Temperatur auf Redoxphänomene untersucht. Insbesondere die Kinetik der Reduktion von Np(V) zu Np(IV) wurde in unterschiedlichen redoxaktiven Systemen analysiert. Die Arbeiten von Fellhauer bzw. Lee et al. „*Redox Chemistry of Np(V)/Np(IV) in reducing aqueous solutions at T = 23 and 80°C"* sollen ebenfalls in wissenschaftlichen Fachzeitschriften publiziert werden.

Für dreiwertige Actiniden wurden Löslichkeitsstudien bei höheren Temperaturen anhand des chemischen Analogons Neodym realisiert. Wie bei den oben dargestellten U(VI)-Systemen konnten neue qualitative und quantitative Informationen zu den löslichkeitsbestimmenden Festphasen und den relevanten wässrigen Spezies abgeleitet werden. Der Vergleich mit Schätzmethoden, bzw. hierüber bestimmten thermodynamischen Daten, ermöglicht eine Einschätzung der Anwendung der Schätzmethoden.

Innerhalb der Verlängerungsphase von ThermAc, untersuchte KIT-INE den Einfluss der Temperatur auf die Löslichkeit, Hydrolyse und Carbonatkomplexierung von Th(IV). Die Untersuchungen wurden in sauren bis hyperalkalischen pH-Bedingungen durchgeführt. Die Arbeiten wurden in die Masterarbeit von Christian Kiefer integriert und lieferten neue Informationen zu löslichkeitsbestimmenden Festphasen, insbesondere deren Partikelgröße und Hydratationsgrad in hydrolysedominierten Systemen und ausgewählten carbonathaltigen Lösungen.

Die Arbeiten der Unterauftragnehmer GRS, PSI-LES und Amphos[21] zielen auf die Bestimmung von Redoxprozessen (Arbeiten im Fe-System) und die Anwendung und Bewertung verschiedener Schätzmethoden für thermodynamische Daten ab. Die Arbeiten und Ergebnisse der Unterauftragnehmer werden für diese Partner nachfolgend zusammengefasst und sind in dem Abschlussbericht von KIT-INE als ausführliche separate Teilberichte der jeweilige Unterauftragnehmer enthalten.

Gesellschaft für Anlagen- und Reaktorsicherheit (GRS):

Die GRS arbeitete an der Verbesserung grundlegender Methoden zur Messung des Redoxpotentials in wässriger Lösung, insbesondere auch in Systemen mit hohen gelösten Salzkonzentrationen. Das Redoxpotential ist ein wesentlicher Parameter zur Einschätzung der Oxidationsstufenverteilung von verschiedenen endlagerrelevanten Radionukliden. Die experimentellen Arbeiten stützten sich primär auf detaillierte Analysen gezielt präparierter Lösungen von Fe(II)- und Fe(III)-Spezies.

Auf Basis früherer Arbeiten wurde eine rechnerische Methode entwickelt, die es erlaubt, die primären potentiometrischen Messdaten in einem zweistufigen Verfahren zunächst in ein Konzentrationsverhältnis zweier redoxsensitiver Spezies und anschließend in ein alternatives Maß für den Redoxstatus in Lösung umzurechnen. Die Methode beruht auf der Auswertung systematischer Messungen des Redoxpotentials von Hexacyanoferrat(II)/ Hexacyanoferrat(III)-Mischungen in Lösungen der Salze NaCl und $MgCl_2$. Die Methode steht für unterschiedliche weiterführende Anwendungen zu Verfügung.

Ein Modell zur quantitativen Beschreibung der Komplexbildung von Fe^{2+} mit Chlorid in Lösungen von NaCl, KCl und $MgCl_2$ fehlte bislang. Darum wurden UV-spektrophotometrische Messungen durchgeführt, um die Komplexbildung in diesen Lösungen wie auch in LiCl-Lösungen bei 25 bis 80°C zu untersuchen. Für den Komplex $FeCl^+$ wurde eine Bildungskonstante und Pitzer-Koeffizienten für die Wechselwirkung mit den Ionen Cl^-, Na^+, K^+ und Mg^{2+} abgeleitet. Mit ihrer Hilfe ist es möglich, die beobachtete Speziation über den größten Teil der betrachteten Konzentrationen sehr gut zu beschreiben.

Paul Scherrer Institut (PSI-LES, Schweiz)

Der Beitrag des PSI-LES zu den Arbeiten in ThermAc besteht in zwei komplementären Aktivitäten: (i) Evaluierung und systematische Anwendung der isocoulombischen Schätzmethode zur Extrapolation von Gleichgewichtskonstanten zu höheren Temperaturen, und (ii) die Revision und Erweiterung der existierenden frei verfügbaren PMATCHC Software für das Management von intern konsistenten thermodynamischen Datensätzen.

Die Arbeiten zur Anwendung des isocoulombischen Schätzansatzes, war zum einen auf die Validierung verschiedener potentiell möglicher alternativer isocoulombischer Reaktionen zur Schätzung von log $K°_T$ ausgerichtet. Hier wurden insbesondere die wässrigen Komplexbildungsreaktionen von Lanthaniden und Actiniden betrachtet und vergleichende Analysen ermöglicht. Der isocoulombische Ansatz wurde zudem auf ausgewählte Feste-Lösungen Systeme (solid solutions) angewendet. Im Rahmen einer wissenschaftlichen Kooperation innerhalb von ThermAc von PSI-LES mit dem Projektpartner FZJ wurde das System $(Ba,Sr,Ra)SO_4(s)–H_2O(l)$ analysiert.

Die Arbeiten von PSI-LES nutzen zu einem wesentlichen Maß das von PSI-LES entwickelte frei verfügbare GEMS Softwarepaket und erweiterte dieses gezielt für die Arbeiten in ThermAc. Hierdurch steht dem Projekt ein neues Tool zur Modellierung von Prozessen der Radionuklidchemie bei höheren Temperaturen zu Verfügung. Ein wichtiger Erfolg war hier die Entwicklung von ThermoEcos, einer integrierten Software zur Verwaltung, Abschätzung und Berechnung von thermodynamischen Daten als Funktion von Druck und Temperatur. Hierin wurde die C++ Bibliothek ThermoFun für die Korrektur von Temperatureinflüssen auf thermodynamische Daten, das ThermoHub Datenpaket zur Speicherung von thermodynamischen Daten, und der ThermoMatch Code zur Verwaltung der thermodynamischen Daten und zur Erzeugung von entsprechenden digitalen Ausgabefiles integriert.

Amphos[21] Consulting (Spanien)

Amphos[21] arbeitete an der Evaluierung von verschiedenen Schätzmethoden mit dem Ziel die verfügbaren thermodynamischen Daten für Radionuklide in aquatischen Systemen im Temperaturbereich höher als 25°C deutlich zu verbessern. Der Fokus der

Arbeiten liegt in der kritischen Anwendung und nachfolgenden spezifischen Verifizierung verschiedener potentiell geeigneter Schätzmethoden. Basierend auf den hiermit geschätzten thermodynamischen Daten konnten Löslichkeitsgrenzen oder Speziationsschemata für Radionuklide berechnet, und mit experimentellen Daten verglichen werden, welche in vielen Fällen von Partnern innerhalb des ThermAc Projekts gewonnen wurden.

Die Arbeiten fokussierten auf wässrige Spezies bzw. Radionuklidkomplexe in Lösung, und potentielle löslichkeitsbestimmende Festphasen. Die Arbeiten zielten auf dreiwertige Lanthanide (als Analoga für dreiwertige Actiniden) und Curium(III) ab, und konnten zudem wichtige Informationen zu weiteren relevanten Actinidensystemen wie Np(V), U(VI) oder Th(IV) liefern. Neben der Hydrolyse, welche eine fundamentale Größe in allen wässrigen Systemen ist und als Basisinformation zur Einschätzung des Verhaltens insbesondere von Actiniden in englagerrelevanten Systemen zwingend erforderlich ist, wurden auch weitere relevante Liganden wie Chlorid, Sulfat, Carbonat oder Phosphat analysiert. Auch für diese zusätzlichen Liganden erfolgten Vergleiche mit experimentellen Daten des Kit-INE, aber auch mit Arbeiten von anderen Projektpartnern in ThermAc. Der betrachtete Temperaturbereich wurde auf bis zu 90°C eingegrenzt und auf wässrige Systeme bei niedrigen bis mittleren Ionenstärken fokussiert, für welche die zuverlässigsten Ergebnisse generiert werden können. Die Arbeiten beinhalten eine systematische Zusammenstellung verschiedener Schätzmethoden, wobei deren Referenzen, Angaben zur wissenschaftlichen Basis der Methode, prinzipielle Anwendbarkeit auf einzelne Systeme, die geschätzten Parameter und die wesentlichen grundlegenden Gleichungen zusammengestellt und kommentiert wurden. Zudem wurden Datentabellen für die geschätzten Systeme erstellt und den Projektpartnern zu Verfügung gestellt. Hier sind die abgeschätzten thermodynamischen Größen wie die Stabilitätskonstanten enthalten und auch die intern berechneten Enthalpiewerte angeben. Die in diesen Berechnungen verwendeten thermodynamischen Daten für den Referenzzustand und die jeweiligen Masterspezies werden ebenfalls angegeben.

TEILBERICHT A

Arbeiten des KIT-INE

Nachfolgend werden die Arbeiten von KIT-INE innerhalb von ThermAc (inklusive der Verlängerungsphase) dargestellt.

Karlsruher Institut für Technologie

Abschlussbericht

Teilbericht des Instituts für Nukleare Entsorgung, Karlsruher Institut für Technologie (KIT-INE)

"Aufklärung von Thermodynamik und Speziation von Actiniden bei höheren Temperaturen in Kombination von Schätzmethoden, spektroskopischen und quantenchemischen Methoden"

Akronym: ThermAc3

Teilprojekt: Untersuchungen zur aquatischen Chemie und Thermodynamik von Actiniden bei erhöhten Temperaturen

Autoren:

Marcus Altmaier, Francesco Endrizzi, David Fellhauer, Xavier Gaona, Christian Kiefer, Jun-Yeop Lee

Inhaltsverzeichnis

Deutschsprachige Zusammenfassung

Die Arbeiten von KIT-INE innerhalb von ThermAc ermöglichen ein verbessertes Verständnis von grundlegenden Aspekten der aquatischen Chemie ausgewählter Actiniden in den Oxidationsstufen +III, +IV, +V und +VI bei höheren Temperaturen. Der Fokus der Untersuchungen liegt auf den vier Hauptaspekten: Löslichkeit, Hydrolyse, Redoxverhalten und Carbonatkomplexierung. Dieses trägt zu einem verbesserten wissenschaftlichen Kenntnisstand der Actinidenchemie im Kontext der Endlagerung hochaktiver, wärmeentwickelnder radioaktiver Abfälle bei, und hat zudem potentielle Relevanz für andere Forschungsbereiche in denen eine quantitative Beschreibung der aquatischen Chemie von Metallen und Radionukliden bei höheren Temperaturen erforderlich ist. Hauptaugenmerk liegt auf (geo)chemischen Bedingungen und Systemen für welche relevante Datenlücken in den thermodynamischen Datenbasen identifiziert wurden, oder auf Themen für welche aktuell kontroverse Diskussionen in der wissenschaftlichen Fachöffentlichkeit anhängig sind. Die durchgeführten Arbeiten wurden im Kontrollbereich des KIT-INE durchgeführt, und nutzen die vorhandenen exzellenten analytisch/spektroskopischen Möglichkeiten insbesondere für die Untersuchung von Radionukliden. Eine Liste der innerhalb von ThermAc von KIT-INE erstellten Publikationen und Fachvorträgen bzw. Posterpräsentationen bei Konferenzen und Workshops ist am Ende dieses Teilberichts aufgeführt.

Die **Löslichkeit von Nd(III)** wurde in **0.1 – 5.0 M NaCl** Lösungen bei ***T* = 25 – 80 °C** im pH_m-Bereich 6.5–9 (mit $pH_m = -\log [H^+]$, $[H^+]$ in molalen Einheiten) untersucht. Die nach Abschluss der Löslichkeitsexperimente isolierten Neodym-Festphasen wurden detailliert mittels Pulver-XRD untersucht. Die initial eingesetzten Festphasen waren in allen untersuchten 0.1 und 0.5 M NaCl Probenlösungen stabil. Eine Festphasentransformation unter Ausbildung eines chloridhaltigen $Nd(OH)_2Cl(s)$ Bodenkörpers wurde beobachten, wenn $Nd(OH)_3(s)$ in 5 M NaCl Lösung bei $pH_m < 8$ equilibriert wurde. Die Konzentration von Nd(III) in Lösung war in diesem Fall deutlich niedriger als diejenige, die für $Nd(OH)_3(s)$ auf Basis aktueller thermodynamischer Daten und Modelle berechnet wird. Dieses stützt den Befund, dass $Nd(OH)_2Cl(s)$ die löslichkeitsbestimmende Festphase von Nd(III) in Lösungen mit [NaCl] = 5.6 m und $pH_m < 8$ ist. Die bei erhöhten Temperaturen gewonnenen neuen Löslichkeitsdaten für $Nd(OH)_3(s)$ erlauben es nicht, ein thermodynamisches Modell (mit Enthalpiedaten) für dieses System abzuleiten. Die in den Untersuchungen gewonnenen Daten erlauben jedoch die qualitative Aussage, dass erhöhte Temperaturen nur einen vergleichsweise moderaten Einfluss auf die Löslichkeit von Nd(III) innerhalb der untersuchten experimentellen Rahmenbedingungen hat.

Der **Temperatureinfluss auf Festphasen, Löslichkeit und Carbonatkomplexierung von Th(IV)** wurde systematisch unter Ar-Schutzgasatmosphäre untersucht. Ausgangsmaterial in den Untersuchungen war jeweils eine frisch ausgefällte amorphe ThO_2(am, hyd) Festphase. Die Alterung der frisch ausgefällten ThO_2(am, hyd) Festphase in Lösung bei T = 80 °C bewirkt eine signifikante Zunahme der Festphasenkristallinität bzw. der Partikelgröße. Dieses wurde durch XRD Messungen bestätigt. Alle in dieser Arbeit verwendeten Methoden zur Festphasencharakterisierung konnten jedoch keine klaren Unterschiede in den Festphasen, die unterschiedlich lange und bei verschiedenen pH_m – Werten equilibriert wurden, zeigen. Löslichkeitsexperimente bei Abwesenheit von Carbonat mit frisch gefällten oder gealterten Th(IV) Festphasen bei T = 22 °C zeigen eine eindeutige Abnahme der Löslichkeit in Experimenten, in denen die Festphasen bei T = 80 °C behandelt wurden. Im Gegensatz zu den Befunden aus der Festphasencharakterisierung haben die Alterungsdauer und der pH_m während der Alterung einen wesentlichen Einfluss auf die Löslichkeit gemessen bei T = 22 °C. Diese scheinbar widersprüchlichen Ergebnisse können konsistent dadurch erklärt werden, dass die Löslichkeit durch nur wenige Monolagen der ThO_2(s, hyd) Festphasenoberfläche kontrolliert wird, was durch die hier verwendeten experimentellen Methoden jedoch nicht detailliert abgebildet werden kann. Die in dieser Arbeit gewonnenen experimentellen Daten zeigen weiterhin, dass, obwohl die Tendenz zur Carbonatkomplexierung bei höheren Temperaturen zunimmt, dieser Effekt auf die Löslichkeit durch die erhöhte Kristallinität der ThO_2(s, hyd) Festphase bei erhöhten Temperaturen und die hierdurch bedingte niedrigere Löslichkeit kompensiert wird. Der Vergleich der in dieser Arbeit gewonnenen neuen experimentellen Daten mit den berechneten Löslichkeiten unter Verwendung der von Amphos[21] im Rahmen von ThermAc abgeschätzten Enthalpiewerte zeigen, dass dieser Ansatz verwendet werden kann um obere Löslichkeitslimite von Th(IV) in alkalischen Systemen bei Anwesenheit von Carbonat zu bestimmen.

Das **Transformationsverhalten** einer **Np(V)-Hydroxid Festphase** wurde untersucht, indem eine initial eingesetzte NpO_2OH(am,fresh) Festphase in alkalischen NaCl und NaOH Lösungen bei erhöhten Temperaturen (***T* = 80 °C**) über 30 Tage equilibriert wurden. Die Umwandlung in kristalline Festphasen der Zusammensetzung Na-Np(V)-OH wurde durch XRD und SEM-EDS Analysen bestätigt. Im Gegensatz zu amorphem NpO_2OH(am,fresh) sind die ternären Na-Np(V)-OH Festphasen durch wohldefinierte XRD Diffraktogramme und charakteristische Peaks charakterisiert, die auf das Vorliegen von (mikro)kristallinen Np(V) Transformationsprodukten hinweisen. Chemische Analysen, SEM-EDS, und XPS zeigen die Bildung von zwei unterschiedlichen Np(V) Festphasen mit spezifischen Np:Na Verhältnissen. Dieser Befund ist konsistent mit den Resultaten aus den XRD Analysen. Die vorliegende Arbeit bestätigt, dass bei erhöhten Temperaturen neue Np(V)-Festphasen gebildet werden können. Weitere experimentelle Arbeiten werden benötig, um zu einer abschließenden Klärung der Relevanz dieser Festphasen für die Bewertung der Np(V)-Chemie in aquatischen Systemen zu gelangen.

Das **Redoxgleichgewicht zwischen Np(V) und Np(IV) bei *T* = 80 ºC** wurde als Funktion des pH_m untersucht, wobei das Redoxpotential in Lösung durch verschiedene redoxaktive Chemikalien kontrolliert wurde. Die teilweise oder vollständige Reduktion des initial eingesetzten Np(V)(aq) unter Ausbildung schwerlöslicher Np(IV) Festphasen wurde in allen untersuchten Proben beobachtet. Bei Anwesenheit von reduzierenden Chemikalien, z.B. AH_2QDS, Eisenpulver, $SnCl_2$ oder Hydrochinon bei $pH_m \geq 8.1$, bzw. Fe(II)/Fe(III) bei $pH_m \geq 6.2$, wurden mehr als 99% des initial eingesetzten Np(V) innerhalb von weniger als 35 Tagen reduziert. Für Proben mit Hydrochinon oder Fe(II)/Fe(III) und niedrigeren pH_m-Werten war die Reduktion von Np(V) signifikant langsamer. Verglichen mit analogen Experimenten des KIT-INE, die mit gleichem experimentellen Ansatz bei Raumtemperatur durchgeführt wurden, sind die kinetischen Raten für die Np(V) Reduktion bei T = 80°C signifikant größer.

Die **Löslichkeit und Hydrolyse von U(VI)** wurde in **0.1 – 5.0 M NaCl** Lösungen bei ***T* = 25 – 80°C**, mit den initial eingesetzten Festphasen $UO_3 \cdot H_2O$(cr) ($4 \leq pH_m \leq 7$) und $Na_2U_2O_7 \cdot H_2O$(cr) ($4 \leq pH_m \leq 7$) untersucht. Es wurden detaillierte Analysen der Festphasen sowohl vor als auch nach Abschluss der Experimente durchgeführt. Die neuen experimentellen Untersuchungsergebnisse erlaubten es, den Einfluss der Temperatur und der Lösungszusammensetzung (Hintergrundelektrolyt) auf die Löslichkeit der verschiedenen Uran(VI)-Festphasen detailliert zu bewerten. Hierbei wurde die Stabilität der Spezies und strukturelle Änderungen in den Festphasen analysiert. Für Metaschöpit $UO_3 \cdot 2H_2O$(cr) wurde eine Umwandlung in eine dem Natriumuranat ähnliche Festphase gefunden. Dieser Prozess wurde unter sauren Bedingungen beobachtet, wobei das initial eingesetzte Festphasenmaterial in Lösungen mit [NaCl] = 0.51 und 5.6 m bzw. T = 55 und 80 °C equilibriert wurde. Eine Alteration der löslichkeits-bestimmenden Festphase wurde in den Experimenten bei T = 25 °C nicht gefunden. Die Festphase $Na_2U_2O_7 \cdot H_2O$(cr) ist unter den untersuchten Rahmenbedingungen thermodynamisch stabil. Unter hyperalkalischen pH_m-Bedingungen wird die Löslichkeit von of U(VI) durch die prädominante Hydrolysespezies $UO_2(OH)_4^{2-}$ in Lösung bestimmt. Die hiermit korrelierte Löslichkeit wurde in den Untersuchungen bei höheren Temperaturen verglichen mit dem gleichen System bei 25 °C signifikant um 2.5 logarithmische Einheiten erhöht. Dieser Effekt ist primär mit einer erhöhten Wasser-Azidität bei höheren Temperaturen korreliert. Die Temperaturabhängigkeit des Löslichkeitsprodukts von $Na_2U_2O_7 \cdot H_2O$(cr) und der Hydrolysekonstante von $UO_2(OH)_4^{2-}$ liefern Argumente, dass der beobachtete Effekt konsistent durch die abnehmende Stabilität des Festkörpers $Na_2U_2O_7 \cdot H_2O$(cr) und einer Stabilisierung der wässrigen Spezies $UO_2(OH)_4^{2-}$ bei höheren Temperaturen erklärt werden kann. Das für dieses System abgeleitete thermodynamische Modell (d.h. Löslichkeitsprodukte der Festphasen, Komplexbildungskonstanten und Enthalpiedaten) erlauben eine genaue und robuste Beschreibung bzw. Berechnung der Löslichkeit und chemischen Speziation von U(VI) bei erhöhten Temperaturen unter alkalischen bis hyperalkalischen Bedingungen.

Die **Löslichkeit im ternären Systems Ca-U(VI)-CO_3 bei T = 22 und 80 °C** wurde experimentell untersucht. Es wurde eine wesentliche Auflösung des eingesetzten Liebigits, $Ca_2UO_2(CO_3)_3 \cdot 10H_2O$(cr), nach Erreichen des Gleichgewichtszustands bei T = 22 °C in Lösungen mit [NaCl] ≤ 0.5 M nachgewiesen, und $Ca_2UO_2(CO_3)_3 \cdot 10H_2O$(cr) als löslichkeitsbestimmende Festphase unter den untersuchten Bedingungen bestätigt. Deutlich niedrigere U(VI) Gleichgewichtskonzentrationen wurden in 5 M NaCl Lösung bei T = 22 °C gefunden. Chemische Analysen, XRD, und SEM-EDS Untersuchungen bestätigen in diesem System eine Transformation von Liebigit in Andersonit, $Na_2CaUO_2(CO_3)_3 \cdot 6H_2O$(cr), d.h. eine Festphase mit Na und Ca in der Struktur. Bei erhöhten Temperaturen erfolgt eine Destabilisierung des Liebigits und Umwandlungen in Ca-Uranat bzw. Na-Uranat Festphasen. Auf Basis der experimentellen Löslichkeitsdaten (gemessen bei T = 22 °C) wurden thermodynamische Löslichkeitsprodukte für Liebigit und Andersonit abgeleitet.

Die im Rahmen der Untersuchungen von KIT-INE verwendete Kombination aus experimentellen Löslichkeitsstudien, Redoxexperimenten, ausführlichen Festphasenanalysen und thermodynamischen Analysen ermöglicht eine signifikant verbesserte wissenschaftliche Beschreibung und Quantifizierung des Einflusses der Temperatur auf die aquatische Chemie von An(III)/Ln(III), An(IV), An(V) und An(VI) unter endlagerrelevanten geochemischen Bedingungen. Die gewonnenen Ergebnisse liefern zudem signifikant verbesserte Möglichkeiten zur Validierung der innerhalb ThermAc entwickelten Schätzmethoden für thermodynamische Daten und Eigenschaften von Festphasen und gelösten wässrigen Spezies. Die ermittelten thremodynamischen Daten können ggf. zu einem späteren Zeitpunkt in die thermodynamische Referenzdatenbasis THEREDA (www.thereda.de) integriert werden.

Beschreibung der wissenschaftlichen Arbeiten von KIT-INE innerhalb ThermAc

1. Introduction and scope of work

Temperature is one of the parameters that will vary during the different phases of operation of a high level radioactive waste (HLW) repository. Elevated temperature conditions (up to 200°C depending on hostrock system and repository concept) will affect actinide chemistry in the near-field of a HLW repository. Under the reducing conditions foreseen after the closure of the repository due to the anoxic corrosion of iron, the oxidation states +III and +IV are expected to dominate the solution chemistry of the actinides. Tetravalent actinides are characterized by strong hydrolysis and the formation of sparingly soluble amorphous hydrous oxides in aquatic systems. The transition of these amorphous solids, AnO_2(am, hyd), into the thermodynamically stable crystalline phases AnO_2(cr), is kinetically hindered and is generally not observed in aqueous systems. Temperature may facilitate this transition with the consequent decrease of the overall solubility. Pentavalent Np attracts some attention with respect to environmental questions because of its broad stability fields (pH and E_h), its rather great mobility and high solubility under many solution conditions. However, the impact of temperature on the redox behaviour of the Np(V/IV) couple as well as on the Np(V) solid phases controlling the solubility under alkaline to hyperalkaline conditions has been scarcely investigated. Uranium is the main element present in spent nuclear fuel and accordingly contributes with the largest inventory to the nuclear waste. Although a large number of studies have previously investigated the solution chemistry of uranium, a number of key uncertainties remain with respect to its chemical behavior at elevated temperatures, especially in the alkaline to hyperalkaline pH conditions of relevance for nuclear waste disposal.

In this context, this work by KIT-INE aims at a comprehensive description of the impact of temperature on the solution chemistry of Nd(III), Th(IV), Np(IV/V) and U(VI). The study covers pH conditions ranging from acidic to hyperalkaline, covers oxidizing to very reducing systems and extends from dilute to concentrated salt systems (up to 5 M NaCl). Experiments with Th(IV) and U(VI) are conducted both in the absence and in the presence of carbonate. The combination of fundamental research with an applied character is highlighted throughout the discussion of the results obtained within this project. As ultimate goals, this work aims at providing robust solubility upper limits to be considered in source term estimations, as well as at deriving comprehensive thermodynamic models including enthalpy data for the investigated systems. These thermodynamic data can be implemented in thermodynamic databases (*i.e. THEREDA* or NEA–TDB) and further used in geochemical calculations of relevance in the framework of the nuclear waste disposal. This work also contributes to sound experimental data for the validation of the estimation methods developed by Amphos[21] and PSI-LES within the ThermAc project for the evaluation of thermodynamic properties at elevated temperatures.

2. Executive summary

The work performed by KIT-INE within ThemAc provides an improved fundamental scientific understanding on the solution chemistry of selected actinides in the oxidation states +III, +IV, +V and +VI at elevated temperature, with focus on four main aspects, namely solubility, hydrolysis, redox behavior and complexation with carbonate. This contributes to an improved scientific description of actinide chemistry in the context of high level nuclear waste disposal, and other fields of environmental concern where a quantitative description of actinide solution chemistry at elevated temperature is required. Focus is given to conditions and systems for which relevant thermodynamic datagaps have been identified or controversial discussions were ongoing in the interested scientific/technical community. The reported studies were performed in the controlled area of KIT-INE, making use of the excellent analytical and spectroscopic tools available for the work on radionuclides at this facility. A list of peer reviewed publications by KIT-INE in ThermAc is provided at the end of this report, together with several dissemination activities at workshops and conferences.

The **solubility of Nd(III)** was investigated in **0.1 – 5.0 M NaCl** solutions at ***T* = 25 – 80 °C** in the pH_m range 6.5 – 9 (with $pH_m = -\log [H^+]$, $[H^+]$ in molal units). The solid phases collected after completing the solubility experiments were isolated and characterized with powder XRD. The initial solid phase material was stable when equilibrated in 0.1 and 0.5 M NaCl, in all conditions of testing. A solid phase transformation leading to the formation of $Nd(OH)_2Cl(s)$ occurred when $Nd(OH)_3(s)$ was equilibrated in 5 M NaCl solutions with $pH_m < 8$. The concentration of Nd(III) in solution under these conditions was markedly lower than the one predicted for $Nd(OH)_3(s)$ based on recent thermodynamic models. This supports that $Nd(OH)_2Cl(s)$ is the solid phase controlling the solubility of Nd(III) in solutions with [NaCl] = 5.6 m at $pH_m < 8$. Solubility data collected for $Nd(OH)_3(s)$ at elevated temperature does not allow deriving a thermodynamic model for this system including enthalpy data. However, the results obtained in this work qualitatively confirm that temperature has a modest impact of the solubility of Nd(III) within the investigated boundary conditions.

The **influence of temperature on Th(IV) solid phases, solubility and complexation with carbonate** was systematically investigated under Ar atmosphere using a freshly precipitated ThO_2(am, hyd) solid phase as starting material. The ageing of the freshly precipitated ThO_2(am, hyd) solid phase at *T* = 80 °C induces a significant increase of the crystallinity and particle size, as confirmed by XRD measurements. However, all solid phase characterization methods used in this work are unable to resolve clear differences between solid phases aged for different time periods or at different pH_m values. Solubility experiments with fresh and aged Th(IV) solid phases conducted in the absence of carbonate

at T = 22 °C show a clear decrease in the solubility of the solid phases aged at T = 80 °C. In contrast to the observations gained by solid phase characterization, the ageing time and ageing pH_m have a very important impact on the solubility measured at T = 22 °C. These apparently discordant observations can be explained in a consistent manner by claiming a solubility control by a few monolayers in the surface of the ThO_2(s, hyd) solid, which cannot be properly probed by any of the techniques considered in this work. Experimental data obtained in this work indicate that although complexation with carbonate is enhanced by elevated temperature, this effect is mostly compensated by the increased crystallinity of ThO_2(s, hyd) at elevated temperature with the consequent decrease in solubility. The comparison of experimental data with solubility calculations using enthalpy estimates generated by Amphos[21] within this project show that this approach can be used to assess upper solubility limits of Th(IV) in alkaline systems in the presence of carbonate.

The **transformation behavior of solid Np(V)-hydroxide** was investigated by equilibrating initial NpO_2OH(am,fresh) in alkaline NaCl and NaOH solutions at elevated temperature (***T* = 80 °C**) for 30 days. Transformation into crystalline Na-Np(V)-OH solid phases was confirmed by XRD and SEM-EDS analyses. In contrast to amorphous NpO_2OH(am,fresh), the ternary Na-Np(V)-OH solid phases reveal well-defined XRD patterns with characteristic peaks pointing to the presence of (micro)crystalline Np(V) transformation products. Chemical analysis, SEM-EDS, and XPS reveal the formation of two different Np(V) solid phases with individual Np : Na ratios, which is consistent with the result obtained from the XRD. The present work confirms that new solid compounds of Np(V) can form at elevated temperature. Further dedicated experimental efforts are required to clarify their potential relevance for the assessment of Np(V) chemistry in aqueous systems.

The **redox equilibrium between Np(V) and Np(IV) was studied at *T* = 80 °C** as a function of pH_m and the redox potential adjusted by chemically different reducing agents. Partial or complete reduction of initial Np(V)(aq) to sparingly soluble Np(IV) was observed for all samples investigated. In the presence of reducing chemicals, i.e. AH_2QDS, Fe powder, $SnCl_2$ or hydroquinone with $pH_m \geq 8.1$, and Fe(II)/Fe(III) with $pH_m \geq 6.2$, more than 99% of initial Np(V) was reduced within less than 35 days. For hydroquinone and Fe(II)/Fe(III) samples with lower pH_m values, reduction of Np(V) was significantly slower. Compared to analogous experiments performed at room temperature conditions using the same approach, the rates for Np(V) reduction are significantly greater at T = 80°C.

The **solubility and hydrolysis of U(VI)** was investigated in 0.1 – 5.0 M NaCl solutions **at *T* = 25 – 80°C**, using $UO_3 \cdot H_2O$(cr) ($4 \leq pH_m \leq 7$) and $Na_2U_2O_7 \cdot H_2O$(cr) ($4 \leq pH_m \leq 7$) as starting materials. An

extensive characterization of the solid materials before and after the completion of the solubility experiments was conducted. Results from the different experimental approaches allowed to evaluate the impact of temperature and of the ionic medium on the solubility of the different materials, the stability of the solid phases and possible structural changes occurring. A partial solid phase transformation of $UO_3 \cdot 2H_2O$(cr) into a sodium uranate-like material was observed. This process occured in acidic conditions, when the initial material was equilibrated in solutions with [NaCl] = 0.51, 5.6 m at T = 55, 80 °C. An alteration of the solid phase was not observed in experiments conducted at T = 25 °C. $Na_2U_2O_7 \cdot H_2O$(cr) resulted thermodynamically stable within the investigated boundary conditions. In hyperalkaline pH_m conditions, the solubility of U(VI) was governed by the formation of $UO_2(OH)_4^{2-}$ and it was significantly enhanced by temperature, up to 2.5 $\log_{10}$-units with respect to the same system at 25 °C. This effect was mainly attributed to an increased acidity of water at higher temperatures. The temperature dependence of the solubility product $Na_2U_2O_7 \cdot H_2O$(cr) and of the hydrolysis constant of $UO_2(OH)_4^{2-}$ also suggests that minor contributions also derive from a decreased stability of $Na_2U_2O_7 \cdot H_2O$(cr), together with an enhanced stabilization of $UO_2(OH)_4^{2-}$ at higher temperatures. The thermodynamic model derived (including solubility constants, hydrolysis constants and enthalpy data) allow accurate solubility and speciation calculations of U(VI) at elevated temperatures and high pH_m.

The **solubility of the ternary system Ca-U(VI)-CO_3 was investigated at T = 22 and 80 °C**. Considerable dissolution of liebigite, $Ca_2UO_2(CO_3)_3 \cdot 10H_2O$(cr), was observed after reaching the equilibrium at T = 22 °C in solutions with [NaCl] ≤ 0.5 M. $Ca_2UO_2(CO_3)_3 \cdot 10H_2O$(cr) was confirmed as the solubility controlling solid phase under these conditions. Remarkably lower U(VI) equilibrium concentrations were observed in 5 M NaCl solutions at T = 22 °C. Chemical analysis, XRD, and SEM-EDS confirmed a transformation of liebigite into andersonite, $Na_2CaUO_2(CO_3)_3 \cdot 6H_2O$(cr), in this system. At elevated temperature, destabilization of liebigite and transformation into Ca-urante and Na-diuranate phases took place. Based on the experimental solubility data obtained at T = 22 °C, the solubility products of liebigite and andersonite were quantitatively derived.

The methodology adopted by KIT-INE in ThermAc, using a combination of comprehensive solubility studies, redox experiments, extensive solid phase characterization and thermodynamic evaluation, provides a significantly improved scientific basis for the quantitative evaluation of the impact of temperature on the solution chemistry of An(III)/Ln(III), An(IV), An(V) and An(VI) under geochemical conditions of relevance in the context of nuclear waste disposal. The results also contribute to the validation of estimation methods developed within the ThermAc project for the evaluation of thermodynamic properties at elevated temperature of radionuclide solid compounds and aqueous species and can eventually be integrated into THEREDA (www.thereda.de) at a later stage.

3. Experimental

3.1 Chemicals. pH and E_h measurements

All solutions were prepared with deionized water obtained from the water purification system (18.2 MΩ·cm, Milli-Q®, Merck Millipore). NaCl (p.a.), NaOH-Titrisol®, HCl-Titrisol® and Suprapur®-grade HNO_3 were purchased from Merck. Detailed descriptions of the chemicals used and the sample preparation are provided in the corresponding subchapters.

The pH_m was measured with combination glass electrodes (*Orion ROSS*). Prior to the sampling, electrodes were calibrated against diluted commercial pH buffer solutions at T = 22, 25, 55 or 80 °C (Merck, pH 2 – 12 at T = 20 °C, the corresponding pH values at different temperatures were provided by the manufacturer) to relate the potential of the electrode to a value of pH_{exp}, according to the Nernst's law. pH_m was calculated as $pH_m = pH_{exp} + A_m$, where A_m is an empirical parameter accounting for both the junction potentials of the electrode and the activity of H^+. A_m depends both on the ionic medium and the temperature. Values of A_m were experimentally determined in the present study by measuring the pH_{exp} of HCl solutions with known concentrations (from $1.25 \cdot 10^{-3}$ to 0.02 m) prepared in different NaCl–HCl media (0.10, 0.51, 5.6 m) at the different temperatures.
In the case of the batches with $pH_m > 12$, outside the calibration range of the electrode, $[H^+]$ was instead calculated from the analytical (initial) concentration of hydroxide OH^-. In these highly alkaline conditions pH_m was reasonably assumed to be stable throughout the studies.

The E_h values of selected samples were measured by using combined Pt ring electrodes with Ag/AgCl reference system filled with 3 M KCl solution (Metrohm). The experimental redox potentials were corrected with respect to the potential of the standard hydrogen electrode (SHE). The redox electrodes employed in the present work were regularly tested with redox standard solutions (220 mV versus SHE, Schott Instruments).

3.2 Solubility experiments with $Nd(OH)_3(s)$

$Nd(OH)_3(s)$ was prepared by contacting 0.5 g of $Nd_2O_3(cr)$ (*Merck*) in MilliQ deionized water, preliminarily boiled and degassed under a stream of Ar. The batch was equilibrated at room temperature until the solid was fully hydrated. The solid was preliminarily equilibrated in MilliQ water, at T =80 °C for 30 days. Results from the characterizations of the material isolated at the end of the equilibration process confirmed the expected composition and morphology of the desired material.

Solubility experiments were conducted in an Ar glovebox, in conditions excluding of CO_2 and hence carbonate in solution. Batch solutions composed of 15 – 20 mL of NaCl / NaOH / HCl solutions, depending on the desired pH and on the total ionic strength were contacted with 5 – 15 mg of $Nd(OH)_3(s)$. In the case of experiments conducted at T = 22 and 25 °C batches were prepared in 20 mL HDPE screw-cap vials. Batch systems to be equilibrated at T = 55 or 80 °C were prepared in 25 mL PTFE screw-cap vials (*Semadeni Plastic Group*). To verify that no organic substances were released from the PTFE vessels in solution, test vials were preliminarily filled with NaCl solutions with different concentration (0.1 to 5.6 m), pH 4 -13.7 and equilibrated at T = 25 – 80 °C. Total organic carbon analyses were then conducted with a *Shimadzu 5000* TOC instrument. Results excluded the presence of organic carbon above the detection limit of the technique (~ 0.1 ppm), and hence underline that the adopted methodology does not introduce artefacts related to leached organic components from the vessels.

Batches to be equilibrated at T = 55 or 80 °C were placed into compact ovens (*Falc Instruments*) fitted into the glovebox. The precision of the temperature during the equilibration of the samples was (22 and 25 ± 1 °C), (55 ± 0.5 °C), (80 ± 2 °C). Nd concentrations were determined by Inductively-Coupled Plasma Mass Spectrometry (ICP–MS, *Perkin Elmer ELAN 6100*). In all samples equilibrated at room temperature, an aliquot of 0.075 – 0.100 mL of supernatant solution was taken and the solid phase was separated by ultrafiltration (10 kD filters; *NanoSep Merck Millipore*, pore size ≈ 2 nm). For the separation of the solid phases equilibrated at elevated temperatures, a rapid syringe filtration (*Pall Acrodisc*® filters, pore size 0.1 μm, PTFE membrane) was used. This step was performed within $t < 10$ seconds and involved a slight decrease in temperature of the filtrate to $T > 70$ °C. The comparison of this approach with other methods indicated no impact of the separation method on the measured metal concentration.

Morphological characterization of the solid phases isolated both after their preparation and at the end of the solubility experiments were conducted with X-ray diffraction of the dried powders (XRD), differential thermal analysis (DTA) and scanning electron microscopy with X-ray analysis of the scattered electrons (SEM–EDS). Elementary analyses were also performed by means of ICP-OES after dissolution of the solids in 2% HNO_3.

3.3 Solubility experiments with ThO_2(s, hyd) in the absence and presence of carbonate

A nitrate-free $^{232}ThCl_4$ solution was prepared by the slow titration of a 0.15 M Th(IV) nitrate solution with 1.0 M NaOH to pH ≈ 10-11. The resulting solid, *i.e.* ThO_2(am,hyd), was centrifuged for 10-15 minutes at 4000 *g* in order to separate the nitrate-rich supernatant. The remaining precipitate after centrifugation was dissolved in 0.1 M HCl. This procedure was repeated until nitrate was washed out

(< 10 ppm, determined with the colorimetric test strips Merck MQuant®). Approximately 1.2 g of ThO_2(am,hyd) solid phase was obtained as the result of a final slow precipitation by using a 1.0 M NaOH solution to reach pH ≈ 11.

The original ThO_2(am,hyd) suspension was divided into 9 aliquots of approximately 130 mg each with the aim of investigating the impact of pH, temperature and aging time on the crystallinity and solubility of the Th(IV) solid phases. Eight of the suspensions were prepared in either 0.1 M HCl-NaCl ($pH_m \approx 3$) or 0.1 M NaOH ($pH_m = 12.8$) at T = (22 ± 2) °C, and aged at T = (80 ± 2) °C for 1, 2, 4.5 and 5.5 months. An additional aliquot was used to characterize the freshly precipitated solid phase. Note that because of the increase of the pK_w of water with temperature, the actual pH_m of the 0.1 M NaOH suspensions was significantly lower at T = (80 ± 2) °C, *i.e.* pH_m(T = 80 °C) = 11.2. All solid phases were characterized before and after equilibration by means of X-ray powder diffraction (XRD). For comparison with the Th(IV) solid phases synthesized and aged in this study, a solid phase precipitated in 2008 and aged for 12 years at room temperature was also investigated.

The solid phases described above were used for the preparation of different series of solubility samples in the absence and presence of carbonate at T = 22 and 80 °C. Each solubility sample was prepared with 1.5 – 3 mL of the corresponding solid suspension (fresh precipitate or solid phases aged at T = 80 °C). This aliquot was centrifuged for 5 minutes at 4000 *g*, separated from the supernatant, and washed 2 times with the corresponding equilibration solution. After the last washing step, the solid phase was contacted with 5-20 mL (depending upon pH_m) of the equilibration solution.

Seven series of solubility experiments were prepared in the absence of carbonate, using a freshly precipitated ThO_2(am,hyd), and ThO_2(s) aged for 1, 2 and 4.5 months ($pH_m = 3$ and 12.8) at T = (80 ± 2) °C. After the given ageing time at elevated temperature, the samples were equilibrated at T = 22 °C in 0.1 M NaCl solutions with $2.3 < pH_m < 6.3$. Concentration of Th and pH were monitored at regular time intervals until equilibrium conditions were attained (defined by constant [Th] and pH_m readings). Thorium concentrations were measured by ICP-MS after a filtration step.

One series of solubility samples was prepared in 0.1 M NaOH solutions containing $[CO_3^{2-}]_{tot}$ = 0.01, 0.03, 0.1, 0.3, 0.6, 1.0 and 1.5 M. Experiments were conducted with a ThO_2(s) solid phase aged for 2 months at T = 80 °C and pH_m(25 °C) = 12.8. In contrast to the experiments in the absence of carbonate, the samples containing carbonate were equilibrated both at T = (22 ± 2) °C and T = (80 ± 2) °C. The experiments at T = (22 ± 2) °C are analogous to those described in Altmaier et al. (2005) [1], although in the present study a tempered ThO_2(s,hyd) phase instead of a freshly precipitated ThO_2(am,hyd) was used. The concentration of Th and pH were monitored at regular time intervals.

A phase separation step was conducted in all cases before ICP-MS measurements in order to separate colloids and suspended particles. For the samples in the absence of carbonate (T = 22 °C), an aliquot of

the supernatant of each sample was centrifuged (12000 g) with 10 kD filters. The phase separation of the samples equilibrated in carbonate solutions (T = 22 and 80 °C) was carried out using syringe filters (Whatman 13 mm Disposable Filter Device, PTFE, 0.1 µm). The solubility samples containing carbonate and equilibrated at T = 80 °C were placed in a block heater (IKA Dry Block Heater 3) during the sampling process in order to ensure constant temperature conditions. The filtrate obtained after the 10 kD or syringe filtration was diluted using 2 % ultrapure HNO_3. A dilution factor of 1:25 to 1:10^6 was considered as a function of the concentrations of salt and Th (expected) in the corresponding sample.

3.4 Solid phase transformation of Np(V)

All experiments were conducted under controlled Ar atmosphere conditions (O_2 < 5 ppm) in glove boxes. An ion-exchange column purified and oxidation state pure $^{237}NpO_2^+$ stock solution (0.055 m NpO_2^+ in 0.1 m HCl) was used for the experiment. For the preparation of initial NpO_2OH(am,fresh), 2.5 ml of 0.2 m NaOH was added to a solution containing 6.2 ml of the 0.055 m $^{237}NpO_2^+$ stock solution and 20 ml of H_2O. NaCl and NaOH were used to prepare NaCl-NaOH (I = 0.1 and 5.6 m) background electrolyte solutions with constant ionic strength and $pH_m \approx 13$. Approximately 5 mg of the freshly precipitated NpO_2OH(am,fresh) were equilibrated with 20 ml of the corresponding background electrolyte solutions in PTFE-lined stainless steel/titanium autoclaves. The autoclaves were tempered at T = 80 ± 5 °C for 30 days. After heating, the autoclaves were gradually cooled down to room temperature over 96 hours. Subsequently, the pH_m and E_h values of all samples were measured at room temperature and total Np concentrations in the aqueous phase were determined by liquid scintillation counting (LSC; Quantulus, Ultima Gold cocktail) after ultrafiltration with 10 kD filters (Pall, Omega Nanosep 10K).

3.5 Np(IV)/Np(V) redox behavior

All samples were prepared and handled in an Ar glove box (O_2 < 5 ppm), and stored inside a lab oven (Falc instruments) at T = 80 °C using PTFA vials. The redox conditions in the investigated samples were controlled by additions of homogeneous or heterogeneous chemical redox reagents in 15 mL of 0.1 m NaCl, namely

(i) 1.2 mmol/L anthraquinone (AQDS) + 0.4 mmol/L anthrahydroquinone-2,6-disulfonate (AH_2QDS) (obtained by partial reduction with $Na_2S_2O_4$),

(ii) Fe powder (*ca.* 4 mg Fe powder; Merck, ≥ 99.5 %, grain size: 10 µm),

(iii) 3 mmol/L $SnCl_2$ (Sigma-Aldrich, 98%),

(iv) 1.0 mmol/L $FeCl_2$ + 0.1 mmol/L $FeCl_3$ (Sigma-Aldrich), and

(v) 1 mmol/L hydroquinone (Sigma-Aldrich).

The pH_m values in the samples were between 5 and 10, partly fixed by using 0.01 mol/l of MES, HEPES, and CHES buffer solutions. After equilibration of the (inactive) redox matrix solutions at T = 80°C for 2 – 4 weeks, aliquots of a 12 mM NpO_2^+ stock solution were spiked to the different samples resulting in initial Neptunium concentrations $[Np(V)]° = (5\pm1)\cdot10^{-5}$ m. The pH_m and E_h values of supernatant solutions were regularly monitored at T = 80 ± 0.5 °C using a dry block heater system (IKA). Total Np concentrations in the aqueous phase were determined by liquid scintillation counting (LSC; Quantulus, Ultima Gold cocktail) and high-resolution ICP-MS after ultrafiltration with 10 kD filters (Pall, Omega Nanosep 10K). As Np(IV) is sparingly-soluble under the experimental conditions with $[Np(IV)] < 1\cdot10^{-8}$ M, and as sorption of Np(V) is negligible in the redox samples, a decrease of the initial [Np(V)]° represents a reduction of Np(V) to Np(IV).

3.6 Solubility experiments with $UO_3\cdot2H_2O$(cr) and $Na_2U_2O_7\cdot H_2O$(cr)

Solubility experiments were conducted in NaCl 0.10, 0.51. 5.6 m at T = 25, 55, 80 °C. The starting solid phase materials were synthesized as follows: metaschoepite was prepared by the slow titration of a solution having 0.01 M of uranyl nitrate ($UO_2(NO_3)_2\cdot6H_2O$, Merck) with 0.05 M NaOH. The pH was kept in the range pH ~ 4–5 to avoid the incorporation of Na^+ into the layered structure of metaschoepite expected at higher pH. The solid phase was separated and stored in Milli-Q water at room temperature. For the preparation of sodium uranate, a batch of metaschoepite was precipitated in a solution with NaCl 1.0 M. The fresh precipitate was titrated with 0.1 M NaOH up to pH = 11. The solid phase transformation was quantitatively achieved in one week. Before starting the solubility experiments, the solid phases were equilibrated in aqueous solution at *T* = 80 °C for 30 days. This procedure ensured the same degree of crystallinity of the initial phases in the different experiments. In particular, metaschoepite was equilibrated in milliQ water and sodium uranate in aqueous solution of [NaCl] = 2.5 M, [NaOH] = 0.05 M. Characterizations of the tempered materials confirmed the stoichiometry and the morphology expected for the desired products.

Solubility experiments were performed following the same approach as described in chapter 3.2 for Nd(III). Metaschoepite was used as starting material in all experiments at $pH_m \leq 6$, whereas sodium uranate was considered for all alkaline samples. The solid phases were characterized both after their preparation and at the end of the solubility experiments with the techniques described in chapter 3.2.

Additionally, time-resolved laser induced luminescence analyses were carried out on selected $UO_3\cdot2H_2O$(cr) solid phases, isolated before and after the solubility experiments in NaCl 0.10, 0.51, 5.6

m at T = 25, 55, 80 °C. Experiments were performed by using the 4th harmonic of a Nd:Yag laser (*SpitLight Compact 100, InnoLas Laser*) at 266 nm and 7 ns pulse duration as excitation source.

3.7 Solubility experiments with Ca-U(VI)-CO_3(s) phases

Solubility experiments in the ternary system Ca-U(VI)-carbonate were performed by equilibrating about 250 mg of synthetic liebigite, $Ca_2UO_2(CO_3)_3 \cdot 10H_2O$(cr), provided by Helmholtz-Zentrum Dresden Rossendorf (Dr. Steudner and Dr. Brendler) in 5 ml of (i) deionized water, (ii) 0.51 m NaCl, and (iii) 5.61 m NaCl solution. The pH_m of the samples was adjusted to 7.9 – 8.2 by using HCl/NaCl and NaOH/NaCl solutions of the same ionic strength. After the pH adjustment, the ionic strength of sample (i) is calculated to be *ca.* 0.03 m NaCl, according to the HCl/NaCl and NaOH/NaCl solutions spiked into the sample. A lab oven (Falc Instruments) was used for maintaining elevated temperature conditions (T = 80 °C). The pH_m value and U(VI) concentrations were regularly monitored within a period of 132 days. Total concentrations of U(VI) and Ca in the solutions were determined by using inductively-coupled plasma – mass spectrometry (ICP-MS, Perkin Elmer ELAN 6100) and inductively-coupled plasma – optical emission spectrometry (ICP–OES, Perkin Elmer OPTIMA 2000™), respectively, after phase separation by syringe filtration (Pall Acrodisc® filters, pore size 0.1 μm, PTFE membrane).

4. Results and discussion

4.1. Solubility and hydrolysis of $Nd(OH)_3(s)$ in NaCl 0.1, 0.5, 5.6 m at T = 25, 55, 80 °C

4.1.1 Solubility experiments

Figure 1 shows the solubility data of $Nd(OH)_3(s)$ at different temperatures and ionic media. A comparison of the newly measured solubility data with relevant literature data is provided. The solubility of $Nd(OH)_3(s)$ measured at T = 25 °C in [NaCl] = 0.10 and 0.51 m, is in good agreement with the corresponding data by Neck et al. in the same background electrolyte media [2]. In the present study and in the one by Neck et al., the initial material was prepared with the same procedure, involving the hydration of $Nd_2O_3(cr)$ in MilliQ water (18 MΩ/cm) at room temperature. In the present work, $Nd(OH)_3(s)$ was preliminary equilibrated at 80 °C before being used in all solubility experiments. The comparable solubilities of $Nd(OH)_3(s)$ prepared in the two works suggest little impact of temperature on the crystallinity of the solid phase. The measured solubility in [NaCl] = 5.6 m at pH_m = 8.6 compares well with the one determined by Neck et al., but it is significantly lower in the more acidic solutions, by up to two orders of magnitude at pH_m = 7 – 7.5.

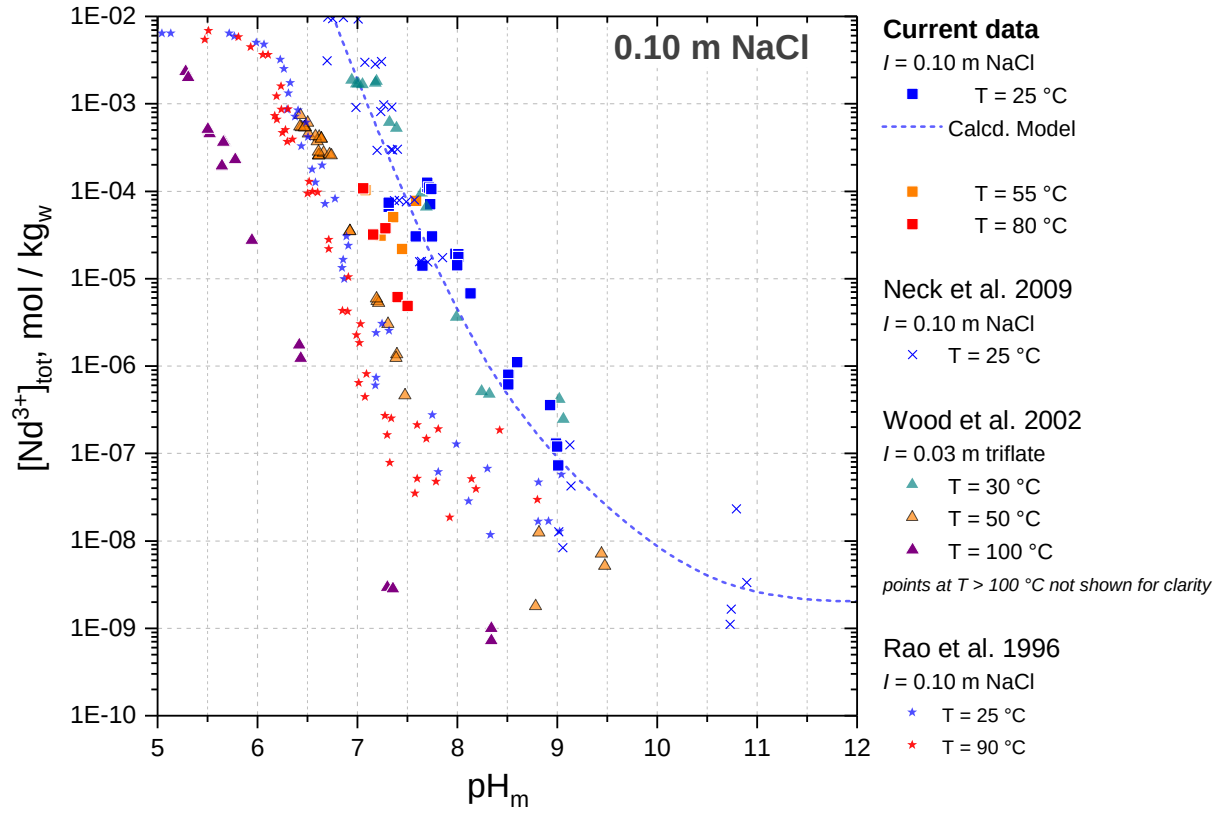

(a)

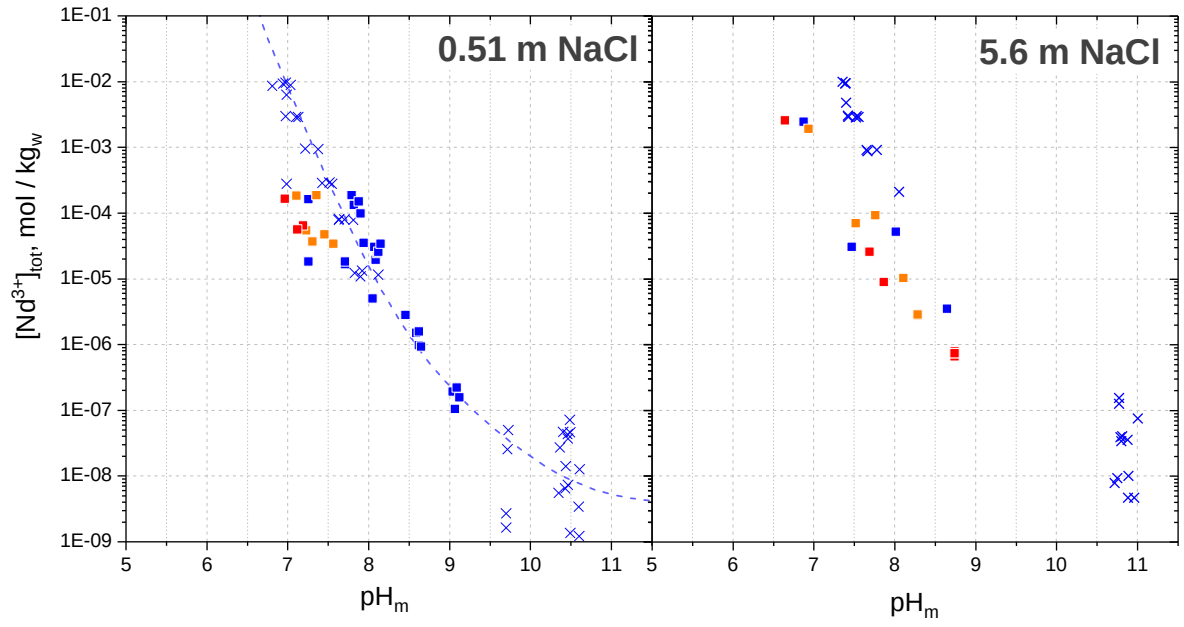

(b) (c)

Figure 1. *Solubility of $Nd(OH)_3(s)$ in [NaCl] = 0.1 (a), 0.51 (b), and 5.6 m (c) at T = 25, 55, 80 °C. Experimental data: Nd(III) concentration vs pH_m. Dashed lines: SIT model calculations at T = 25 °C. Relevant literature data also displayed for comparison: Neck et al. 2009 [2], Wood et al. 2002 [3], Rao et al. 1996 [4].*

The solubility of $Nd(OH)_3$(cr) determined by Wood et al. [3] ([$Na(CF_3SO_3)$] (Na-triflate) = 0.03 m, T = 30 °C) is in reasonable agreement with the one measured in the present work in [NaCl] = 0.10 m at T = 25 °C. Wood et al. prepared $Nd(OH)_3$(cr) by equilibration of Nd_2O_3(cr) in MilliQ water at T = 200-250 °C and saturated vapor pressure (2 weeks). Characterizations of the initial material by means of XRD, TGA and IR spectroscopy were consistent with $Nd(OH)_3$(cr). The similar solubility of the material prepared by Wood et al., with respect to the one in the present work, suggests that the crystallinity of the two $Nd(OH)_3$(s) solids does not depend significantly on the temperature of equilibration of the initial oxide.

The solubility of $Nd(OH)_3$(cr) measured by Rao et al. [4] in [NaCl] = 0.10 m at T = 25 °C is significantly lower than the one determined in the present work. It appears that the solid phase considered in Rao et al. was significantly more crystalline than the one investigated in the present work. In the work by Rao et al., $Nd(OH)_3$(cr) was prepared by firstly precipitating amorphous $Nd(OH)_3$(am) phase from a solution of $NdCl_3$ in the presence of concentrated NaOH. A slurry of the initial material was then aged in 5 M NaOH at 90 °C. The characterization conducted with XRD confirmed the solid initially precipitated turned into a crystalline material, $Nd(OH)_3$(cr) after aging. This preparative procedure should yield a material with a solubility similar to the one in the present work. Wood et al. [3] suggested that the solubility of Nd(III) determined by Rao et al. [4], significantly lower than expected, instead, could be attributed to the formation of a surface $Nd(OH)CO_3$(s) layer, less soluble than the hydroxide, not detectable by XRD, but controlling the overall solubility. In a previous contribution, Diakonov et al. also indicated that stable $Nd(OH)CO_3$(s) phases should already form in condition of CO_2 partial pressures as low as 10^{-6}–10^{-5} bar [5]. Thus, a great care is needed to avoid CO_2 contamination, during the preparation of $Nd(OH)_3$(cr) and the sampling operations.

Solubility data of $Nd(OH)_3$(s) determined at T = 55, 80 °C are shown in Figure 1 as orange and red bullets, respectively. Although these experiments were initially designed to cover the pH_m range 7 – 9.5, significant pH_m shifts were observed to occur overtime, as the solid phases equilibrated. Generally, an increase of pH_m was observed in samples with an initial pH_m < 7, while a decrease of pH_m occurred overtime in samples with pH_m above 8. In the first case, attempts were made to correct the alkalinity by addition of volumes of HCl solutions conveniently prepared in the same medium of the sample treated. The amounts and concentrations of these solutions were analytically calculated and a glass electrode was used to monitor the pH_m change following the dropwise additions. Despite this care, in some samples a quantitative dissolution of the solid phase occurred due to the acidification. Such samples were therefore discarded.

Due to these drawbacks, only few solubility data at T = 55, 80 °C were obtained and limited to a relatively narrow pH_m range. These data are too scarce to allow the modelling of the solubility of $Nd(OH)_3$(s) at the two higher temperatures, but a qualitative description can be provided. As shown in

Figure 1, the temperature has a modest impact on the solubility of $Nd(OH)_3(s)$. The solubility at T = 25, 55 °C appears comparable, within the uncertainties in [NaCl] = 0.10, 5.6 m. Data from experiments conducted in 0.51 m NaCl indicate a decrease of about ~ 0.5 log [Nd] units at T = 55 °C, with respect to the same data at T = 25 °C; a similar decrease is observed in solutions of [NaCl] = 0.1 – 5.6 m at T = 80 °C, with respect to corresponding data at T = 25°C in the same pH_m conditions.

These data are consistent with the results by Rao et al. (see Figure 1) [4], where a decrease of about ~ 0.8 log [Nd] units was observed at T = 90 °C, with respect to the concentration measured at T = 25 °C at the same pH_m. As already pointed above, in the work by Rao et al. the solubility of $Nd(OH)_3(cr)$ at T = 25 °C was significantly lower than the one in the present work. In the work by Wood et al. (Na-triflate 0.03 m, T = 30 – 290 °C) [3], a significant dependence of the solubility of $Nd(OH)_3(cr)$ on the temperature was found, instead, as evidenced by the data comparison in Figure 1. As opposed to the data previously published by Rao [4] and in the indications in the present work, the solubility of $Nd(OH)_3(cr)$ measured by Wood et al. was more than 4 orders of magnitude lower at 100 °C, with respect to the data at 30 °C. Such large differences between the three sets of experimental data by Wood, Rao and in the present work cannot be explained by the different background electrolytes used in the different works. The concentrations of Nd in the present work, being significantly higher than the one determined by Wood et al. [3], could instead be related to the formation of suspended colloidal phases with an average diameter < 100 nm, passing unfiltered during the sampling process. However, this is not supported by the current observations and the literature data. In fact, the solubility data at T = 80 °C show a linear trend of log[Nd] with pH_m ($\log[Nd]/pH_m \sim -3.0$) whereas, usually, the metal ion concentration in the colloidal fraction is expected to be mostly pH_m independent. In addition, Wood et al. [3] achieved the separation of the solid phases by using 0.2 µm pore-size PVDF filters, similarly to the one used in the present work. In the previous contribution by Rao et al. [4], the separation of the solid phases in experiments at T = 90 °C was achieved by centrifugating the samples at 2000 g, 20 min, 90 °C, followed by pipetting of the supernatants. As discussed by Neck and co-workers [2], the separation of potential colloidal particles with a diameter of about 10 – 50 nm cannot be achieved by regular centrifugation, but it requires ultracentrifugation / ultrafiltration procedures. This notwithstanding, for samples at T = 25 °C Rao et al. also compared the Nd concentrations of ultra-filtered (1.8 nm pore size) and unfiltered samples. The concentrations of Nd at $pH_m < 7.5$ were reproducible in the two sets. At $pH_m > 8$ a slightly higher Nd concentration in unfiltered samples, with respect to the filtered ones, was observed, suggesting the presence of possible colloidal fractions. Given the low Nd concentration at $pH_m > 8$ ([Nd] = $\sim 10^{-8}$ m), the samples collected in more acidic conditions were not affected by the presence of colloids, anyhow.

Another possible explanation is an alteration of the initial $Nd(OH)_3(cr)$ when equilibrating at T = 55 or 80 °C. On this regard, in both the previous contributions by Wood et al. [3] and Rao et al. [4], a characterization of the solid phases collected at the end of the solubility experiments was not conducted

or it is not reported in the publications. Wood et al. indicated that previous studies already showed that the $Nd(OH)_3$(cr) solid to be the stable phase in the Nd-O-H system from room temperature, up to ~ 800 °C, above which it transformed to NdOOH [6]. In the present work, the results of the post-experiment analysis of the solid phases equilibrated in dilute NaCl media (0.1, 0.5 m), discussed in the next section, consistently indicate that $Nd(OH)_3$(cr) is a stable phase up to T = 80 °C.

4.1.2 Characterization of the solid phases

The TGA analysis of the $Nd(OH)_3$(s) solid after its preparation (Figure 2a) is consistent with the expected stoichiometry. An overall weight loos of 9% was observed in the temperature range 210 – 550 °C, consistent with the decomposition reaction (1). The TGA diagrams suggest the reaction to occur in two steps, with formation of NdO(OH)(s) at T = 210 – 375 °C (1a), decomposing to Nd_2O_3(s) at T = 375 – 550 °C (1b). The percentage weight loss of the solid and the trend of the decompositions as function of temperature is consistent with the analogous analysis conducted by Wood et al. on the same initial material [3].

$$Nd(OH)_3(s) \rightarrow 0.5\ Nd_2O_3(s) + 1.5\ H_2O(g) \qquad T = 210 - 550\ °C \qquad (1)$$

$$Nd(OH)_3(s) \rightarrow NdO(OH)(s) + H_2O(g) \qquad T = 210 - 375\ °C \qquad (1a)$$

$$NdO(OH)(s) \rightarrow 0.5\ Nd_2O_3(s) + 0.5\ H_2O(g) \qquad T = 375 - 550\ °C \qquad (1b)$$

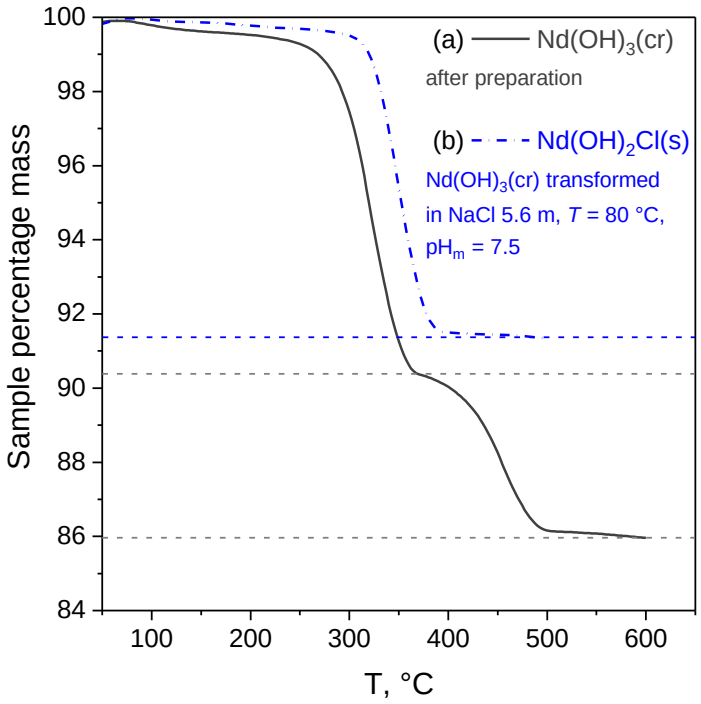

***Figure 2**. Thermo-Gravimetric Analaysis (TGA) diagrams of (a) $Nd(OH)_3(s)$ after preparation; (b) material equilibrated in NaCl 5.6 m, T = 80 °C, pH_m = 7.5, transformed into a solid consistent with the stoichiometry $Nd(OH)_2Cl(s)$ (XRD characterization in Figure 3).*

Figure 3 shows the XRD spectra of the solid phases isolated before (a) and after the solubility experiments at T = 80 °C (b – e). Reference XRD patterns of well-characterized solid phases are shown for comparison ($Nd(OH)_3$(cr), JSPD file 70-0215 [7], $Nd(OH)_2Cl$(cr), JSPD file 72-1812 [8]).

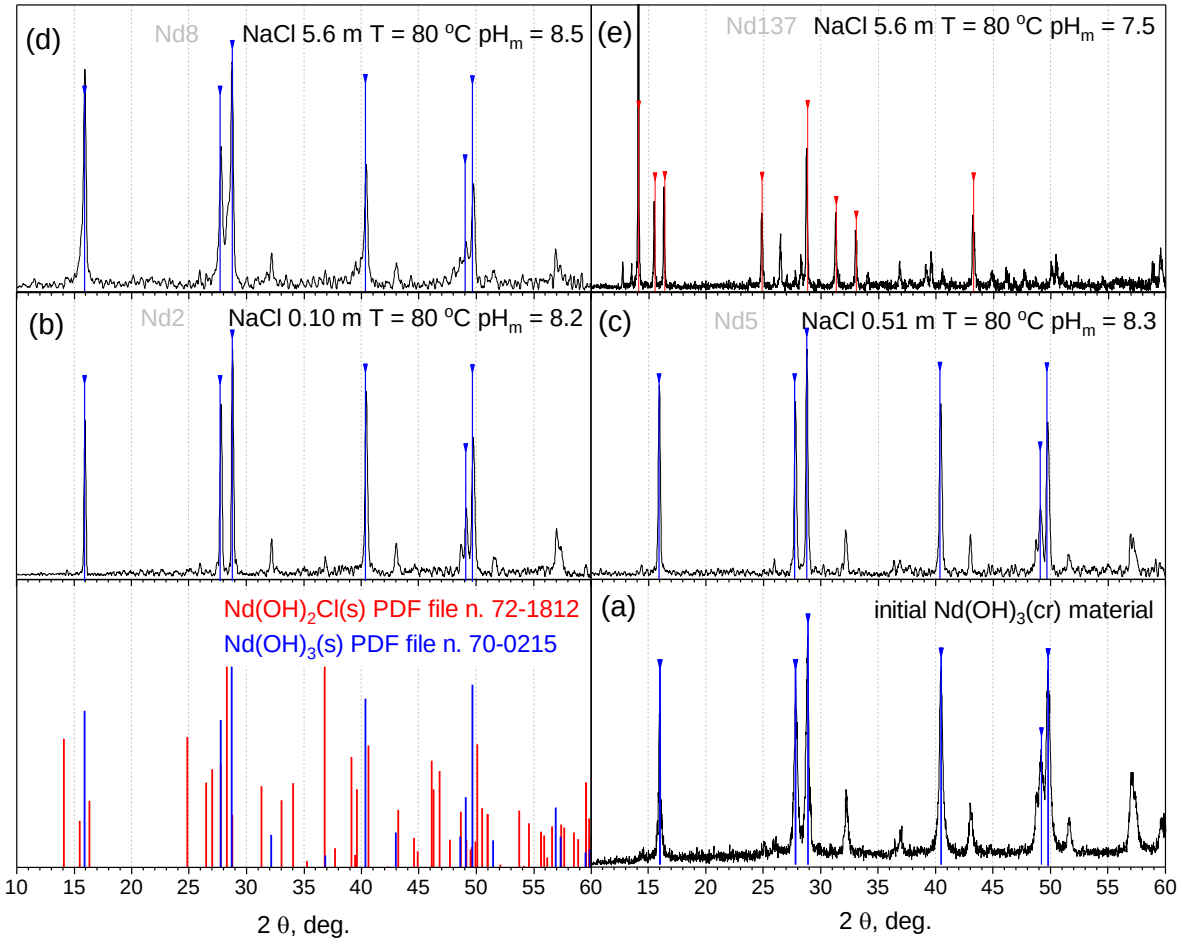

Figure 3. *Bottom, left: XRD patterns of known solid phases $Nd(OH)_3$(cr) (PDF file n. 70-0215 [7]) and of $Nd(OH)_2Cl$(cr) (PDF file n. 72-1812 [8]). (a) Initial material, characterized as $Nd(OH)_3$(s); (b) $Nd(OH)_3$(s) equilibrated in [NaCl] = 0.10 m, T = 80 °C, pH_m 8.2; (c) $Nd(OH)_3$(s) equilibrated in [NaCl] = 0.51 m, T = 80 °C, pH_m 8.3; (d) $Nd(OH)_3$(s) equilibrated in [NaCl] = 5.6 m, T = 80 °C, pH_m 8.5; (e) $Nd(OH)_3$(s) equilibrated in [NaCl] = 0.10m, T = 80 °C, pH_m 7.5.*

Results indicate that the starting $Nd(OH)_3$(s) material is stable in [NaCl] = 0.10 and 051 m in all equilibration conditions at elevated temperatures. XRD patterns of these solid phases are consistent with that of the initial material and of the reference $Nd(OH)_3$(s). In solutions with [NaCl] = 0.10 and 051 m at T = 25, 55 °C the initial material also proved stable over time, consistently with the results from previous publications [2, 9]. In solutions with [NaCl] = 5.6 m, T = 80 °C, pH_m = 8.5 the initial material also turned out to be stable. At lower pH_m, a solid phase transformation was observed. The pattern of the transformed material (Figure 3e) is consistent with that of the ternary $Nd(OH)_2Cl$(cr) [8] (Figure 3, red). A TGA analysis of the transformed solid (Figure 2b) also suggests this stoichiometry. A single-step decomposition was observed in the temperature range 290 – 500 °C, characterized by a weight loss of 8.5 % of the initial material, consistently with the decomposition reaction (2)

$$Nd(OH)_2Cl(s) \rightarrow NdOCl(s) + H_2O(g) \quad (2)$$

In a recent work, a similar solid phase transformation was observed to occur at room temperature in concentrated brine systems with $[Mg^{2+}] > 4.05$ m, $[Cl^{-}] > 5.82$ m [9, 10]. The transformation occurs according to the equilibrium (3), only in the presence of high chloride concentrations at $pH_m < 8.5$.

$$Nd(OH)_3(s) + Cl^- \Leftrightarrow Nd(OH)_2Cl(s) + OH^- \quad (3)$$

The concentration of Nd(III) in solutions where the transformation of the solid phase occurred was markedly lower that the one of $Nd(OH)_3(s)$ based on the model by Neck et al. [2]. This suggests a control of the solubility by $Nd(OH)_2Cl(s)$ in these conditions.

4.2 Impact of elevated temperature on Th(IV) solid phases and solubility

4.2.1 Solubility experiments in the absence of carbonate

Figures 4 and 5 show the experimentally measured solubility of Th(IV) hydrous oxide (freshly precipitated, or aged at T = 80 °C for t = 1, 2 and 4.5 months at $pH_m = 3$ and 12.8). The figures also show the solubility curves corresponding to freshly precipitated, aged and crystalline ThO_2 solid phases calculated using the thermodynamic selection in the NEA-TDB [11].

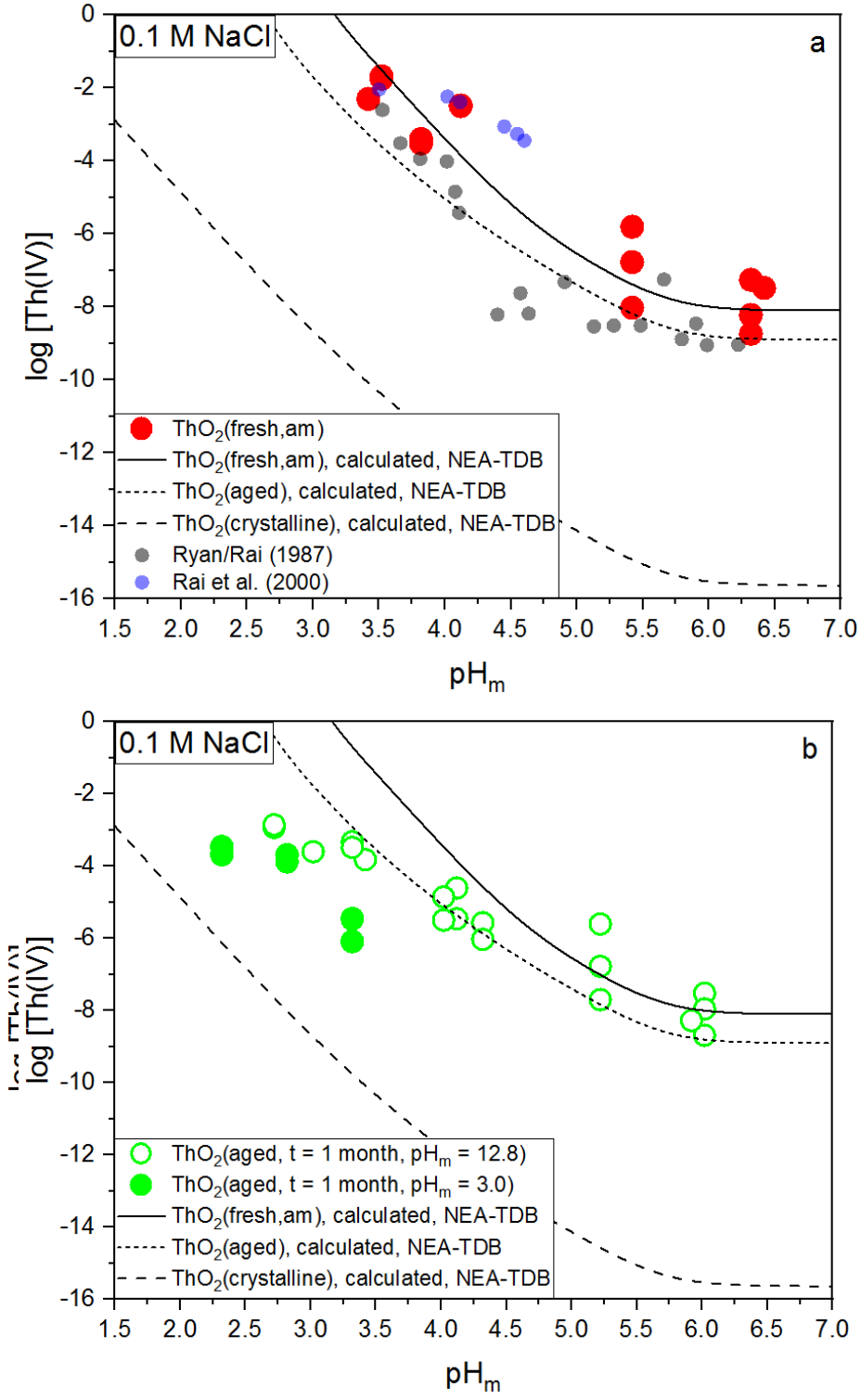

Figure 4. *Solubility of Th(IV) hydrous oxide: (a) freshly precipitated; (b) aged for 1 month at T = 80 °C and pH_m = 3 and 12.8. All solubility experiments conducted in 0.1 M NaCl. Experimental solubility data reported in the literature for ThO_2(am, hyd) in 0.1 M NaCl and $NaClO_4$ systems appended for comparison [12, 13]. Solid, dotted and dashed lines correspond to the solubility curves for ThO_2(am, hyd, fresh), ThO_2(am, hyd, aged) and ThO_2(cr) using thermodynamic data selected in the NEA-TDB [11].*

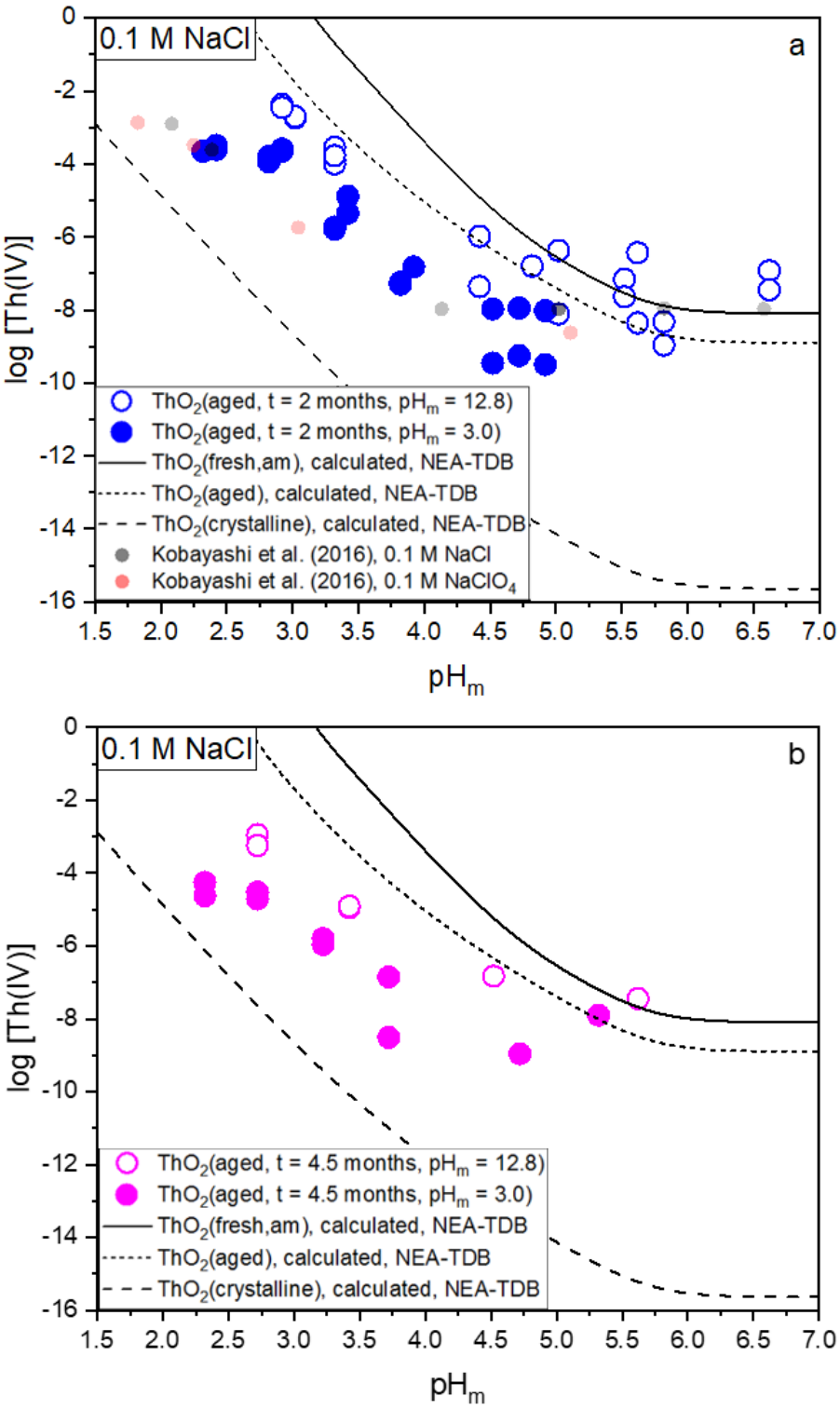

Figure 5. *Solubility of Th(IV) hydrous oxide: (a) aged for 2 months at T = 80 °C and pH_m = 3 and 12.8; (b) aged for 4.5 months at T = 80 °C and pH_m = 3 and 12.8. All solubility experiments conducted in 0.1 M NaCl. Experimental solubility data reported in the literature for ThO_2(am, hyd) in 0.1 M NaCl and $NaClO_4$ systems appended for comparison [14]. Solid, dotted and dashed lines correspond to the solubility curves for ThO_2(am, hyd, fresh), ThO_2(am, hyd, aged) and ThO_2(cr) using thermodynamic data selected in the NEA-TDB [11].*

The experimental data on the freshly precipitated Th(IV) hydrous oxide agrees well with the solubility calculated for ThO_2(am, hyd, fresh) using the thermodynamic data selected in the NEA-TDB. Experimental data are also in moderate agreement with previous studies reporting on the solubility of ThO_2(am, hyd) at T = 25 °C in 0.1 M NaCl or $NaClO_4$ [12, 13]. All aged Th(IV) solid phases show lower solubilities than ThO_2(am, hyd, fresh), consistently with the increase in particle size / crystallinity observed by XRD. Solubility data obtained for the Th(IV) solid phase aged for two months at $pH_m = 3$ is also in good agreement with experimental data reported by Kobayashi and co-workers for a solid phase aged at T = 90 °C during 6-8 weeks (see Figure 5a) [14]. Note, however, that Kobayashi et al. followed a different ageing approach as used in this study – each independent solubility sample was aged at T = 90 °C at the target pH (ranging between ≈ 1.5 and ≈ 9), whereas in the present work the solid phase used in each solubility series was aged at a single pH. Because of the impact of pH in the ageing process (see also next paragraph), the different ageing approach followed in Kobayashi et al. and in this work may lead to differences in the solubility data, especially in the less acidic samples.

Experimental data in Figure 4 and Figure 5 show that the solubility of the Th(IV) hydrous oxide slightly decreases with the ageing time at T = 80 °C. Unexpectedly, the pH at which the Th(IV) solid phase was aged has a strong effect on the solubility measured at T = 22 °C. Hence, the solid phases aged at $pH_m = 3$ show up to 2 orders of magnitude lower solubility than the solid phases aged at $pH_m = 12.8$. This effect is reproduced for the solid phases aged during 1, 2 and 4.5 months. These observations are apparently in contradiction with the minor differences observed by XRD, TG-DTA and XPS for Th(IV) solid phases aged for different contact times and at different pH values. However, these results can be made consistent by claiming a solubility control established by a few monolayers of the ThO_2(s, hyd) surface. Such few monolayers have a minor weight in bulk characterization methods (XRD, TG-DTA) but also in "surface-sensitive" methods like XPS, which provides average values of a ≈ 4 nm layer. This hypothesis is also in line with previous studies by Grambow, Vandenborre and co-workers [15, 16], who claimed that solubility measurements of ZrO_2(s), ThO_2(s) and UO_2(s) are not representative of the bulk phase, but are rather controlled by surface processes of a few monolayers of the corresponding oxide. Although the starting materials used in these studies were crystalline oxides sintered at very high temperatures (400-1000 °C), the authors claimed that "solubility" of Th(IV) system was controlled by "$ThO_x(OH)_y(H_2O)_z$" present at the grain boundaries.

4.2.2 Solubility experiments in the presence of carbonate

Experimental solubility data at T = 22 and 80 °C determined in this work for the aged solid phase ThO_2(ncr,hyd, t = 2 m, $pH_m = 12.8$) in 0.1 M NaOH systems with $0.01\ M \leq [CO_3^{2-}]_{tot} \leq 1.5\ M$ are shown in Figure 6. The figure also shows solubility data at T = 22-25 °C previously reported by Altmaier et al. and Rai et al. under analogous carbonate concentrations [17-19]. Solid blue line in the figure corresponds

to thermodynamic calculations conducted for the solid phase ThO_2(ncr, hyd, t = 2 m, pH_m = 12.8) considering enthalpy data provided by Amphos[21] in the context of the ThermAc project for the solid phase $ThO_2 \cdot H_2O$(s) and the ternary Th(IV)-OH-CO_3 complexes expected to dominate the Th(IV) aqueous speciation in the investigated carbonate systems.

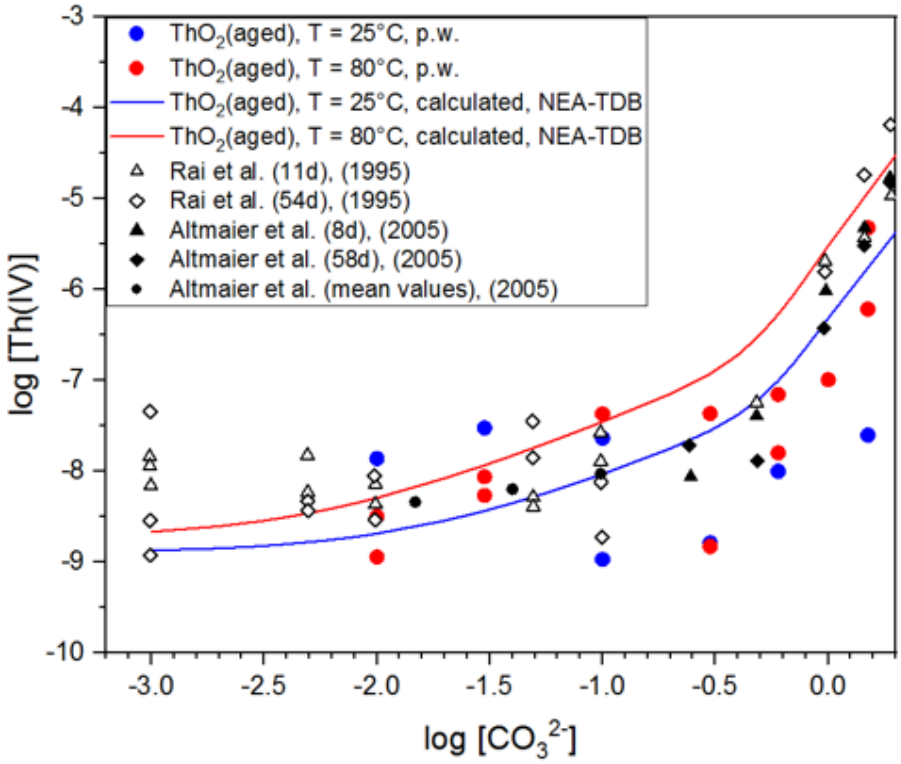

Figure 6. *Solubility of the aged phase ThO_2(ncr, hyd, t = 2 m, pH = 12.8) at T = 22 and 80 °C determined in this work in 0.1 M NaOH systems with 0.01 M ≤ $[Na_2CO_3]_{tot}$ ≤ 1.5 M. Experimental solubility data at T = 22-25 °C reported by Altmaier et al. [17] and Rai et al. [17-19] are appended for comparison. Solid lines correspond to thermodynamic calculations at T = 22 and 80 °C using thermodynamic data derived in this work, selected in the NEA-TDB and estimated by Amphos[21] (see text).*

Experimental data determined in this work show a large dispersion, and only data at the highest carbonate concentration show a clear increase in the solubility, both at T = 22 and 80 °C. Although not evident because of the data dispersion, solubility data at T = 22 °C are slightly lower than solubility data previously reported by Altmaier et al. [17]). This is in agreement with the lower solubility observed in this work for a solid phase previously aged for two months at T = 80 °C, ThO_2(ncr, hyd, t = 2 m, pH_m = 12.8). At high $[Na_2CO_3]_{tot}$, slightly higher Th concentrations are measured at T = 80 °C compared to solubility data at T = 22 °C. This trend is consistent with thermodynamic calculations performed using the estimated enthalpy values.

Experimental data obtained in this work indicate that although complexation with carbonate is enhanced by temperature, this effect is mostly compensated by the increased crystallinity of ThO_2(s, hyd) with the corresponding decrease in solubility. Experimental data determined in this work do not allow deriving thermodynamic data for the Th(IV)-OH-CO_3 system at elevated T, but enthalpy estimates in combination with equilibrium constants selected in the NEA-TDB can be used to assess upper solubility limits in alkaline systems in the presence of carbonate.

4.2.2 Solid phase characterization by powder XRD

The powder diffractograms collected for the solid phases investigated within this study are shown in Figure 7.

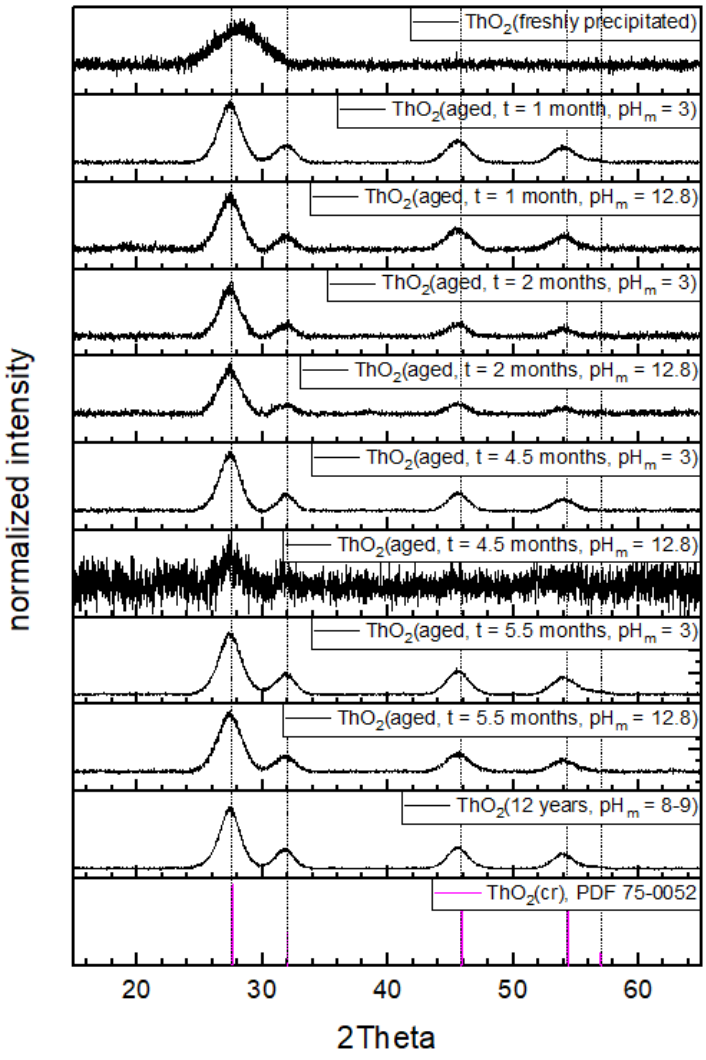

Figure 7. *Diffractograms of the Th(IV) solid phases synthesized in this work and equilibrated at T = 80 °C and pH_c(25 °C) = 3 and 12.8, except for sample "ThO_2(freshly precipitated)" measured 2 days after precipitation. Vertical dashed lines refer to the ThO_2(cr) reference (PDF 75-0052).*

An XRD pattern corresponding to a rather amorphous material is observed for the freshly precipitated Th(IV) solid phase. This is in line with previous observations reported in the literature for freshly precipitated Th(IV) hydrous oxide [14]. In all other cases, XRD patterns show broad peaks with well-defined 2Θ positions, reflecting a higher degree of crystallinity for the Th(IV) aged samples. No significant differences are visually observed in the diffractograms of Th(IV) solid phases aged for different times or at different pH values. The peak positions in the XRD of the aged samples are in good agreement with reference data reported for ThO_2(cr) in the JCPDS database, *i.e.* with main reflections at 2Θ = 27.6, 32.0, 45.9, 54.4 and 57.0. Good agreement is also obtained with the peak positions in the XRD reported by Kobayashi and co-workers for Th(IV) solid phases aged at T = 90 °C for 3-6 weeks in 0.1-2.0 M $NaClO_4$ and 0.1-3.0 M NaCl [14].

The Scherrer analysis is used to gain insight on the particle size of the solid phases on the basis of the evaluation of the full width at half maximum (FWHM) intensity of the XRD peaks. The results of this analysis are summarized in Table 1.

Table 1. *Scherrer analysis of selected Th(IV) solid phases investigated in this work.*

Sample	**particle size/nm***
ThO_2(freshly precipitated)	1.5
ThO_2(aged, t = 1 month, pH_m = 3)	4.4
ThO_2(aged, t = 1 month, pH_m = 12.8)	4.1
ThO_2(aged, t = 2 months, pH_m = 3)	4.7
ThO_2(aged, t = 2 months, pH_m = 12.8)	4.1
ThO_2(aged, t = 4.5 months, pH_m = 3)	4.8
ThO_2(aged, t = 4.5 months, pH_m = 12.8)	n.d.
ThO_2(aged, t = 5.5 months, pH_m = 3)	4.6
ThO_2(aged, t = 5.5 months, pH_m = 12.8)	4.1
ThO_2(12 years, pH_m = 8-9)	4.9

n.d.: not determined due to the poor quality of the diffractogram; * uncertainty estimated as ± 0.5 nm.

A large difference between the particle size of freshly precipitated and aged solid phases is observed. In addition to that, data reported in Table 1 hint to a slight increase in the particle size with aging at pH_m = 3 compared to the samples aged at pH_m = 12.8 for the same period. This behaviour might be related to the higher solubility of Th(IV) at pH_m = 3 (≈ 10^{-2} M, calculated at T = 25 °C for ThO_2(am,hyd,aged)) than at pH_m = 12.8 (≈ 10^{-8} M), which is expected to trigger a faster increase in the particle size through enhanced dissolution and precipitation reactions.

Using also the Scherrer analysis, Kobayashi and co-workers reported particle sizes between 3.1 and 4 nm for selected Th(IV) solid phases aged at T = 90 °C [14]. Note, however, that the strategy followed by these authors was different than the one considered in the present work. Hence, Kobayashi *et al.* equilibrated the Th(IV) solid phases at elevated temperature within a range of pH_c values (1.2-9.4). Then, the samples were cooled down, and solubility measurements were performed at T = 25 °C without further modification of the pH_c. The values of particle size indicated above were measured for Th(IV) solid phases aged at $5.6 \leq pH_c \leq 9.4$ (Figure 4 in [14]), but no XRD were collected for solid phases aged in more acidic conditions.

4.3 Transformation of Np(V) solid phases at elevanted temperatures

4.3.1 Solubility measurements

The aqueous phase of the Np samples are analyzed for [Np], pH_m, and E_h before and after 30 days of heating. As shown in Table 2, pH_m values did not significantly change after equilibration at T = 80 °C due to the high OH^- content. In both cases, measured E_h values have slightly increased after heating, presumably indicating that Np(VI) had partially formed during heating. Indeed, the measured $pe + pH_m$ values are located within the stability field of Np(VI), *cf.* Pourbaix diagrams for Np in the literature [20]. The total Np concentrations in the samples after 30 days of heating are displayed in Figure 8 in comparison to the calculated solubility of NpO_2OH(am,fresh) using the computational code PHREEQC [21] with ThermoChimie database (v.9a) [22]. The experimental solubility data obtained in 0.1 M NaOH are relatively consistent with the theoretical values in 0.1 m.

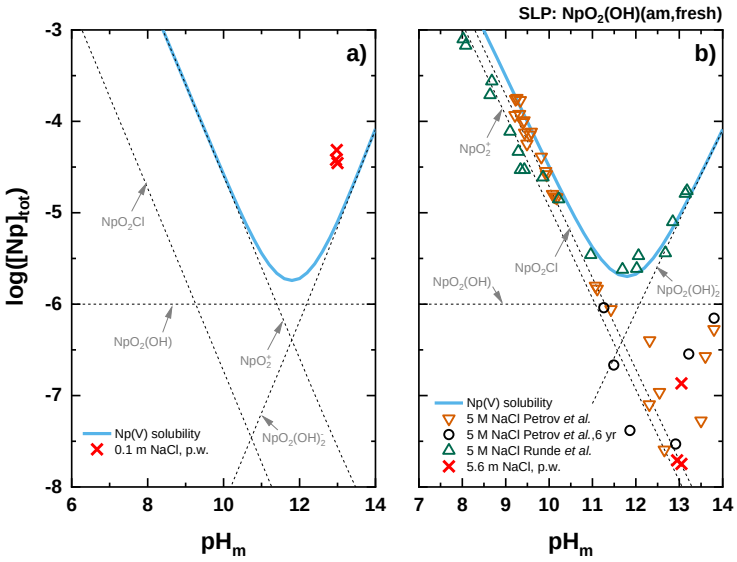

Figure 8. *Experimental Np(V) solubility in (a) 0.1 m NaOH and (b) 5.6 m NaCl solutions determined after 30 days of heating period in comparison to the solubility data of $NpO_2OH(am)$ in 5 M NaCl reported by [23, 24]. Solid lines represent the calculated solubility of $NpO_2(OH)(am,fresh)$.*

This indicates that the initial $NpO_2OH(am,fresh)$ controlled the Np(V) solubility after the heating period in these samples, even though partial transformation is evident in these samples based on results discussed in section 4.3.2. Considerably lower solubility compared to the calculated level of $NpO_2OH(am,fresh)$ is observed for sample in 5.6 m NaCl under hyper-alkaline condition, which can be explained by the complete transformation of initial $NpO_2OH(am,fresh)$ into more stable Np(V) solid phases.

4.3.2 Solid phase characterization

After 30 days of heating, partial or complete transformation of the initial greenish $NpO_2OH(am,fresh)$ into violet, crystalline Np(V) phase takes place in 0.1 m NaOH and 5.6 m NaCl with $pH_m \approx 13$. Additional analysis by XRD, SEM-EDS, and XPS are performed with the violet transformation products as shown in Table 2.

Table 2. *Characteristics of transformed Np(V) solid phases tempered at T = 80 °C for 30 days.*

Sample	Background solution	pH_m		E_h (mV)		Color of solid	$[Np]_{aq}$ (mol/l)	Np : Na ratio		
		Initial	Final	Initial	Final			ICP-MS/OES	SEM-EDS	XPS
3	0.1 m NaCl	12.9	13.0	+82	+203	Violet	3.5×10^{-5}	1 : 0.6	1 : 0.4	1 : 0.6
5	5.6 m NaCl	13.0	13.1	-18	+132	Violet	1.8×10^{-8}	1 : 0.9	1 : 0.7	1 : 1.3

The patterns of the two Np(V) solids studied by powder XRD analysis are displayed in Figure 9. In comparison to the amorphous NpO_2OH(am,fresh) starting material, the tempered solid phases show sharp and well localized peaks. This confirms transformation into crystalline Np(V) compounds upon heating.

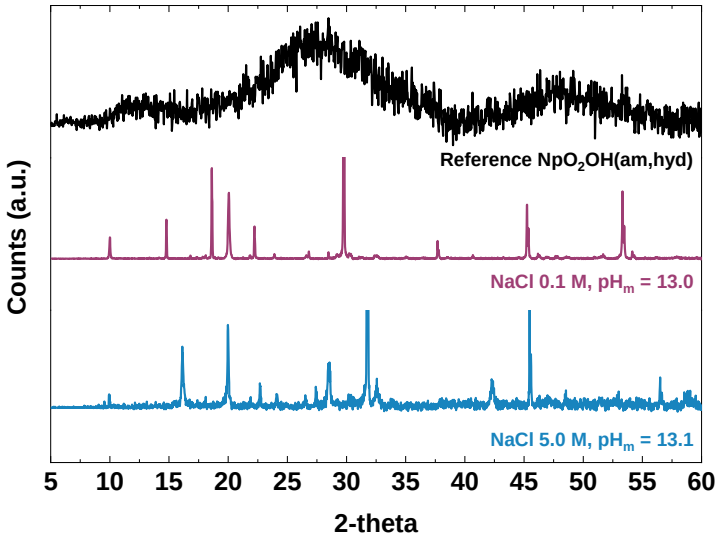

Figure 9. *Powder X-ray diffraction patterns of the transformed Np(V) solid phases in comparison to the one for NpO_2OH(am,fresh) [25].*

SEM pictures of the investigated Np(V) transformation products are displayed in Figure 10. Both samples show relatively well-defined crystalline morphologies, as expected by the characteristic powder XRD patterns.

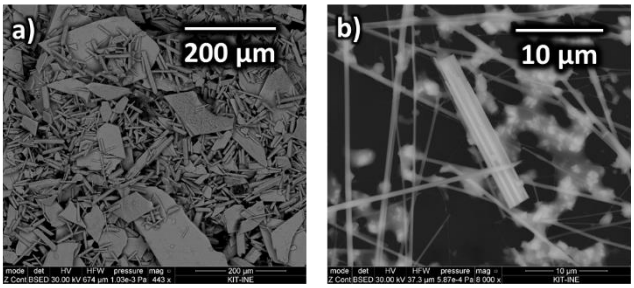

Figure 10. *SEM images of the transformed Np(V) solid phases. (a) 0.1 m NaOH; (b) 5.6 m NaCl, pH_m = 13.0.*

Formation of large platelet-like crystals is identified for the sample tempered at 0.1 m NaOH. The experimental Np : Na ratio of 1 : 0.6 determined by ICP-MS/OES agrees well the SEM-EDS results (1 : 0.4). For the system with 5.6 m NaCl and pH_m = 13.1, the transformed Np(V) solid phase has a needle-like morphology, providing Np : Na ratios of 1 : 0.9 (ICP-MS/OES) and 1 : 0.7 (SEM-EDS). Petrov et al. [24] observed the transformation of initial NpO_2OH(am,fresh) in 5.6 m NaCl at room temperature into a crystalline Na-Np(V)-O(H) solid phase which shows very similar morphology and Na : Np ratio. The powder XRD pattern reported by Petrov et al. matches the one reported for $Na[Np(V)O_2(OH)_2]$ [26], but mismatches the one of the present work.

Further detailed information on the oxidation state and structural characteristics of the transformed Np solid phases are obtained from the XPS. The Np4f and O1s XPS peaks of the transformed Np(V) phases are displayed in Figure 11. The basic lines of the Np4f doublet directly related to the spin orbit splitting ($4f_{5/2}$ and $4f_{7/2}$) are similar to other reference Np solid phases [27-29].

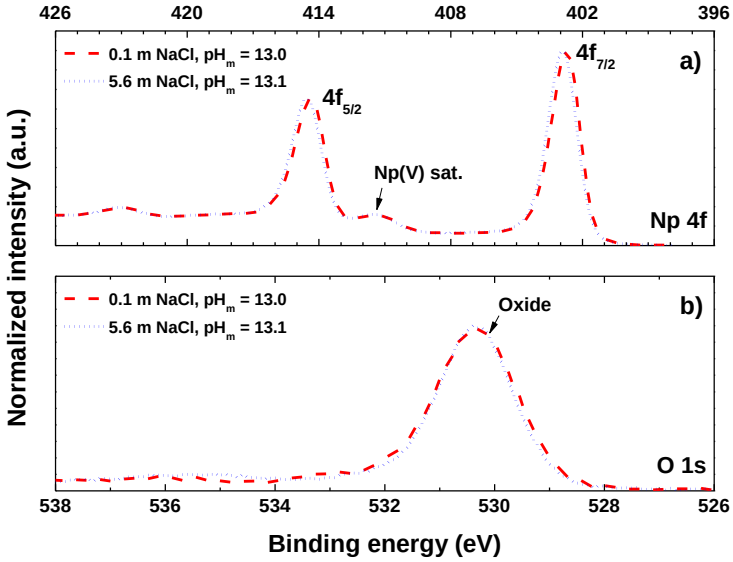

Figure 11. *XPS spectra of (a) Np4f- and (b) O1s-signal of the investigated Np solid phases.*

Pentavalent Np as predominant oxidation state in the transformed solid phases is confirmed from the binding energy relevant to Np4f. As listed in Table 3, the average binding energy distance, $\Delta E_{sat.}$, between the $Np4f_{7/2}$ basic line and its satellite is determined to be 8.6 eV for the transformed Np solid phases. This is in good agreement with reported data for other Np(V) compounds and clearly hints to the presence of pentavalent Np(V), especially as tetravalent or hexavalent Np solid phases show significantly different values ($\Delta E_{sat.}$ = 7.0 eV for $Np(IV)O_2$ and $\Delta E_{sat.}$ = 3.5 eV for $Cs_2Np(VI)O_2Cl_4$, respectively).

Table 3. *XPS binding energies of the transformed Np(V) solid phases.*

Solids	Binding energy (eV)			Ref.
	$Np4f_{7/2}$	$Np4f_{5/2}$	$\Delta E_{sat.}(Np4f_{7/2})$	
0.1 m NaOH	402.7	414.5	8.6	p.w.
5.61 m NaCl pH_m 13	402.9	414.4	8.6	p.w.
$Np(IV)O_2$	402.5	414.3	7.0	[27]
$RbNp(V)O_2(NO_3)_2 \cdot 2H_2O$	403.6	415.3	9.2	[29]
$Cs_2Np(V)O_2(OAc)_3$	403.0	414.6	9.2	[29]
$Cs_3Np(V)O_2Cl_4$	403.4	415.2	9.4	[28]
$Cs_2Np(VI)O_2Cl_4$	404.6	416.4	3.5	[28]

4.4 Np(IV)/Np(V) redox behavior

In the AQDS/AH_2QDS redox system, measured pH_m values remained at a constant level in most of the samples within the 316 days of investigation. The maximum deviation between initial and final E_h values within the timeframe of the experiment was less than 90 mV for all cases. As shown in Figure 12a, quantitative decrease of the initial Np(V) concentration takes place within 1 day for all AH_2QDS/AQDS samples. As the experimental E_h values were quite negative and clearly within the stability of Np(IV) in all cases, this observation can be explained by the quantitative reduction of initial Np(V) to sparingly soluble NpO_2(am,hyd) according to equation (4):

$$NpO_2^+ + e^- \leftrightarrow NpO_2(am,hyd) \quad (4)$$

Table 4. *The pH_m and E_h values of the redox system with Np(IV)/Np(V) equilibrated at T = 80 °C.*

Redox system	pH buffer	pH_m		E_h (mV)[a]	
		Initial	Final	Initial	Final
AQDS	MES	5.5	5.5	– 149	– (134 ± 9)
	HEPES	6.6	6.7	– 221	– (158 ± 19)
	CHES	8.0	8.0	– 287	– (211 ± 2)
	NaOH	9.9	10.0	– 329	– (253 ± 16)
Fe powder	HEPES	6.6	6.6	– 163	– (113 ± 7)
	CHES	8.1	8.1	– 279	– (239 ± 18)
	NaOH	10.1	10.2	– 65	– (345 ± 1)
$SnCl_2$	MES	5.6	5.7	– 149	– (166 ± 3)
	HEPES	6.8	6.8	– 263	– (280 ± 4)
	CHES	8.2	8.2	– 298	– (418 ± 4)
	NaOH	9.9	10.0	– 591	– (627 ± 8)
Hydroquinone	MES	5.5	5.6	89	19 ± 2
	HEPES	6.6	6.6	57	– (13 ± 8)
	CHES	8.1	8.1	– 47	– (115 ± 3)
	NaOH	9.9	10.0	– 234	– (253 ± 5)
Fe(II)/Fe(III)	MES	5.0	5.0	163	26 ± 8
	HEPES	6.2	6.2	135	– (6 ± 1)
	CHES	8.0	8.1	186	– (80 ± 1)
	NaOH	9.8	10.0	23	– (188 ± 2)

a. compensated to standard hydrogen electrode

According to the equilibrium reaction (4), the reduction of initial aqueous NpO_2^+ to solid NpO_2(am,hyd) becomes more favorable at lower E_h values. The reduction rate, empirically defined in terms of the slope of log [Np(V)] versus reaction time, can provide insight into the reaction kinetics for given system.
As the first sampling after 1 day already indicated complete reduction of the initial Np(V), only an upper-limit value for the reduction rate can be estimated for the AQDS system. Assuming a pseudo first-order rate law for the Np(V) reduction by AH_2QDS (as the amount of reducing reagent in the system is much higher than that of Np(V), this assumption is justified) with the empirical rate law

$$[Np]_{tot}(t) = [Np]_{tot}(0) \cdot \exp(-k \cdot t) \quad (5)$$

where $[Np]_{tot}(t)$ is the total aqueous Np concentration measured as a function of time t and k represents empirical rate constant, $k \geq \approx 3 \pm 0.5$ day^{-1} can be obtained.

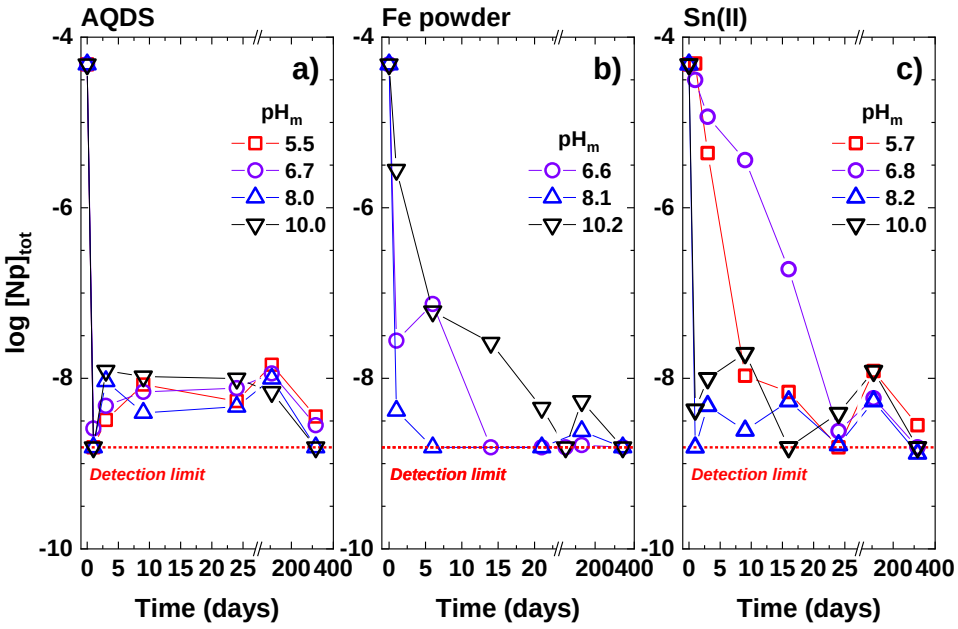

Figure 12. *Total aqueous Np concentration measured as a function of reaction time at T = 80 °C with (a) AH_2QDS/AQDS, (b) Fe powder, (c) $SnCl_2$ redox system at various pH_m conditions. Dashed line indicates detection limit of quantification analysis.*

Similar reducing tendency of Np(V) towards Np(IV) is observed for the redox systems with Fe powder and $SnCl_2$. The difference between the initial and final E_h values is found to be $\Delta E_h \leq 75$ mV, except for Fe powder system at $pH_m = 6.7$ ($\Delta E_h = 112$ mV). Figure 12b shows the results obtained in the Fe powder redox system. In all samples ($pH_m = 6.6$ to 10.2), initial Np(V) is quantitatively reduced within 1 to 25 days. The reduction is the slower the higher pH_m (and, likewise, the lower E_h) is. This is in contrast to the results obtained for the other redox systems, and might be explained by a specific passivation of the iron powder at greater alkalinity. In $SnCl_2$ containing solutions with pH_m 5.7 to 10.0 and experimental redox potentials of – (166 ± 3) mV to – (627 ± 8) mV, initial Np(V) was quantitatively reduced within maximum 25 days. In spite of showing the lowest redox milieu $pe+pH_m$ of all investigated systems, the reduction rates were at an average level. This may be due to the fact that the initial $SnCl_2$ is mainly present as $SnO{\cdot}xH_2O$(s) under the experimental conditions so that the equilibrium concentration of dissolved Sn(II)(aq), that can be considered as the actual reducing agent, is rather low.

In hydroquinone samples with $pH_m \geq 8.1$ and in Fe(II)/Fe(III) buffered solutions with $pH_m \geq 6.2$, more than 99% of the initial Np(V) is reduced within 35 days. Significantly slower reduction rates are observed for the hydroquinone and Fe(II)/Fe(III) samples equilibrated at lower pH_m values, see Figure 13. Particularly at the respective lowest pH_m values, reduction of initial Np(V) to Np(IV) was still ongoing at the termination of the experiment at t = 316 days. The sluggish Np(V) reduction rates in these

systems correlate with relative positive redox potentials (E_h = 19 ± 2 mV and 26 ± 8 mV for hydroquinone and Fe(II)/Fe(III), resp.) which are the most positive values of all investigated samples.

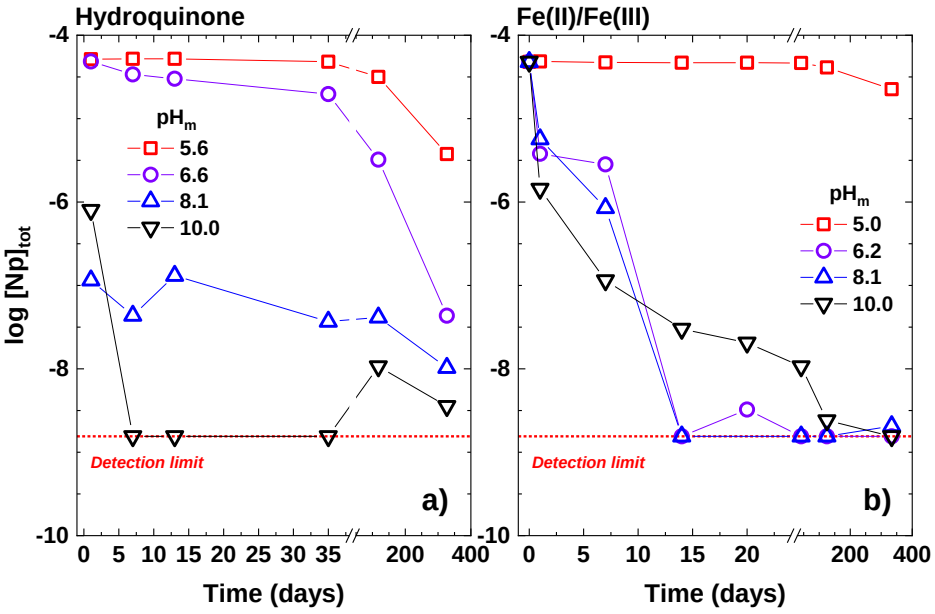

Figure 13. *Total aqueous Np concentration measured as a function of reaction time at T = 80 °C with (a) hydroquinone and (b) Fe(II)/Fe(III) redox system at various pH_m conditions. Dashed line represents detection limit of quantification analysis.*

4.5 Solubility and hydrolysis of U(VI) at elevated temperature

4.5.1 Solubility experiments

Figure 14 shows the solubility data determined in this work for $UO_3 \cdot 2H_2O$(cr) and $Na_2U_2O_7 \cdot H_2O$(cr) in [NaCl] = 0.1, 0.51 and 5.6 m solutions at *T* = 25, 55 and 80 °C. The figure shows also solubility data determined in 0.51 m NaCl at *T* = 22 and 80 °C, as well as data reported in Altmaier et al. at *T* = 22 °C in 0.51 and 5.61 m NaCl solutions [30].

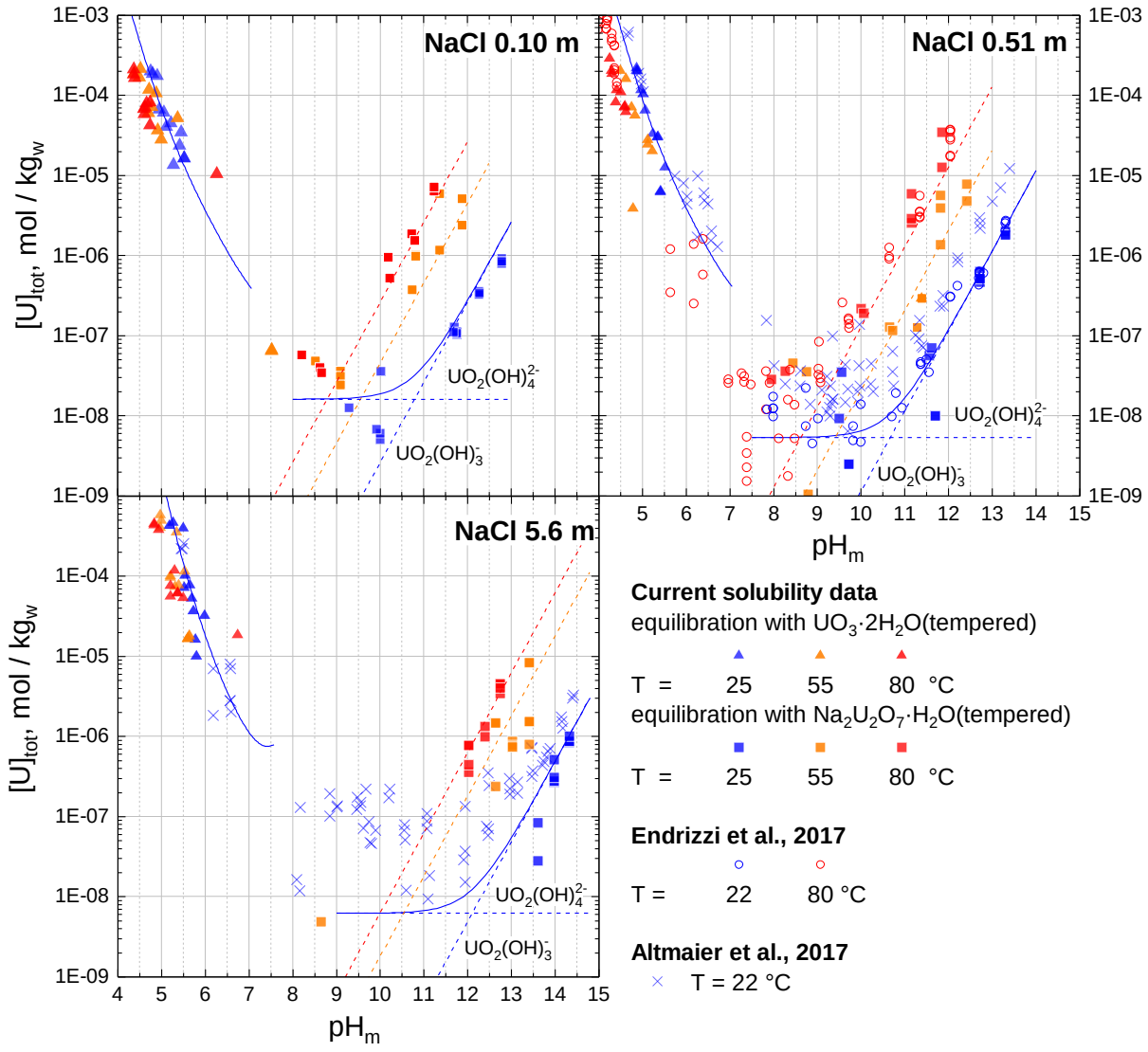

Figure 14. *Solubility of $UO_3{\cdot}2H_2O$(cr) and $Na_2U_2O_7{\cdot}H_2O$(cr) in [NaCl] = 0.1, 0.51 and 5.6 m at T = 25, 55, 80 °C. Solid thick lines correspond to the solubility at T = 25 °C calculated using the SIT model. Dashed lines indicate the contribution to the solubility of the $UO_2(OH)_4^{2-}$ (1,4) species. Data reported by Endrizzi et al. and Altmaier et al. are included for comparison [30, 31].*

The solubility at room temperature of $UO_3{\cdot}2H_2O$(cr) in acidic 0.51 m NaCl compares well with the one determined by Altmaier et al. in the same conditions [30]. The solubility of the same material measured at T = 55 and 80 °C is lower (up to 1 order of magnitude at T = 80 °C) with respect to the corresponding one measured at room temperature at the same pH_m. Since the starting material used in the solubility experiments at 25, 55 and 80 °C had been already equilibrated at 80 °C, we reasonably exclude that this effect is related to an increased crystallinity of the initial material, kinetically favored at the higher temperatures. A good agreement is observed for the experimental datasets available for the solubility of metaschoepite and sodium uranate in [NaCl] = 0.51 m at T = 80 °C. Reproducible trends of log [U] as a function of pH_m (with a slope of ~ – 2) were also consistently observed in the acidic to near neutral

pH_m range. In the near-neutral to moderately alkaline pH_m range the solubility of uranium is ~10^{-8} m in [NaCl] = 0.10 and 0.51 m and mostly independent of the pH_m. The measured uranium concentration in this pH_m range was affected by relatively high uncertainties. This is due to the very low uranium concentration, close or lower than the detection limit of the analytical technique, after the required dilution of the sampled volume. For the same reason, meaningful solubility data could not be collected for most batches prepared with [NaCl] = 5.6 m in this pH_m range. Due to these limitations, a clear effect of the temperature on the solubility of uranium in the near-neutral to moderately alkaline pH_m range could not be observed.

The solubility of $Na_2U_2O_7{\cdot}H_2O$(cr) in the alkaline and hyper-alkaline range increases with pH_m with well-defined slope of +1 (log [U] *vs* pH_m). This trend is consistent through the three temperatures investigated, with a significant enhancement of the solubility of $Na_2U_2O_7{\cdot}H_2O$(cr) observed as an effect of temperature. The concentrations of uranium in the contacting solutions at T = 55 and 80 °C are higher than the corresponding ones at room temperature by means of 1.3 to 1.7 and 2.1 to 2.5 orders of magnitude, respectively (Figure 14).

At T = 25 °C, the solubility of $Na_2U_2O_7{\cdot}H_2O$(cr) in 0.51 m NaCl is systematically lower (~0.3 log [U] units) than the one determined by Altmaier et al. for the same solid [30]. In the present work, the batch of $Na_2U_2O_7{\cdot}H_2O$(cr) was preliminarily equilibrated in solution at T = 80 °C prior to be used in the solubility experiments at room temperature, whereas in the work by Altmaier et al. the solid phase was prepared and used at room temperature. The observed decrease of solubility of $Na_2U_2O_7{\cdot}H_2O$(cr) is likely related to an increase of crystallinity of the initial material as an effect of temperature.

4.5.2 Solid phase characterization

Metaschoepite

Figure 15b shows the XRD spectrum of $UO_3{\cdot}2H_2O$(cr) prepared and pre-equilibrated at T = 80 °C. The diffraction pattern is consistent with the one of the same material prepared at room temperature and not equilibrated at elevated temperatures. The spectrum shows the characteristic pattern of the reference metaschoepite (Fig. 15a, red, JSPD File n. 43-0364 [32]), with main features at 2θ = 12.1, 24.2, 24.8, 25.5 deg.

Figure 16 shows the thermal decomposition of $UO_3{\cdot}2H_2O$(cr) measured by TGA analysis. The solid decomposed with a percentage weight loss of 10.9 – 12.2 % in the temperature range 100 – 675 °C, consistently with the expected loss of two water molecules.

Elementary analyses conducted with ICP-OES and with SEM-EDS excluded the presence of Na in the material initially prepared. SEM analyses (Figure 17) revealed the expected platelet-like structure of the crystallites, with an average diameter of about 0.5 – 3 µm.

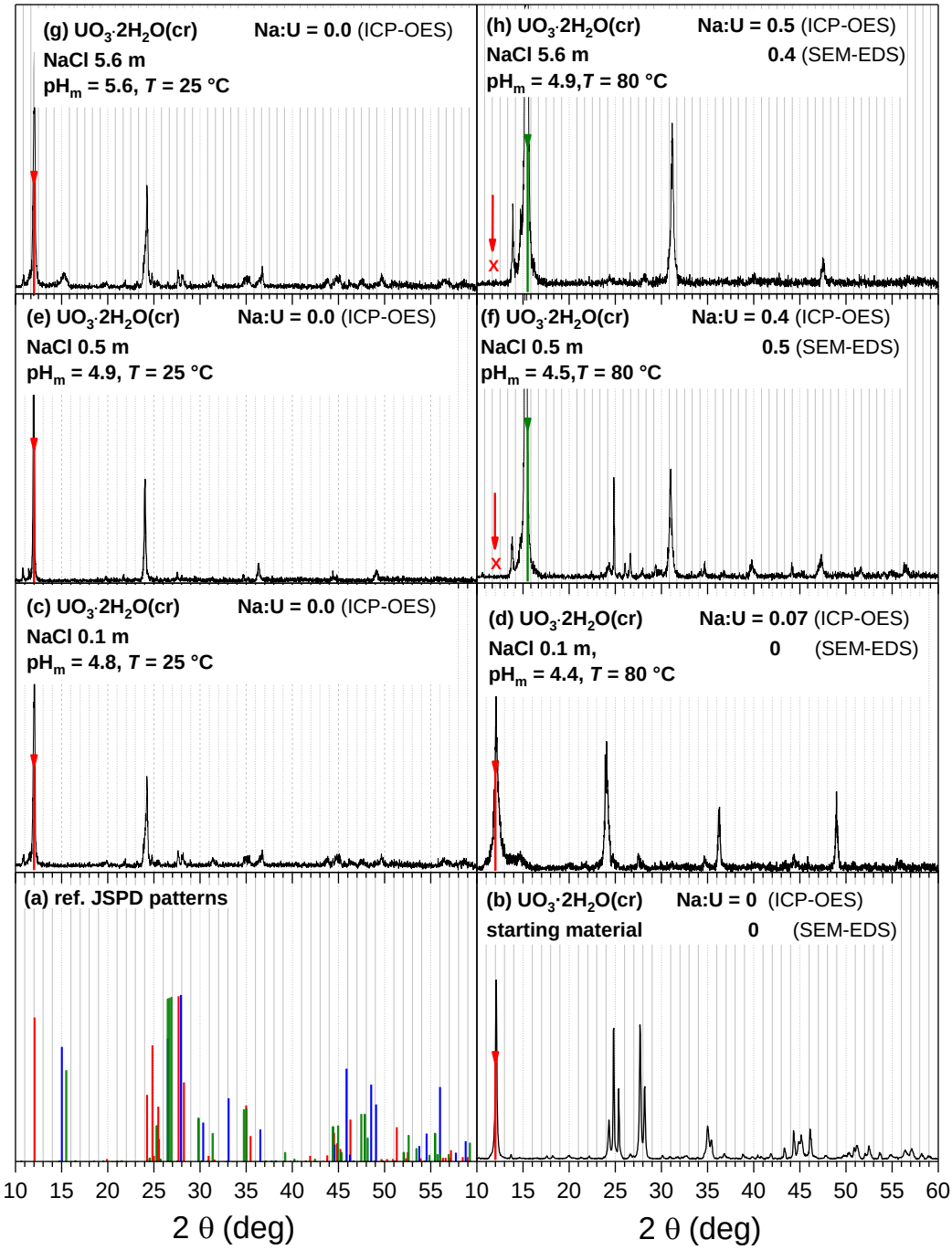

Figure 15. *Powder XRD patterns of $UO_3{\cdot}2H_2O$(cr) investigated in the p.w. (a) reference patterns of $UO_3{\cdot}2H_2O$(cr) (red, JSPD file 43-0364 [32]), $Na(UO_2)O(OH)$(cr) (blue, JSPD file 50-1586 [33]), $Na_2U_3O{\cdot}10H_2O$ (green, JSPD file 41-0840 [34]). (b) $UO_3{\cdot}2H_2O$(cr) before solubility experiments (pre-equilibrated at T = 80 °C). (c) $UO_3{\cdot}2H_2O$(cr) equilibrated 260 days, T = 80 °C, [NaCl] = 0.1 m, pH_m = 4.4. (d) $UO_3{\cdot}2H_2O$(cr) equilibrated 260 days, T = 25 °C, [NaCl] = 0.5 m, pH_m = 4.5. (e) $UO_3{\cdot}2H_2O$(cr) equilibrated 260 days, T = 80 °C, [NaCl] = 0.5 m, pH_m = 4.9. (f) $UO_3{\cdot}2H_2O$(cr) equilibrated 260 days, T = 80 °C, [NaCl] = 5.6 m, pH_m = 4.9.*

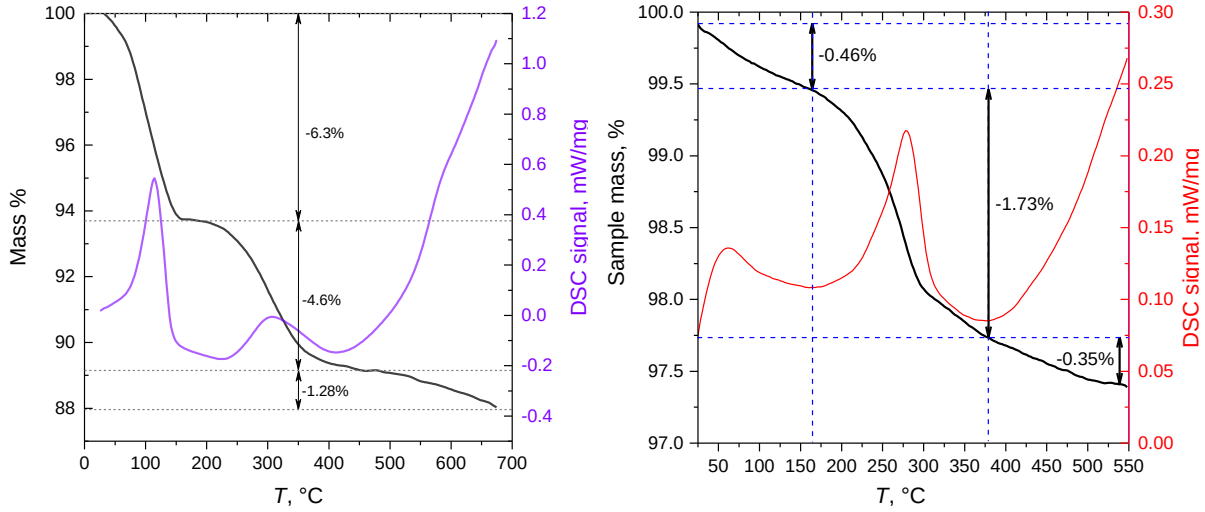

Figure 16. *Thermogravimetric diagram of $UO_3 \cdot 2H_2O$(cr) (left) and $Na_2U_2O_7 \cdot H_2O$(cr) (right).*

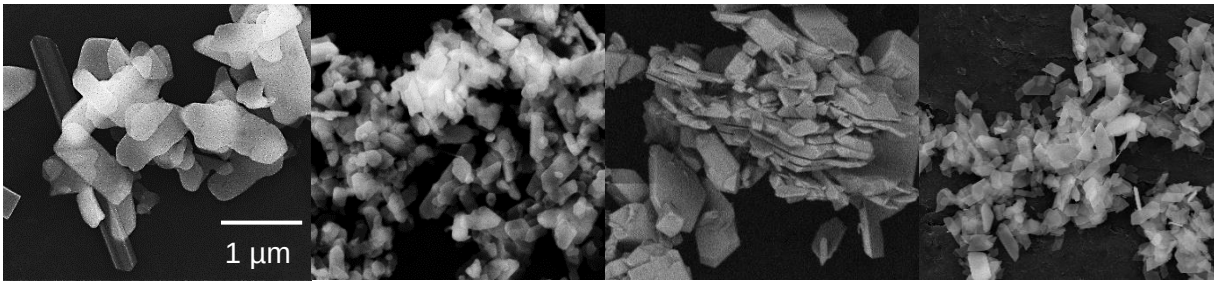

Figure 17. *SEM images of $UO_3 \cdot 2H_2O$(cr) (a) after preparation; (b) aged in [NaCl] = 0.10 m, T = 80 °C, pH_m = 4.4; (c) aged in [NaCl] = 0.51 m, T = 80 °C, pH_m = 4.3; (d) aged in [NaCl] = 5.6 m, T = 80 °C, pH_m = 4.9.*

Results of the characterization of the solid phases of $UO_3 \cdot 2H_2O$(cr) isolated after the solubility experiments indicate that the starting $UO_3 \cdot 2H_2O$(cr) material was stable in all solutions equilibrated at T = 25 °C. XRD confirmed the absence of of sodium-uranate-like phases (Figure 15, c, e, g). ICP-OES elementary analyses showed no inclusion of Na in the solid phase. Similarily, $UO_3 \cdot 2H_2O$(cr) was shown to be thermodynamically stable, when equilibrated in the presence of [NaCl] = 0.10 m, up to T = 80 °C (Figure 15d).

A partial solid phase transformation of metaschoepite into a sodium uranate-like material was conversely observed in batches of $UO_3 \cdot 2H_2O$(cr) contacted with solutions [NaCl] = 0.51 m or higher, at T = 55, 80 °C at pH_m = 4.4 and above. Sodium uranate-like solid phases with Na:U molar ratios lower than 1 have also previously reported in the literature [35], including the sodium triuranate whose XRD pattern is shown in Figure 15a [34]. Figure 15 shows XRD spectra of selected samples of $UO_3 \cdot 2H_2O$(s)

collected at the end of the solubility experiments conducted at T = 80 °C in acidic conditions (pH_m = 4.2 – 4.9), in [NaCl] = 0.10 m (c), 0.51 m (e) and 5.6 m (f). The values of the Na : U molar ratio, measured through elementary analyses (ICP-OES and SEM-EDX) are also reported in the same figure.

The batches of $UO_3 \cdot 2H_2O$(cr) equilibrated in [NaCl] = 0.10 m at T = 25, 55, 80 °C show all, invariably, an absence or a negligible inclusion of Na (Na:U = 0.07 at T = 80 °C). The XRD spectra of these phases do not show any XRD feature corresponding to sodium uranate ("clarkeite", reference JSPD file n. 50-1586 [33] in Figure 15a, blue) or of other known sodium uranate-like phases ($Na_2U_3O_{10} \cdot H_2O$, ref. JSPD file n. 41-0840 [34] in Figure 15a, green). The XRD spectrum of the material collected from experiments in 0.51 m NaCl, T = 80 °C (Figure 15e) shows indications of a possible solid phase transformation: two distinct peaks at 2θ = 15.3, 31.0 deg. could be assigned to a sodium-uranate-like phase, although not matching exactly the peaks of the reference sodium uranate (2θ = 15.0, 30.3, 33.0 deg., Figure 15a, blue). The peak at 2θ = 12.1, assigned to metaschoepite, was instead not distinctly detected. ICP-OES and EDS elementary analyses indicated a Na:U = 0.4-0.5 molar ratio. The results suggest that a partial solid phase transformation of metaschoepite occurred, leading to a solid phase, different from metaschoepite and sodium uranate and composed by a non-stoichiometric Na : U ratio according to $((NaO)_{0.4}(UO_2)(OH)_{1.6} \cdot (0.6)H_2O(s))$.

The batch of metaschoepite equilibrated in [NaCl] = 5.6 m (Figure 15f) showed a XRD spectrum very similar to the one of the solid equilibrated in [NaCl] = 0.51 m (Figure 15e), and the same Na : U molar ratio (0.4-0.5) within uncertainties. This result suggests that the same alteration product was possibly obtained at the end of the experiments in [NaCl] = 0.51 and 5.6 m, hinting that the transformation of metaschoepite at the end of the solubility experiments in these two media was possibly complete, and the transformed phase to be stable in the equilibration condition.

Figure 18 shows the emission spectra at near liquid He temperature (6K) of the metashoepite and transformed metashoepite solid phases of this experiment. Spectral feature typical from uranyl compounds can be observed in both spectra including vibronic bands with specific peak spacing, or peak maxima. In both cases the positions of the spectral bands are red-shifted as compared to those from carbonates or phosphate uranyl minerals [36, 37]. The mentioned spacing between the vibronic bands corresponds to the symmetric stretching frequency of the O = U= O moiety. This frequency is inversely correlated to the strength of the coordination of U(VI) with the coordination ligand in the equatorial plane. The ν_1 values measured here in both metaschoepite phases are between 720 -780 cm^{-1}. Usually, low symmetric stretching frequency values are associated to minerals of uranyl silicate and oxyhydroxide. This fact can be explained by the stronger ionic interaction of uranyl (hard acid) with anions with stronger basicity (larger pK_a values) [36]. A bathochromic shift of ~5 nm in the position of the first-peak maxima is also observed for the transformed metaschoepite. According to Gorobets et al.

[38], an increase of the basicity of the molecules in the uranyl solvation or coordination sphere could induce a shift of the luminescence spectrum to low frequencies. The reason is a stronger chemical bond of the uranium atom with the ligand and a weakening of the stretching in the U=O bond.

Luminescence lifetimes were also calculated for the analyzed metaschoepite phases, obtaining in both cases a bi-exponential decay. In the case of metaschoepite the two components of the decay are: (15.4 ± 0.3) µs and (81.8 ± 0.6) µs. For the transformed metaschoepite both times are shorter (5.6 ± 0.8) µs and (63.2 ± 35.2) µs. This effect has been already observed for uranyl minerals at low temperature K [36, 37, 39, 40]. In the paper by Volodko et al. the bi-exponential decay is explained as a redistribution of energy occurring after excitation [39]. Perry and Brittain argue with the presence of two geometrically similar uranyl coordination environments [40].

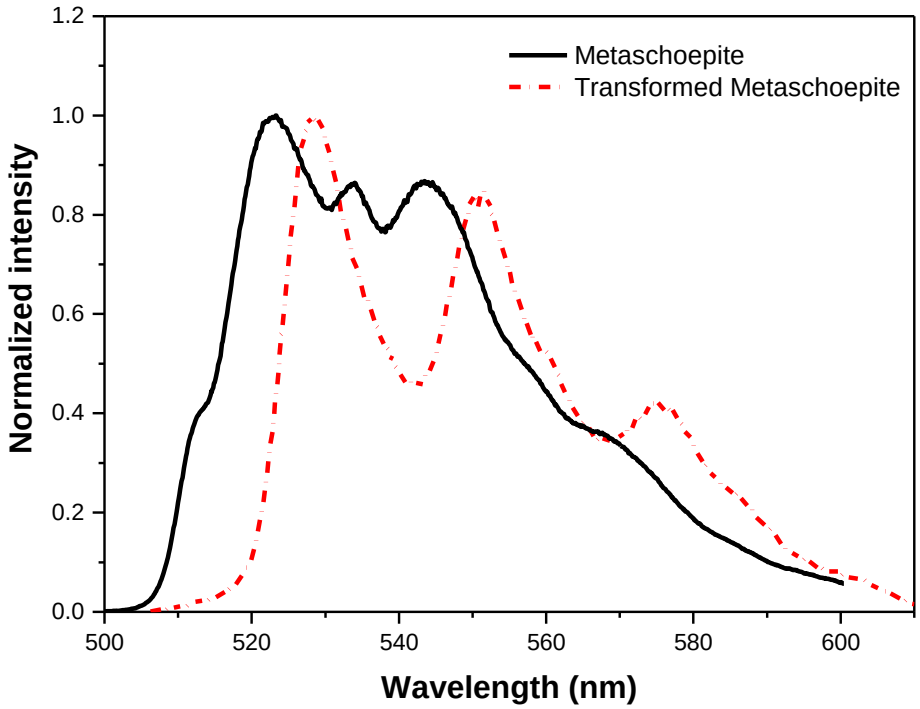

Figure 18. *Luminescence spectra of metaschoepite (solid line) and transformed metaschoepite (short dash dot line). Spectra measured at ~6 K, 1 µs delay,1 ms integration time,500 accumulations. Laser:* λ_{ex} *= 266 nm; 600µJ/pulse.*

Sodium uranate

Figure 19b shows the XRD spectrum of the starting material of sodium uranate. The diffraction pattern is consistent with the one of the reference $Na_2U_2O_7 \cdot H_2O$(cr) material (clarkeite, Figure 19a, JSPD file 50-1586 [33]), with relevant peaks at 2θ = 15.0, 26.4, 27.6, 30.4 deg. Elemental analyses conducted with ICP-OES indicated a 1:1 Na/U molar ratio in the solid phase.

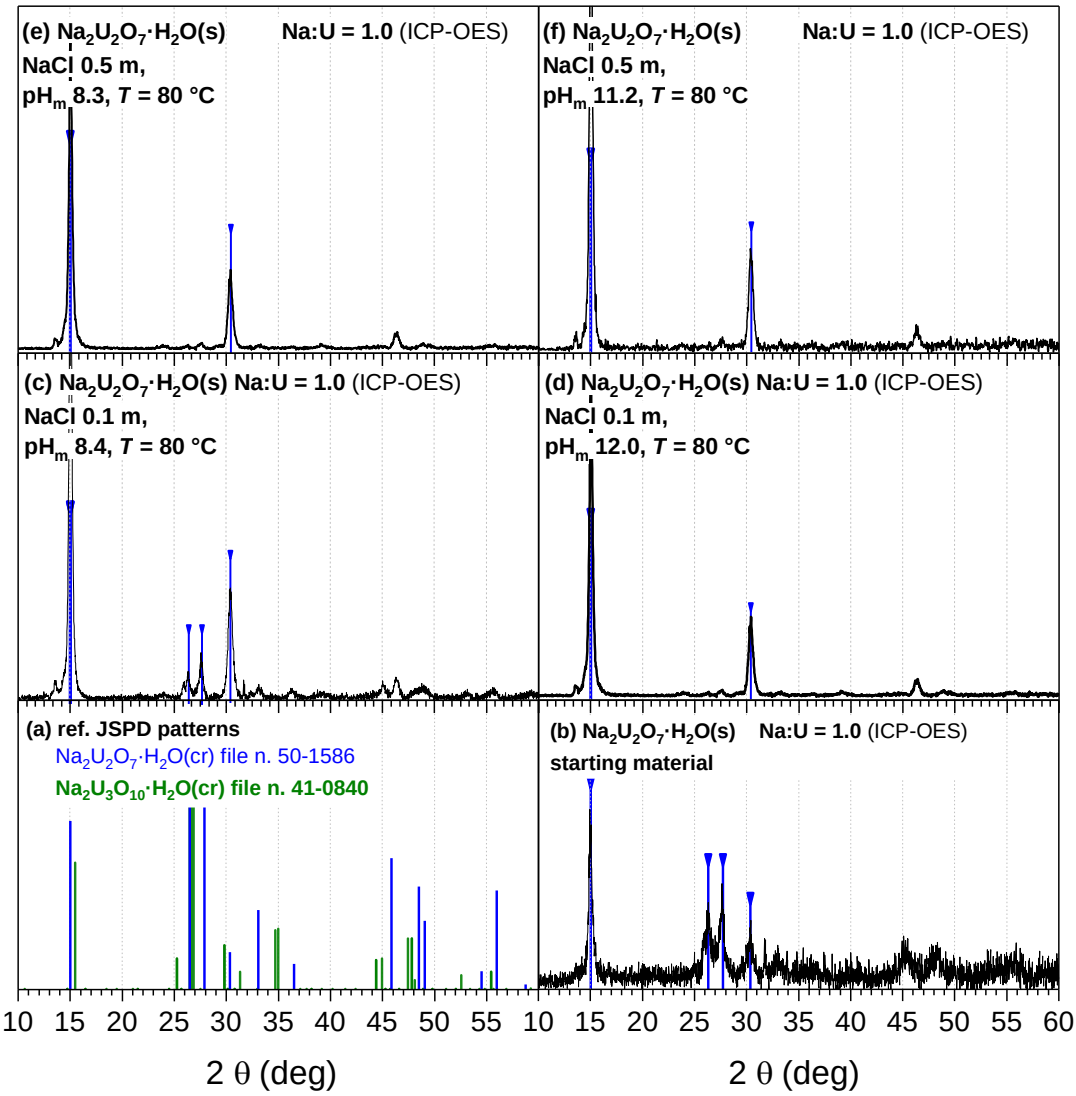

Figure 19. *Powder XRD patterns of $Na_2U_2O_7{\cdot}H_2O$(cr) investigated in the p.w. (a) blue: reference patterns of $Na(UO_2)O(OH)$(cr) (JSPD file 50-1586 [33]); green: reference patterns of $Na_2U_3O_{10}{\cdot}H_2O$(s) (JSPD file 41-0840 [34]). (b) $Na_2U_2O_7{\cdot}H_2O$(cr) before solubility experiments. Pre-equilibrated at T = 80 °C. (c) $Na_2U_2O_7{\cdot}H_2O$(cr) equilibrated 292 days, T = 80 °C, [NaCl] = 0.1 m, pH_m = 8.2. (d) $Na_2U_2O_7{\cdot}H_2O$(cr) equilibrated 292 days, T = 80 °C, [NaCl] = 0.1 m, pH_m = 12.0. (e) $Na_2U_2O_7{\cdot}H_2O$(cr) equilibrated 268 days, T = 80 °C, [NaCl] = 0.1 m, pH_m = 8.3. (f) $Na_2U_2O_7{\cdot}H_2O$(cr) equilibrated 292 days, T = 80 °C, [NaCl] = 0.5 m, pH_m = 12.0.*

Figure 16 shows the TGA diagram of $Na_2U_2O_7{\cdot}H_2O$(cr). The solid decomposed with a weight loss of 2.5 -2.6 % in the temperature range 50 – 550 °C, consistent with the loss of 0.9 water molecules. A quantitative decomposition of $Na_2U_2O_7{\cdot}H_2O$(cr) should have been consistent with the release of 1 water molecules. However, a clear plateau was not reached at the end of the experiments, suggesting that the decomposition of $Na_2U_2O_7{\cdot}H_2O$(cr) with release of water was not quantitative, consistently with the observations in a previous study [41]. Elementary analyses conducted with ICP-OES and SEM-EDS indicated a 1:1 Na : U molar ratio and the absence of chloride in the solid.

Analyses of the solid phases of $Na_2U_2O_7 \cdot H_2O$(cr) collected at the end of the solubility experiments confirmed that the initial material was thermodynamically stable in all the experimental conditions tested. Figure 19 shows selected XRD spectra of $Na_2U_2O_7 \cdot H_2O$(cr) collected at the end of the solubility experiments in 0.10 m NaCl, T = 80 °C, at pH_m = 8.2 (c) and pH_m = 12.0 (d), 0.5 m NaCl, T = 80 °C, at pH_m = 8.3 (e) and pH_m = 11.2 (f). The XRD pattern of the solid phase in the figure matches the one of the initial material, as well as the Na:U stoichiometry (1:1). It is worth noticing that the spectra in Figure 19d – f lack the relevant peaks at 2θ = 26.4, 27.6 assigned to $Na_2U_2O_7 \cdot H_2O$(cr). The patterns are very similar to those already collected by Gorman-Lewis et al. for the same materials [42]. This is considered to be an artifact related to the method of preparation of the sample measured with XRD, which leads to a deposition of the sample powders on the sample holder according to a preferential orientation, rather than anisotropically. In particular, spectra (d – f) show an enhancement of the base peak at 2θ = 15.0, and of the other peaks close to the integer multiples of the base peak (2θ = 30.4, 47.0).

4.5.3 Thermodynamic interpretation

Based on the solubility data and the extensive solid phase characterization, a comprehensive thermodynamic model was derived including solubility constants for $UO_3 \cdot 2H_2O$(cr) and $Na_2U_2O_7 \cdot H_2O$(cr), as well as hydrolysis constants for the hydrolysis species forming in alkaline conditions, $UO_2(OH)_3^-$ and $UO_2(OH)_4^{2-}$. The thermodynamic model includes also enthalpy data for $Na_2U_2O_7 \cdot H_2O$(cr) and $UO_2(OH)_4^{2-}$, thus allowing solubility and speciation calculations at elevated temperatures in hyperalkaline systems. A detailed description of the thermodynamic model is provided in Endrizzi *et al.* (2018) and Endrizzi *et al.* (2019) [31, 43].

4.6 Solubility experiments with Ca-U(VI)-CO_3(s) phases

4.6.1 Solubility data

Figure 20 shows the experimental U(VI) solubility data obtained in the three NaCl systems at T = 22 °C and 80 °C. Further detailed information regarding initial and final pH_m along with the results of the chemical analysis for [U(VI)] and [Ca] contents in the aqueous solution are listed in Table 5. After attaining the equilibrium condition, relatively high concentrations of aqueous U(VI) are determined at

T = 22 °C in 0.03 m and 0.51 m NaCl solutions. However, significantly lower U(VI) solubilities are observed for the systems in 5.61 m NaCl solution at T = 22 °C, and all three systems equilibrated at elevated temperature condition. As shown in Table 5, significant shifts in pH_m towards higher values are observed, in particular for the samples at T = 80 °C. According to Henry's law, the partial pressure of $CO_2(g)$ in water is enhanced as temperature increases. Subsequent degassing of $CO_2(g)$ from the solution produces further consumption of protons for the compensation of hydrated carbon dioxide, inducing the increase in pH_m. In contrast, no remarkable change in pH_m is observed for solutions equilibrated at T = 22 °C, seemingly representing that the $CO_2(g)$ equilibrium in the solution is relatively well maintained during the equilibrium reaction.

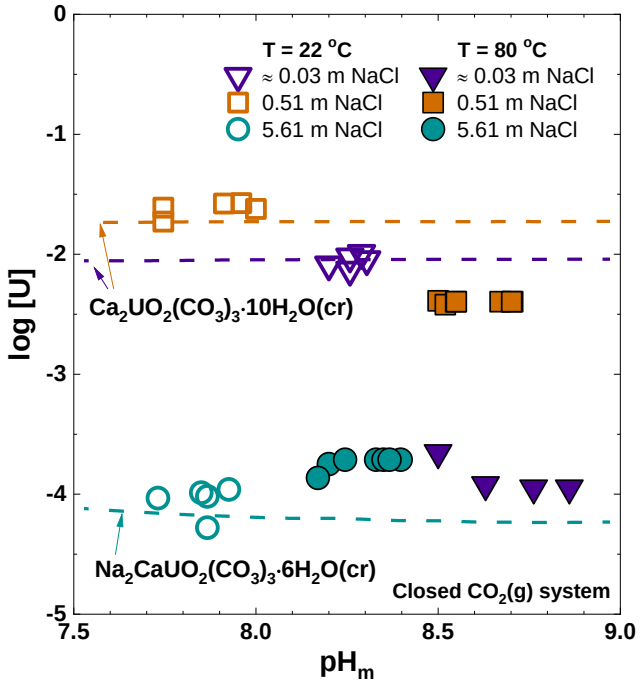

Figure 20. *Experimental U(VI) solubility of initial $Ca_2UO_2(CO_3)_3{\cdot}10H_2O(cr)$ equilibrated in ca. 0.03 m, 0.51 m, and 5.61 m NaCl solutions at T = 22 °C and 80 °C. Dashed lines indicate the solubility curves predicted at room temperature according to the solubility products of $Ca_2UO_2(CO_3)_3{\cdot}10H_2O(cr)$ and $Na_2CaUO_2(CO_3)_3{\cdot}6H_2O(cr)$.*

Relatively high concentrations of both U(VI) and Ca are observed for the systems with $I_m \leq 0.51$ m equilibrated at T = 22 °C, showing a relative ratio of [U(VI)] to [Ca] of *ca.* 1 : 2. This observation is in agreement with a congruent dissolution of liebigite, $Ca_2UO_2(CO_3)_3{\cdot}10H_2O(cr)$, and indicated that no precipitation of other solid phases containing Ca such as calcite in the system took place. However, sample C equilibrated in 5.61 m NaCl at T = 22 °C shows significantly decreased aqueous U(VI) concentration compared with sample A and B, whilst retaining relatively high concentration of calcium in solution. It apparently indicates the transformation of the initial liebigite into a new solid phase with considerably lower solubility and calcium content (solid phase ratio Ca : U << 2).

The concentrations of dissolved U(VI) and Ca determined in the samples at T = 80 °C significantly differ from the analogous samples with $I_m \leq 0.51$ m equilibrated at T = 22 °C. In 5.61 m NaCl, the aqueous U(VI) concentrations obtained at both T = 22 °C and 80 °C are similar to each other, whereas a remarkably lower Ca concentration is measured at elevated temperature condition. The experimental observations, *i.e.* the pH_m shift towards higher values and the low Ca concentrations, made for the solubility samples at elevated temperature are in agreement with the precipitation of calcite, $CaCO_3$.

Table 5. *pH_m, [U] and [Ca] in the investigated solubility samples after attaining equilibrium conditions.*

Sample	T (°C)	pH_m		[NaCl] (m)	Concentration ($\times 10^{-3}$ m)		Ca : U ratio
		Initial	Final		[U]	[Ca]	
A	(22 ± 3)	8.1	8.3	≈ 0.03*	8.5	17.9	2.1
B		8.1	7.8	0.51	21.6	40.0	1.9
C		8.1	7.9	5.61	0.08	65.4	785
D	(80 ± 5)	8.2	9.0	≈ 0.03*	0.05	n.d.	n.d.
E		8.2	8.7	0.51	3.6	n.d.	n.d.
F		7.9	8.4	5.61	0.15	0.18	1.2

* Resulting from the pH_m titration; deionized water as original solution.

4.6.2 Solid phase characterization

After 132 days, U(VI) solid phases were recovered from the solubility experiments. Bright yellow solid particles are found for all samples at T = 22 °C bearing the same appearance as the initial liebigite. However, samples at T = 80 °C show the formation of orange-yellow solid phases, which are relatively comparable to $Na_2U_2O_7 \cdot H_2O$(cr), indicating the transformation of solid U(VI) phase at elevated temperature condition.

Powder XRD patterns of the solid U(VI) phases are presented in Figure 21. The XRD patterns collected for samples equilibrated at T = 22 °C and at low ionic strength conditions (sample A and B) match the reference pattern for liebigite, $Ca_2UO_2(CO_3)_3 \cdot 10H_2O$(cr) (JCPDS file number 49-1056). The powder pattern of sample C, equilibrated at T = 22 °C at high ionic strength, is clearly different from A and B, and agrees well with the reference pattern for andersonite ($Na_2CaUO_2(CO_3)_3 \cdot 6H_2O$) (JCPDS file number 46-1368). The XRD data obtained in this work are also in excellent agreement with literature datapreviously reported by Amayri et al [44]. No indications for the presence of calcite are found at T = 22 °C based on the XRD results, which is in good accordance with the results obtained from the solubility data.

A clear transformation of the initial liebigite is observed for all samples at elevated temperature condition. The transformation into $Na_2U_2O_7 \cdot H_2O$(cr) is evident for the samples with 0.51 m (sample E) and 5.61 m of NaCl (sample F), based on the characteristic XRD pattern, *c.f.* reference data reported in [30]. On the contrary, a different XRD pattern is obtained for sample D (0.03 m NaCl), presenting remarkably shifted XRD peak towards lower 2θ values compared to the reference pattern of $Na_2U_2O_7 \cdot H_2O$(cr) (JCPDS file number 87-1714). The XRD pattern of sample D show considerable similarity with the pattern of $CaU_2O_7 \cdot 3H_2O$(cr) [45], which was found to control the U(VI) solubility in dilute to concentrated alkaline $CaCl_2$ solutions in the absence of carbonate. Sharp XRD peaks located at *ca*. 2θ = 29.4°, identified for all solid U(VI) phases equilibrated at T = 80 °C, indicate the main reflection of calcite (104), confirming the precipitation of calcite during equilibration at elevated temperature.

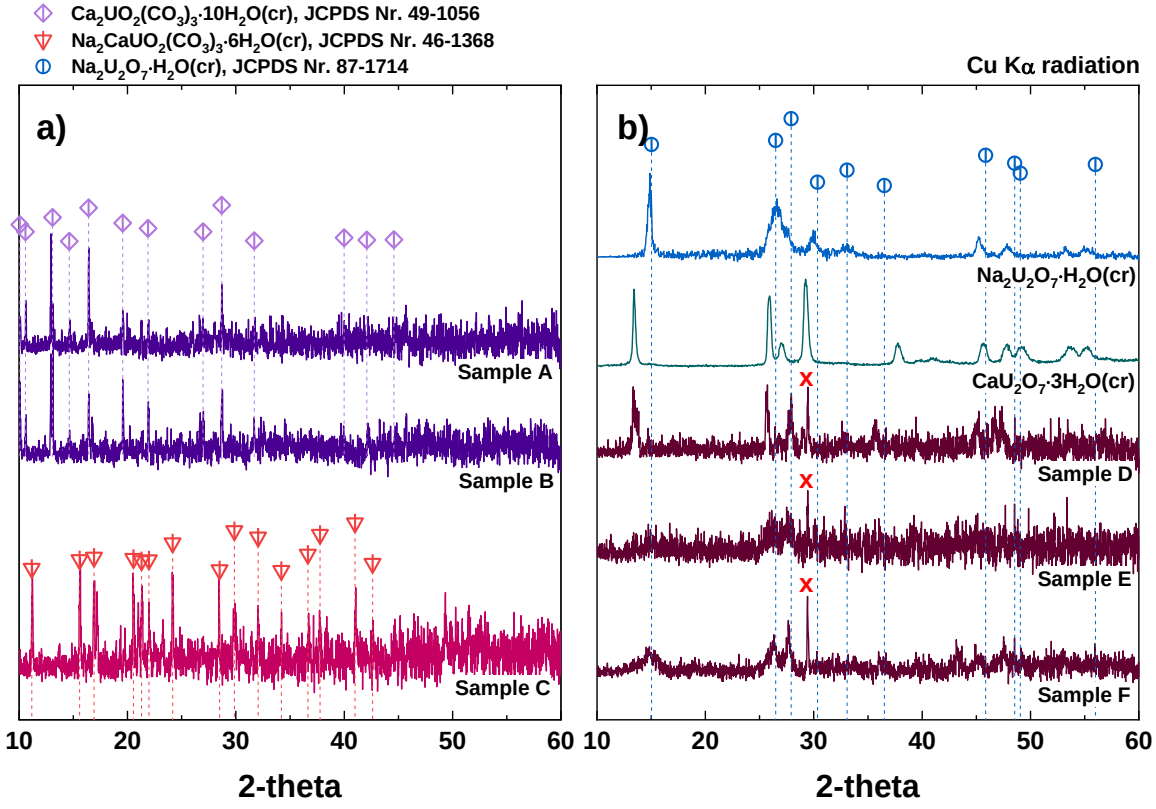

Figure 21. *Powder X-ray diffraction patterns of solid U(VI) phases equilibrated at (a) T = 22 °C and at (b) T = 80 °C. Symbols indicate the reference XRD patterns reported in the JCPDS database for $Ca_2UO_2(CO_3)_3 \cdot 10H_2O$(cr), $Na_2CaUO_2(CO_3)_3 \cdot 6H_2O$(cr) and $Na_2U_2O_7 \cdot H_2O$(cr). In addition, XRD patterns reported by Altmaier et al. [30, 45] for $CaU_2O_7 \cdot 3H_2O$(cr) and $Na_2U_2O_7 \cdot H_2O$(cr) are showed for the comparison. Red crosses in (b) indicate the main reflection peak of calcite (104).*

As shown in Table 6, the ratio Ca : U and Na : U obtained for the solid U(VI) phases by using SEM-EDS and quantitative chemical analysis are in good agreement with XRD data, pointing to $Ca_2UO_2(CO_3)_3 \cdot 10H_2O$(cr) (samples A and B) and $Na_2CaUO_2(CO_3)_3 \cdot 6H_2O$(cr) (sample C) as the main U(VI) solid phases in the systems at T = 22 °C. For samples equilibrated at T = 80 °C, remarkably higher

solid phase ratios of Ca : U are determined by chemical analysis than by SEM-EDS. In general, chemical analysis by combined ICP-OES (for [Ca]) and ICP-MS (for [U]) give an average value for the Ca : U ratio that is representative for the entity of all the solid phases present in the system, while SEM-EDS provide insight into the elemental composition of the targeted solid U(VI) phases. Therefore, the ratios Ca : U ≈ 2 obtained with chemical analysis for those samples equilibrated at T = 80 °C reveals the total inventories of U and Ca originated from the initial mineral liebigite. In addition, the ratio Na : U ≈ 1.5 determined by using both SEM-EDS and chemical analysis for sample F provides complementary support on the formation of $Na_2U_2O_7 \cdot H_2O$(cr) in concentrated NaCl solution at T = 80 °C. SEM-EDS results for sample D and E represent the co-existence of Na and Ca in the solid U(VI) phases, supporting that the initial liebigite transformed into Na- and Ca-diuranates at T = 80 °C.

Table 6. *Ca : U and Na : U ratios in the solid U(VI) phases quantified by SEM–EDS and chemical analysis (U: ICP–MS; Ca: ICP–OES).*

Sample	T (°C)	[NaCl] (m)	SEM–EDS		ICP–MS/OES	
			Ca : U	Na : U	Ca : U	Na : U
A	(22 ± 3)	≈ 0.03	2.3	–	2.1	–
B		0.51	1.8	–	2.0	–
C		5.61	1.0	2.0	1.1	1.9
D	(80 ± 5)	≈ 0.03	0.5	0.4	2.3	0.2
E		0.51	0.6	1.2	2.3	0.9
F		5.61	0.2	1.6	2.3	1.7

4.6.3 Thermodynamic model calculation

Solid phases controlling the overall U(VI) solubility in the background electrolyte solutions investigated in this work at T = 22 °C are unambiguously identified to be $Ca_2UO_2(CO_3)_3 \cdot 10H_2O$(cr) (for *ca.* 0.03 m and 0.51 m NaCl) and $Na_2CaUO_2(CO_3)_3 \cdot 6H_2O$(cr) (for 5.61 m NaCl). Based on the experimental solubility results and the thermodynamic data available for the aqueous U(VI) speciation in the presence of Ca and carbonate, the solubility products of $Ca_2UO_2(CO_3)_3 \cdot 10H_2O$(cr) and $Na_2CaUO_2(CO_3)_3 \cdot 6H_2O$(cr) are calculated at infinite dilution. The solubility data obtained at T = 80 °C are not employed for thermodynamic model calculations as the solubility controlling U(VI) solid phases remain undetermined and as the free carbonate concentration in the solution are unknown due to the partial loss of CO_2(g) for all samples at elevated temperature.

The dissolution of $Ca_2UO_2(CO_3)_3 \cdot 10H_2O$(cr) and $Na_2CaUO_2(CO_3)_3 \cdot 6H_2O$(cr) is controlled by the equilibrium reactions (6) and (7), respectively.

$$Ca_2UO_2(CO_3)_3{\cdot}10H_2O(cr) \Leftrightarrow 2\ Ca^{2+} + UO_2^{2+} + 3\ CO_3^{2-} + 10\ H_2O(l) \quad (6)$$

$$Na_2CaUO_2(CO_3)_3{\cdot}6H_2O(cr) \Leftrightarrow 2\ Na^{+} + Ca^{2+} + UO_2^{2+} + 3\ CO_3^{2-} + 6\ H_2O(l) \quad (7)$$

The solubility products of $Ca_2UO_2(CO_3)_3{\cdot}10H_2O(cr)$ and $Na_2CaUO_2(CO_3)_3{\cdot}6H_2O(cr)$ can then be described according to equations (8) – (9) (for $I \neq 0$) and equations (10) – (11) (for infinite dilution):

$$\log K'_{s,0}\{Ca_2UO_2(CO_3)_3{\cdot}10H_2O(cr)\} = 2 \log [Ca^{2+}] + \log [UO_2^{2+}] + 3 \log [CO_3^{2-}] \quad (8)$$

$$\log K'_{s,0}\{Na_2CaUO_2(CO_3)_3{\cdot}6H_2O(cr)\} = 2 \log [Na^{+}] + \log [Ca^{2+}] + \log [UO_2^{2+}] + 3 \log [CO_3^{2-}] \quad (9)$$

and

$$\log K°_{s,0}\{Ca_2UO_2(CO_3)_3{\cdot}10H_2O(cr)\} = \log K'_{s,0}\{Ca_2UO_2(CO_3)_3{\cdot}10H_2O(cr)\} + 2 \log \gamma\{Ca^{2+}\} + \log \gamma\{UO_2^{2+}\} + 3 \log \gamma\{CO_3^{2-}\} + 10 \log a_w \quad (10)$$

$$\log K°_{s,0}\{Na_2CaUO_2(CO_3)_3{\cdot}6H_2O(cr)\} = \log K'_{s,0}\{Na_2CaUO_2(CO_3)_3{\cdot}6H_2O(cr)\} + 2 \log \gamma\{Na^{+}\} + \log \gamma\{Ca^{2+}\} + \log \gamma\{UO_2^{2+}\} + 3 \log \gamma\{CO_3^{2-}\} + 6 \log a_w \quad (11)$$

where γ is the activity coefficient of an ion and a_w is the water activity. For the evaluation of the solubility products of $Ca_2UO_2(CO_3)_3{\cdot}10H_2O(cr)$ and $Na_2CaUO_2(CO_3)_3{\cdot}6H_2O(cr)$, the required activity coefficients are calculated with the SIT (specific ion interaction theory) approach. Total carbonate concentrations are estimated assuming a congruent dissolution of the initial liebigite ($C_{tot} = 3 \times [U]_{tot}$) for *ca.* 0.03 m and 0.51 m NaCl solutions. In 5.61 m NaCl, the total carbonate concentration is calculated from the mass-balance by considering the experimental total concentration of U(VI) and Ca ions. Solubility products of $Ca_2UO_2(CO_3)_3{\cdot}10H_2O(cr)$ and $Na_2CaUO_2(CO_3)_3{\cdot}6H_2O(cr)$ extrapolated to $I = 0$ with SIT approach are listed in Table 7. The values for $\log K°_{s,0}\{Ca_2UO_2(CO_3)_3{\cdot}10H_2O(cr)\}$ obtained in *ca.* 0.03 m and 0.51 m NaCl solutions are in good agreement with each other. For the value of $\log K°_{s,0}\{Na_2CaUO_2(CO_3)_3{\cdot}6H_2O(cr)\}$, a relatively large uncertainty of ± 0.5 was assumed as only one experimental dataset, namely 5.61 m NaCl, was available for the evaluation.

Calculated solubility products are further employed to calculate the solubility of U(VI) at room temperature under the experimental conditions investigated in this work. As shown in Figure 20, the experimental and calculated solubility of U(VI) are in excellent accordance with each other for various background electrolyte systems. A more detailed description of this work is provided by Lee *et al.* [46].

Table 7. *Solubility products of $Ca_2UO_2(CO_3)_3 \cdot 10H_2O(cr)$ and $Na_2CaUO_2(CO_3)_3 \cdot 6H_2O(cr)$ calculated from experimental solubility data at room temperature.*

Reactions	[NaCl] (m)	log $K'_{s,0}$	log $K°_{s,0}$
$Ca_2UO_2(CO_3)_3 \cdot 10H_2O(cr)$ $\Leftrightarrow 2\ Ca^{2+} + UO_2^{2+} + 3\ CO_3^{2-} + 10\ H_2O(l)$	≈ 0.03 m	–(30.8 ± 0.3)	–(32.4 ± 0.3)
	0.51 m	–(27.9 ± 0.1)	–(32.2 ± 0.1)
$Na_2CaUO_2(CO_3)_3 \cdot 6H_2O(cr)$ $\Leftrightarrow 2\ Na^{+} + Ca^{2+} + UO_2^{2+} + 3\ CO_3^{2-} + 6\ H_2O(l)$	5.61 m	–(26.8 ± 0.2)	–(31.8 ± 0.5)

5. References

[1] M. Altmaier, V. Neck, R. Muller, T. Fanghanel, Radiochim. Acta, 93 (2005) 83-92.

[2] V. Neck, M. Altmaier, T. Rabung, J. Lutzenkirchen, T. Fanghanel, Pure Appl. Chem., 81 (2009) 1555-1568.

[3] S.A. Wood, D.A. Palmer, D.J. Wesolowski, P. Benezeth, Spec. Publ. - Geochemical Soc., 7 (Water-Rock interactions, ore deposits, and environmental geochemistry) (2002) 229-256.

[4] L.F. Rao, D. Rai, A.R. Felmy, Radiochim. Acta, 72 (1996) 151-155.

[5] I.I. Diakonov, B.R. Tagirov, K.V. Ragnarsdottir, Radiochim. Acta, 81 (1998) 107-116.

[6] M.N. Viswanathiah, J.A.K. Tareen, T.R.N. Kutty, Mater Res Bull, 15 (1980) 855-859.

[7] G.W. Beall, W.O. Milligan, D.R. Dillin, R.J. Williams, J.J. Mccoy, Acta Crystallogr. B, 32 (1976) 2227-2229.

[8] V.I. Bukin, Dokl Akad Nauk Sssr+, 207 (1972) 1332-1335.

[9] M. Herm, X. Gaona, T. Rabung, D. Fellhauer, C. Crepin, K. Dardenne, M. Altmaier, H. Geckeis, Pure Appl. Chem., 87 (2015) 487-502.

[10] M. Herm, in, KIT, 2015.

[11] M. Rand, J. Fuger, I. Grenthe, V. Neck, D. Rai, Chemical Thermodynamics Vol. 11. Chemical Thermodynamics of Thorium, Elsevier, North Holland, Amsterdam, 2009.

[12] J.L. Ryan, D. Rai, Inorg. Chem., 26 (1987) 4140-4142.

[13] D. Rai, D.A. Moore, C.S. Oakes, M. Yui, Radiochim. Acta, 88 (2000) 297-306.

[14] T. Kobayashi, T. Sasaki, I. Takagi, H. Moriyama, J Nucl Sci Technol, 53 (2016) 1787-1793.

[15] J. Vandenborre, B. Grambow, A. Abdelouas, Inorg. Chem., 49 (2010) 8736-8748.

[16] J. Vandenborre, A. Abdelouas, B. Grambow, Radiochim. Acta, 96 (2008) 515-520.

[17] M. Altmaier, V. Neck, M.A. Denecke, R. Yin, T. Fanghanel, Radiochim. Acta, 94 (2006) 495-500.

[18] A.R. Felmy, D. Rai, S.M. Sterner, M.J. Mason, N.J. Hess, S.D. Conradson, J. Solution Chem., 26 (1997) 233-248.

[19] D. Rai, A.R. Felmy, S.M. Sterner, L.F. Rao, Abstr Pap Am Chem S, 212 (1996) 89-Nucl.

[20] D. Fellhauer, M. Altmaier, X. Gaona, J. Lützenkirchen, T. Fanghänel, Radiochimica Acta, 104 (2016) 381-397.

[21] S.R. Charlton, D.L. Parkhurst, Computers & Geosciences, 37 (2011) 1653-1663.

[22] E. Giffaut, M. Grivé, P. Blanc, P. Vieillard, E. Colàs, H. Gailhanou, S. Gaboreau, N. Marty, B. Madé, L. Duro, Appl. Geochem., 49 (2014) 225-236.

[23] W. Runde, M.P. Neu, D.L. Clark, Geochim. Cosmochim. Acta, 60 (1996) 2065-2073.

[24] V.G. Petrov, D. Fellhauer, X. Gaona, K. Dardenne, J. Rothe, S.N. Kalmykov, M. Altmaier, Radiochimica Acta, 105 (2017) 1-20.

[25] D. Fellhauer, J. Rothe, M. Altmaier, V. Neck, J. Runke, T. Wiss, T. Fanghänel, Radiochimica Acta, 104 (2016) 355-379.

[26] P.M. Almond, S. Skanthakumar, L. Soderholm, P.C. Burns, Chem. Mater., 19 (2007) 280-285.

[27] B.W. Veal, D.J. Lam, H. Diamond, H.R. Hoekstra, Physical Review B, 15 (1977) 2929-2942.

[28] Y.A. Teterin, S.G. Gagarin, Russ. Chem. Rev., 65 (1996) 825.

[29] Y.A. Teterin, A.Y. Teterin, Russ. Chem. Rev., 73 (2004) 541-580.

[30] M. Altmaier, E. Yalçıntaş, X. Gaona, V. Neck, R. Müller, M. Schlieker, T. Fanghänel, The Journal of Chemical Thermodynamics, 114 (2017) 2-13.

[31] F. Endrizzi, X. Gaona, M.M. Fernandes, B. Baeyens, M. Altmaier, J. Chem. Thermodyn., 120 (2018) 45-53.

[32] P.C. Debets, B.O. Loopstra, J. Inorg. Nucl. Chem., 25 (1963) 945-953.

[33] R.J. Finch, R.C. Ewing, Am. Mineral., 82 (1997) 607-619.

[34] L.M. Kuznetsov, A.N. Tsvigunov, Radiokhimiya, 22 (1980) 600-602.

[35] D.E. Giammar, J.G. Hering, Environ. Sci. Technol., 38 (2004) 171-179.

[36] Z. Wang, J.M. Zachara, C. Liu, P.L. Gassman, A.R. Felmy, S.B. Clark, Radiochim. Acta, 96 (2008) 591-598.

[37] Z.M. Wang, J.M. Zachara, P.L. Gassman, C.X. Liu, O. Qafoku, W. Yantasee, J.G. Catalano, Geochim. Cosmochim. Acta, 69 (2005) 1391-1403.

[38] B.S. Gorobets, S.S. Engoyan, G.A. Sidorenko, Soviet Atomic Energy, 42 (1977) 196-202.

[39] L.V. Volodko, Sevchenk.An, A.I. Komyak, D.S. Umreiko, Dokl Akad Nauk Belar, 18 (1974) 601-603.

[40] H.G. Brittain, D.L. Perry, J. Phys. Chem-Us, 84 (1980) 2630-2634.

[41] V. Baran, M. Tympl, Z Anorg Allg Chem, 347 (1966) 184-190.

[42] D. Gorman-Lewis, J.B. Fein, P.C. Burns, J.E.S. Szymanowski, J. Converse, J. Chem. Thermodyn., 40 (2008) 980-990.

[43] F. Endrizzi, X. Gaona, Z.C. Zhang, C. Xu, L.F. Rao, C. Garcia-Perez, M. Altmaier, Radiochim. Acta, 107 (2019) 663-678.

[44] S. Amayri, T. Arnold, T. Reich, H. Foerstendorf, G. Geipel, G. Bernhard, A. Massanek, Environ. Sci. Technol., 38 (2004) 6032-6036.

[45] M. Altmaier, V. Neck, R. Müller, T. Fanghänel, in: International Conference on Chemistry and Migration Behaviour of Actinides and Fission Products in the Geosphere, Avignon, France, 2005.

[46] J.-Y. Lee, S. Amayri, V. Montoya, D. Fellhauer, X. Gaona, M. Altmaier, Appl. Geochem., 111 (2019) 104374.

6. List of Figures

Figure 1. *Solubility of $Nd(OH)_3(s)$ in [NaCl] = 0.1 (a), 0.51 (b), and 5.6 m (c) at T = 25, 55, 80 °C. Experimental data: Nd(III) concentration vs pH_m. Dashed lines: SIT model calculations at T = 25 °C. Relevant literature data also displayed for comparison: Neck et al. 2009 [2], Wood et al. 2002 [3], Rao et al. 1996 [4].*

Figure 2*. Thermo-Gravimetric Analaysis (TGA) diagrams of (a) $Nd(OH)_3(s)$ after preparation; (b) material equilibrated in NaCl 5.6 m, T = 80 °C, pH_m = 7.5, transformed into a solid consistent with the stoichiometry $Nd(OH)_2Cl(s)$ (XRD characterization in Figure 3).*

Figure 3. *Bottom, left: XRD patterns of known solid phases $Nd(OH)_3(cr)$ (PDF file n. 70-0215 [7]) and of $Nd(OH)_2Cl(cr)$ (PDF file n. 72-1812 [8]). (a) Initial material, characterized as $Nd(OH)_3(s)$; (b) $Nd(OH)_3(s)$ equilibrated in NaCl 0.10 m, T = 80 °C, pH_m 8.2; (c) $Nd(OH)_3(s)$ equilibrated in NaCl 0.51 m, T = 80 °C, pH_m 8.3; (d) $Nd(OH)_3(s)$ equilibrated in NaCl 5.6 m, T = 80 °C, pH_m 8.5; (e) $Nd(OH)_3(s)$ equilibrated in NaCl 0.10m, T = 80 °C, pH_m 7.5.*

Figure 4. *Solubility data of Th(IV) hydrous oxide: (a) freshly precipitated; (b) aged for 1 month at T = 80 °C and pH_m = 3 and 12.8. All solubility experiments conducted in 0.1 M NaCl. Experimental solubility data reported in the literature for $ThO_2(am, hyd)$ in 0.1 M NaCl and $NaClO_4$ systems appended for comparison [12, 13]. Solid, dotted and dashed lines correspond to the solubility curves for $ThO_2(am, hyd, fresh)$, $ThO_2(am, hyd, aged)$ and $ThO_2(cr)$ using thermodynamic data selected in the NEA-TDB [11].*

Figure 5. *Solubility data of Th(IV) hydrous oxide: (a) aged for 2 months at T = 80 °C and pH_m = 3 and 12.8; (b) aged for 4.5 months at T = 80 °C and pH_m = 3 and 12.8. All solubility experiments conducted in 0.1 M NaCl. Experimental solubility data reported in the literature for $ThO_2(am, hyd)$ in 0.1 M NaCl and $NaClO_4$ systems appended for comparison [14]. Solid, dotted and dashed lines correspond to the solubility curves for $ThO_2(am, hyd, fresh)$, $ThO_2(am, hyd, aged)$ and $ThO_2(cr)$ using thermodynamic data selected in the NEA-TDB [11].*

Figure 6. *Solubility of the aged phase $ThO_2(ncr, hyd, t = 2 m, pH = 12.8)$ at T = 22 and 80 °C determined in this work in 0.1 M NaOH systems with $0.01 M \leq [Na_2CO_3]_{tot} \leq 1.5 M$. Experimental solubility data at T = 22-25 °C reported by Altmaier et al. [17] and Rai et al. [17-19] are appended for comparison. Solid lines correspond to thermodynamic calculations at T = 22 and 80 °C using thermodynamic data derived in this work, selected in the NEA-TDB and estimated by Amphos[21] (see text).*

Figure 7. *Diffractograms of the Th(IV) solid phases synthesized in this work and equilibrated at T = 80 °C and pH_c(25 °C) = 3 and 12.8, except for sample "ThO_2(freshly precipitated)" measured 2 days after precipitation. Vertical dashed lines refer to the $ThO_2(cr)$ reference (PDF 75-0052).*

Figure 8. *Experimental Np(V) solubility in (a) 0.1 m NaOH and (b) 5.6 m NaCl solutions determined after 30 days of heating period in comparison to the solubility data of $NpO_2OH(am)$ in 5 M NaCl reported by [23, 24]. Solid lines represent the calculated solubility of $NpO_2(OH)(am,fresh)$.*

Figure 9. *Powder X-ray diffraction patterns of the transformed Np(V) solid phases in comparison to the one for $NpO_2OH(am,fresh)$ [25].*

Figure 10. *SEM images of the transformed Np(V) solid phases. (a) 0.1 m NaOH; (b) 5.6 m NaCl, pH_m = 13.0.*

Figure 11. *XPS spectra of (a) Np4f- and (b) O1s-signal of the investigated Np solid phases.*

Figure 12. *Total aqueous Np concentration measured as a function of reaction time at T = 80 °C with (a) $AH_2QDS/AQDS$, (b) Fe powder, (c) $SnCl_2$ redox system at various pH_m conditions. Dashed line indicates detection limit of quantification analysis.*

Figure 13. *Total aqueous Np concentration measured as a function of reaction time at T = 80 °C with (a) hydroquinone and (b) Fe(II)/Fe(III) redox system at various pH_m conditions. Dashed line represents detection limit of quantification analysis.*

Figure 14. *Solubility of $UO_3{\cdot}2H_2O(cr)$ and $Na_2U_2O_7{\cdot}H_2O(cr)$ in NaCl 0.1, 0.51, 5.6 m at T = 25, 55, 80 °C. Solid thick lines correspond to the solubility at T = 25 °C calculated using the SIT model. Dashed lines indicate the contribution to the solubility of the $UO_2(OH)_4^{2-}$ (1,4) species. Data reported by Endrizzi et al. and Altmaier et al are included for comparison [30, 31].*

Figure 15. *Powder XRD patterns of $UO_3{\cdot}2H_2O(cr)$ investigated in the p.w. (a) reference patterns of $UO_3{\cdot}2H_2O(cr)$ (red, JSPD file 43-0364 [32]), $Na(UO_2)O(OH)(cr)$ (blue, JSPD file 50-1586 [33]), $Na_2U_3O{\cdot}10H_2O$ (green, JSPD file 41-0840 [34]). (b) $UO_3{\cdot}2H_2O(cr)$ before solubility experiments (pre-equilibrated at T = 80 °C). (c) $UO_3{\cdot}2H_2O(cr)$ equilibrated 260 days, T = 80 °C, NaCl 0.1 m, pH_m = 4.4. (d) $UO_3{\cdot}2H_2O(cr)$ equilibrated 260 days, T = 25 °C, NaCl 0.5 m, pH_m = 4.5. (e) $UO_3{\cdot}2H_2O(cr)$ equilibrated 260 days, T = 80 °C, NaCl 0.5 m, pH_m = 4.9. (f) $UO_3{\cdot}2H_2O(cr)$ equilibrated 260 days, T = 80 °C, NaCl 5.6 m, pH_m = 4.9.*

Figure 16. *Thermogravimetric diagram of $UO_3{\cdot}2H_2O(cr)$ (left) and $Na_2U_2O_7{\cdot}H_2O(cr)$ (right).*

Figure 17. *SEM images of $UO_3{\cdot}2H_2O(cr)$ (a) after preparation; (b) aged in NaCl 0.10 m, T = 80 °C, pH_m = 4.4; (c) aged in NaCl 0.51 m, T = 80 °C, pH_m = 4.3; (d) aged in NaCl 5.6 m, T = 80 °C, pH_m = 4.9.*

Figure 18. *Luminescence spectra of metaschoepite (solid line) and transformed metaschoepite (short dash dot line). Spectra measured at ~6 K, 1 µs delay,1 ms integration time,500 accumulations. Laser: λ_{ex} = 266 nm; 600µJ/pulse.*

Figure 19. *Powder XRD patterns of $Na_2U_2O_7{\cdot}H_2O(cr)$ investigated in the p.w. (a) blue: reference patterns of $Na(UO_2)O(OH)(cr)$ (JSPD file 50-1586 [33]); green: reference patterns of $Na_2U_3O_{10}{\cdot}H_2O(s)$ (JSPD file 41-0840 [34]). (b) $Na_2U_2O_7{\cdot}H_2O(cr)$ before solubility experiments. Pre-equilibrated at T =*

80 °C. (c) $Na_2U_2O_7 \cdot H_2O$(cr) equilibrated 292 days, T = 80 °C, NaCl 0.1 m, pH_m = 8.2. (d) $Na_2U_2O_7 \cdot H_2O$(cr) equilibrated 292 days, T = 80 °C, NaCl 0.1 m, pH_m = 12.0. (e) $Na_2U_2O_7 \cdot H_2O$(cr) equilibrated 268 days, T = 80 °C, NaCl 0.1 m, pH_m = 8.3. (f) $Na_2U_2O_7 \cdot H_2O$(cr) equilibrated 292 days, T = 80 °C, NaCl 0.5 m, pH_m = 12.0.

Figure 20. *Experimental U(VI) solubility of initial $Ca_2UO_2(CO_3)_3 \cdot 10H_2O$(cr) equilibrated in ca. 0.03 m, 0.51 m, and 5.61 m NaCl solutions at T = 22 °C and 80 °C. Dashed lines indicate the solubility curves predicted at room temperature according to the solubility products of $Ca_2UO_2(CO_3)_3 \cdot 10H_2O$(cr) and $Na_2CaUO_2(CO_3)_3 \cdot 6H_2O$(cr).*

Figure 21. *Powder X-ray diffraction patterns of solid U(VI) phases equilibrated at (a) T = 22 °C and at (b) T = 80 °C. Symbols indicate the reference XRD patterns reported in the JCPDS database for $Ca_2UO_2(CO_3)_3 \cdot 10H_2O$(cr), $Na_2CaUO_2(CO_3)_3 \cdot 6H_2O$(cr) and $Na_2U_2O_7 \cdot H_2O$(cr). In addition, XRD patterns reported by Altmaier et al. [30, 45] for $CaU_2O_7 \cdot 3H_2O$(cr) and $Na_2U_2O_7 \cdot H_2O$(cr) are showed for the comparison. Red crosses in (b) indicate the main reflection peak of calcite (104).*

7. List of Tables

C Wissenschaftliche Veröffentlichungen und Konferenzbeiträge

C.1 Veröffentlichungen in wissenschaftlichen (peer-reviewed) Zeitschriften

(1) Endrizzi, F., Gaona, X., Marques Fernandes, M., Baeyens, B., Altmaier, M. (2018). Solubility and hydrolysis of U(VI) in 0.5 mol/kg NaCl solutions at T = 22 and 80 °C. Journal of Chemical Thermodynamics, 120, 45-53

(2) Endrizzi, F., Gaona, X., Zhang, Z., Xu, C., Rao, L., Garcia-Perez, C., Altmaier, M. (2019). Thermodynamic description of U(VI) solubility and hydrolysis in dilute to concentrated NaCl solutions at T = 25, 55 and 80 °C. Radiochimica Acta, 107 (8), pp. 663-678.

(3) Lee, J.-Y., Amayri, S., Montoya, V., Fellhauer, D., Gaona, X., Altmaier, M. (2019). Solubility and stability of liebigite, $Ca_2UO_2(CO_3)_3 \cdot 10H_2O$(cr), in dilute to concentrated NaCl and $NaClO_4$ solutions at T = 22–80 °C. Applied Geochemistry, 111, art. no. 104374.

(4) Fellhauer, D., Lee, J.-Y., Gaona, X., Vespa, M., Schild, D., Johnsen, A., Altmaier, M. Transformation of Np(V) solid phase at elevated temperature (2022, in preparation).

(5) Lee, J.-Y., Fellhauer, D., Gaona, X., Schild, D., Altmaier, M. Redox Chemistry of Np(V)/Np(IV) in reducing aqueous solutions at T = 80°C (2022, in preparation).

C.2 Sonstige Veröffentlichungen und Publikationen

(1) Kiefer, C., Masterarbeit zu " Impact of temperature on Th(IV) solid phases and solubility", Karlsruhe Institut für Technologie, 2020.

C.3 Vorträge bei wissenschaftlichen Konferenzen und Workshops

(1) Altmaier, M. et al. "ThermAc - a collaborative project investigating aquatic chemistry and thermodynamics of actinides at elevated temperature conditions". Plutonium Futures: The Science, September 18-22, 2016, Baden-Baden (Germany).

(2) Endrizzi, F. et al. "Uranium(VI) Solubility and Hydrolysis in NaCl Solutions at Elevated Temperatures". 9th International Conference on Nuclear and Radiochemistry - NRC9, August 29 - September 2, 2016, Helsinki (Finland).

(3) Gaona, X. et al. "Effect of elevated temperatures on actinide solubility and speciation - studies performed by KIT-INE within the German project ThermAc". ACS meeting, April 2-6, San Francisco (USA).

(4) Gaona, X. et al. "Role of Np(V) solid phases in the solution chemistry of neptunium under alkaline pH conditions". ACS meeting, August 20-24, 2016, Washington (USA).

(5) Altmaier, M. et al. "Thermodynamik und Speziation von Actiniden bei höheren Temperaturen" anlässlich 3. Projektstatusgespräch zur BMBF geförderten Nuklearen Sicherheitsforschung, Dresden, 27. - 28. April 2017.

(6) Lee, J.-Y. et al. "Temperature effect on solid transformation and redox behavior of Np(V)". 18th International Symposium on Solubility Phenomena and Related Equilibrium Processes (ISSP18), July 15-20, 2018, Tours (France).

(7) Altmaier, M. et al. "Conclusions from the ThermAc project - A dedicated collaborative project to investigate actinide chemistry at elevated temperature conditions". 17th International Conference on the Chemistry and Migration Behaviour of Actinides and Fission Products in the Geosphere, Migration 2019, September 15 - 20, 2019, Kyoto (Japan).

(8) Altmaier, M. et al. "Overview of the BMBF funded ThermAc project". 3rd International Workshop on High Temperature Aqueous Chemistry - HiTAC (III), June 27, 2019, Karlsruhe (Germany).

(9) Gaona, X. et al. "Studies on actinide chemistry at elevated temperatures at KIT-INE within the German collaborative ThermAc project". 3rd International Workshop on High Temperature Aqueous Chemistry - HiTAC (III), June 27, 2019, Karlsruhe (Germany).

C.4 Poster bei wissenschaftlichen Konferenzen und Workshops

(1) Altmaier, M. et al. "ThermAc - a joint project on aquatic actinide chemistry and thermodynamics at elevated temperature conditions". 15th International Conference on the Chemistry and Migration Behaviour of Actinides and Fission Products in the Geosphere, Migration 2015, September 13 - 18, 2015, Santa Fe (USA).

(2) Altmaier, M. et al. "ThermAc - a collaborative project on aquatic chemistry and thermodynamics of actinides at elevated temperature conditions". 17th International

Symposium on Solubility Phenomena and Related Equilibrium Processes (ISSP17), July 24-29, 2016, Geneva (Switzerland).

(3) Lee, J.-Y. et al. "Complexation Behavior and Solubility of the Ternary Systems Ca/Mg-UO2-CO3 under Weakly Alkaline Conditions". Plutonium Futures: The Science, September 18-22, 2016, Baden-Baden (Germany).

(4) Gaona, X. et al. "Solution chemistry of radionuclides at elevated temperature: the uranium case". Geothermische Fluide in salinaren Systemen, November 24-25, Karlsruhe (Germany), 2017.

(5) Altmaier, M. et al. "ThermAc: a collaborative project on aquatic chemistry and thermodynamics of actinides at elevated temperature conditions". Actinide and Brine Chemistry in a Salt Repository Workshop (V), March 26-28, 2017, Ruidoso NM (USA).

(6) Altmaier, M. et al. "ThermAc - a collaborative project on aquatic chemistry and thermodynamics of actinides at elevated temperature conditions". 16th International Conference on the Chemistry and Migration Behaviour of Actinides and Fission Products in the Geosphere, Migration 2017, September 10 - 15, 2017, Barcelona (Spain).

(7) Lee, J.-Y. et al. "Solid phase transformation of Np(V) at elevated temperature in NaCl/CaCl2/MgCl2 solutions". 16th International Conference on the Chemistry and Migration Behaviour of Actinides and Fission Products in the Geosphere, Migration 2017, September 10 - 15, 2017, Barcelona (Spain).

(8) Altmaier, M. et al. "Studies on radionuclide chemistry at elevated temperature conditions within the collaborative ThermAc project". 18th International Symposium on Solubility Phenomena and Related Equilibrium Processes (ISSP18), July 15-20, 2018, Tours (France).

(9) Altmaier, M. et al. "Studies on actinide chemistry at elevated temperatures at KIT-INE within the German collaborative ThermAc project". ACS meeting, August 19-23, 2018, Boston (USA).

(10) Cevirim-Papaioannou, N. et al "Solution chemistry and thermodynamics of U(IV) and U(VI): solubility, hydrolysis and the ternary Ca-U(VI)-carbonate system". 17th International Conference on the Chemistry and Migration Behaviour of Actinides and Fission Products in the Geosphere, Migration 2019, September 15 - 20, 2019, Kyoto (Japan).

(11) Fellhauer, D. et al "Redox chemistry of Np(V)/Np(IV) in reducing aqueous solutions at T = 23 and 80 °C". 17th International Conference on the Chemistry and Migration Behaviour of Actinides and Fission Products in the Geosphere, Migration 2019, September 15 - 20, 2019, Kyoto (Japan).

TEILBERICHT B

Arbeiten der GRS

Der von GRS an KIT-INE übermittelte Bericht zu den durchgeführten Arbeiten innerhalb von ThermAc (inklusive der Verlängerungsphase) ist nachfolgend dargestellt.

Methods for the determination of the redox state of saline solutions

Sven Hagemann

October 2020

Acknowledgement:

The underlying work of this report was commissioned by the Karlsruhe Institute of Technology, Institute for Nuclear Waste Disposal (INE) under the contract number KIT 320/20599764/INE/GFB (as part of the BMBF project “ThermAc3” contract number 02 NUK039A)

The work was carried out by Gesellschaft für Anlagen- und Reaktorsicherheit (GRS) gGmbH,

Table of Contents

Zusammenfassung

Der Redoxzustand im Nahfeld eines Endlagers hat einen bedeutenden Einfluss auf die Löslichkeit von Radionukliden. Er wird üblicherweise als Redoxpotential ausgedrückt, das durch potentiometrische Messung mit einer Messkette aus Platin-Elektrode und Silber-Silberchlorid-Referenzelektrode bestimmt wird. Diese Messungen führen jedoch in salinaren Lösungen zu systematischen Abweichungen, die sich auf thermodynamischem Wege nicht quantifizieren lassen. Auf Basis früherer Arbeiten wurde eine rechnerische Methode entwickelt, die es erlaubt, die primären potentiometrischen Messdaten in einem zweistufigen Verfahren zunächst in ein Konzentrationsverhältnis zweier redoxsensitiver Spezies und anschließend in ein alternatives Maß für den Redoxstatus umzurechnen.

Die Methode beruht auf der Auswertung systematischer Messungen des Redoxpotentials von Hexacyanoferrat(II)/ Hexacyanoferrat(III)-Mischungen in Lösungen der Salze NaCl und $MgCl_2$. Hierdurch konnte ein empirischer Bezug zwischen dem Redoxpotential, der Salzkonzentration (NaCl oder $MgCl_2$) und dem bekannten Mischungsverhältnis der Hexacyanoferrate hergestellt werden. Diese Beziehung lässt sich auch in Lösungen anwenden, die keine Hexacyanoferrate, sondern andere redoxsensitive Stoffe enthalten. Das berechnete Mischungsverhältnis der Hexacyanoferrate ist bereits ein alternatives Maß für den Redoxzustand. Es ist aber eher ungewöhnlich und sollte in gebräuchlichere Größen umgewandelt werden. Hierzu eignet sich z.B. der negative Logarithmus des Partialdruckes von Sauerstoff.

Die Umrechnung vom Mischungsverhältnis in den Sauerstoff-Partialdruck erfordert neben der Wasserstoffionenkonzentration (pcH) ein Modell zur Beschreibung der Aktivitätskoeffizienten von Hexacyanoferrat-Ionen in NaCl- und $MgCl_2$-Lösungen. Hierfür wurden Literaturdaten gesammelt und ausgewertet. Es standen jedoch für alle betrachteten binären und ternären Lösungssysteme keine oder nicht ausreichende Daten zur Verfügung. Deshalb wurden isopiestische Messungen durchgeführt, um Dampfdruckdaten bei 25, 40 und 60°C zu gewinnen. Einige Löslichkeitsmessungen wurden bei 25, 40 und 60°C durchgeführt. Die Messungen dienten in Kombination mit Literaturdaten als Grundlage zur Ableitung eines Pitzer-Modells für binäre und ternäre Systeme. Für Systeme mit Natriumhexacyanoferraten kann dieses Modell zuverlässig die Aktivitätskoeffizienten beschreiben. Bei magnesiumhaltigen Systemen gelingt dies nur teilweise. Hier wirkt sich offenbar eine starke Komplexbildung zwischen Mg^{2+} und Hexacyanoferraten aus.

Besonders stark ist dieser Effekt zwischen Mg^{2+} und $Fe(CN)_6^{4-}$. Er führt dazu, dass sich das binäre System $Mg_2Fe(CN)_6$-H_2O nur schwierig und das ternäre System $Mg_2Fe(CN)_6$-$MgCl_2$-H_2O nur in Ansätzen beschreiben lässt. Hier sind entweder weitere Messungen notwendig, um die Komplexbildung quantitativ beschreiben zu können oder aber Untersuchungen mit einem anderen Redoxpaar, in dem die genannten Schwierigkeiten nicht auftreten.

Unter stark reduzierenden Bedingungen, wie sie bei der Korrosion von Stahl im Endlager auftreten, tritt gelöstes Eisen praktisch nur noch in der Oxidationsstufe +II auf. Aus früheren Arbeiten war bekannt, das es in konzentrierten Chlorid-Lösungen zur Komplexbildung zwischen Fe^{2+} und Cl^- kommt. Dies wird auch als einer der Gründe angesehen, weshalb die Modellierung von Löslichkeitssystemen mit hohen Chloridgehalten, KCl-$FeCl_2$-H_2O nicht zufriedenstellend gelingt. Ein Modell zur quantitativen Beschreibung der Komplexbildung von Fe^{2+} mit Chlorid in Lösungen von NaCl, KCl und $MgCl_2$ fehlte bislang. Darum wurden UV-spektrophotometrische Messungen durchgeführt, um die Komplexbildung in diesen Lösungen wie auch in LiCl-Lösungen bei 25 bis 80°C zu untersuchen. Die erhaltenen Spektren wurden anschließend rechnerisch in Einzelspeziesspektren getrennt und die Konzentration der einzelnen Spezies bestimmt. Es zeigte sich, dass sich ab einer Chlorid-Konzentration von etwa 1 mol/kg Cl-Gehalt ein erster Komplex zeigt. Diesem konnte die Zusammensetzung $FeCl^+$ zugeordnet werden. Erst bei Chlorid-Konzentrationen von etwa 8 mol/kg tritt ein zweiter Komplex auf. Hierbei handelt es sich wahrscheinlich um $FeCl_2$(aq). Weitere Komplexe lassen sich bis zu einer Cl-Konzentration von 16 mol/kg (in LiCl-Lösungen) selbst bei 80°C nicht nachweisen.

Für den Komplex $FeCl^+$ wurde eine Bildungskonstante und Pitzer-Koeffizienten für die Wechselwirkung mit den Ionen Cl^-, Na^+, K^+ und Mg^{2+} abgeleitet. Mit ihrer Hilfe ist es möglich, die beobachtete Speziation über den größten Teil der betrachteten Konzentrationen sehr gut zu beschreiben. Nur bei den höchsten Konzentrationen sind zunehmend Abweichungen zu beobachten. Das Modell wurde anschließend angewandt, um die Löslichkeiten in den Systemen NaCl-$FeCl_2$-H_2O und KCl-$FeCl_2$-H_2O zu beschreiben. Obwohl die auftretenden Eisen-Konzentrationen in diesen Systemen wesentlich größer sind als in den photometrischen Messungen und auch Wechselwirkungen zwischen verschiedenen Eisen-Spezies relevant werden, ist die Übereinstimmung zwischen berechneten und beobachteten Löslichkeiten über weite Strecken sehr gut.

Obwohl die Leistung des Modells zufriedenstellend war, zeigte der ungewöhnliche Wert der Ionenwechselwirkungskoeffizienten für $FeCl^+$ und die Abweichung der berechneten

Komplexbildungskonstante von den Literaturwerten, dass das Modell mit etwas Vorsicht behandelt werden sollte. Es sind zusätzliche wissenschaftliche Anstrengungen erforderlich, um das Spektren-Trennungsverfahren zu verbessern und die Fe(II)-Speziation in Lösungen mit höheren Eisenkonzentrationen aufzuklären. Dies würde einen Weg für eine unabhängige Abschätzung der Ionenwechselwirkungskoeffizienten für Fe^{2+}, $FeCl^{+}$ und möglicherweise $FeCl_2(aq)$ eröffnen. Diese Werte können aus Lösungen, in denen Fe(II) nur eine Spurenkomponente ist, nicht bestimmt werden.

Analoge Messungen in Natriumsulfat-Lösungen konnten keinen eindeutigen Nachweis für eine Komplexbildung erbringen. Die Komplexbildung zwischen Fe^{2+} und SO_4^{2-} ist zwar bekannt, aber sie macht sich in den Absorptionsspektren nicht signifikant bemerkbar.

1 Introduction

Within the scope of the joint project ThermAc3, the partners aimed to extend the thermodynamic database for actinides, long-lived fission products and relevant matrix elements in aquatic systems at higher temperatures, using estimation algorithms, new experimental investigations and quantum-chemically supported structural information.

The mobility of radionuclides in the near field of a repository is largely dependent on the oxidation level prevailing in the geochemical near field environment. Each oxidation stage is linked to a specific set of possible complex compounds, sorption patterns and options for solid phase formation that can increase or decrease the solubility of radionuclides by many orders of magnitude.

The predominant oxidation stages of the radionuclides are a product of geochemical boundary conditions, especially the overall redox status of the near field system. It is mainly determined by redox-active steel corrosion phases and the corrosion hydrogen. As iron is the main component of most container materials, liners, and other metallic materials, it can be assumed that solid and dissolved iron compounds are mainly responsible for determining the redox level in the near field. Dissolved iron is also an important partner for redox reactions with radionuclides. For a deeper understanding of the near-field processes, especially under different redox conditions, a sufficiently good knowledge of the thermodynamic properties of dissolved iron compounds, especially those of the prevailing iron(II) oxidation stage is of high importance.

A related challenge is the interference-free measurement of the redox level in high-saline systems. When using the standard measuring systems, a medium-dependent diffusion potential always occurs at the reference electrode. It alters the measured cell potential with increasing salinity, so it no longer represents the thermodynamic redox potential. Approaches for compensated determination of a redox level have already been developed for 25°C (Hagemann et al. 2014), but they were derived at very low pH values and are limited to 25°C. Consequently, it is not possible to obtain reliable information on the redox level at temperatures above 25°C.

The study aimed at providing methods and models that allow a bias-free determination of the redox level of saline solutions at neutral to alkaline pH values at 25°C and higher temperatures.

Concerning the aqueous chemistry of iron, it was planned to investigate the speciation of Fe(II) with chloride in sulphate solutions and to develop a model that describes complex formation and solubility in saline systems.

2 Measurement of redox potential in saline solutions

2.1 Previous approaches for bias-free redox determinations

In aqueous solutions, the redox potential (Eh) is usually determined with a combination of a platinum redox electrode and a reference electrode (usually Ag/AgCl/3 M KCl). The method provides reliable information on the redox state of solutions with low salt content, as long as the solution is sufficiently redox buffered, contains sufficient ions of reversibly reacting redox pairs or is in equilibrium with rapidly reacting redox-sensitive solids. This can be achieved in laboratory tests if certain redox buffers such as mixtures of Fe^{2+}/Fe^{3+} or $Fe(CN)_6^{4-}/Fe(CN)_6^{3-}$ are added.

However, the method no longer provides reliable information if the salt content increases. In that case, the diffusion potential between the internal electrolyte of the reference electrode and the measuring solution, which is regarded as constant, changes. The same effect occurs during pH measurements when a reference electrode is used. Except under special experimental conditions that are not always given, the level of the diffusion potential can neither be reliably calculated nor measured so that the measured cell voltage no longer corresponds to the redox potential and cannot be converted into this.

An approach to overcome this problem was developed by Hagemann et al. (2014). It is based on determining the relationship between cell voltage and a known or measurable redox-sensitive variable and deriving from this a model that allows the conversion of the cell voltage into a redox level. Activity ratios of salts (e.g. $FeCl_2/FeCl_3$), concentration ratios of redox pairs (e.g. $Fe(CN)_6^{4-}/Fe(CN)_6^{3-}$) or the partial pressure of oxygen (pO_2/H^+) can be considered as redox-sensitive variables.

Corresponding models were derived from acid solutions containing mixtures of $FeCl_2/FeCl_3$ or $FeSO_4/Fe_2(SO_4)_3$. Chlorides or sulphates of sodium, potassium or magnesium were used as background salts. In Bischofer et al. (2016) the approach was extended to neutral solutions containing potassium hexacyanoferrate.

The determination method consists of two steps:

1. The apparent redox potential of a solution is measured with a normal redox combination electrode.

2. The apparent redox potential (E_{app}) is transformed into an alternative redox measure (Rx_0) by adding an empirical correction term ΔRx that expresses the difference between the theoretical redox potential in the measuring solutions and the apparent value.

Determination of ΔRx and its empirical formula requires a thermodynamic model for the calculation of activity coefficients of Fe(II) and Fe(III) in the measuring solutions. The following formula shows the mathematical relationship for a chloride-containing solution:

$$\Delta Rx = E_{app} - U_0 + 0{,}059\, log\, \frac{a_{Fe^{2+}} a_{Cl^-}^2}{a_{Fe^{3+}} a_{Cl^-}^3}$$

If the background salt concentration is changed, the difference ΔRx between the measured and calculated redox potential can be represented by a simple mathematical expression. The relationship between the difference ΔRx and the background salt concentration c can usually be expressed by a two-parameter expression:

$$\Delta Rx = a\, ln\, c + b$$

where a, b = empirical parameters,

2.2 Activity models for Fe(II) and Fe(III) species in salt solutions

For Fe(II) and Fe(III), the required Pitzer activity models are available at 25°C. They allow the calculation of the activity coefficients of Fe^{2+} in solutions of the salts NaCl, KCl, $MgCl_2$, $CaCl_2$, Na_2SO_4, K_2SO_4 and $MgSO_4$ and for Fe^{3+} in solutions of salts NaCl, KCl, $MgCl_2$, $CaCl_2$ (Moog and Hagemann 2004). For Fe(III) complementary models for Fe^{3+} in solutions of salts K_2SO_4 and $MgSO_4$ were developed (Hagemann et al. 2014). No experimental basis for the Na_2SO_4-$Fe_2(SO_4)_3$-H_2O system was available. These models simplify the chemical reality as they implicitly express complex formation of Fe(III) and Fe(II) with chloride and sulphate in terms of strong ion interactions.. Although the models work quite well in the binary and ternary systems considered for model development, the robustness of the models cannot be guaranteed in multi-ion media. Moreover, these models may be applied only in very acidic solutions. Even at very low pH values, Fe^{3+} starts to form hydroxo complexes that soon predominate the speciation of Fe(III).

While the principal approach of determining the redox level with the help of an empirical activity model for a redox couple was an important step forward, the limited applicability of the thermodynamic model for Fe^{2+} and Fe^{3+} at relevant pH values represented a major draw-back.

As part of the VESPA project, the use of a different redox couple was tested: hexacyanoferrate(II)/ hexacyanoferrate(III) (Bischofer et al. 2016). Both ions have the important advantage of being stable at slightly acidic to mildly alkaline conditions. They do not form strong complexes with chloride, sulphate or alkali metal ions so that their solution chemistry is rather simple. The redox reaction between hexacyanoferrate(II) and hexacyanoferrate(III) is quite fast and reversible.

Some solubility measurements in the systems $K_4Fe(CN)_6$-KCl-H2O and $K_3Fe(CN)_6$-KCl-H_2O have been conducted to complete the available database for potassium hexacyanoferrates. The project VESPA provided a proof of concept that an approach based on this redox couple would be a viable way for a method to determine the redox level at neutral pH values. .

2.3 Experimental approach

The work programme was divided into two parts. On the one hand, redox measurements were carried out on NaCl, $MgCl_2$ and mixed NaCl/$MgCl_2$ solutions. In these solutions, the pH value was determined by adding a buffer. The redox potential was adjusted by adding equal amounts of potassium hexacyanoferrate(II) and potassium hexacyanoferrate(III).

For the evaluation of these investigations it was necessary to develop a model to describe the activity coefficients of $Fe(CN)_6^{3-}$ and $Fe(CN)_6^{2-}$ in binary solutions with Na+, K^+, and Mg^{2+} as well as in mixed solutions with NaCl, KCl and $MgCl_2$. Since the experimental data required for this were insufficient, they had to be supplemented by new experimental data. For this purpose, isopiestic measurements were conducted.

3 Investigation of aqueous solutions containing hexacyanoferrate(II) and hexacyanoferrate(III)

3.1 Preparation of hexacyanoferrate compounds and stock solutions

3.1.1 Sodium hexacyanoferrate(II) – $Na_4Fe(CN)_6$

Sodium hexacyanoferrate(II) (sodium ferrocyanide) – $Na_4Fe(CN)_6 \cdot 10H_2O$ - was obtained from Sigma Aldrich (≥99% Art No. 13425). It was recrystallized once from hot water. A stock solution was prepared by dissolving the solid salt in deionized water and filtering the resulting solution. The concentration of the solution was determined by ICP-OES (both Na and Fe).

3.1.2 Sodium hexacyanoferrate(III) – $Na_3Fe(CN)_6$

Sodium hexacyanoferrate(III) (sodium ferricyanide) – $Na_3Fe(CN)_6$ could not be obtained from commercial suppliers and had to be synthesized in our laboratory. A couple of synthesis methods were described in the literature, most of which included the oxidation of hexacyanoferrate(II) by a strong reagent such as chlorine or hydrogen peroxide (see Williams 1948). The methods depend on a reliable source of ferrocyanide acid which is difficult to synthesize in pure form or leads to impure products.

Instead, we developed an entirely new approach. 92.62 g $NaClO_4 \cdot H_2O$ (Merck Emsure) were dissolved in 73 ml deionized water. A second solution was prepared by adding 67.48 g $K_3Fe(CN)_6$ (Merck) to 167 ml water. The sodium perchlorate solution was added stepwise to the ferrocyanide solution. Immediately a voluminous precipitate of potassium perchlorate formed according to the reaction

$$NaClO_4(aq) + K_3Fe(CN)_6(aq) \rightarrow Na_3Fe(CN)_6(aq) + KClO_4(s)$$

The resulting solution is red. The precipitate settled only slowly. The mixture was given through a folded filter and the filtrate put in a refrigerator. After two days a pale-yellow precipitate has formed. Rinsing with water turned it white so that it was assumed to be $KClO_4$. The filtrate was filtered again, and its volume reduced by heating in a rotary evaporator under a slight vacuum. Red crystals (needles) formed that were sucked dry on a

glass frit and further dried between sheets of filter paper. The product was dissolved in water until just all red crystals dissolved. Few white crystals of $KClO_4$ remained that were removed by filtering. The product was stored in the dark in a desiccator under vacuum above $CaCl_2$. The water content was found to be in the order of 3 to 4 mol per formula unit.

Another batch of sodium hexacyanoferrate(III) was prepared the same way. However, after putting the concentrated solution in the refrigerator at 4°C, no dark red needles but orange cubic crystals formed. Allowing the crystals to heat up at ambient temperature led to their destruction and formation of a red solution. The water content of the orange crystals was in the order of 14 mol per mol $Fe(CN)_6$. However, a second attempt to produce this solid resulted in an oversaturated solution from which only the low hydrate salt formed.

The final solid products contained about 1-3 mol-% potassium in relation to sodium. Consequently, the stock solutions made by the dissolution of this material had the same composition. If sodium ferricyanide was used for solubility measurements in the system $Na_3Fe(CN)_6$-NaCl-H_2O potassium accumulated in the remaining solid hexacyanoferrate(III) phase. The potassium content of the solid increased to 15 to 25 mol-% with respect to Na. Almost no potassium was found in the solid phase when instead halite was the solubility limiting phase.

No further effort was undertaken to identify the phase composition of the hexacyanoferrate(III) solids. It was noted that already Reindel (1867) observed the formation of a mixed sodium potassium ferricyanide $KNa_2Fe(CN)_6$ when he attempted to synthesize pure $Na_3Fe(CN)_6$ from potassium-containing solutions. Therefore, we assume that the potassium-rich ferricyanide is either a mixture of $Na_3Fe(CN)_6 \cdot xH_2O$ and a Na, K double salt or a solid solution $(Na,K)_3Fe(CN)_6 \cdot xH_2O$.

3.1.3 Potassium hexacyanoferrate(II) – $K_4Fe(CN)_6$ and potassium hexacyanoferrate(III) – $K_3Fe(CN)_6$

The salts potassium hexacyanoferrate(II) and potassium hexacyanoferrate(III) were recrystallized once from commercial products (Merck p.a.).

3.1.4 Barium hexacyanoferrate(II) – $Ba_2Fe(CN)_6$

The synthesis of $Mg_2Fe(CN)_6$ required the preparation of barium ferrocyanide. It was prepared as follows: 303 g $Na_4Fe(CN)_6 \cdot 10H_2O$ (Sigma Aldrich >99%) were dissolved in 500 ml deionized water. A second solution was prepared by dissolving 305 g $BaCl_2 \cdot 2H_2O$ (Merck p.a.) in 600 ml deionized water. Both solutions were mixed. Immediately a yellow precipitate formed that settled quickly. The precipitate was washed several times with deionized water to remove traces of sodium chloride. It was dried in an oven at 80°C. The amount of water in the final product was determined by dissolving 0.1916 g of the solid in 100 ml water and measuring the barium content with ICP-OES. The ferrocyanide content in the solid may then be calculated from the charge balance, the water content from the mass balance. The water content of our product could be expressed by the following formula: $Ba_2Fe(CN)_6 \cdot 4.38H_2O$. It is a fine pale yellow powder that easily loses hydrate water upon heating. Changing the heating temperature or the heating duration led to different water contents.

3.1.5 Magnesium hexacyanoferrate(II) – $Mg_2Fe(CN)_6$

This compound was prepared by dissolving 49,28 g of magnesium sulphate heptahydrate (Merck Emsure) in 200 g water and adding a slight excess of solid barium hexacyanoferrate(II) - $Ba_2Fe(CN)_6 \cdot 4.38H_2O$ (60,36 g) and boiling the mixture for 4.5 h. The result was a yellow solution above a white precipitate. The solution was filtered through a 0.45 µm syringe filter. Contact with air soon led to a greenish colour of the solution, possibly caused by a partial decomposition of ferrocyanide, subsequent oxidation of Fe^{2+} to Fe^{3+} and formation of of Prussian blue. The solution was concentrated in a rotary evaporator until a moist solid remained. It was dissolved in little water, filtered and put back into the evaporator. This procedure was repeated once. The final product was dried between sheets of filter paper and later in an oven at 50°C. Its water content was determined by dissolving the solid in water and measuring the iron, barium and magnesium content. The resulting formula was $(Mg_{0.987}Ba_{0.013})Fe(CN)_6 \cdot 9.4H_2O$.

3.1.6 Magnesium hexacyanoferrate(III) - $Mg_3[Fe(CN)_6]_2$

The preparation of magnesium hexacyanoferrate(III) was performed in two steps. In the first step, hexacyanoferrate(III) acid was synthesised by slowly adding 86.86 g cold (0°C) perchloric acid (VWR Analar Normapur 70%, concentration determined by titration to be

69.42 wt.-%) to a solution of potassium hexacyanoferrate(III) (65.85 g in 200 ml water). The reaction was done under Argon in a three-necked Erlenmeyer flask immersed in an ice bath. A precipitate of $KClO_4$ formed immediately according to the formula

$HClO_4(aq) + K_3[Fe(CN)_6](aq) \rightarrow KClO_4(s) + H_3[Fe(CN)_6](aq)$

After 30 minutes stirring the mixture was filtered. A second mixture was prepared by adding 17.49 g $Mg(OH)_2$ to 20 ml of water. The hexacyanoferrate(III) acid solution was slowly given to this mixture. Since magnesium hydroxide was in excess, parts of it didn't react. The resulting pH = 6 showed that no free acid remained. The mixture was filtered and put in a refrigerator. Solid magnesium hexacyanoferrate(III) was obtained by transferring the solution to a darkened desiccator where it was stored under vacuum above $CaCl_2$. After nine days a colourless precipitate formed, possibly $KClO_4$. It was filtered off. After 13 days the solution weight was reduced from 312 to 124 g. The solution was decanted into a new cup. Another week later 50 g of a dark red solid could be removed from the dish, was dried between filter paper and further dried in a desiccator.

The product was purified by dissolving in water and drying in a desiccator nearly to dryness. The supernatant solution was discarded, the crystals dried. An analysis showed that the solid still contained some potassium. The ratio K/Mg was 0.023. The water content was 14.3 mol per formula unit. Further purification may have been possible but due to the low amount of solid magnesium hexacyanoferrate(III) available the losses of the purification process would have been too large.

3.1.7 Determination of the solubility of hexacyanoferrates

To have a good estimate of the maximum solution concentration of sodium and magnesium hexacyanoferrates some experiments were conducted to test their solubility. Small amounts of water were added to the dried solids in screw-capped glass flasks and immersed in a water bath at 25.0°C. The flasks were shaken from time to time to allow for a faster equilibration. After one day samples were taken both from the solution and the solid. The solids were dried between sheets of filter paper and then dissolved in water. They may contain minor amounts of a saturated solution. The results are summarized in Tab. 3.1.

Tab. 3.1 Solubility of sodium and magnesium hexacyanoferrates

Salt	Concentration of saturated solution [mol/kg]	Minor components in solution [mol/mol]	Minor components in solid [mol/mol]
$Na_3Fe(CN)_6 \cdot 2.4H_2O \cdot$	3.2	K/Na: 0.016	K/Na: 0.099
$Mg_3[Fe(CN)_6]_2 \cdot 15.1H_2O$	0.86	K/Mg: 0.045	K not detectable
$Mg_2Fe(CN)6 \cdot 12.9H_2O$	1.45	Ba/Mg: 0.016	Ba/Mg: 0.004

3.1.8 Preparation and analysis of stock solutions

Stock solutions were prepared by dissolving weighed amounts of hexacyanoferrate compounds in deionized water. Their concentration was determined by analysis of iron, the corresponding cation (K, Na, Mg) as well as minor constituents (Ba, K).

Stock solutions of sodium chloride and calcium chloride were prepared by dissolution of NaCl and $CaCl_2 \cdot 4H_2O$ (both Merck suprapur) in deionized water. In the case of NaCl, the concentration of the concentration was determined from the weighed masses of NaCl and water. It was checked and adjusted using the solution density (measured using an Anton Parr DMA 5000 M density oscillator with ±0,000001 g/cm^3) and the density/ concentration relationship established by Romankiw and Chou (1983).

The concentration of $CaCl_2$ solutions was determined based on the solution density and the density/ concentration relationship published by Laliberté and Cooper (2004). This model allows a determination of the $CaCl_2$ concentration within an uncertainty margin (95%) of 0.1% (rel.).

3.2 Description of the isopiestic method

Isopiestic measurements were performed at 25 to 90°C. The method has been described earlier in detail by Moog and Hagemann (2004). As for this project isopiestic measurements were to be conducted at higher temperatures, the experimental set up from earlier experiments at 25 °C underwent some revision. Up to 40 °C, isopiestic vessels were placed in an open water bath as shown below (Fig. 3.1).

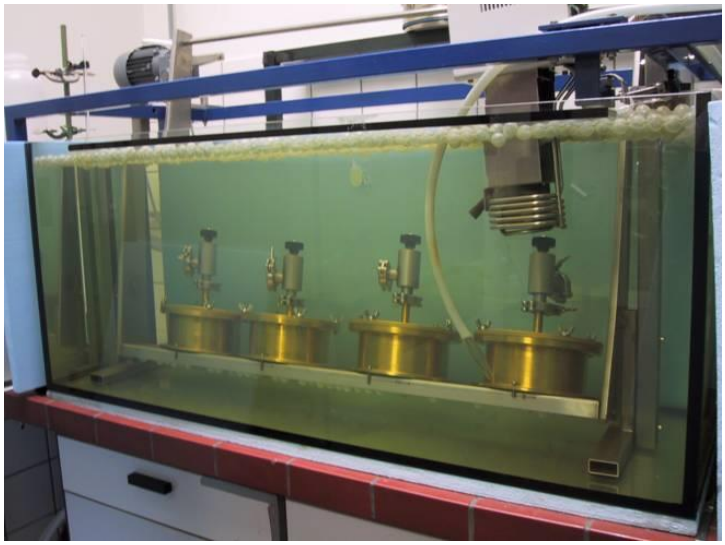

Fig. 3.1 Experimental set up for isopiestic measurements up to 40 °C

For higher temperatures, the vessels were stored in ovens, whose temperature was controlled at the required temperature (60 or 90°C) and was regularly checked by separate thermometers. It was found to be within a 0.1 °C margin around the desired value. The vessels were slowly rocked on a board that was moved by a device placed outside the oven (Fig. 3.3).

For temperatures above 40 °C, a second lid was installed inside the vessel, just above the cups, which on its lower side was covered with a special rubber. Upon removal from the thermostat, the lid of the vessel was opened, and the second lid was screwed down onto to the cups After that the vessel was closed again and left to cool down. When the vessel was at room temperature the outer and inner lids were opened. The cups were closed with small plastic lids and then weighed. Between the opening of the vessel and the closure of the cups with the rubber lid, some water from the solution may vaporise and get lost to the atmosphere. This will lead to increased solution concentrations in the cups. On the other hand, some of the water in the saturated hotter atmosphere above the cups gets trapped inside the cups and will condensate during the following cooling period. This process would lead to a decrease in solution concentrations. No tests were performed to estimate the amount of lost or gained water, but it is assumed to be small. As the water activity is the same in all cups, it is also assumed that the water loss per time unit is also roughly the same, so that the impact on the concentrations of the solutions is similar. Both effects (water loss and condensation) vary from cup to cup and cause a scattering of the analytical data that increases with temperature.

Fig. 3.2 Isopiestic vessel inside an oven

Fig. 3.3 This picture shows a motor fixed at the outside of an oven to exert a gentle rocking motion to the board on which the isopiestic vessels rest

The compositions of equilibrated solutions were determined by reweighing. Each cup was visually inspected for clues as to oxidation of the solution, or droplets occurring at the surface of the rubber.

Typically, the variance between the smallest and highest concentration of binary salts in parallel cups was less than 0.1 wt.-% at 25°C and less than 0.3 wt.-% at higher temperatures.

3.3 The system $Na_4Fe(CN)_6$-H_2O

3.3.1 Previous thermodynamic investigations

The first investigation of this system has been conducted by Berkeley et al. (1916). They measured the osmotic pressure Π of $Na_4Fe(CN)_6$ at 0°C and concentrations between 0.08 and 0.3 mol/kg. These data were recalculated into water activities (and subsequently into osmotic coefficients) using the Raoult-Lewis equation

$$\Pi = \frac{-ln a_{H_2O}}{V_0} \mathrm{R}T \tag{3.1}$$

V_0: molar volume of water at temperature T

Π =

The molar volume of water at 0°C ($1.80181 \cdot 10^{-5}$ m^3/mol) was calculated from its density at the same temperature (0,999843 kg/l, Wagner and Pruss 2002).

Silvester and Rock (1973) measured the mean activity coefficient of $Na_4Fe(CN)_6$ potentiometrically between 0.0005 and 0.1 mol/kg.

3.3.2 Water activities of solutions in the system $Na_4Fe(CN)_6$-H_2O

In total 24 pairs of NaCl and of $Na_4Fe(CN)_6$ solutions were brought into equilibrium. All results are summarized in Tab. 9.1. Some experiments at 60°C resulted in cloudy solutions or precipitation. The long test duration (up to several months for all three temperatures) and the repeated contact with atmospheric oxygen led to partial decomposition of the hexacyanoferrates. Such experiments were excluded from further evaluation.

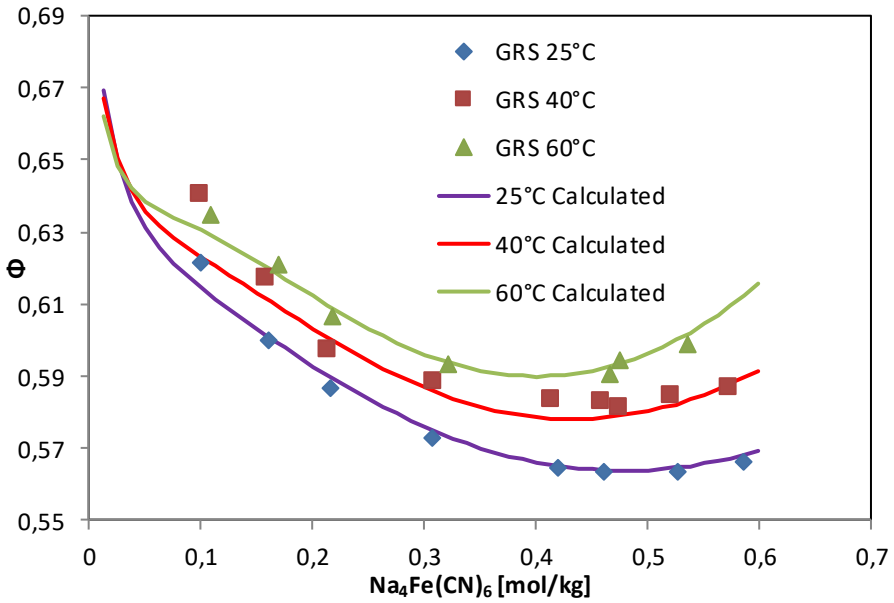

Fig. 3.4 Osmotic coefficients of $Na_4Fe(CN)_6$ solutions at 25 to 60°C

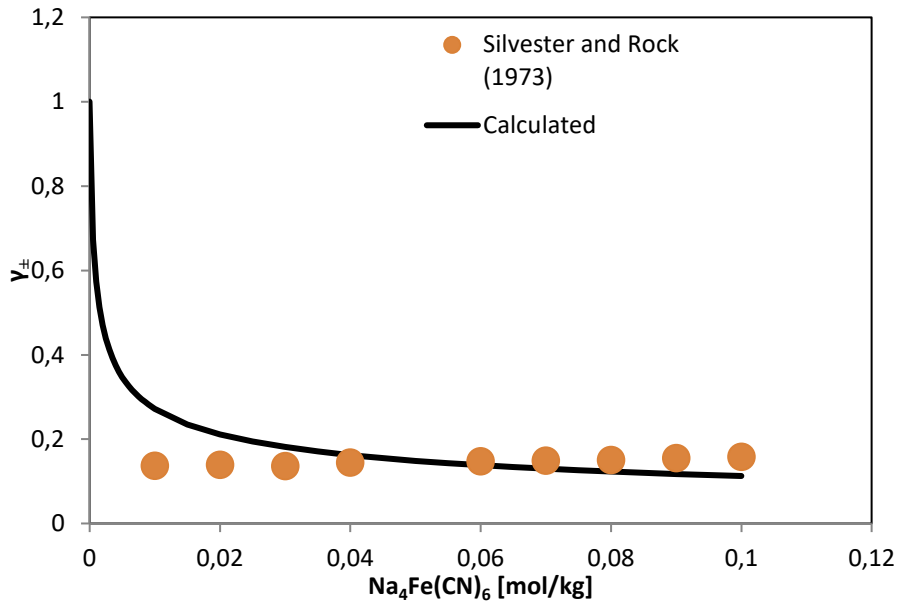

Fig. 3.5 Activity coefficients of $Na_4Fe(CN)_6$ solutions at 25°C

Discussion

Our results are shown in **Fig. 3.4**. At all temperatures, the measured values show the same course. Up to approx. 0.3 mol/kg a continuous decrease can be observed. After that, the osmotic coefficients are almost constant. There is little difference between the

data at 25, 40 and 60°C. The osmotic coefficients calculated from the data of Berkeley et al. (1916) are noticeably lower and are not shown in the diagram. This observation also applies to other salt solutions he and his collaborators have investigated. It can therefore be assumed that the measurements made by Berkeley et al. (1916) were influenced by a systematic error.

A set of Pitzer ion interaction parameters was developed based on our experimental results and the potentiometric data from Silvester and Rock (1973). It became clear that it was not possible to represent the potentiometric data without introducing the parameter $\beta^{(2)}$ for the interaction between Na^+ and $Fe(CN)_6^{4-}$. It reflects the complex formation between the two ions at low ionic strength and was calculated form the complex formation constant log β_1 = 2,36 (Capone et al. 1986):

$\beta^{(2)}_{Na+,Fe(CN)64-} = \beta_1/2 = -114$

The temperature dependence of Pitzer interaction coefficients for $Na_4Fe(CN)_6$ as well as for all other systems considered in this study is expressed by the following general formula:

$$P = P(T_{Ref}) + a_2\left(\frac{1}{T} - \frac{1}{T_{Ref}}\right) + a_3 ln\left(\frac{T}{T_{Ref}}\right) + a_4(T - T_{Ref}) + a_5(T^2 - T_{Ref}^2) + a_6\left(\frac{1}{T^2} - \frac{1}{T_{Ref}^2}\right)$$

Tab. 3.2 Pitzer interaction coefficients for the system $Na_4Fe(CN)_6$-H_2O at 25 to 60°C

Parameter	**P(25°C)**	**a_2**
$\beta^{(0)}$ (Na^+,$Fe(CN)_6^{4-}$)	0.3310	-0.000829
$\beta^{(1)}$ (Na^+,$Fe(CN)_6^{4-}$)	7.0287	0.049566
$\beta^{(2)}$ (Na^+,$Fe(CN)_6^{4-}$)	-114	not determined
C^{γ} (Na^+,$Fe(CN)_6^{4-}$)	0.001716	0.00055473
$\alpha^{(1)}$ (Na^+,$Fe(CN)_6^{4-}$)	1.4	
$\alpha^{(2)}$ (Na^+,$Fe(CN)_6^{4-}$)	12	

With these parameters, the data in homogenous solutions could be represented well (Fig. 3.4, Fig. 3.5).

3.3.3 Solubility of sodium hexacyanoferrate(II)

Data on the solubility of $Na_4Fe(CN)_6$ were presented by numerous investigators in the temperature range -1 to 104 °C (Tab. 3.3). Further data were published by Klenk et al. (1987) but their data source is not clear. The results are quite consistent up to a temperature of about 80°C. This region is marked by the occurrence of $Na_4Fe(CN)_6 \cdot 10H_2O$. Above 81.5 °C a salt with less hydrate water becomes stable (Farrow 1926, **Fig. 3.6**). Neither Conroy (1898) nor Friend et al. (1929) reported a new salt although there is a remarkable bend in their solubility data at this temperature as well. The number of water molecules has not been determined but the independence of the solubility from temperature leads to the assumption that the salt is free of hydrate water (as observed for other Na 2:1 salts such as Na_2SO_4). Between -1 and 80°C the solubility may be calculated from the empirical formula (3.2).

$$m_{sat}\ (\mathrm{Na_4Fe(CN)_6 \cdot 10H_2O}) = 0{,}678 + 0{,}06009(T - T_R) - 0{,}000241(T^2 - T_R^2) + 3{,}79 \cdot 10^{-7}(T^3 - T_R^3) \quad (3.2)$$

At 25°C, the solubility is 0.678 mol/kg.

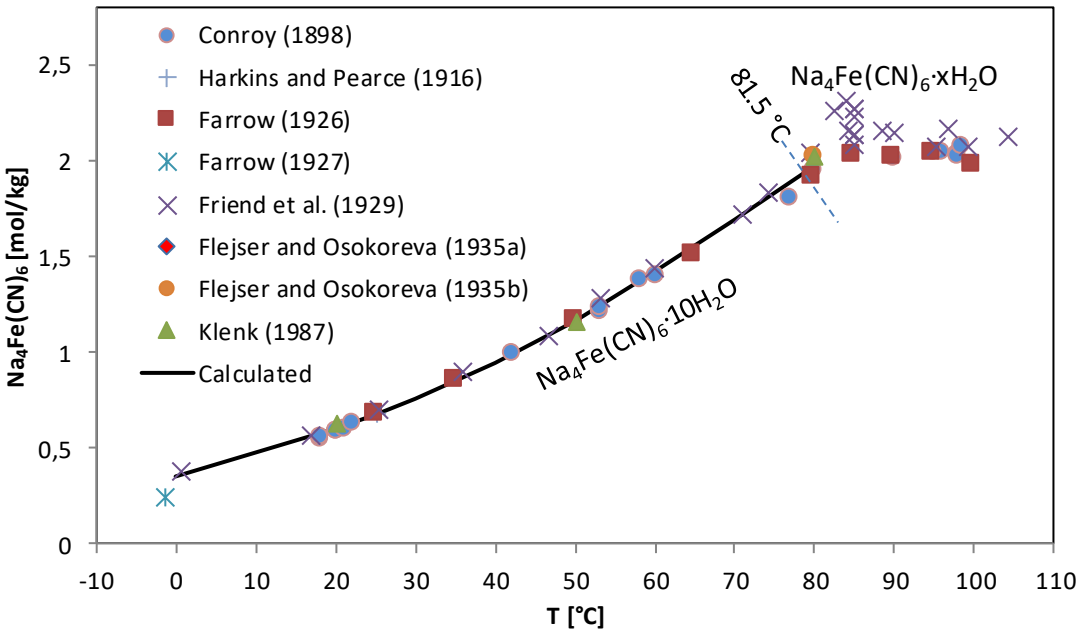

Fig. 3.6 Solubility in the system $Na_4Fe(CN)_6$-H_2O

Tab. 3.3 Data on the solubility of $Na_4Fe(CN)_6$ in water

Source	Temperature range [°C]	No. of data points
Conroy (1898)	18-98	19
Harkins and Pearce (1916)	25	1
Farrow (1926)	25-100	9
Farrow (1927)	-1	1
Friend et al. (1929)	0 – 104	36
Fleysher and Osokoreva (1935a)	25	1
Fleysher and Osokoreva (1935b)	80	1

Using the Parameters developed above the solubility constant may be expressed by the following equation:

$$\log K\ (Na_4Fe(CN)_6 \cdot 10H_2O) = -5{,}100 + 1139 \ln (T/T_R) - 7{,}744\ (T-T_R) + 0{,}006641\ (T^2-T_R^2).$$

In the same manner, the solubility constant was calculated for the water-free $Na_4Fe(CN)_6$. The quite scattered data from Friend et al. (1929) were omitted.

$$\log K\ (Na_4Fe(CN)_6) = -1{,}77 + 0{,}0681\ (T-T_R).$$

The solubility is calculated very well even at temperatures that are beyond those used for the determination of the interaction parameters (Fig. 3.6).

3.4 The system $K_4Fe(CN)_6$-H_2O

3.4.1 Previous thermodynamic investigations

Robinson (1937) was the first to determine the vapour pressure of $K_4Fe(CN)_6$ solutions using the isopiestic method. His measurements concentrate on 25°C. At the same time, Bovalini and Fabris (1937) measured the vapour pressure of saturated solutions between 25 and 104°C. Adie (1891) and Berkeley et al. (1909) determined the osmotic pressure at 15 and 0°C, respectively. Several measurements of the freezing point depression were performed at the turn of the 19th century that could be used as complementing information (Guthrie 1878, Jones 1906, Noyes and Johnston 1909, Fabris 1921).

3.4.2 Water activities of solutions in the system $K_4Fe(CN)_6$-H_2O

34 solutions of $K_4Fe(CN)_6$ were equilibrated. The results are summarized in Tab. 9.5. Some experiments at 60°C resulted in cloudy solutions or precipitation. The long test duration (up to several months for all three temperatures) and the repeated contact with atmospheric oxygen led to partial decomposition of the hexacyanoferrates. Such experiments were excluded from further evaluation.

Discussion

Our three lines of isopiestically determined osmotic coefficients at 25, 40 and 60°C are only comparable to the measurements of Robinson (1937). Both Berkeley et al. (1909) and Bovalini and Fabris (1937) published quite scattered point groups that obviously are of lower quality (not shown in Fig. 3.7). Robinson's data at 25°C differ from ours at concentrations below 0.55 mol/kg. The reason for this observation is not obvious. Robinson (1937) published only interpolated data while the original composition of equilibrium concentrations are not available. Moreover, his last point at the highest concentration is well above the solubility of $K_4Fe(CN)_6 \cdot 3H_2O$ at this temperature.

The three data lines are in equal distance at concentrations above 0.1 mol/kg. A set of Pitzer ion interaction parameters was developed based on our experimental results and the data of Robinson (1937). As has been done for the system $Na_4Fe(CN)_6$-H_2O, the parameter $\beta^{(2)}$ for the interaction between K^+ and $Fe(CN)_6^{4-}$ was introduced to reflect the complex formation between the two ions at low ionic strength. It was calculated from the complex formation constant $\log \beta_1 = 2{,}35$ (Eaton et al. 1967, similar values determined by Cohen and Plane 1957, Robertis et al. 1984).

$$\beta^{(2)}_{K+,Fe(CN)64-} = \beta_1/2 = -112$$

With these parameters, the data in homogenous solutions could be represented well (Fig. 3.7).

Tab. 3.4 Pitzer interaction coefficients for the system $K_4Fe(CN)_6$-H_2O at 25 to 60°C

Parameter	P(25°C)	$T-T_R$
$\beta^{(0)}$ (K^+,$Fe(CN)_6^{4-}$)	0.3074	0.001794
$\beta^{(1)}$ (K^+,$Fe(CN)_6^{4-}$)	6.4075	0.037576
$\beta^{(2)}$ (K^+,$Fe(CN)_6^{4-}$)	-112	not determined
C^{γ} (K^+,$Fe(CN)_6^{4-}$)	-0.005608	1.938E-05
$\alpha^{(1)}$ (K^+,$Fe(CN)_6^{4-}$)	1.4	
$\alpha^{(2)}$ (K^+,$Fe(CN)_6^{4-}$)	12	

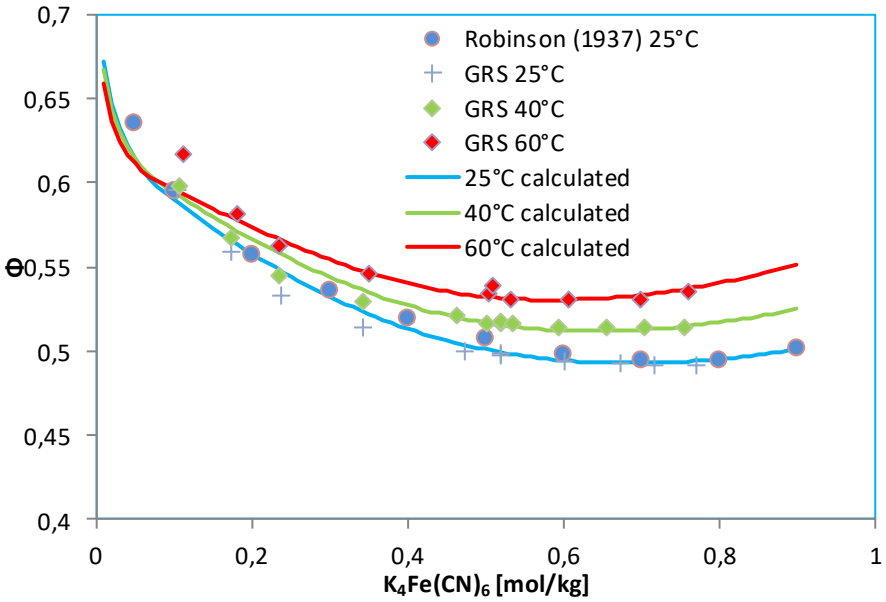

Fig. 3.7 Osmotic coefficients of $K_4Fe(CN)_6$ solutions at 25 to 60°C

3.4.3 Solubility of potassium hexacyanoferrate(II)

Most literature data on the solubility of $K_4Fe(CN)_6$ in water are well consistent (Tab. 3.5, Fig. 3.8). Between 0 and 100°C, there is an almost linear increase. The data of Conroy (1898) as well of Harkins and Pearce (1916) are somewhat too low. Up to a temperature of 87,3°C, $K_4Fe(CN)_6$ crystallises with three water molecules. At higher temperature, the salt is free of hydrate water. Careful investigation by Vallance (1927) showed a weak breaking point at about 17.7°C but no crystallographic or chemical difference could be

found between the solids appearing before and after this temperature. At 25°C, the solubility amounts to 0.857 mol/kg.

Tab. 3.5 Data on the solubility of $K_4Fe(CN)_6$ in water

Source	Temperature range [°C]	No. of data points
Conroy (1898)	22-97	5
Harkins and Pearce (1916)	25	1
Fabris (1921)	0-100	15
Vallance (1922)	10-25	6
Farrow (1926)	25-100	6
Vallance (1927)	10-25	7
Fabris (1931)	86-93	5
Fabris (1932)	70-104	24
Bovalini and Fabris (1933)	-2-104	9
Tettamanzi (1933)	18	1
Regner and Baley (1957)	15-80	4

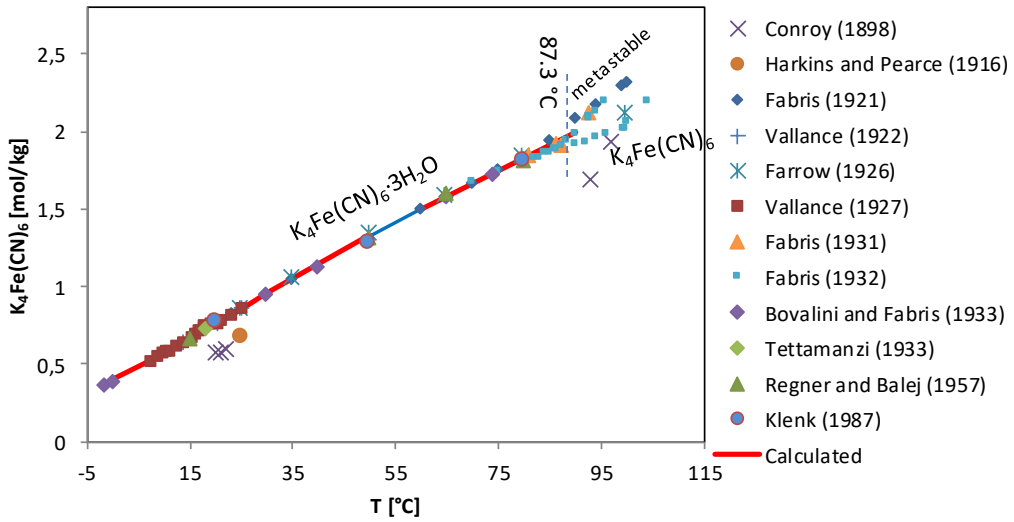

Fig. 3.8 Solubility in the system $K_4Fe(CN)_6$-H_2O

Using the Parameters developed above the solubility constant may be expressed by the following equation:

$$\log K\ (K_4Fe(CN)_6 \cdot 3H_2O) = -5{,}204 + 0{,}0984\ (T-T_R) - 0{,}0001100\ (T^2-T_R^2).$$

The solubility is calculated very well even at temperatures that are beyond those used for the determination of the interaction parameters

3.5 The system $Mg_2Fe(CN)_6$-H_2O

3.5.1 Previous thermodynamic investigations

So far, there have been neither solubility nor vapour pressure measurements of magnesium Hexacyanoferrate(II) solutions. Two measurements of the osmotic pressure by Berkeley et al. (1916) suffer from the same issues as Berkeley's other measurements and are not very reliable. The heat of dilution for some very diluted solutions has been determined by Langer and Miederer 1956.

It has been found that there is considerable complex formation between Mg^{2+} and $Fe(CN)_4^{2+}$ as it could be expected for a 2:4 system (e.g. Aruga 1982).

3.5.2 Water activities of solutions in the system $Mg_2Fe(CN)_6$-H_2O

In total, 42 solutions of $Mg_2Fe(CN)_6$ were brought into equilibrium at 25, 40 and 60°C. The results are summarized in Tab. 9.1. Some experiments at 60°C resulted in cloudy solutions or precipitation. Such experiments were excluded from further evaluation.

Discussion

Our three lines of isopiestically determined osmotic coefficients at 25, 40 and 60°C are only comparable to the measurements of Berkeley et al. (1916), from which they differ considerably. While our observed osmotic coefficients at 25 and 40°C lie close to each other, data at 60°C are considerably lower. But there is no hint that the data that were produced in different experiments are consistently wrong.

The magnesium ion forms a strong complex with hexacyanoferrate(II).

$$Mg^{2+} + Fe(CN)_6^{4-} \rightleftharpoons MgFe(CN)_6^{2-}$$

Several authors determined the formation constant and found consistent values (**Tab. 3.6**). Based on the data of Jackman and Lister (1975) between 15 and 35 the temperature dependence may be written as

$\log \beta_1 = 3.77 - 70.5\ (T-T_R)$.

Tab. 3.6 Equilibrium constant for the formation of the complex formation

Source	**Temperature [C]**	**log β_1**
Cohen and Plane (1957)	25	3.81
Jackman and Lister (1975)	15.2 24.8 35	3.659 3.766 3.866
Hedwig and Watson (1981)	25	3.77
Aruga (1982)	25	3.77

Due to the strong effect of ionic strength on the activity coefficient of $Fe(CN)^{4-}$ the Magnesium hexacyanoferrate complexes have only a limited stability field. In $Mg_2Fe(CN)_6$ solutions about 0.1 mol/kg they are not expected to exist in significant concentrations.

A set of ion interaction parameters was developed based on isopiestic data. The calorimetric data of Langer and Miederer (1956) were omitted since the concentration range of their measurements did not coincide with any other data and the potential effects of complex formation could not be evaluated. The parameter $\beta^{(2)}$ was calculated from the complex formation constant as decribed above.

Using the parameters in Tab. 3.2, the experimental results are represented quite well, but rising deviations exist at the highest concentrations. The calculated line at 40° only in part corresponds with the data points. This is an indication that either the results at 40°C or 60°C are erroneous. The overall impression is that the underlying chemistry is not well reflected by the simple Pitzer model. More research is needed to understand the extent of complexation in concentrated $Mg_2Fe(CN)_6$ solutions.

Tab. 3.7 Pitzer interaction coefficients for the system $Mg_2Fe(CN)_6$-H_2O at 25 to 60°C

Parameter	P(25°C)	ln(T/T$_R$)	T-T$_R$
$\beta^{(0)}$ (Mg^{2+}, $Fe(CN)_6^{4-}$)	2.0437		0.000289
$\beta^{(1)}$ (Mg^{2+},$Fe(CN)_6^{4-}$)	57.5982 (α_1=2)		0.210230
$\beta^{(2)}$ (Mg^{2+},$Fe(CN)_6^{4-}$)	-2918 (α_2=12)	6259727	n.d.
C^{γ} (Mg^{2+},$Fe(CN)_6^{4-}$)	-0.08142		n.d.
$\alpha^{(1)}$ (Mg^{2+},$Fe(CN)_6^{4-}$)	1.4		
$\alpha^{(2)}$ (Mg^{2+},$Fe(CN)_6^{4-}$)	12		

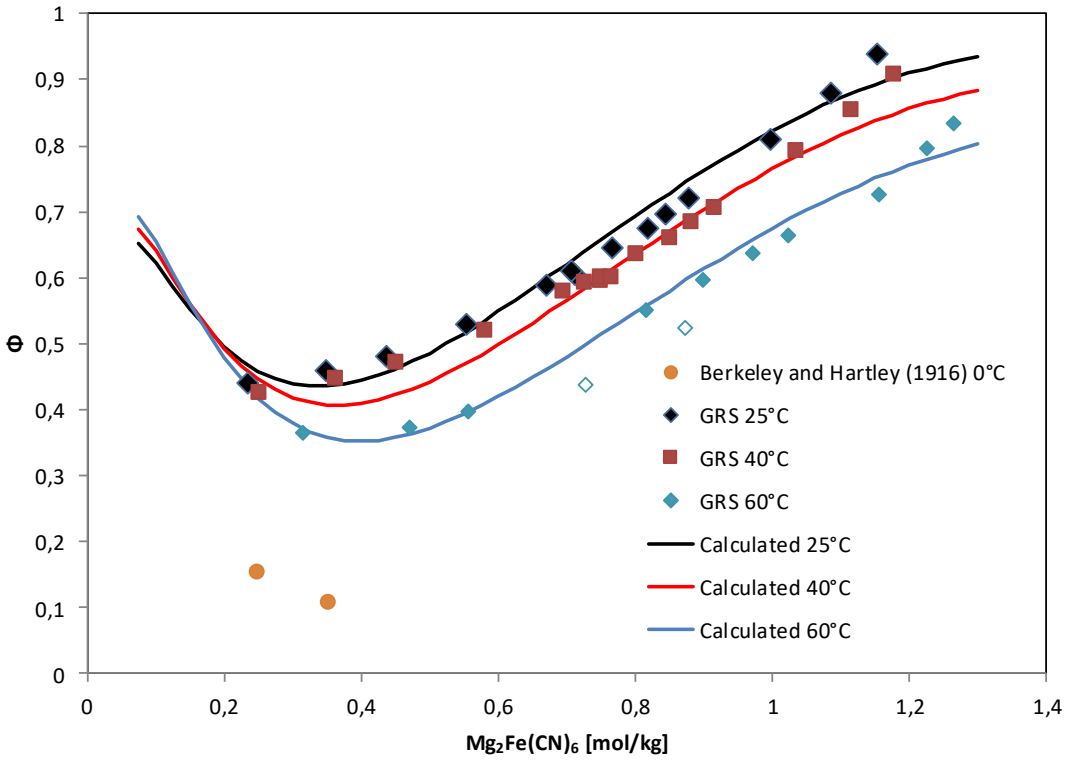

Fig. 3.9 Osmotic coefficients of $Mg_2Fe(CN)_6$ solutions at 25 to 60°C

3.5.3 Solubility of magnesium hexacyanoferrate(II)

A thermogravimetric investigation by Cappellina and Bubani (1954) found that the number of water molecules in the solid compound at 20°C is nine. At about 85°C it decomposes to $Mg_2Fe(CN)_6 \cdot 7H_2O$, two more molecules are lost at about 110°C.

However, solubility measurements in the system $MgCl_2$-$Mg_2Fe(CN)_6$-H_2O evaluated by the Schreinemakers method revealed that the solid in equilibrium with the solutions at low $MgCl_2$ concentration had the composition $Mg_2Fe(CN)_6 \cdot 11H_2O$. Its solubility at 25°C was 1.38 mol/kg.

Only one source could be found that reported a solubility for $Mg_2Fe(CN)_6$ (Kunze 2004). No primary source is given. The solubility is given as 330 g/l but in absence of a density, this value cannot be recalculated into a molality. The density of the saturated solution in our laboratory was about 1.22 kg/l. This would lead to a molality of about 1.42 mol/kg which is very close to our result.

At the concentration of 1.38 mol/kg, the calculated ion activity product is

Log K = -9.32

Originally, it was planned to extend the solubility measurements in this system to higher temperatures as well. The serious problems in understanding the underlying chemistry and modelling of this system (see below) led to the conclusion that speciation must better be understood in the first place.

3.6 The system $Na_3Fe(CN)_6$-H_2O

3.6.1 Water activities of solutions in the system $Na_3Fe(CN)_6$-H_2O

So far, the water activity of $Na_3Fe(CN)_6$ has not been tested before. Our results at 25, 40, and 60°C are shown in Fig. 3.10. They do not differ very much at different temperatures. Only at concentrations above 2 mol/kg, the branches of osmotic coefficients spread slightly. For the calculation of ion interactions coefficients, the calorimetric measurements of Lange and Secrest (1957) in very diluted solutions were not considered as they could not be brought into coherence with our results.

Based on the isopiestic data ion interaction coefficients in Tab. 3.8 were derived. They represent the experimental data very well (Fig. 3.10).

Tab. 3.8 Pitzer interaction coefficients for the system $Na_3Fe(CN)_6$-H_2O at 25 to 60°C

Parameter	P(25°C)	$T-T_R$
$\beta^{(0)}$ (Na^+, $Fe(CN)_6^{3-}$)	0.4076	0.001862
$\beta^{(1)}$ (Na^+,$Fe(CN)_6^{3-}$)	5.6800	0.014276
C (Na^+,$Fe(CN)_6^{3-}$)	-0.005507	-0.00012423
$\alpha^{(1)}$ (Na^+,$Fe(CN)_6^{3-}$)	2	

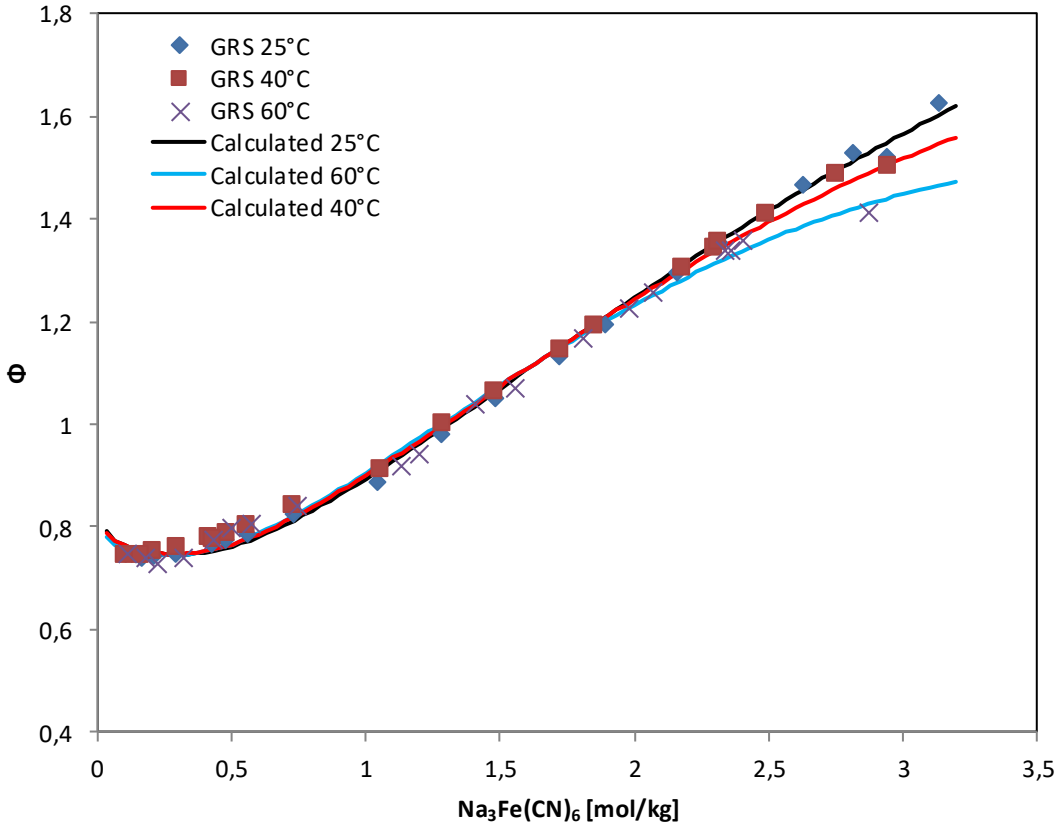

Fig. 3.10 Osmotic coefficients of $Na_3Fe(CN)_6$ solutions at 25 to 60°C

3.6.2 Solubility sodium hexacyanoferrate(III)

At room temperature sodium hexacyanoferrate(II) crystallizes as a dihydrate, $Na_3Fe(CN)_6 \cdot 2H_2O$ (Neumark 1944, Katila et al. 1980). As stated above, we found that at about 4°C the solid may contain up to 14 molecules of water.

In his compilation, Kunze (2004) reported that the solubility of $Na_3Fe(CN)_6$ would be 189 g/l but no primary source is given or the composition of the solubility limiting phase. Bette (1837) published data on the solubility in “cold” and “hot” water (recalculated as 0.67 and 2.37 mol/kg). At 25°C, we found that the solubility is about 3.27 mol/kg. This results in a solubility constant of log K = 2.20.

3.7 The system $K_3Fe(CN)_6$-H_2O

3.7.1 Water activities of solutions in the system $K_3Fe(CN)_6$-H_2O

Among all hexacyanoferrate salts, potassium hexacyanoferrate(III) has been investigated most intensively. Scientific work included isopiestic, osmotic, potentiometric, calorimetric, and freezing point measurements (Tab. 3.9). Additional isopiestic measurements were performed in this study.

Tab. 3.9 Thermodynamic data on $K_3Fe(CN)_6$ solutions

Source	Method	Temperature [°C]
Guthrie (1878)	Freezing point depression	<0
Kistiakowsky (1890)	Freezing point depression	<0
Jones (1906)	Freezing point depression	<0
Bedford (1910)	Freezing point depression	<0
Berkeley et al. (1916)	Osmotic pressure	0
Robertson and La Mer (1931)	Freezing point depression	<0
Robinson and Levien (1946)	Isopiestic	25
Lange and Miederer (1956)	Dilution enthalpy	25
Hepler et al. (1960)	Solution enthalpy	25
Malatesta et al. (1994)	Potentiometric	25

For the determination of interaction coefficients, only the potentiometric and isopiestic measurements were used. It became clear that especially the potentiometric data could

only be fitted by applying a $\beta^{(2)}$ value to express the weak but notable complex formation between K^+ and $Fe(CN)_6^{3-}$ at low ionic strengths. In a first approach, the medium value for the complex formation constant was calculated from five literature sources (Tab. 3.9). This strongly improved the agreement of predicted and experimental data. However, optimizing $\beta^{(2)}$ further improved the situation (Fig. 3.12, Fig. 3.13,). Even for 0°C and lower, for which data have not been taken into account, experimental and calculated data correspond very well (Fig. 3.11). The final set of parameters is given in Tab. 3.11.

Tab. 3.10 Complex formation constant for $KFe(CN)_6^{2-}$

Source	**Method**	**Value**
James and Monk (1950)	Conductivity	1,2
Tanaka et al. (1966)	IR Spectroscopy	1,3
Rutkovskii and Mironov (1967)	Solubility	*0,9031*
Eaton et al. (1967)	Potentiometric	1,46
Lemire and Lister (1976)	Conductivity	1,4771
Dehury et al. (2012)	Conductivity	1,50
Medium value (without Rutkovskii and Mironov 1967)		**1,39**
Calculated from $\beta^{(2)}$= -14,3004 (this work)		1,46

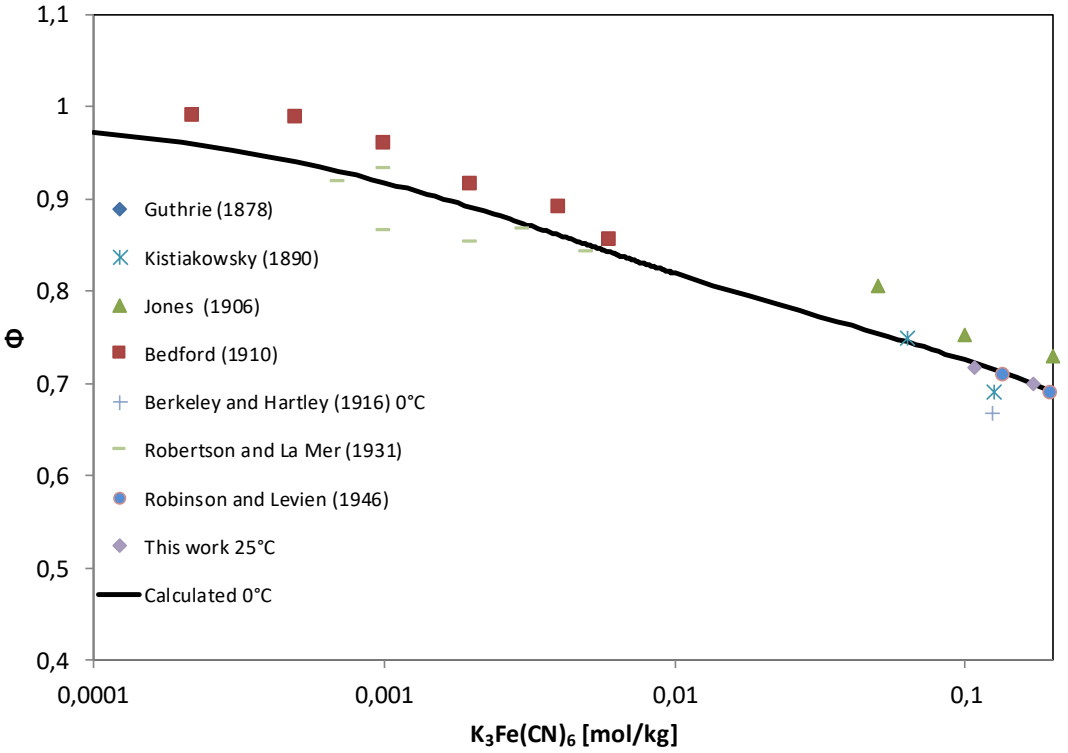

Fig. 3.11 Osmotic coefficients of $K_3Fe(CN)_6$ solutions at or below 0°C

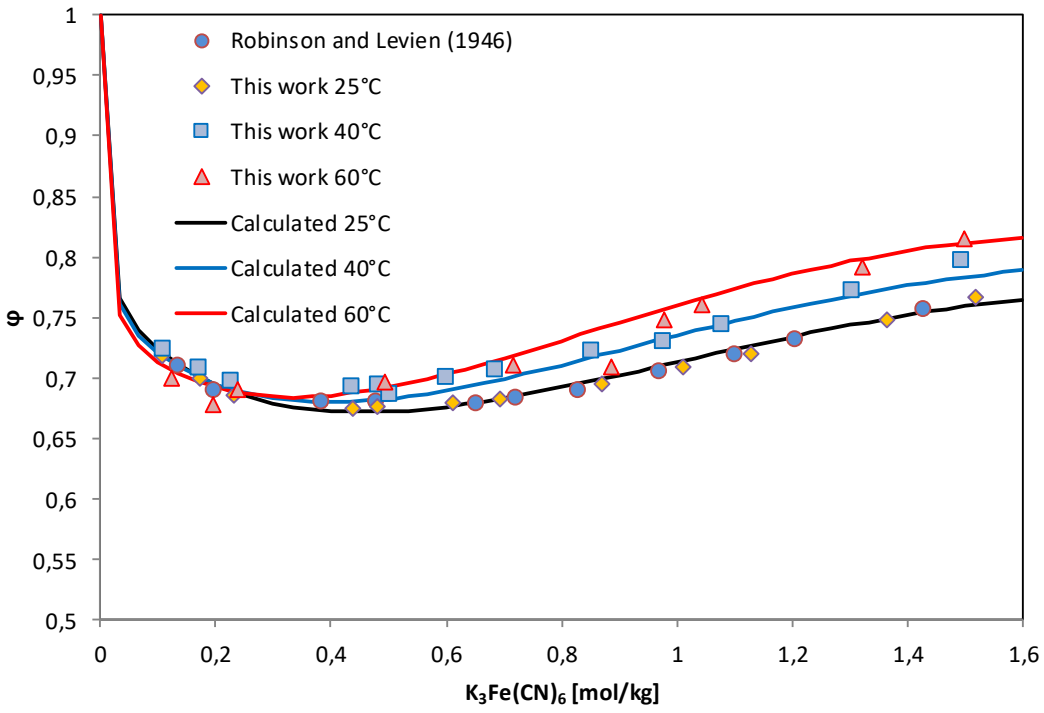

Fig. 3.12 Osmotic coefficients of $K_3Fe(CN)_6$ solutions at 25, 40 and 60°C

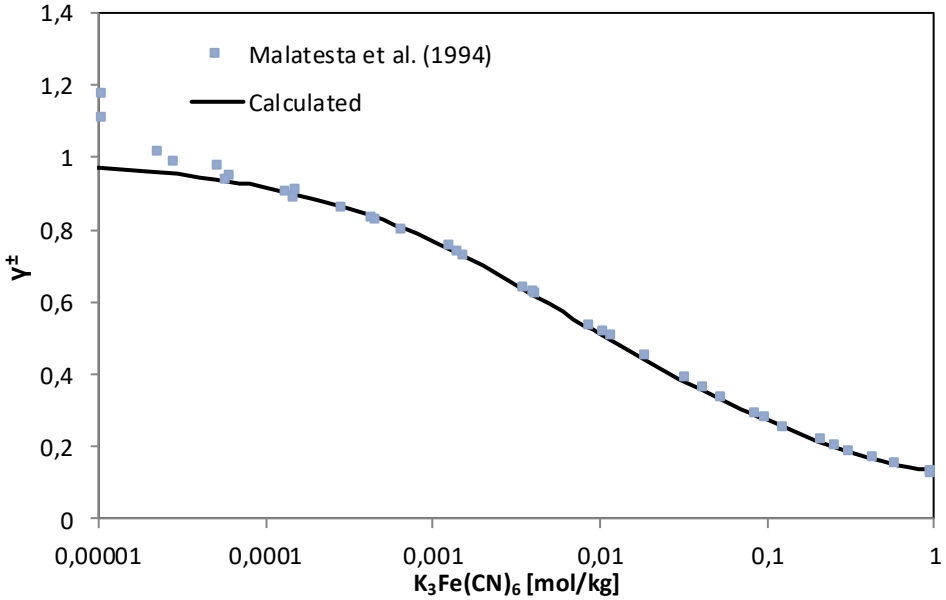

Fig. 3.13 Activity coefficients of $K_3Fe(CN)_6$ at 25°C

Tab. 3.11 Pitzer interaction coefficients for the system $K_3Fe(CN)_6$-H_2O at 25 to 60°C

Parameter	P(25°C)	$T-T_R$
$\beta^{(0)}$ (K^+, $Fe(CN)_6^{3-}$)	0.3394	0.002825
$\beta^{(1)}$ (K^+, $Fe(CN)_6^{3-}$)	4.6527	0.009299
$\beta^{(2)}$ (K^+, $Fe(CN)_6^{3-}$)	-14.30	not determined
C^{γ} (K^+, $Fe(CN)_6^{3-}$)	-0.01304	-0.0001670
$\alpha^{(1)}$ (K^+, $Fe(CN)_6^{3-}$)	2	
$\alpha^{(2)}$ (K^+, $Fe(CN)_6^{3-}$)	12	

3.7.2 Solubility of potassium hexacyanoferrate(III)

The solubility of $K_3Fe(CN)_6$ in aqueous solutions has been investigated by a couple of groups (Tab. 3.12). Some data are given in Klenk et al. (1987), but their source is not clear. In the temperature range from 0 to 99°C only the anhydrous salt is stable (Fig. 3.14). The solubility can be expressed by the formula

$$c_{sat}\ [mol/kg] = 1{,}491 + 0{,}052148\ (T-T_R) - 0{,}00005268\ (T^2-T_R^2)$$

while the formula for the solubility constant reads as follows:

$$\log K = -1{,}477 + 0{,}18202\ (T-T_R) - 0{,}00026384\ (T^2-T_R^2)$$

Tab. 3.12 Data on the solubility of $K_3Fe(CN)_6$ in water

Source	Temperature range [°C]	No. of data points
Friend and Smirles (1928)	0,1-99	18
Akerlof (1937)	25	1
Regner and Baley (1957)	15-80	4

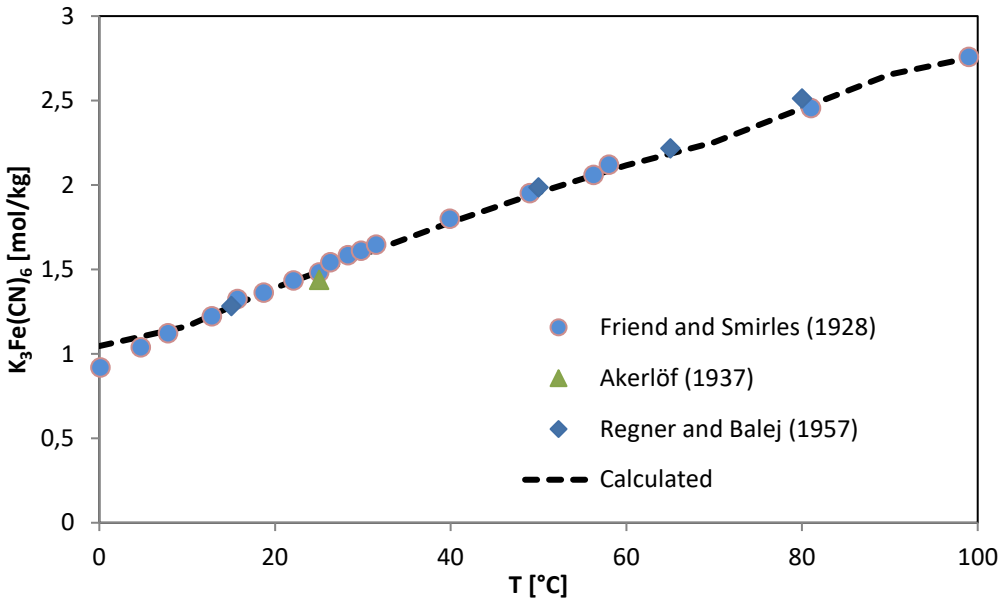

Fig. 3.14 Solubility of $K_3Fe(CN)_6$ between 0,1 and 99 °C

3.8 The system $Mg_3[Fe(CN)_6]_2$-H_2O

3.8.1 Previous investigations and water activity of $Mg_3[Fe(CN)_6]_2$ solutions

So far, there was only one investigation of aqueous solutions containing $Mg_3[Fe(CN)_6]_2$: a potentiometric study by Malatesta et al. (1996) at 25°C. $Mg^{2+}$and $Fe(CN)_6^{3-}$ form a complex $MgFe(CN)_6^-$, whose stability has been determined a few times (Tab. 3.13). Another measurement by Mironov and Rutkovskii (1966) could not be evaluated further as

it was conducted in a 3 M $LiClO_4$ solution. The results differ considerably and do not give a consistent picture (Tab. 3.13).

Tab. 3.13 Complex formation constant for $Mg_3[Fe(CN)_6]_2^-$

Source	Method	K
Gibby and Monk (1952)	Conductivity	3.21
Tanaka et al. (1966)	IR-Spectroscopy	2.79
Aruga (1982)	Calorimetry	1.44
This work (calculated from $\beta^{(2)}$ = -80,98)		2.21

The water activity of $Mg_3[Fe(CN)_6]_2$ solutions was investigated at 25, 40 and 60°C (Tab. 9.11). The three lines of osmotic coefficients lie close to each other (Fig. 3.15).

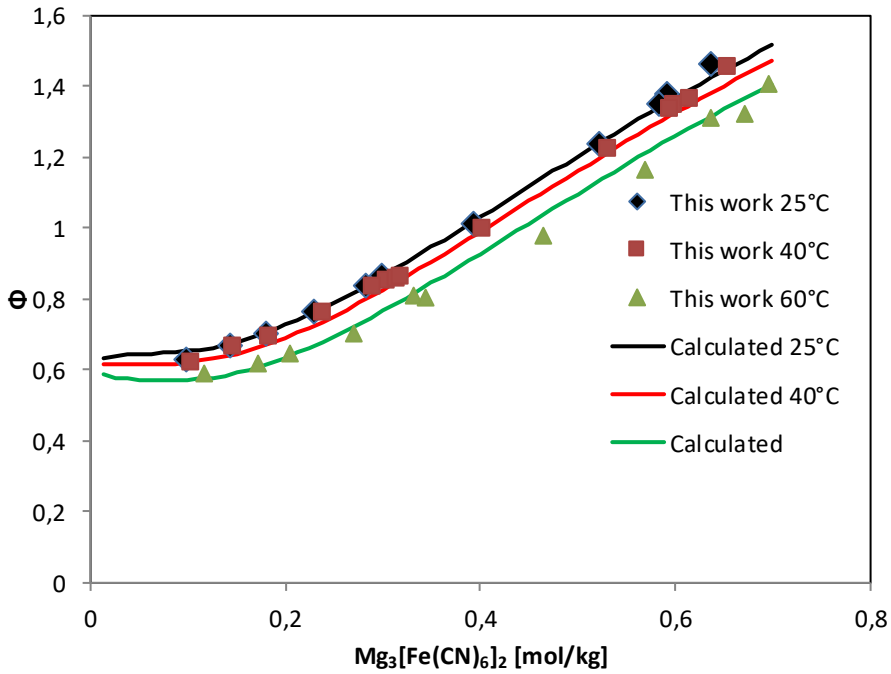

Fig. 3.15 Osmotic coefficients of $Mg_3[Fe(CN)_6]_2$ solutions

Ion Interaction coefficients were calculated based on our measurements. It was not sufficient to use a $\beta^{(2)}$ calculated from previously determined complex formation constants. Instead, $\beta^{(2)}$ was optimized as well. Introduction of temperature coefficients did not improve the fitting sufficiently and was consequently omitted. The resulting parameters may

be found in **Tab. 3.14**. With their help, the potentiometric as well as the isopiestic data could be modelled quite well (**Fig. 3.15**, **Fig. 3.16**).

Tab. 3.14 Pitzer interaction coefficients for the system $Mg_3[Fe(CN)_6]_2$-H_2O at 25 to 60°C

Parameter	P(25°C)
$\beta^{(0)}$ (Mg^{2+}, $Fe(CN)_6^{3-}$)	1.66
$\beta^{(1)}$ (Mg^{2+}, $Fe(CN)_6^{3-}$)	21.1446
$\beta^{(2)}$ (Mg^{2+}, $Fe(CN)_6^{3-}$)	-80.9787
C (Mg^{2+}, $Fe(CN)_6^{3-}$)	-0.05422
$\alpha^{(1)}$ (Mg^{2+}, $Fe(CN)_6^{3-}$)	2
$\alpha^{(2)}$ (Mg^{2+}, $Fe(CN)_6^{3-}$)	12

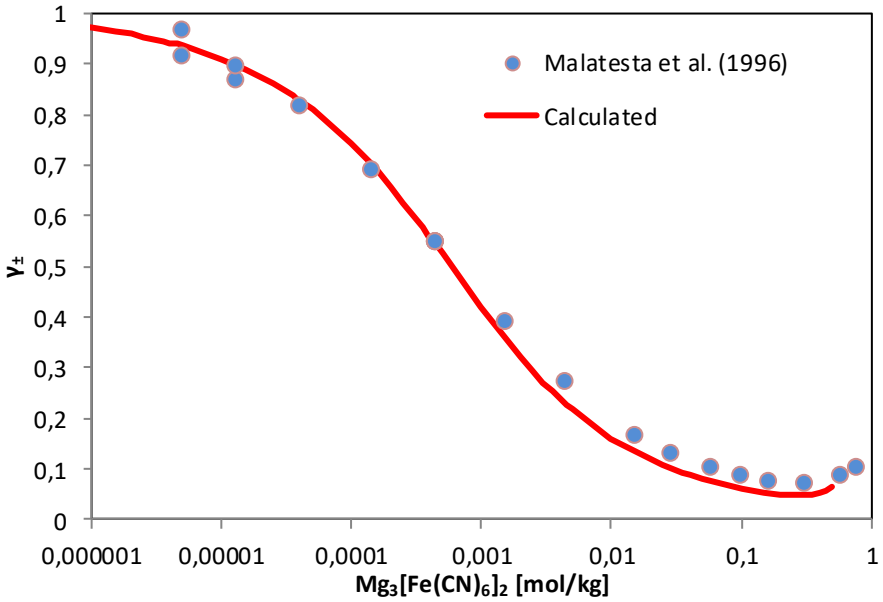

Fig. 3.16 Activity coefficients of $Mg_3[Fe(CN)_6]_2$ at 25°C

3.8.2 Solubility of magnesium hexacyanoferrate(III)

No information on the solubility of $Mg_3[Fe(CN)_6]_2$ in water could be found. Williams (1948) reported that $Mg_3[Fe(CN)_6]_2$ crystallises with 10 water molecules while Jiménez-Gallegos et al. (2012) reported 13. Our investigation of the pure phase resulted in approximately 14 mols per unit. A Schreinemakers evaluation of the solubilities in the system $MgCl_2$-

$Mg_3[Fe(CN)_6]_2$-H_2O lead to a mean water content of 13 per formula unit, so that it may be assumed that $Mg_3[Fe(CN)_6]_2 \cdot 13H_2O$ is indeed the stable phase at 25°C. The solubility of the pure phase was found to be 0.87 mol/kg. The corresponding solubility constant for the reaction

$3\ Mg^{2+} + 2\ Fe(CN)_6^{3-} \rightarrow Mg_3[Fe(CN)_6]_2 \cdot 13H_2O$

is log K = -2,20

3.9 The hexacyanoferrate acids $H_4Fe(CN)_6$ and $H_3Fe(CN)_6$

At low pH values, hexacyanoferrate(II) and hexacyanoferrate(III) are transformed into hydrogen compounds and finally into acids.

$x\ H^+ + Fe(CN)_6^{4-} \rightarrow H_xFe(CN)_6^{4-x}$ (x=1-4)

$x\ H^+ + Fe(CN)_6^{3-} \rightarrow H_xFe(CN)_6^{3-x}$ (x=1-3)

Both acids, $H_4Fe(CN)_6$ and $H_3Fe(CN)_6$, are strong so that the formation of hydrogen hexacyanoferrate takes place only at considerable acidity (Tab. 3.15, Tab. 3.16).

Tab. 3.15 Dissociation constants of $H_4Fe(CN)_6$

Source	**log K_2**	**log K_3**	**log K_4**
Jordan and Ewing (1962)		-2.22	-4.17
Hanania et al. (1967)		-2.30	-4.28
Crozes et al. (2012)	0	-2.0	-3.9

Tab. 3.16 Dissociation constants of $H_3Fe(CN)_6$

Source	**log K_1**	**log K_2**	**log K_3**
Domingo et al. (1990)	-6.25	-3.23	-0.6

4 Ternary systems containing hexacyanoferrate(II) or hexacyanoferrate(III)

4.1 The system NaCl-$Na_4Fe(CN)_6$-H_2O

Previous investigations of the system NaCl-$Na_4Fe(CN)_6$-H_2O are listed in Tab. 4.1. They include potentiometric and solubility measurements in the temperature range 5 to 90°C. Conroy's data probably includes too high values for hexacyanoferrate concentrations as the author assumed himself. The source of William's data is uncertain so that they cannot be relied upon as well. According to Fleysher and Osokoreva (1935a), $Na_4Fe(CN)_6 \cdot 10H_2O$ is the only hexacyanoferrate solid up to 80°C.

To confirm other data, we have conducted some additional measurements. For that purpose small amounts of a NaCl stock solution, solid $Na_4Fe(CN)_6 \cdot 10H_2O$ and water were mixed in 1.5 ml vials and shaken on a rotating plate in an air thermostat at 25, 40, and 60°C for at least two weeks. The temperature was in the range of ± 1°C. The final solutions were analysed by ICP-OES and titration with silver nitrate (Cl). It was found that hexacyanoferrate leads to a systematic but reproducible bias in chloride titration. The resulting apparent chloride concentration expressed in mol/l is indeed the total of the actual chloride concentration plus the $Fe(CN)_6$ concentration times four. The experimental results are shown in Tab. 9.39 to Tab. 9.41 and in Fig. 4.1 and Fig. 4.2.

Tab. 4.1 Previous solubility investigations of the system NaCl-$Na_4Fe(CN)_6$-H_2O

Source	Method	Temperature range [°C]	No. of data points
Conroy (1898)	solubility	21-90	2
Williams (1948) Source unclear	solubility	15.5	4
Fleysher and Osokoreva (1935a)	solubility	25	12
Fleysher and Osokoreva (1935b)	solubility	80	9
Silvester and Rock (1973)	potentiometric	25	9
This work	solubility	25	12
This work	solubility	40	19
This work	solubility	60	5

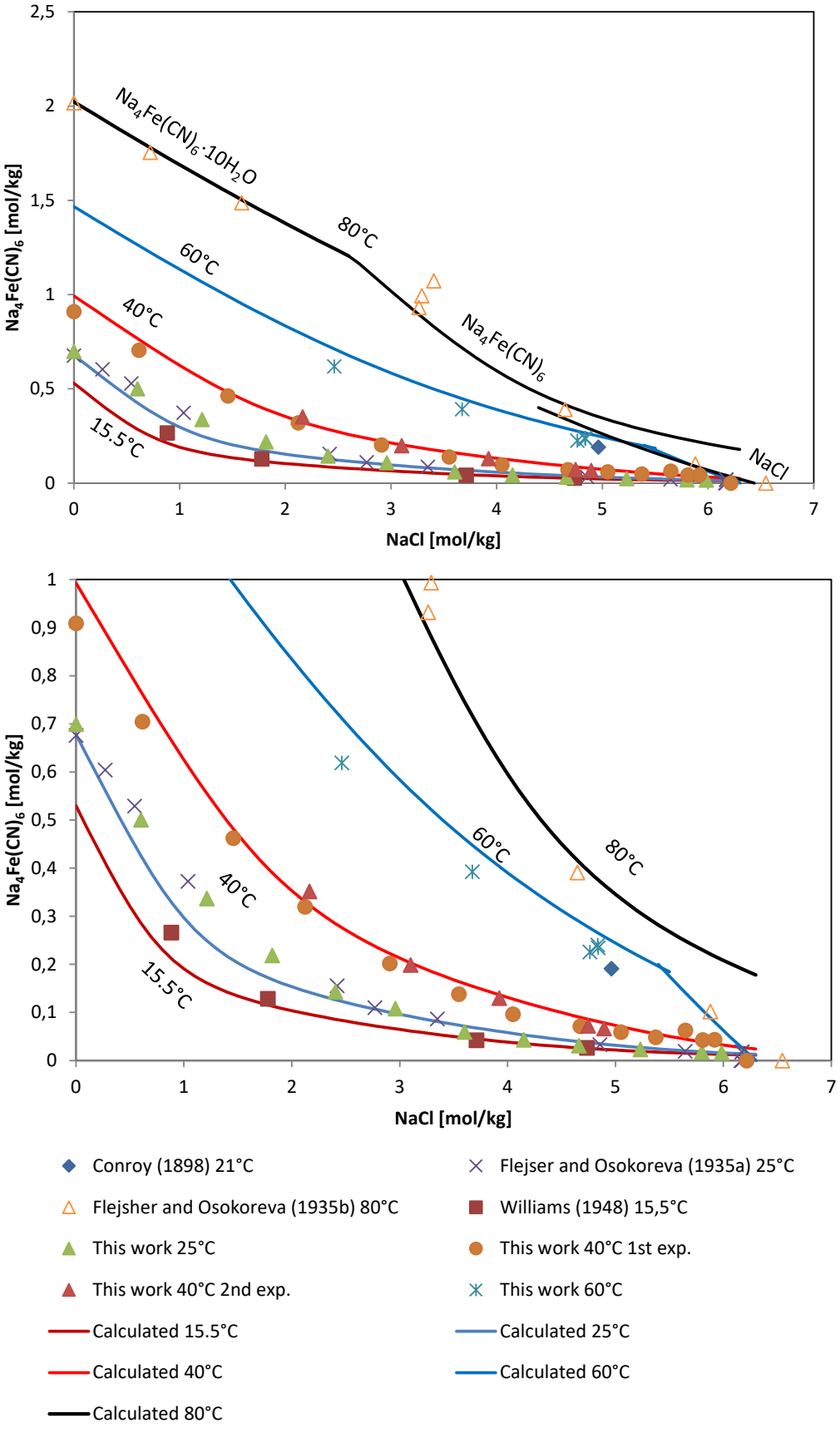

Fig. 4.1 Solubility in the system NaCl-$Na_4Fe(CN)_6$-H_2O at 15.5 to 60°C

Fig. 4.2 Solid/liquid equilibria in the system NaCl-$Na_4Fe(CN)_6$-H_2O at 40°C

4.2 The system KCl-$K_4Fe(CN)_6$-H_2O

This system was investigated by Conroy (1898) at 21 and 99 °C but the author assumed that his ferrocyanide values may have been too high. A solubility measurement was conducted by Bischofer et al. (2016) but later evaluation showed that the analytical potassium concentration was incorrect. The correct solution composition could be obtained from the mass balance taking into account the weighed masses of KCl, H_2O and $K_3Fe(CN)_6$ used for preparing the batches. The results are shown in **Tab. 9.42** and **Fig. 4.3**.

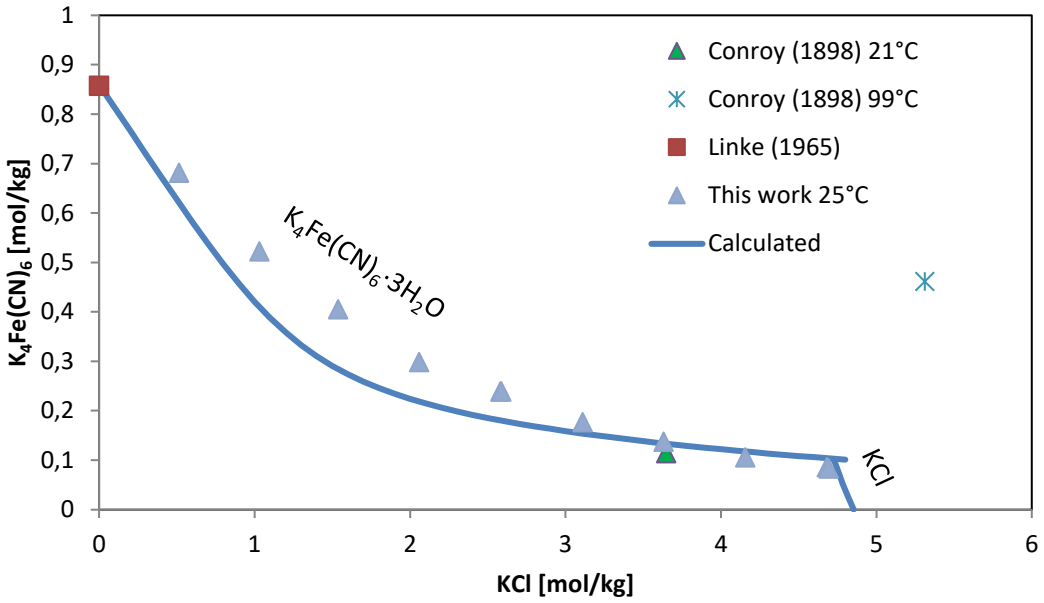

Fig. 4.3 Solubility in the system KCl-$K_4Fe(CN)_6$-H_2O at 25°C

4.3 The system $MgCl_2$-$Mg_4Fe(CN)_6$-H_2O

The system $MgCl_2$-$Mg_4Fe(CN)_6$-H_2O has not been investigated before. Experiments were conducted in the same manner as described before in the system NaCl-$Na_4Fe(CN)_6$-H_2O. Also, the wet solids were analysed chemically (Tab. 9.43). The composition of the solids was evaluated using the Schreinemakers method. Up to a $MgCl_2$ concentration of about 2.4 mol/kg $Mg_2Fe(CN)_6 \cdot 11H_2O$ is the stable solid phase. At higher concentrations, double salts with the formula $xMgCl_2.Mg_2Fe(CN)_6 \cdot yH_2O$ form. There seem to occur two different compounds. At least above 3 mol/kg $MgCl_2$ the equilibrium phase has approximately the following composition:

$MgCl_2$: 11±0,2 mol-%

$Mg_2Fe(CN)_6$: 3.5 ± 0.5 mol-%

H_2O: 85 ± 1 mol-%

The ideal formula would be $3MgCl_2.Mg_2Fe(CN)_6 \cdot 23H_2O$

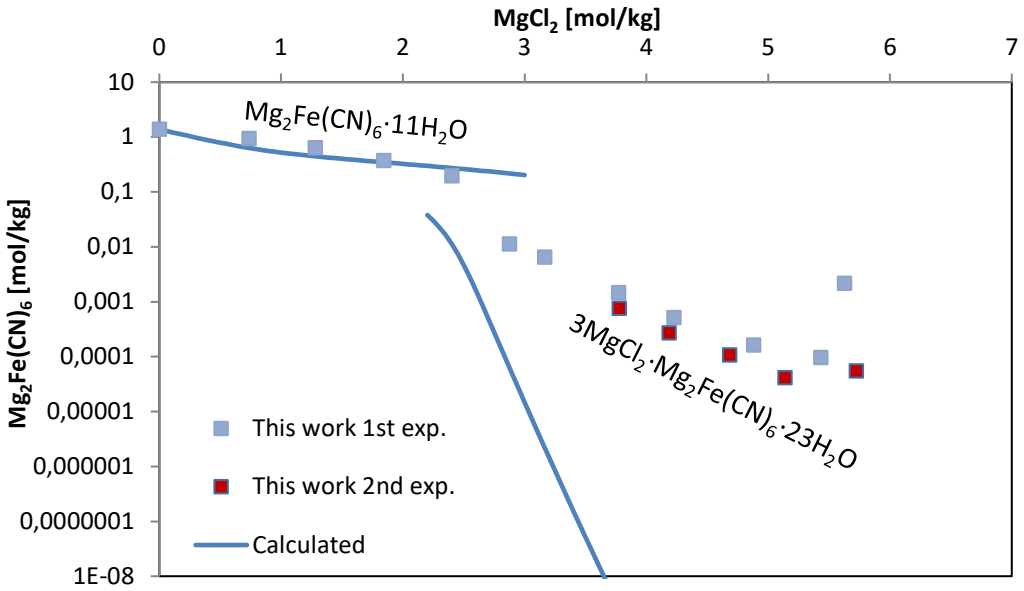

Fig. 4.4 Solubility in the system $MgCl_2$-$Mg_2Fe(CN)_6$-H_2O at 25°C

4.4 Calculation of Pitzer ion interaction coefficients for the systems M^{n+}-Cl^- - $Fe(CN)_6^{4-}$ -H_2O

Experimental and literature data from the systems NaCl-$Na_4Fe(CN)_6$-H_2O, KCl-$K_4Fe(CN)_6$-H_2O and $MgCl_2$-$Mg_2Fe(CN)_6$-H_2O were combined to calculate ternary interaction coefficients. From the system $MgCl_2$-$Mg_2Fe(CN)_6$-H_2O only those data could be used where $Mg_2Fe(CN)_6 \cdot 11H_2O$ was the equilibrium phase. The potentiometric results of Silvester and Rock (1973) in the system NaCl-$Na_4Fe(CN)_6$-H_2O could not be used as they deviated significantly from predicted activity coefficients. The solubility investigations of Fleysher and Osokoreva (1935a) at 80°C were not included in parameter fitting as the temperature exceeded the temperature range of data used for the determination of binary coefficients.

The resulting set of interaction coefficients is listed in Tab. 4.2. The solubility in the NaCl-$Na_4Fe(CN)_6$-H_2O is well represented at all temperatures. Although they were excluded from the parameter optimization, the solubility data of Fleysher and Osokoreva (1935a) at 80°C could be reproduced fairly well if it was assumed that the solubility limiting phase above 2.5 mol/kg NaCl was not $Na_4Fe(CN)_6 \cdot 10H_2O$ but $Na_4Fe(CN)_6$. However, at medium concentrations the calculated solubility of $Na_4Fe(CN)_6 \cdot 10H_2O$ is slightly too low. This is especially visible at 25°C (Fig. 4.1). A similar effect occurs in the system KCl-$K_4Fe(CN)_6$-H_2O. In both cases, it may be assumed that there is a change of chemistry in the aqueous phase because of the increasing ratio of M/$Fe(CN)_6$. Complex formation is a well-known fact both in $Na_4Fe(CN)_6$ and $K_4Fe(CN)_6$ solutions, but so far it has not been investigated and taken explicitly into account in ternary systems.

Such a phenomenon is even more relevant in the system $MgCl_2$-$Mg_2Fe(CN)_6$-H_2O (Fig. 4.4). While it was possible to force the calculated line through the observed points where $Mg_2Fe(CN)_6.11H_2O$ was present, this could not be accomplished in the stability region of the double salt. The calculated solubility decreased much faster than observed in the experiment. Some hypothetical tests revealed that the solubility would better be represented by a salt whose reaction involves one unit of $MgCl_2$ instead of three although this is in contradiction to the analytical composition of the solid: A candidate would be

$$3Mg^{2+} + 2\ Cl^- + Fe(CN)_6^{4-} + xH_2O \rightarrow MgCl_2 \cdot Mg_2Fe(CN)_6.xH_2O$$

Another explanation would be that the main hexacyanoferrate species has a different stoichiometry such as $Mg_2Fe(CN)_6$ (aq).

$3Mg^{2+} + 6\ Cl^- + Mg_2Fe(CN)_6\,(aq) + 23\ H_2O \rightarrow 3MgCl_2 \cdot Mg_2Fe(CN)_6.23H_2O$

Neither of the two concepts could be proven so that for the moment the activity coefficient of hexacyanoferrate in $MgCl_2$ above 2.5 mol/kg cannot be calculated.

Tab. 4.2 Pitzer interaction coefficients for the system MCl_x-$M_yFe(CN)_6$-H_2O at 25 to 60°C

Parameter	P(25°C)	$T-T_R$
$\Psi\ (Na^+,Cl^-, Fe(CN)_6^{4-})$	-0.04086	0.003924
$\Psi\ (K^+,Cl^-, Fe(CN)_6^{4-})$	-0.06689	Not determined
$\Psi\ (Mg^{2+}, Cl^-, Fe(CN)_6^{4-})$	0.02901	Not determined
$\theta\ (Cl^-, Fe(CN)_6^{4-})$	0.7598	-0.01182

4.5 The system $NaCl$-$Na_3Fe(CN)_6$-H_2O

No information was found in the literature on the system $NaCl$-$Na_3Fe(CN)_6$-H_2O. Solubility measurements were undertaken to close this gap (Tab. 9.44). As documented above, the synthesized solid $Na_3Fe(CN)_6$ contained small but considerable amounts of K. After dissolution the liquid phase contained about 0.2 to 1.8 mol-% K in relation to Na. In cases where $Na_3Fe(CN)_6 \cdot 2H_2O$ was the solubility limiting phase, the solid contained 15 to 25% K. If halite was present the content was close to zero. Due to the impact of potassium on the composition and solubility of phases in this system, the results were not further used. Tab. 9.44 contains the analytical results that should be treated with caution.

Also, some isopiestic measurements were conducted. Water activity measurements have the advantage of working with homogenous systems so that the potassium concentration can be derived from the composition of the stock solution. A new stock solution was prepared for this purpose. It had a K/(Na+K) ratio of 2.0%. The system was investigated by five consecutive isoactivity lines ate 25, 50 and 60°C. A final additional measurement at 25°C could not be evaluated because most solutions turned turbid (probably due to decomposition). The isoactivity lines were found to be linear at all temperatures. Numerical results are presented Tab. 9.13 in the Annex.

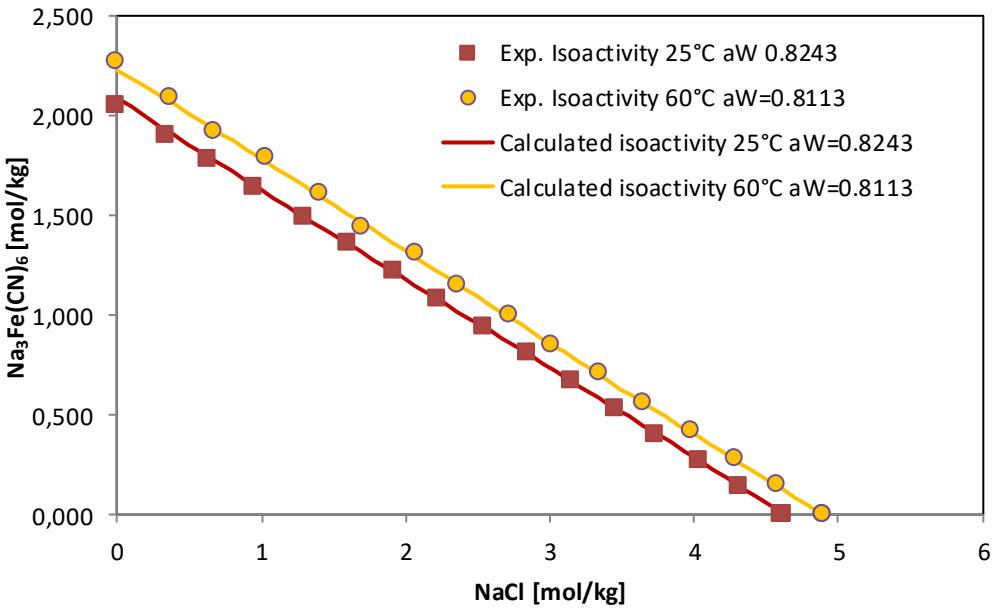

Fig. 4.5 Isoactivity lines (examples) in the system NaCl-$Na_3Fe(CN)_6$-H_2O at 25 and 60°C

4.6 The system KCl-$K_3Fe(CN)_6$-H_2O

This system has been investigated before by Akerlof (1937) and later by Bischofer et al. (2016). A closer consideration of the latter results revealed that the documented KCl concentrations were too high and needed to be corrected. This could be done by considering the weighed amounts of added KCl. The corrected results are listed in Tab. 9.45.

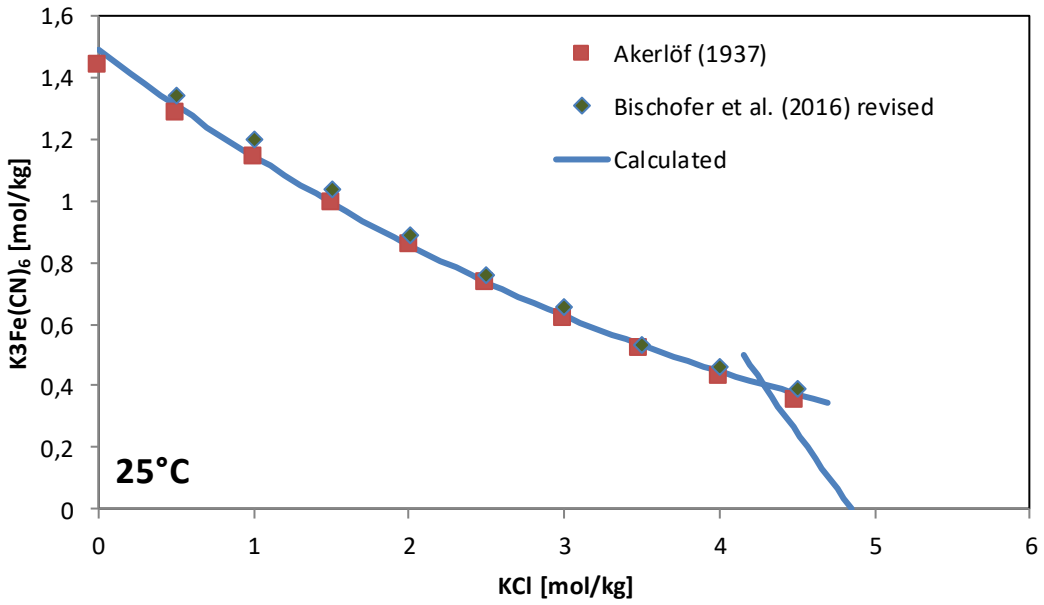

Fig. 4.6 Solubility in the system KCl-$K_3Fe(CN)_6$-H_2O at 25°C

4.7 The system $MgCl_2$-$Mg_3[Fe(CN)_6]_2$-H_2O

The system $MgCl_2$-$Mg_3[Fe(CN)_6]_2$-H_2O was investigated for the first time. Analysis of the liquid and solid phase and subsequent Schreinemakers analysis showed that $Mg_3[Fe(CN)_6]_2 \cdot 11H_2O$ was the limiting phase at all $MgCl_2$ concentrations (Tab. 9.46). Its solubility decreases strongly with increasing $MgCl_2$ concentration (Fig. 4.7).

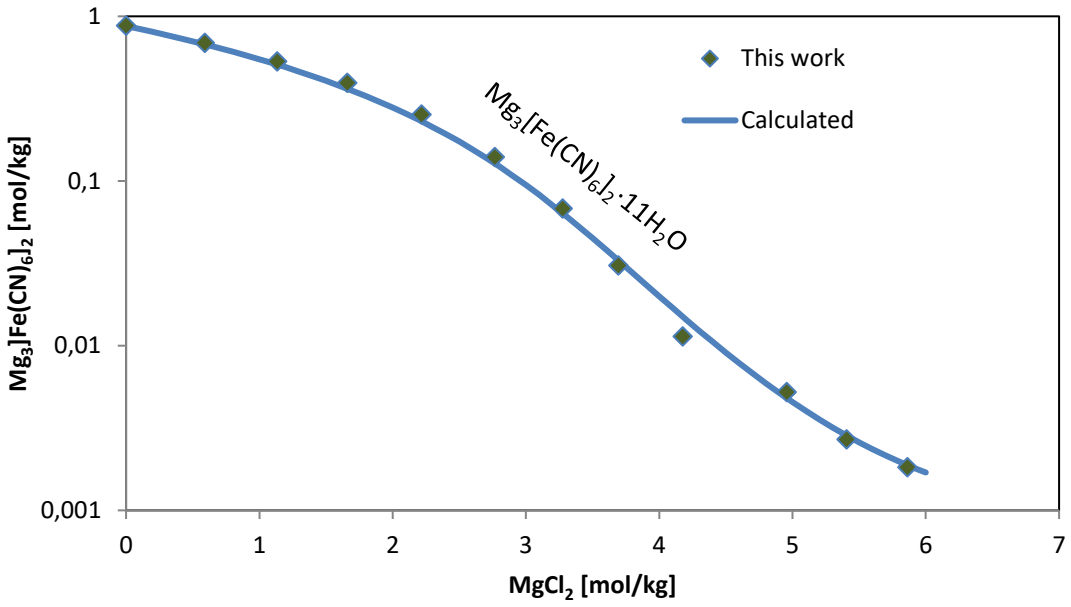

Fig. 4.7 Solubility in the system $MgCl_2$-$Mg_3[Fe(CN)_6]_2$-H_2O at 25°C

4.8 Calculation of Pitzer ion interaction coefficients for the systems M^{n+}-$Fe(CN)_6^{3-}$-H_2O

Based on the above-mentioned experimental data ternary ion interaction parameters were derived for the systems NaCl-$Na_3Fe(CN)_6$-H_2O, KCl-$K_3Fe(CN)_6$-H_2O and $MgCl_2$-$Mg_3[Fe(CN)_6]_2$-H_2O (Tab. 4.3). For all systems, the parameters set allowed very good modelling of the observed solutions properties (Fig. 4.6, Fig. 4.5, Fig. 4.7).

Tab. 4.3 Pitzer interaction coefficients for the systems MCl_x-$M_yFe(III)(CN)_6$-H_2O at 25 to 60°C

Parameter	P(25°C)	$T-T_R$
Ψ (Na^+,Cl^-, $Fe(CN)_6^{3-}$)	0.012461	-0.00204365
Ψ (K^+,Cl^-, $Fe(CN)_6^{3-}$)	0.0231949	Not determined
Ψ (Mg^{2+}, Cl^-, $Fe(CN)_6^{3-}$)	0.0145163	Not determined
θ (Cl^-, $Fe(CN)_6^{3-}$)	0.0951501	0.0115566

5 Determination of the redox properties of saline solutions

5.1 Relation between background concentration and the apparent redox potential

Investigations in previous research projects have shown that the observed redox potential measured with a typical cell consisting of a Pt electrode and a reference electrode (Ag|AgCl) depends on the concentration of background salt such as NaCl, KCl or $MgCl_2$ (Hagemann et al. 2014, Bischofer et al. 2016). The main reason for this behaviour is the rising ionic strength that causes an increase of the liquid junction potential between the investigated solution and the inner solution within the reference electrode (typically 3 M KCl). As a result, the redox potential measured in concentrated salt solutions not only reflects the equilibrium of redox pairs, more exactly the change of their activity coefficients in solution but also includes a concentration-dependent impact (Fig. 5.1).

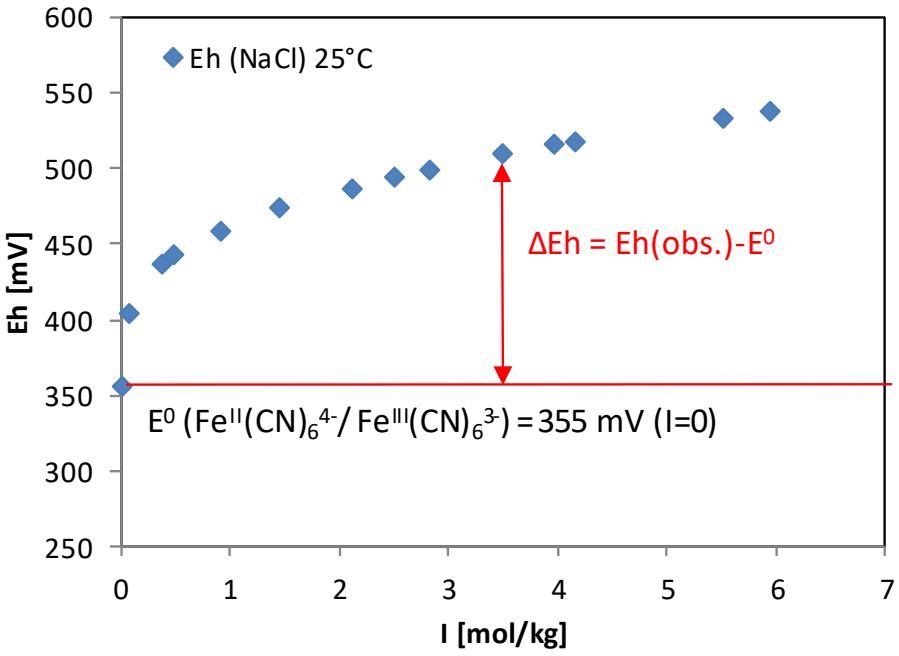

Fig. 5.1 Change of observed ORP (Eh) of a solution with a constant ratio of ferricyanide and ferrocyanide but increasing NaCl concentration

The situation is similar with pH measurements. The pH as a single ion activity can only be derived (and thus measured) by applying conventions that are sufficiently correct

near-zero ionic strength. Parts of the conventions are assumptions regarding the liquid junction potential and the value of the single ion activity coefficient of Cl^-.

In concentrated salt solutions (I > 0.1 mol/kg), these basic assumptions are no longer valid. Under such conditions, the pH itself loses its physical meaning and turns to be a mere construction with a weak relation to reality. However, the concentration of H^+ may be measured with an ordinary pH-electrode combination and suitable calibration. The resulting pcH is an appropriate and thermodynamically sound alternative measure.

$$pcH = pH_{obs} + \Delta pH \tag{5.1}$$

Here, ΔpH is an empirical function related to the concentration of background electrolytes

A similar approach has been developed by Hagemann et al. (2014) and later modified by Bischofer et al. (2016). As redox measurements always relate to an equilibrium between at least one pair of oxidation/ reduction sensitive solutions species (Ox/Red)[1] a slightly different approach needed to be found that is linked to a principally measurable solution property.

The observed cell potential is a combination of the two half-cell potentials (redox equilibrium at the Pt electrode E^0(Ox/Red) and reference electrode E^0(Ag|AgCl) and the liquid junction potential. E_{LJ}, between the measuring solution and the KCl solution in the reference electrode

$$E = E^0 + \frac{RT}{F} ln \frac{c_{Ox}}{c_{Red}} + \frac{RT}{F} ln \frac{\gamma_{Ox}}{\gamma_{Red}} + \Delta E_{LJ} \tag{5.2}$$

The value of E_{LJ} is unknown as well as the exact value of the ratio of individual activity coefficients of the two iron cyanates. Except under defined circumstances that are not given here, individual activity coefficients cannot be determined.

If the ionic strength of the solution differs from zero, the observed redox potential Eh starts deviating from the standard cell potential E_0. The purpose of the present work is to

[1] Also expressed by pε, the activity of a hypothetical free electron

find an empirical expression that reliably describes ΔEh depending on the background electrolyte concentration.

5.2 Redox measurements in mixed ferricyanide/ ferrocyanide solutions

5.2.1 Choice of the redox couple

To investigate the impact of ionic strength ion the observed redox potential a redox couple needs to be chosen that allows measurements at pH values relevant for repository systems (neutral to alkaline), The redox reaction should be reversible and fast, and the solubility not too low in concentrated NaCl and $MgCl_2$ solutions. Although it is possible to avoid air contact to some extent, the redox species should not be too sensible with respect to oxygen. Finally, it should be possible to derive a model for describing the activity coefficients of the redox species. There are not many redox couples that fulfil these conditions. In the first experiments by Hagemann et al. (2014), Fe^{2+}/Fe^{3+} was chosen. Because of the strong complex formation of Fe^{3+} with OH^- very acidic conditions had to be maintained in the experiments. Even then, the formation of hydroxo complexes could not be avoided completely. Moreover, complex formation with chloride and sulphate further complicated the interpretation. Principally organic substances such as quinone and its derivates are interesting, but some of them are almost insoluble in water and deriving activity coefficients for poorly soluble organics requires much higher efforts than available in this project. Among inorganic redox couples, the system hexacyanoferrate(II)/hexacyanoferrate(III) was the most promising. Na, K and Mg salts are well soluble, they are stable at neutral pH and were at least in part, commercially available. Some thermodynamic data already existed so that we had a good starting point. A possible alternative could have been permanganate(VII)/manganate(VI) (MnO_4^-/MnO_4^{2-}), but too little was known about the properties and the stability of manganate(VI) solutions so that we decided to stick with hexacyanoferrates.

5.2.2 Standard potential of the ferricyanide/ferrocyanide and the Ag, AgCl reference cells

Combining a platinum electrode that indicates the equilibrium between ferricyanide and ferrocyanide and an Ag/AgCl reference electrode leads to the following formulation of the standard cell potential:

$$E_0 = E_0(Fe(CN)_6^{3-}/Fe(CN)_6^{4-}) - E_0(Ag|AgCl) \quad (5.3)$$

The half-cell potential for the platinum electrode results from the standard potential for the ferricyanide/ferrocyanide reaction (Hanania et al. 1967)

$$Fe^{III}(CN)_6^{3-} + e^- = Fe^{II}(CN)_6^{4-} \quad (5.4)$$

$$E_0(Fe(CN)_6^{3-}/Fe(CN)_6^{4-}) = 0.355\ V \text{ (25°C)} \quad (5.5)$$

Temperature dependence was calculated from the entropy of the reduction (62,1 cal/ (mol K) (Nordstrom 1977).

$$\frac{dE_0}{dT} = -\frac{\Delta S}{zF} = 0{,}002693\ \frac{V}{K} \quad (5.6)$$

The half-cell potential for the single junction silver/silver chloride with 3 M KCl as an inner electrolyte is provided by the producer of the electrode (Metrohm)

$$Ag_{(s)} + Cl^- + e^- \rightleftharpoons AgCl_{(s)} \quad (5.7)$$

$$E_0(Ag|AgCl) = 0.207\ V \text{ (25°C)} \quad (5.8)$$

The temperature dependence of the half-cell potential was calculated from tabulated values for E^0 (Metrohm, Tab. 9.23)

$$E_0(Ag|AgCl) = 0.207\ V - 0.707\ (T-25) - 9.41\ 10^{-4}\ (T-25)^2 - 1.37\ 10^{-5}\ (T-25)^3 \quad (5.9)$$

At 25°C, The standard cell potential E_0 for the above-defined redox cell would be

$$E_0 = E_0(Fe(CN)_6^{3-}/Fe(CN)_6^{4-}) - E_0(Ag|AgCl) = 0.1634\ V \quad (5.10)$$

The redox potential is normally expressed in relation to the standard hydrogen electrode: Eh. It is calculated by adding the potential of the silver reference electrode:

$$Eh = E + E_0(Ag|AgCl) \quad (5.11)$$

Thus, the Eh of a mixed solution with equal but near-zero concentrations of ferricyanide/ ferrocyanide would be 355 mV at 25°C.

5.2.3 Impact of salinity on the apparent pH

For the evaluation of redox measurements in saline solutions, the hydrogen (H^+) concentration is an important auxiliary parameter. In contrast to the pH value, which is only defined in slightly mineralized waters and can be measured sufficiently reliably, the H^+ concentration in any salt solution can be determined if suitable correction functions are available for converting the apparent pH value. Hagemann et al. (2014)have developed a coherent model for the solutions of oceanic salts which allows this conversion at 25°C. Such approaches are not available for higher temperatures. Additional measurements were necessary to extend these models to higher temperatures.

Solutions were prepared that contained a known concentration of HCl and either NaCl or $MgCl_2$. NIST pH standards (Alfa Aesar) were used to calibrate a Ross pH electrode at 25, 40 or 60°C.

In the measurements, a difference ΔpH occurs between the hydrogen concentration pcH and the apparent pH:

$$\Delta pH = pcH - pH \tag{5.12}$$

Results of the measurements are summarized in **Tab. 9.17**ff. The empirical model used by Hagemann et al. (2014) to describe ΔpH at 25°C could not be applied to higher temperatures. It was necessary to introduce another empirical parameter.

$$\Delta pH = a_1 SIT(I) + a_2 Q_{MX} \tag{5.13}$$

With

$$SIT(I) = \log \gamma_{H^+} = -A(T)\frac{\sqrt{I}}{1 + 1.5\sqrt{I}} \tag{5.14}$$

$$Q_{MX} = \frac{c_M c_X}{\sum c_i z_i} \tag{5.15}$$

$$A(T) = -8.945 + \frac{356}{T} + 1.4505 \ln T \qquad (5.16)$$

The formula for calculating the Debye-Hückel coefficient was presented by Bretti et al. (2006). The model parameters a_1 and a_2 are shown in **Tab. 5.1**.

Tab. 5.1 Model parameters to calculate ΔpH in NaCl and $MgCl_2$ solutions at 25, 40 and 60°C

	NaCl		**$MgCl_2$**	
T [°C]	**a_1 (SIT)**	**a_2 (Q)**	**a_1 (SIT)**	**a_2 (Q)**
25°C	0.399	0.366	0.573	1.108
40°C	0.349	0.344	0.414	1.057
60°C	0.377	0.315	0.527	0.985

The empirical formula allows an excellent representation of ΔpH and thus a calculation of pcH at all NaCl and $MgCl_2$ concentrations between 25 and 60°C (**Fig. 5.2** and **Fig. 5.3**).

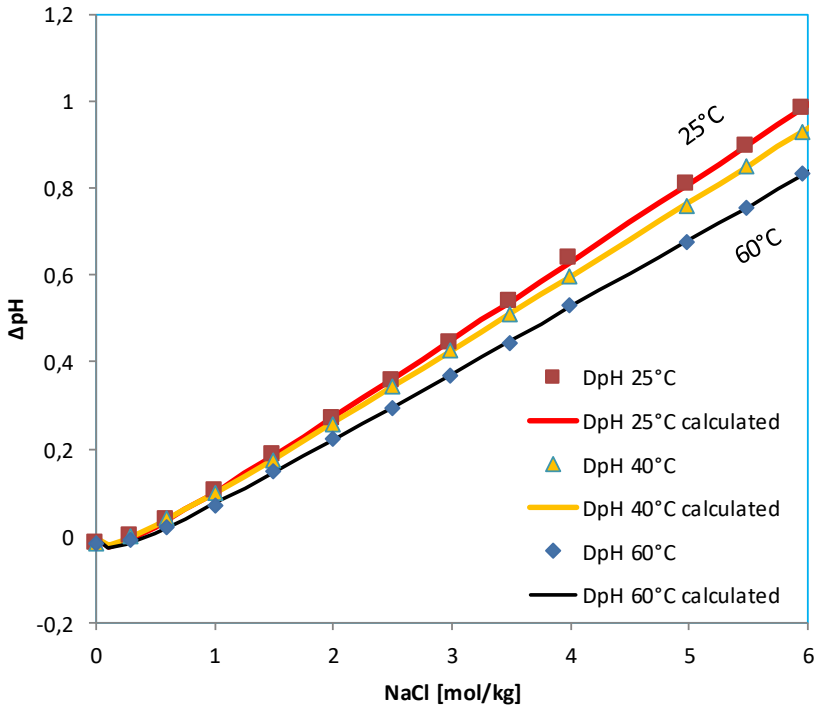

Fig. 5.2 Experimental and calculated ΔpH in NaCl solutions

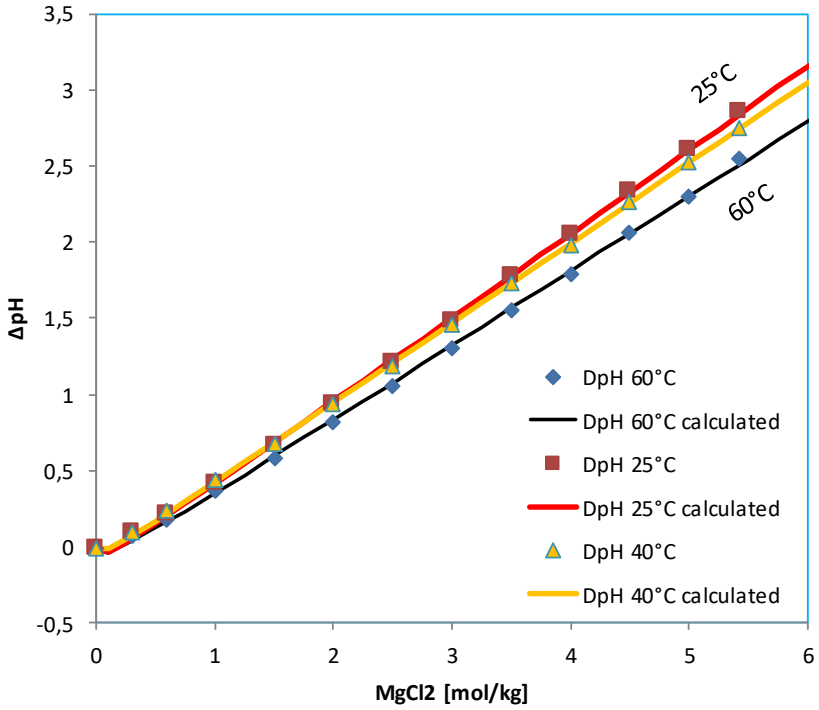

Fig. 5.3 Experimental and calculated ΔpH in $MgCl_2$ solutions

5.2.4 Impact of pH on the redox potential

Formula (5.4) does not contain an expression for the hydrogen activity so that there should be no influence of the pH on the cell potential. In the first set of experiments, this assumption was checked measuring the redox potential of solutions that contained equal amounts of $K_3Fe(CN)_6$ and $K_4Fe(CN)_6$ as well as a pH buffer that fixed the pH close to 7 or 9. The observed redox potentials are the same within the margins of experimental uncertainty (Fig. 5.4).

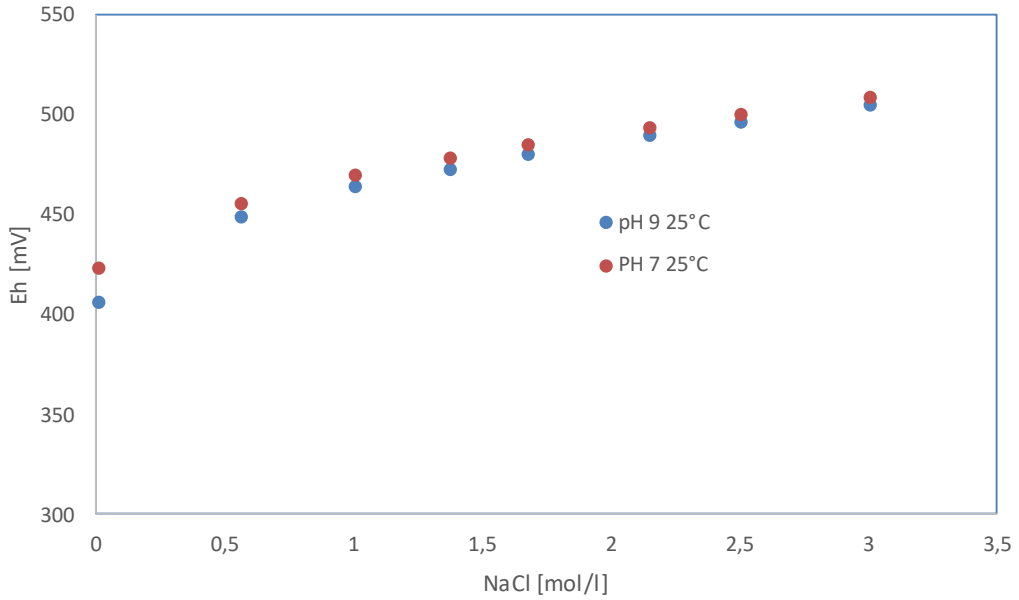

Fig. 5.4 Observed redox potential of equimolar $K_3Fe(CN)_6$ $K_4Fe(CN)_6$ in solutions of NaCl at 25°C

5.2.5 Measurement of the redox potential at fixed pH and increasing background concentrations

The redox potential was measured in solutions of pure and mixed NaCl, $MgCl_2$. Solutions of NaCl were prepared by dissolving solid NaCl in water and adding stock solutions of $K_3Fe(CN)_6$ and $K_4Fe(CN)_6$. These stock solutions had a concentration of about 0.5 mol/l. Aliquots were taken to prepare fresh measuring solutions after which the stock solutions were put into a freezer. The final concentration of the hexacyanoferrates in the measuring solution was about 0.003 to 0.004 mol/l. In some solutions of higher $MgCl_2$ concentrations lower amounts of hexacyanoferrates had to be used to avoid precipitation of insoluble magnesium hexacyanoferrate (II). 0.5 ml of a pH 6.86 phosphate buffer solution were added to 50 ml of the measuring solution to maintain stable pH conditions. $MgCl_2$ containing solutions were prepared by adding weighed amounts of an $MgCl_2$ stock solution. The measuring solutions were filled in closed vials and placed in a bath thermostat at 25°, 40 or 60°C. Aliquots of the solutions were used for measurements at all temperatures. Their composition is shown in Tab. 9.24 ff.

In all solutions, the pH was measured with a Ross pH electrode. Observed pH values were recalculated into pcH values using the method and parameters described in chapter

5.2.3. A Metrohm combination electrode was employed for determining the redox potential. The results are shown in **Tab. 9.28**.

Up to about an ionic strength of about 1 mol/kg, the redox potential increased in the same way in NaCl, KCl and $MgCl_2$ solutions (**Fig. 5.5**). At higher salt contents the increase is strongest in $MgCl_2$, less strong in KCl and weakest in NaCl solutions. Few literature data are comparable to our measurements (**Tab. 5.2**). They fit very well with our results (**Fig. 5.5**).

Tab. 5.2 Previous measurements of the $Fe(CN)_6^{3-}$ / $Fe(CN)_6^{4-}$ redox potential in NaCl and KC solutions

Source	**Solution type**
Kolthoff and Tomiscek (1935)	NaCl, KCl
Krulic et al. (1998)	KCl
Crozes et al. (2012)	NaCl

If the temperature is changed, the increase of the observed redox potential is similar although systematically shifted towards higher voltages (Fig. 5.6).

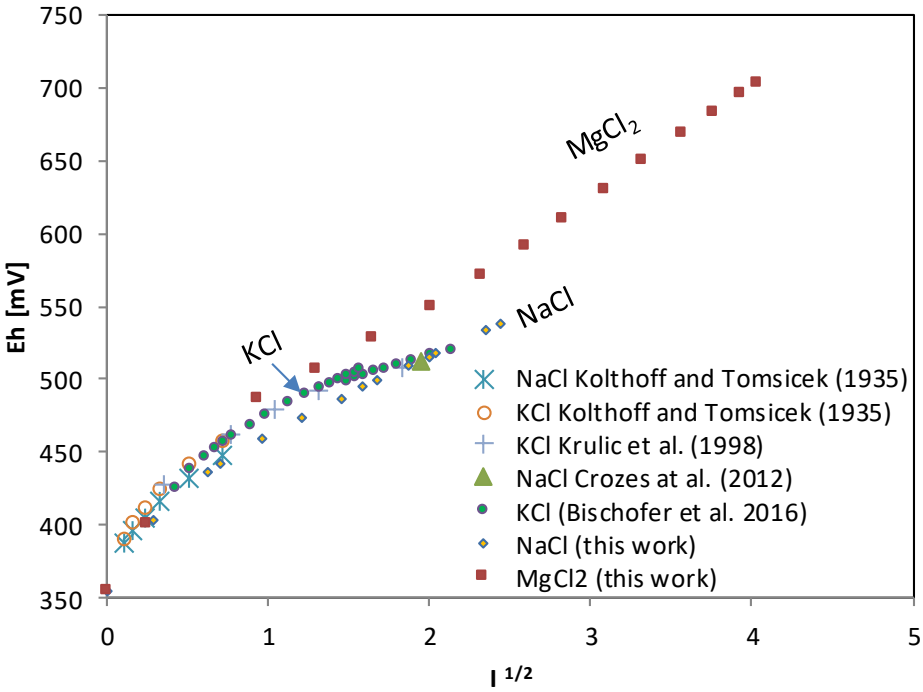

Fig. 5.5 Apparent redox potential of equimolar $Fe(CN)_6^{4-}$/ $Fe(CN)_6^{3-}$ in NaCl, KCl and $MgCl_2$ solutions at 25°C

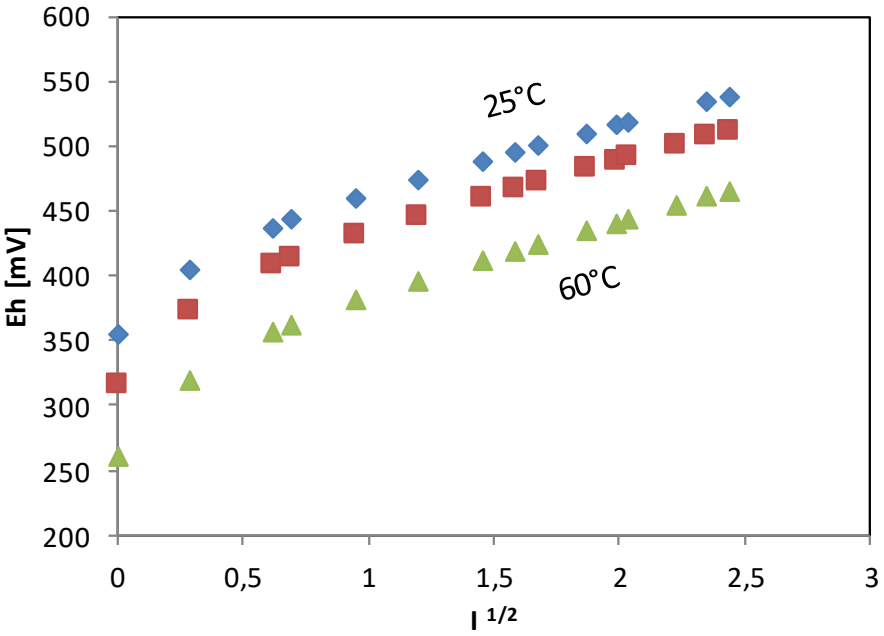

Fig. 5.6 Apparent redox potential of equimolar $Fe(CN)_6^{4-}$/ $Fe(CN)_6^{3-}$ in NaCl solutions at 25, 40 and 60°C

5.2.6 Redox potential in mixed NaCl/$MgCl_2$ solutions

Three series of experiments were conducted with mixed NaCl/$MgCl_2$ solutions (Tab. 9.27 Tab. 9.36 ff.). The purpose of these measurements was to check, whether the binary empirical models could also be applied to ternary solutions.

The results show that the measured redox potentials depend linearly on the $MgCl_2$ content (**Fig. 5.7**).

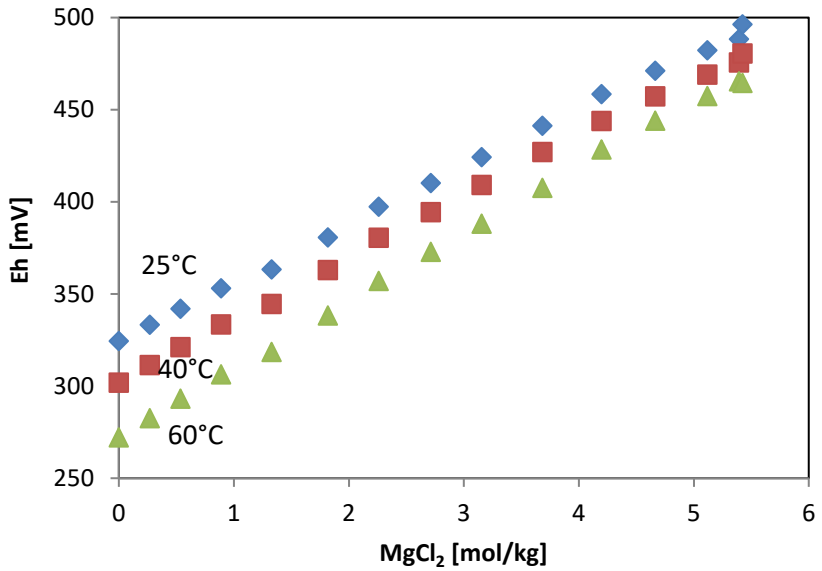

Fig. 5.7 Apparent redox potential of equimolar $Fe(CN)_6^{4-}$/ $Fe(CN)_6^{3-}$ in mixed NaCl/$MgCl_2$ solutions at 25, 40 and 60°C

5.2.7 Relationship between electrolyte concentration and the observed redox potential

The observed redox potential is a combination of the two half-cell potentials (Pt-and reference electrodes) and the liquid junction potential. E_{LJ}, between the measuring solution and the KCl solution in the reference electrode

$$Eh_{obs} = E^0\,(Fe(CN)_6^{3-}/Fe(CN)_6^{4-}) + \frac{RT}{F}\,ln\frac{c_{Fe(CN)_6^{3-}}}{c_{Fe(CN)_6^{4-}}} + \frac{RT}{F}\,ln\frac{\gamma_{Fe(CN)_6^{3-}}}{\gamma_{Fe(CN)_6^{4-}}} + E_{LJ} \quad (5.17)$$

The value of E_{LJ} is unknown as well as the exact value of the ratio of individual activity coefficients of the two iron cyanates. However, a theoretical redox potential at ionic strength zero Eh_0 could be calculated that only includes measurable properties:

$$Eh_0 = E^0\,(Fe(CN)_6^{3-}/Fe(CN)_6^{4-}) + \frac{RT}{F}\,ln\frac{c_{Fe(CN)_6^{3-}}}{c_{Fe(CN)_6^{4-}}} \tag{5.18}$$

The difference between the observed and theoretical redox potential is expressed by the ΔEh, which is a combination of individual activity coefficients and the liquid junction potential at the reference electrode:

$$\Delta Eh = Eh_{obs} - Eh_0 = \frac{RT}{F}\,ln\frac{\gamma_{Fe(CN)_6^{3-}}}{\gamma_{Fe(CN)_6^{4-}}} + E_{LJ} \tag{5.19}$$

$$= Eh_{obs} - E^0\,(Fe(CN)_6^{3-}/Fe(CN)_6^{4-}) - \frac{RT}{F}\,ln\frac{c_{Fe(CN)_6^{3-}}}{c_{Fe(CN)_6^{4-}}}$$

Several approaches were explored to empirically describe the relationship between ΔEh and the medium concentration. In the end, a formulation was chosen that is analogous to the model that describes the impact of ionic strength on the apparent pH value.

$$\Delta Eh = \frac{RTln(10)}{F}(a_1 SIT(I) + a_2 Q_{MX}) \tag{5.20}$$

Eh relates to a potential whereas the two variables SIT(I) and Q are expressions of concentrations and activity coefficients. Therefore, the Nernst factor needs to be added to the formula. Parameters for NaCl and $MgCl_2$ are based on the measurements in this work, those for KCl are calculated from the data in Hagemann et al. (2014) and Kolthoff and Tomiscek (1935) (Tab. 5.3).

Tab. 5.3 Model parameters to calculate ΔEh in NaCl and $MgCl_2$ solutions at 25, 40 and 60°C

T [°C]	NaCl		$MgCl_2$		KCl	
	a_1 (SIT)	a_2 (Q)	a_1 (SIT)	a_2 (Q)	a_1 (SIT)	a_2 (Q)
25°C	-7.91	0.333	-10.04	1.11	-9.72	0.134
40°C	-8.28	0.293	-9.96	1.07		
60°C	-7.70	0.297	-9.95	1.03		

It is interesting to note that the factors a_2 for ΔEh and ΔpH are quite similar. Such behaviour was expected since the liquid junction potential at the reference electrode in both cases depends essentially only on the concentration of the background salt. On the other hand, the ratio of activity coefficients of $Fe(CN)_6^{4-}$ and $Fe(CN)_6^{3-}$ seems to develop in the same way as the individual activity coefficient of H^+, otherwise, the slopes of ΔEh and ΔpH would differ. This may be a coincidence, but it would be interesting to see how other ion pairs behave.

The empirical model represents the relationship between ΔEh and the medium concentration very well (Fig. 5.8ff.).

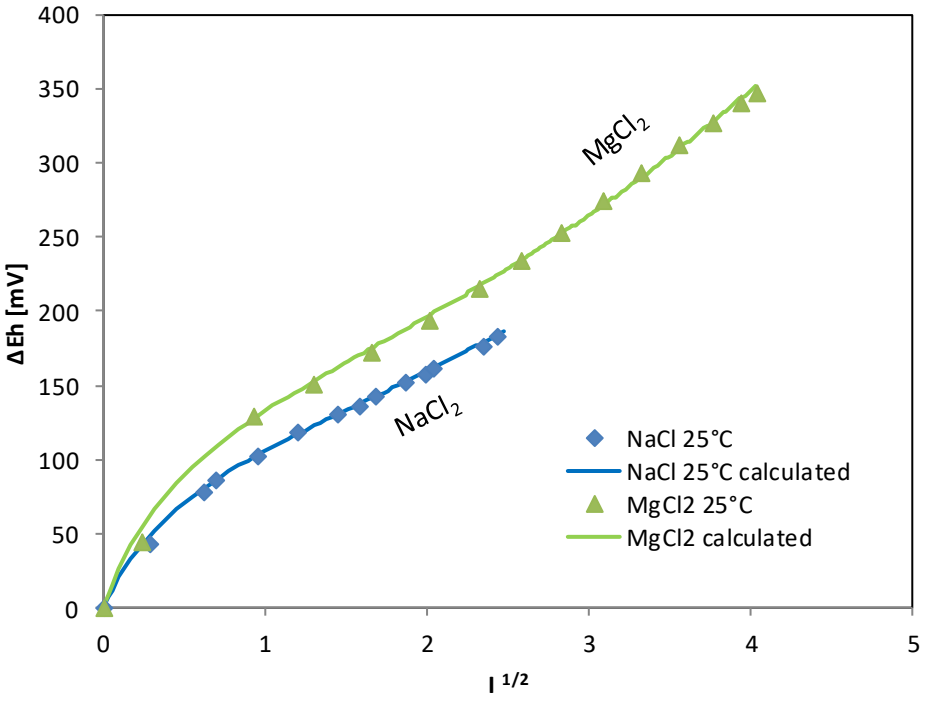

Fig. 5.8 Relationship between ΔEh and the concentration of NaCl and $MgCl_2$ at 25°C

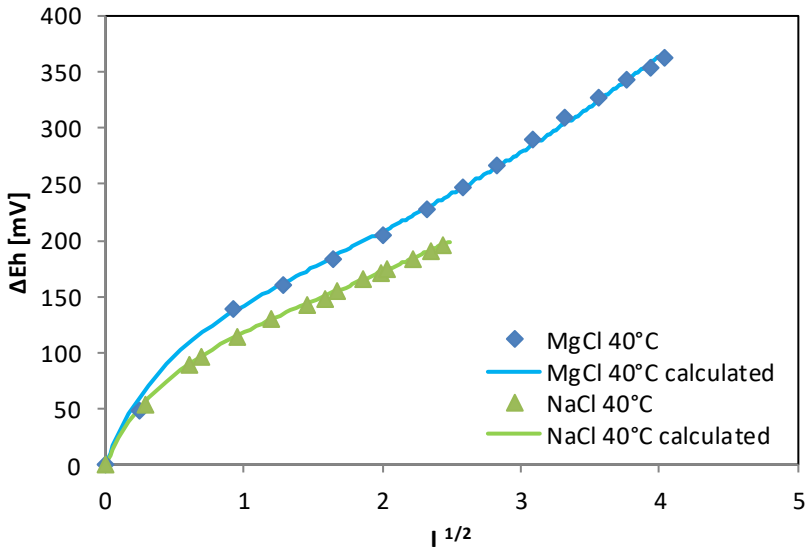

Fig. 5.9 Relationship between ΔEh and the concentration of NaCl and $MgCl_2$ at 40°C

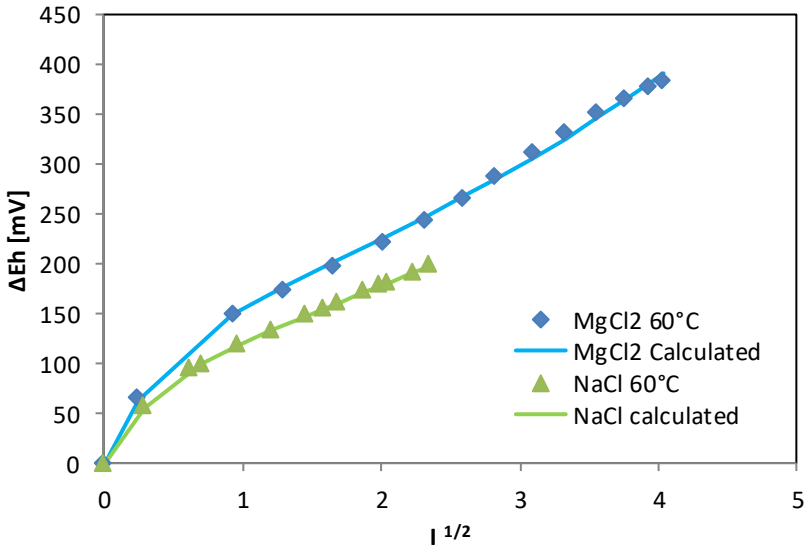

Fig. 5.10 Relationship between ΔEh and the concentration of NaCl and $MgCl_2$ at 60°C

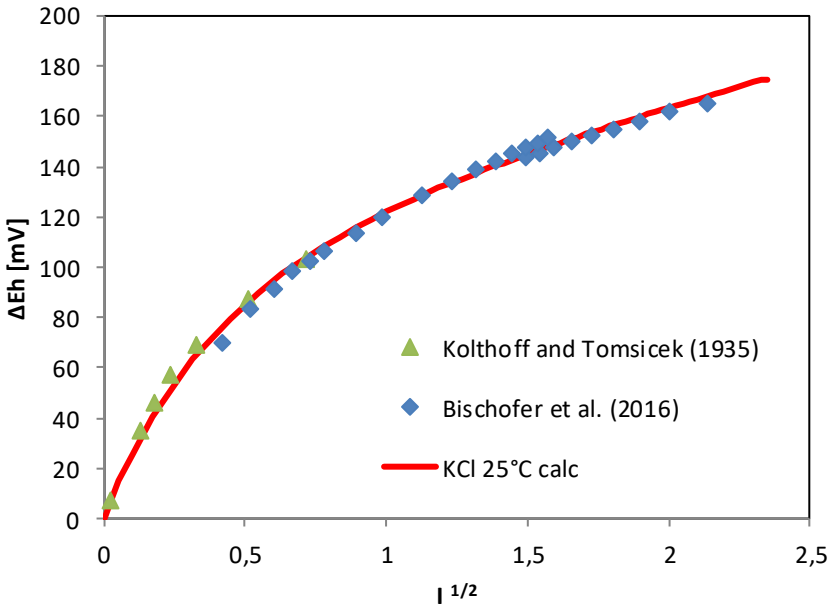

Fig. 5.11 Relationship between ΔEh and the concentration of KCl at 25°C

5.2.8 Application of the empirical model in ternary solutions

In a ternary solution, the empirical model needs to be adapted so that the specific impact of two different salts can be reflected.

$$\Delta Eh = \frac{RTln(10)}{F}\left(a_{1,MX}\frac{c_{MX}}{c_{MX}+c_{NX}}SIT(I) + a_{2.MX}Q_{MX} + a_{2.NX}Q_{NX}\right) \quad (5.21)$$

This formula is fully compatible with the formula for binary solutions presented above. Fig. 5.12 shows that the difference between experimental and calculated ΔEh is only very small at 25°C. The same can be observed at 40°C (Fig. 5.13). At 60°C, a difference of up to 10 mV is noted. As it stretches to solutions with almost pure $MgCl_2$ it may be assumed that there is a systematic error caused by the composition of $MgCl_2$. In some experiments with $MgCl_2$ decomposition of hexacyanoferrates was observed.

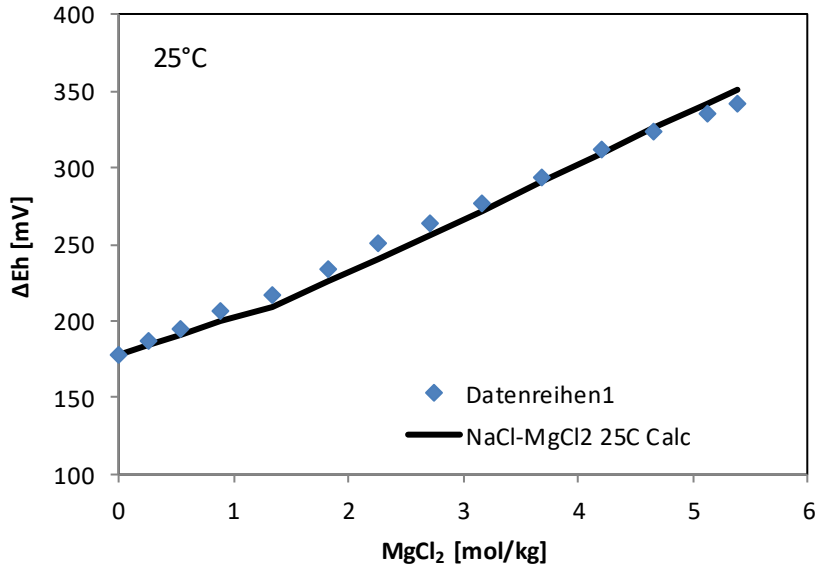

Fig. 5.12 Apparent redox potential of equimolar $Fe(CN)_6^{4-}$/ $Fe(CN)_6^{3-}$ in mixed NaCl/ $MgCl_2$ solutions at 25°C

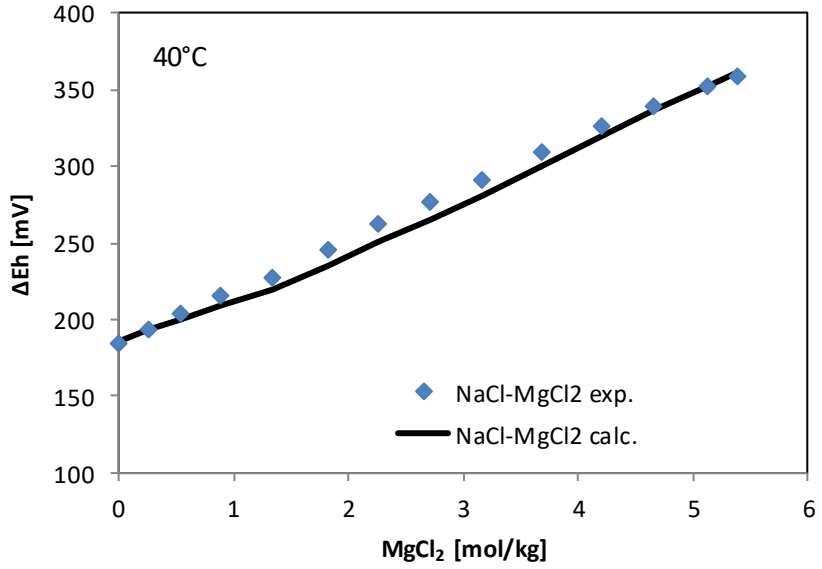

Fig. 5.13 Apparent redox potential of equimolar $Fe(CN)_6^{4-}$/ $Fe(CN)_6^{3-}$ in mixed NaCl/ $MgCl_2$ solutions at 40°C

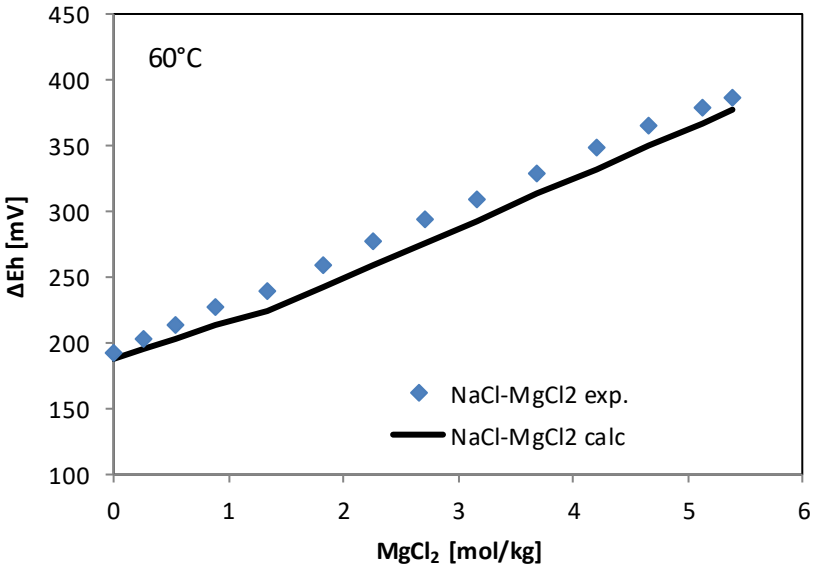

Fig. 5.14 Apparent redox potential of equimolar $Fe(CN)_6^{4-}$/ $Fe(CN)_6^{3-}$ in mixed NaCl/ $MgCl_2$ solutions at 60°C

5.2.9 Expressing the redox state of a solution using the empirical model

The empirical model describes well the deviation of Eh from a hypothetical zero ionic strength solution, but it contributes little to the understanding of the actual redox status. This may be achieved by a two-step approach.

In the first step, the observed redox potential Eh is used as a basis to calculate the actual or virtual concentration ratio of hexacyanoferrates in solution. If ΔEh can be calculated Formula (5.19) may be rearranged into

$$log\frac{c_{Fe(CN)_6^{3-}}}{c_{Fe(CN)_6^{4-}}} = \frac{F}{RT\ln 10}\left(Eh_{obs} - E^0\left(\frac{Fe(CN)_6^{3-}}{Fe(CN)_6^{4-}}\right) - \Delta Eh\right) \quad (5.22)$$

The concentration ratio may also be calculated in cases where the hexacyanoferrates are not even present. It only serves as a concentration-based expression for the redox status. Still, this ratio has little applicability as it depends on the solution composition. But it can be linked to other redox species a scientist is more familiar with. An example is oxygen that may be included in a redox reaction with hexacyanoferrate as follows

$$Fe(CN)_6^{4-} + 1/4O_2 + H^+ \rightleftharpoons Fe(CN)_6^{3-} + ½\ H_2O \quad (5.23)$$

The equilibrium constant for this reaction would be formulated as:

$$K_1 = \frac{a_{Fe(CN)_6^{3-}} a_{H_2O}^{0.5}}{a_{Fe(CN)_6^{4-}} p_{O_2(g)}^{0.25} a_{H^+}} \tag{5.24}$$

The partial pressure of oxygen (more precisely its fugacity whose numerical value is almost the same at or below 1 bar total pressure) can be calculated from the individual redox reaction of ferri-/ferrocyanide and oxygen:

$Fe(CN)_6^{4-} \rightleftharpoons Fe(CN)_6^{3-} + e^-$ (5.25)

$2\ H_2O \rightleftharpoons O_2 + 4H^+ + 4e^-$ (5.26)

The standard potential of the ferri-/ferrocyanide reaction is 0.355 V (Hanania et al. 1967) resulting in an equilibrium constant of log K = 6.00:

$$\log K_2 = -\frac{F}{RT \ln 10} E_0 = 6.00 \tag{5.27}$$

It is combined with the equilibrium constant for reaction (5.26) (log K= -85.984, Hummel et al. 2002) so that the constant for reaction (5.23) amounts to:

$\log K_1 = 27.50$

The partial pressure of gaseous O_2 in equilibrium with a solution containing a known concentration of ferrocyanide and ferricyanide could then be calculated by:

$$p_{O_2(g)} = \frac{c_{Fe(CN)_6^{3-}}^4 \gamma_{Fe(CN)_6^{3-}}^4 a_{H_2O}^2}{c_{Fe(CN)_6^{4-}}^4 \gamma_{Fe(CN)_6^{4-}}^4 a_{H^+}^4 K_1^4} \tag{5.28}$$

Finally, (5.28) may be logarithmized to

$$\log p_{O_2(g)} = 4 \log \frac{c_{Fe(CN)_6^{3-}}}{c_{Fe(CN)_6^{4-}}} + 4 \log \frac{\gamma_{Fe(CN)_6^{3-}}}{\gamma_{Fe(CN)_6^{4-}}} + 2 \log a_{H_2O} - 4 \log \gamma_{H^+} - 4 \log c_{H^+} - 4 \log K_1^4 \tag{5.29}$$

For an evaluation of this formula, it is necessary to have a thermodynamic model that describes the activity coefficients of hexacyanoferrate species in the specific solution

where the redox potential has been measured. Also, a model is needed to convert apparent pH values into hydrogen concentrations. In this work, models have been developed that allow a calculation in NaCl, KCl, $MgCl_2$ and mixed NaCl/$MgCl_2$ solutions at 25°C. At higher temperatures, only a model for NaCl solutions could be derived. Calculations in $MgCl_2$ solutions are limited to about 3.0 mol/kg because it was not possible to extend the model to higher concentrations in the ternary system $MgCl_2$-$Mg_2Fe(CN)_6$-H_2O.

Fig. 5.15 shows an example of pO_2 values calculated from Eh following the procedure as described above. In Fig. 5.16 the same values are corrected for the experimental H+ concentrations and compared with pO_2 values predicted by thermodynamic modelling of equimolar hexacyanoferrate(II) and hexacyanoferrate solutions in NaCl. Both data sets correspond very well.

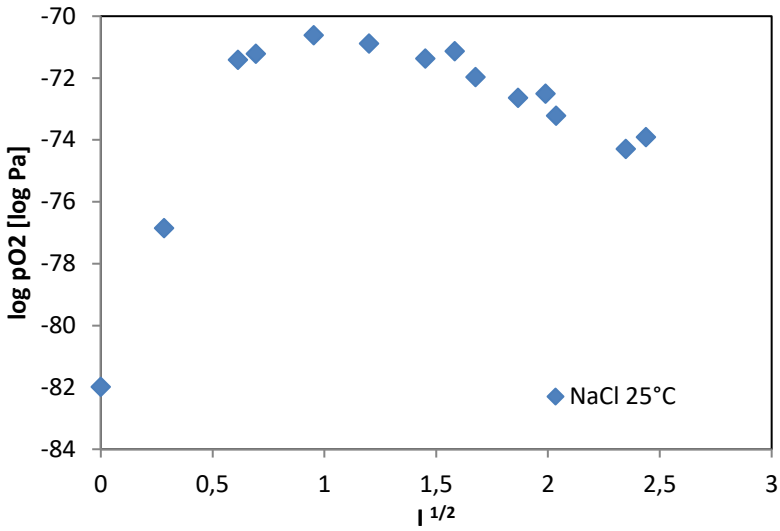

Fig. 5.15 Calculated pO_2 for hexacyanoferrate mixtures in NaCl at 25°C

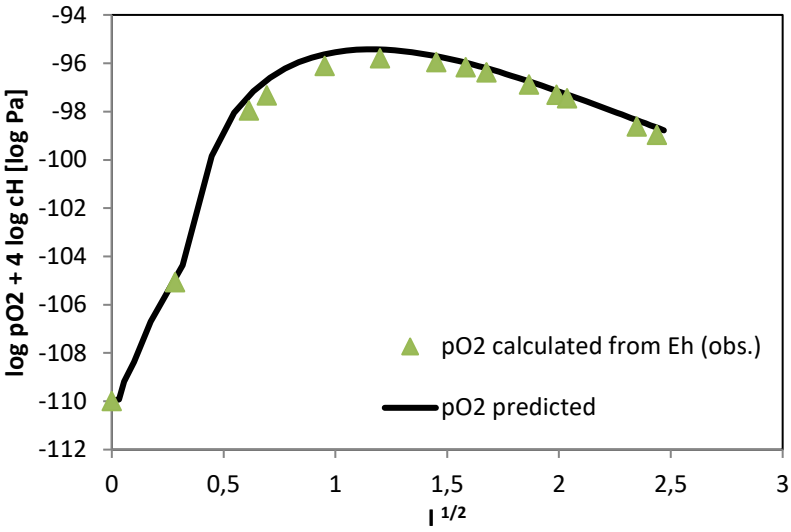

Fig. 5.16 Comparison of pcH corrected pO_2 values calculated from measured Eh and predicted by thermodynamical modelling

6 Complex formation of Fe(II) with chloride and sulphate

6.1 Background and objective

In the near-field of a repository, strongly reducing conditions are to be expected in the long term due to the presence of metallic iron in containers, liners, rails and reinforcing steel. Iron released by corrosion will occur in solution and secondary phases will almost exclusively be formed with ferrous iron.

In the case of saline near-field solutions, as they occur in the host rock formations of salt and North German Lower Cretaceous clays, a model is required that represents the special conditions chemically and physically correctly. A model for iron(II) in saline solutions has already been developed for 25° (Hagemann et al. 2012). However, for simplicity's sake, it assumed that no complex formation with iron(II) occurs in solutions with a high chloride and sulphate content and that Fe^{2+} is always free. In fact, Fe(II) forms complexes with both chloride and sulphate as could be detected by spectroscopic measurements (UV-VIS, IR, XANES, X-ray absorption) (for example Vogel Koplitz et al. 1987, Heinrich and Seward 1990, Zhao and Pan 2001, Liu et al. 2007). The complex formation is probably one reason why the modelling of Fe(II)-containing salt systems was only partially successful (Moog and Hagemann 2004).

There is now a consistent picture of the complexes that may form. According to widely agreed interpretations, the species $FeCl^+$ (octahedral), $FeCl_2$(aq) (octahedral) and $FeCl_4^{2-}$ (tetrahedral) occur in aqueous solutions (Zhao and Pan 2001, Liu et al. 2007, Testemale et al. 2009). The species $FeCl_3^-$ was postulated (Vogel Koplitz et al. 1987), but cannot be reliably derived from spectroscopic data (Testemale et al. 2009).

However, it is not clear at which chloride concentrations the various complexes occur. According to the XANES investigations by Liu et al. (2007), at 25°C the occurrence of $FeCl_2$(aq) would be expected from approx. 2 mol/kg, with $FeCl_4^{2-}$ from 6 mol/kg. Zhao and Pan (2001) suspect $FeCl_2$(aq) only from about 4 to 5 mol/kg, whereas the complex $FeCl_4^{2-}$ can only be detected at 60°C or higher. Testemale et al. (2009) were able to detect significant contributions of the tetrachloro complex only at 300°C.

Studies that investigated the specific influence of important background salts such as NaCl, $MgCl_2$ or KCl on complex formation were previously only available for NaCl/LiCl in

D_2O. A Pitzer model was developed by Zhao and Pan 2001. They describe the complex formation in NaCl and LiCl solutions up to I= 16.38 m. It is noticeable, however, that for the interaction of Fe^{2+} with Cl^- the parameter set of Pitzer (1991) was used, which is only valid up to 2 mol/kg $FeCl_2$ and was also created under the assumption that no complex formation takes place. Since temperature coefficients were not available for the parameters of Fe^{2+}/Cl^-, the coefficients of Co^{2+}/ Cl^- were used without further testing. For the ion pair $FeCl^+/Cl^-$ the value of Haung (1989) for $CuCl^+/Cl^-$ was assumed. However, their model for the system NaCl-$CuCl_2$-H_2O suffers from strong correlations, because a total of 59 parameters were optimized simultaneously. Therefore, the model is highly questionable.

Fe^{2+} also forms at least one complex with sulphate. In the same way, as for chloride, spectrophotometric data were intended to be used to quantify the complexation in Na_2SO_4 solutions.

6.2 Approach

It was planned to investigate the speciation of Fe^{2+} in chloride and sulphate solutions in three steps:

1. UV-spectroscopic measurements of Fe(II) species in solutions of the salts NaCl, KCl, $MgCl_2$, LiCl and Na_2SO_4 in the wavelength range 190 to 800 nm at 25 to 80°C
2. The solution spectra should then be deconvoluted into individual species spectra to determine the number of species present and their concentration.
3. This should then serve as the basis for deriving an ion-specific thermodynamic model.

The spectrophotometric investigations were performed with a two-beam UVVIS spectrometer (Shimadzu UV-2450). An iron-containing solution was measured against an iron-free solution of otherwise identical composition in the wavelength range 190 to 800 nm.

Due to the weak absorptivity of iron(II) species, the concentration of Fe(II) had to be in the range of 0.05 mol/kg. The iron(II) solutions were prepared by mixing a solution of iron(II) perchlorate with a stock solution of NaCl, LiCl, $MgCl_2$ or Na_2SO_4. The perchlorate

was chosen to allow investigations of solutions with low chloride content. An addition of perchloric acid (final concentration in measuring solutions about 0.001 mol/kg) ensured slightly acidic conditions and suppression of hydroxo complexes. Due to the poor solubility of $KClO_4$, KCl solutions were prepared by using a $FeCl_2$ stock solution.

Some solutions with very high chloride concentrations (some batches with LiCl and $MgCl_2$) showed considerably higher absorptions. In these cases, solutions with lower Fe content were prepared.

All solutions were manufactured in a glovebox under exclusion of oxygen. In the reference solutions, $Mg(ClO_4)_2$ of the same concentration was used instead of $Fe(ClO_4)_2$. To avoid oxidation of the solutions outside the glovebox, all measuring solutions in the glovebox were filled into sealable cuvettes.

All measurements were performed in temperature-controlled cell holders. Measurements at higher temperatures (40, 60, 80°C) were performed with pre-temperated cells to accelerate the establishment of thermal equilibrium.

6.3 Results of spectroscopic investigations

6.3.1 Spectra in chloride media

In the absence of chloride and at low chloride contents (up to 0.03 mol/kg) the spectra had a uniform shape and showed a shoulder at 240 nm (41700 cm^{-1}) and a flank rising to the far UV (Fig. 6.1).

At concentrations of 0.1 mol/kg and above, an increase in absorption could be observed in all wavelength ranges. It was small in the beginning but became increasingly clearer and lead to an increase in the absorption in the shoulder region by about 80%, whereby the shoulder shifted continuously to about 250 nm. The flank below 240 nm increased slightly more (approx. 120%) (Fig. 6.2).

A further increase of the chloride concentration (only observable in LiCl) leads to the formation of a maximum at 250 nm, which shifted continuously and was located at 255 nm (39200 cm^{-1}) at the highest LiCl concentration (16.1 mol/kg). In all wavelength ranges, the absorption at the highest chloride concentration was about four times

stronger than at 6.1 mol/kg NaCl. The flank below 240 nm became increasingly strong so that the light beam was extinguished to a large extent. In that case, these parts of the solution spectrum consisted only of noise (Fig. 6.3 and Fig. 6.4).

Whether the solution spectrum at 16.1 mol/kg LiCl was already a limit spectrum that cannot be further changed cannot be said. Fact was that the solution spectrum between 14.4 and 16.1 mol/kg LiCl changed only slightly.

The spectra also showed a weak profile in the range from 300 to 500 nm, which also got stronger at higher chloride concentrations. A comparison with spectra of solutions containing Fe(III) showed that these are probably impurities of Fe(III) (Stefánsson et al. 2019). In chloride-containing solutions, Fe(III) species have a molar absorption about ten times higher than Fe(II) species, especially when the complex $FeCl_4^-$ is present. Rough estimates suggest that, despite extensive precautions, about 1% Fe(III) was present, so that the solution spectra were increased by about 10% in the range 200 to 300 nm. This had to be taken into account when evaluating the spectra.

The spectra at higher temperatures show a similar development as at 25°C. In the absence of chloride, a shoulder is again found at about 240 nm. A change in the spectrum occurs even with the smallest addition of chloride (0.01 mol/kg). The complex formation, therefore, starts earlier. At the highest concentrations of NaCl, LiCl, and $MgCl_2$ the spectra showed a new characteristic. The shoulder at 255 nm further developed into a peak at 261.5 nm. At the same time, the flank below 240 nm increased very strongly (Fig. 6.5 for 80°C). The disturbances by Fe(III) had an even stronger effect. The absorption by Fe(III) species now reaches about 20%.

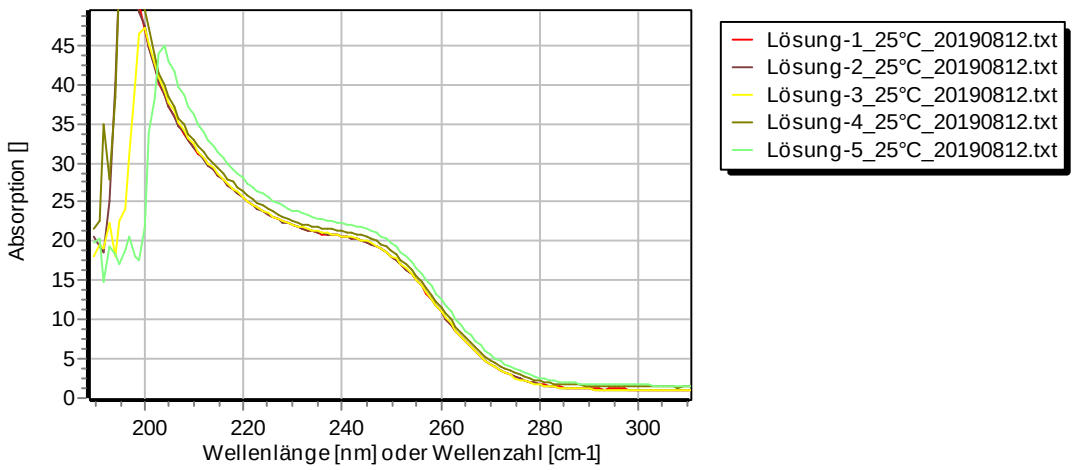

Fig. 6.1 Solution spectra standardised to 1 mol/l Fe in solutions of NaCl (0 to 0.3 mol/kg)

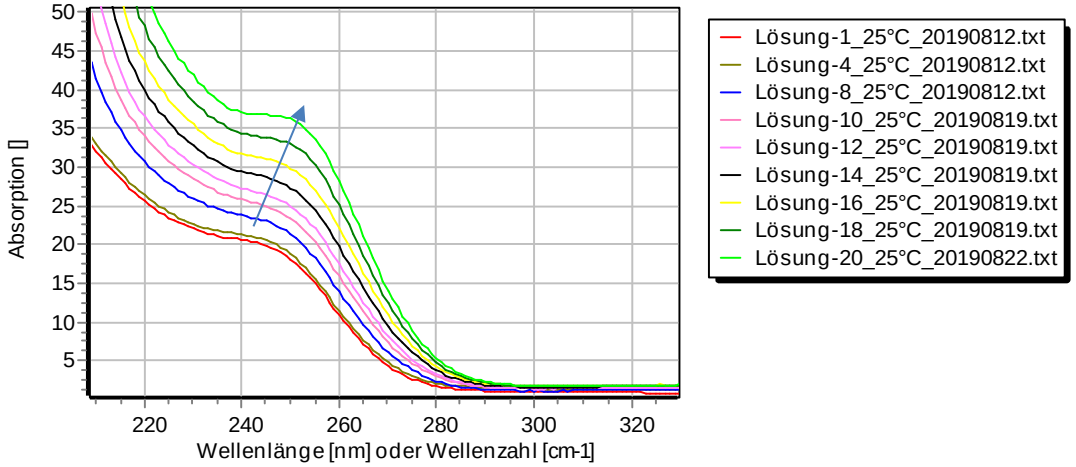

Fig. 6.2 Solution spectra standardised to 1 mol/l Fe in solutions of NaCl (0 to 6.1 mol/kg) at 25°C

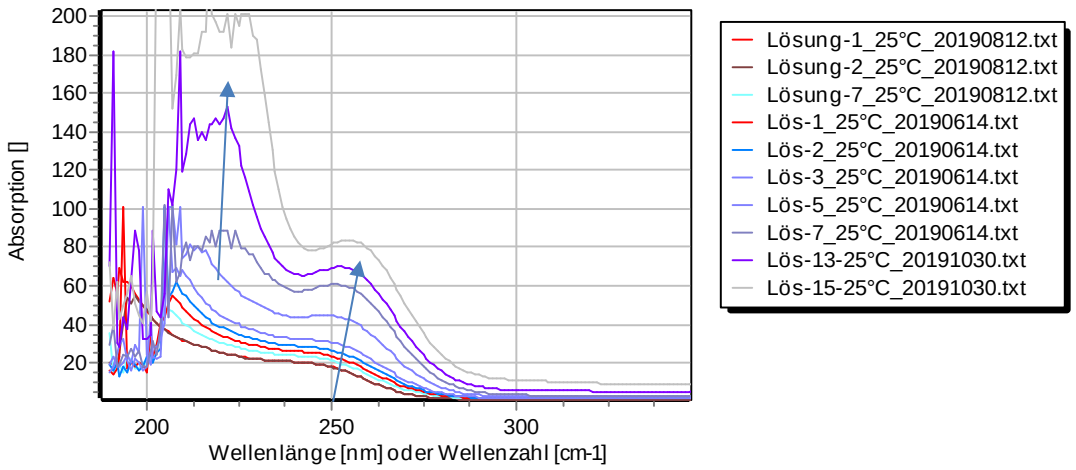

Fig. 6.3 Solution spectra standardised to 1 mol/l Fe in solutions of NaCl and LiCl (0 to 16 mol/kg) at 25°C

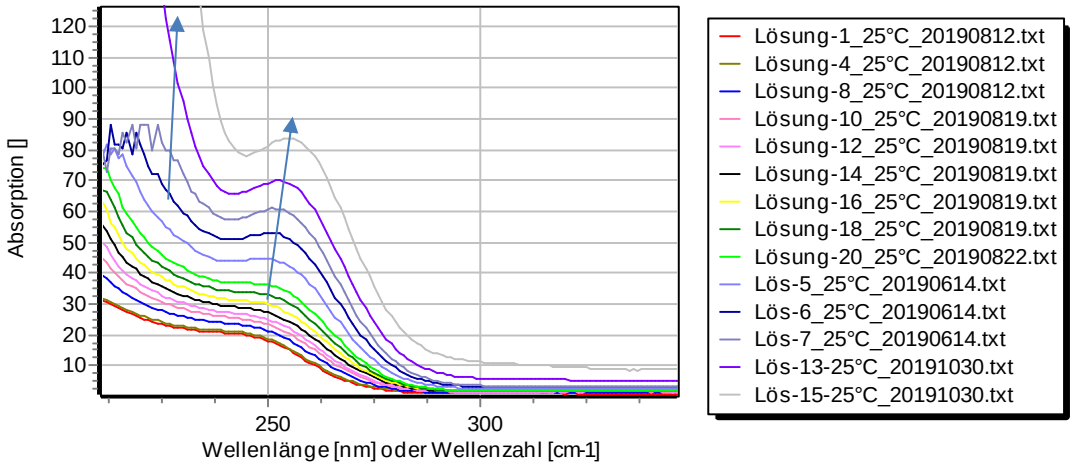

1

Fig. 6.4 Solution spectra standardised to 1 mol/l Fe in solutions of NaCl (0 to 6.1 mol/kg) and LiCl (0 to 16.1 mol/kg)

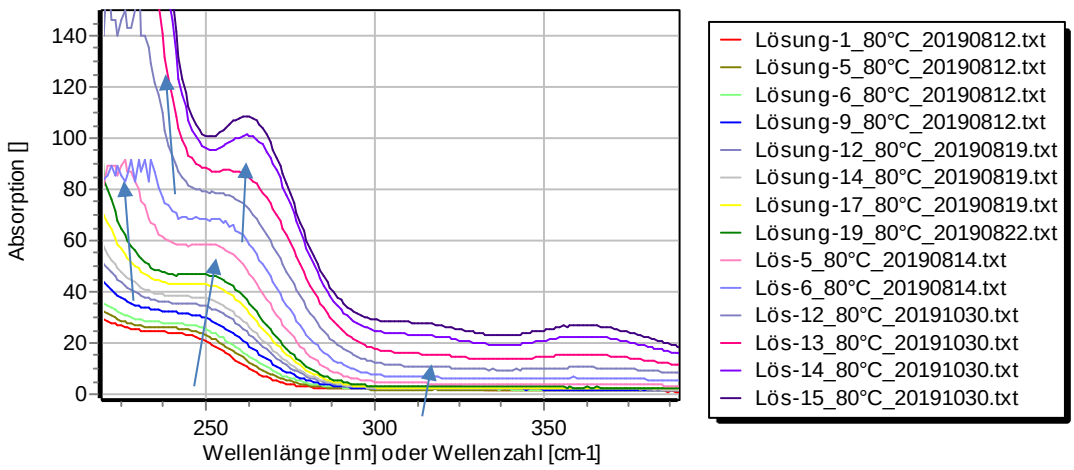

Fig. 6.5 Solution spectra standardised to 1 mol/l Fe in solutions of NaCl (0 to 6.1 mol/kg) and LiCl (0 to 16.1 mol/kg) at 80°C

6.3.2 Spectra in sulphate media

The spectra in sulphate containing solution show rather little change when the concentration of Na_2SO_4 is increased. At all concentrations the spectra are more or less identical to the sulphate free solutions- Only at concentrations of about 0.2 mol/kg and higher the shoulder at 240 nm increases slightly but not more than 20% at the highest Na_2SO_4 concentration (Fig. 6.6 and Fig. 6.7). The shape of the spectrum remains the same and there do not occur any new characteristics. It may well be that minor contaminations of Fe^{3+} have an impact on the absorption in this area. The results of Masłowska (1967) show that in an acid solution (0.2 m $HClO_4$) Fe^{3+} as well as the $FeSO_4^+$ complex have the same absorption at about 240 nm, so a change of Fe(III) speciation would not affect Fe(II) absorption. But the situation is different at slightly acidic conditions were Fe(III) hydroxo complexes dominate. $FeOH^{2+}$ and $Fe(OH)_2^+$ have an extinction coefficient of about 4000 cm^{-1} mol^{-1} l^{-1} (Stefánsson 2007). That is a little bit more than the sulphato complex (about 3500 cm^{-1} mol^{-1} l^{-1}, Masłowska 1967. But if we conservatively assume a contamination of about 5% the differences in the absorption at 240 nm would be marginal. Therefore, the low increase in Fe(II) containing sulphate solutions may be considered significant and specific.

On the other hand, it is not possible to quantify the change of Fe(II) speciation. Data scattering is noticable and spectra deconvolution did not lead to clear results. It is not possible to assign a concentration change based on our data or to deconvolute the

spectra into single species spectra. Using factor analysis, the programme Wotan (Hagemann 2012) predicted two or three distinct species as the optimum choice, but the model was not convincing. The proposed single species spectra were almost identical (Fig. 6.8). Therefore, spectrophotometry was only able to provide a qualitative indication of complex formation. The complex is obviously rather weak. If it occurred in significant amounts in mixed systems such as Na_2SO_4-$FeSO_4$-H_2O it would be visible in isopiestic measurements. Complex formation, even if weak would lead to a significant change of the total concentration of aqueous species. Such a process causes isoactivity lines to bend. No such measurements have been conducted for Fe(II) systems. However, some data exist for the comparable $NiSO_4$ and $CoSO_4$ systems (Hagemann et al. 2015). The isoactivity lines in mixed $NiSO_4$-Na_2SO_4 and $CoSO_4$-Na_2SO_4 solutions clearly show a curvature. It may be expected that the analogous Fe(II) system behave similarly.

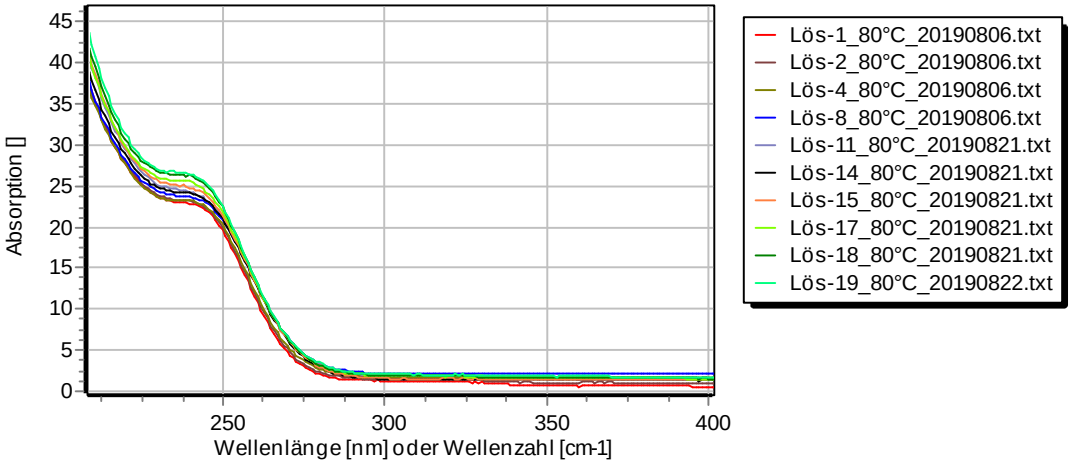

Fig. 6.6 Absorption of Fe(II) containing sulphate solutions at 25°C

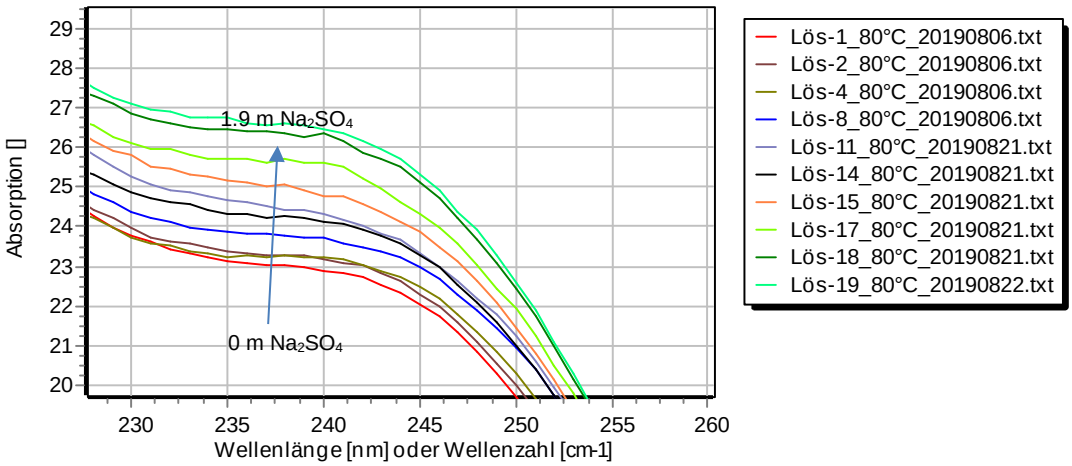

Fig. 6.7 Absorption of Fe(II) containing sulphate solutions at 25°C: shoulder at 240 nm

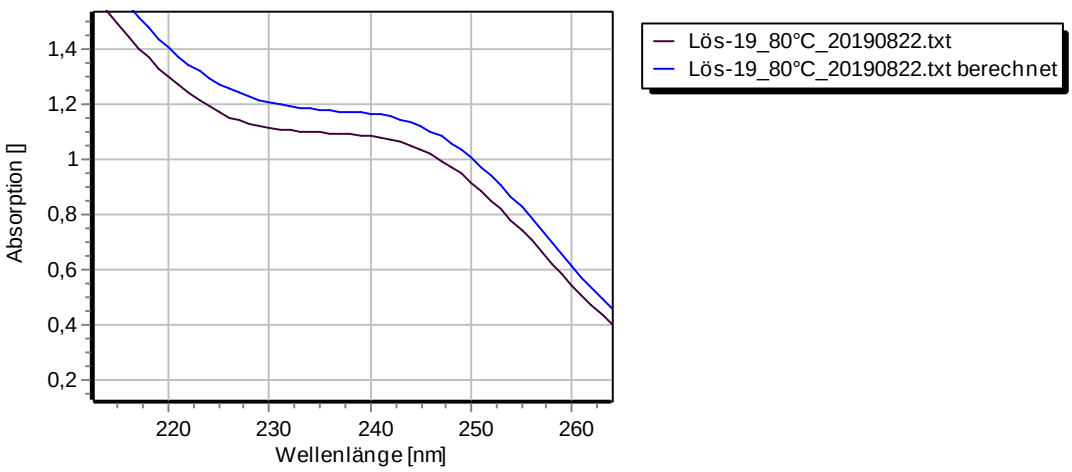

Fig. 6.8 Proposed species spectra in a 2-species model for Fe(II) in sulphate solutions

6.4 Deconvolution of spectra

6.4.1 Method

The spectra were separated into single spectra utilizing evolving factor analysis. The procedure is based on an approach of Gampp et al. (1986) and was implemented in the program Wotan. It consists basically of sorting the measurements in the order of the

ligand concentrations (here: chloride). Afterwards, the determination of the eigenvectors and eigenvalues for the matrix of the absorption spectra is carried out step by step, i.e. with an increasing number of considered measurements. This procedure allows a rough estimate of the concentration development of the existing species and the underlying single-species spectra. Smoothing and correction methods are used to find an optimal solution that minimizes the error square sum for the difference between measured and calculated absorptions. The number of distinguishable species in the system is estimated by statistical methods but ultimately determined by try-and-error. That number of species is chosen for which the error sum of squares is smallest after optimization. More details can be found in Hagemann (2012).

Deconvolution of solution spectra is hampered by the dilemma of apparent limit spectra. In cases of strongly overlapping species spectra, the spectral separation tends to consider the spectrum at the highest ligand concentrations as an invariant boundary spectrum with a maximum concentration of the last/highest complex. The algorithm cannot distinguish whether the last solution spectrum is a pure species spectrum or just a linear combination of two separate species spectra.

6.4.2 Results of spectral deconvolution

The spectral separation of the measurements at 25°C clearly led to three different species. Two species were too few to explain all solution spectra. A three-species model could explain all spectra very well. Smaller deviations might have been caused by Fe(III) species. A four-species Modell did not improve the situation. Instead, the sum of the squares of errors became much larger an at least two calculated species spectra were very similar.

Fig. 6.9 shows the calculated species spectra at 25°C. Spectrum 1 corresponds to Fe^{2+}. Spectra 2 and 3 stand for two Fe(II)-chloro complexes. Their maxima are 251 (60 l mol^{-1} cm^{-1}) and 255 nm (76 l mol^{-1} cm^{-1}).

The measurements at 80°C could also be explained by three spectra. No additional species appeared. The maximum of species spectrum 2 is at 252 nm (67 l mol-1 cm-1), the maximum of the third species spectrum at 264 nm (91 l mol-1 cm-1). While the height and position of the second species spectrum shifted only slightly, a clear change could be seen in the third spectrum, both in position (9 nm redshift) and height (+15 l mol-1

cm-1). This can be interpreted by assuming that the solutions spectrum at 25°C and 16.1 mol/kg LiCl was not yet a boundary spectrum, but only a mixture of the spectra of the second and third species. The calculated species spectrum of the measurements at 80°C is probably closer to the spectrum of the second complex. However, it is by no means certain that the measurement at 16.1 mol/kg is already a boundary spectrum. It could also still be a mixture. This assumption is supported by a comparison of the calculated species spectra at 25, 40, 60, and 80°C. Whereas the spectrum of $FeCl^+$ showed only a slight increase of absorptivity when the temperature was increased while the shape and position remained unchanged (Fig. 6.11), the calculated peak maximum in the spectrum of $FeCl_2(aq)$ shifts from about 245 to 265 nm between 25 and 80°C (Fig. 6.12). The derived species distributions should therefore be treated carefully, at least concerning the third species.

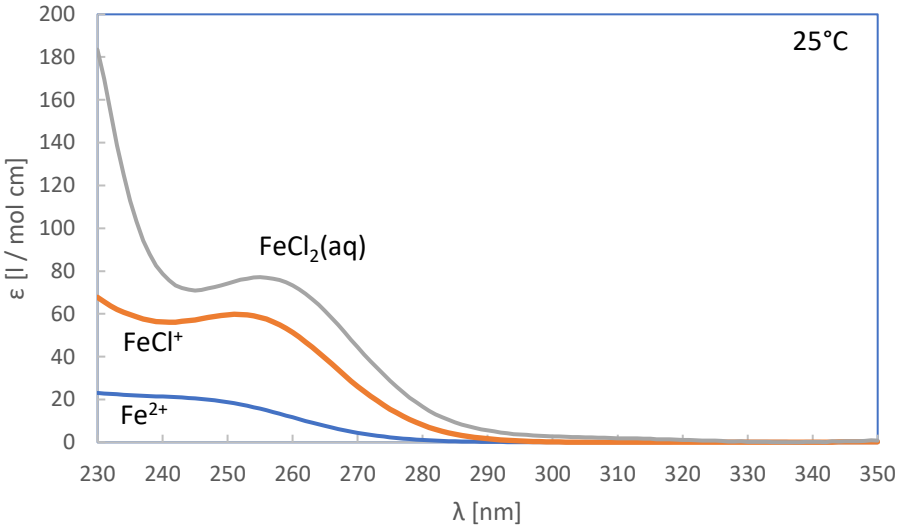

Fig. 6.9 Species spectra of Fe(II) chloro complexes at 25°C

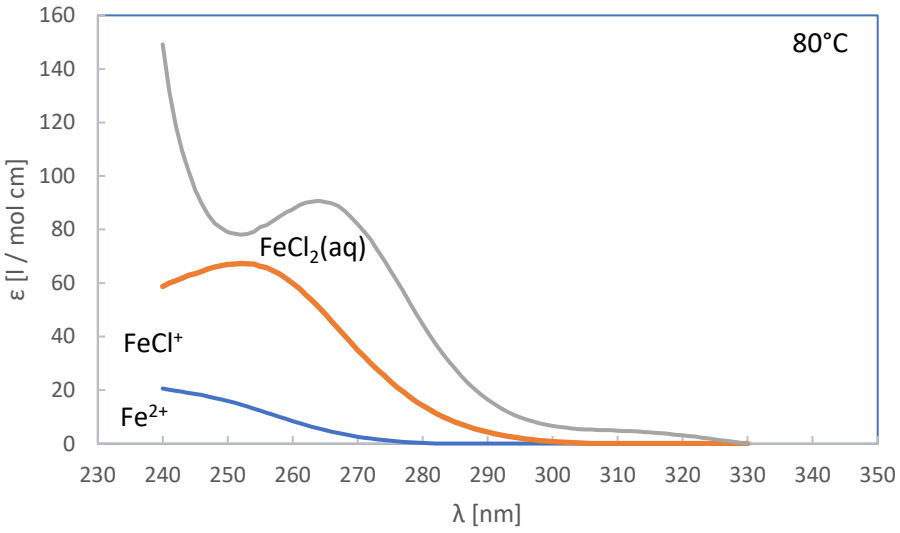

Fig. 6.10 Species spectra at 80°C

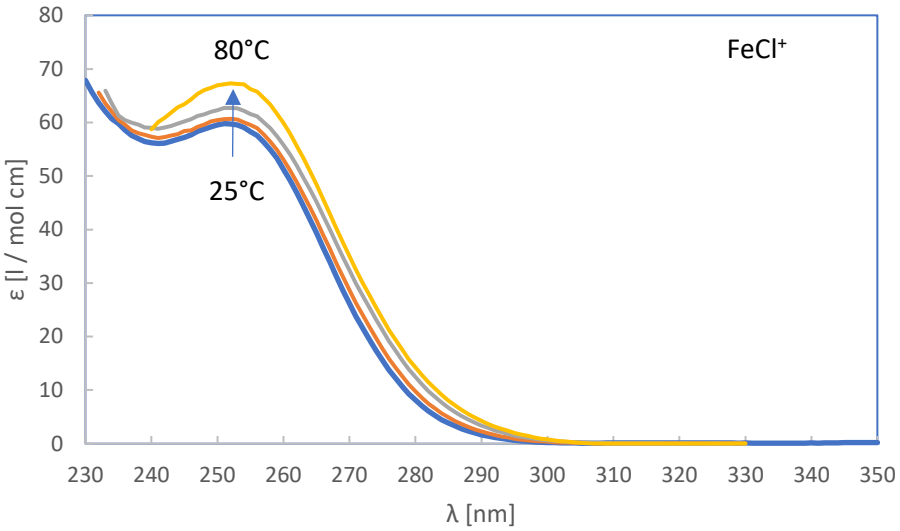

Fig. 6.11 Spectrum of the $FeCl^+$ complex at 25-80°C

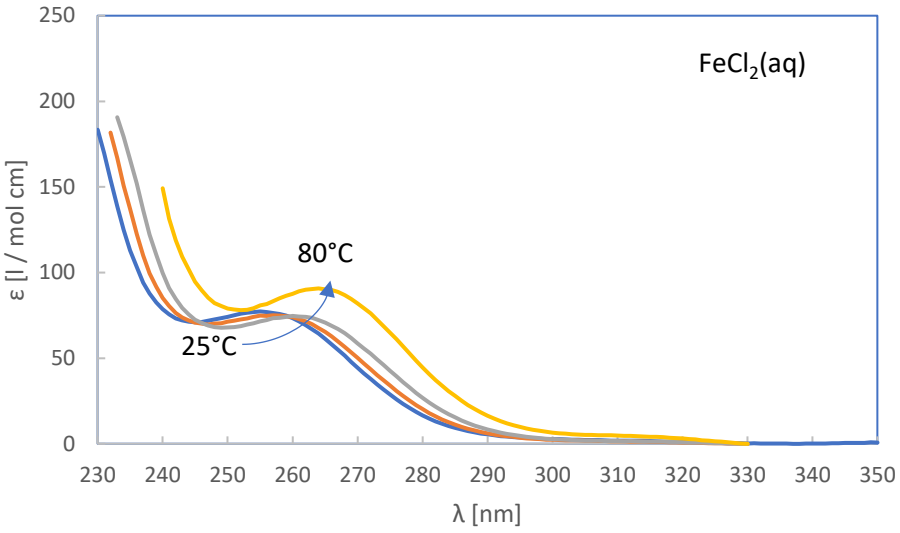

Fig. 6.12 Spectrum of the $FeCl_2(aq)$ complex at 25-80°C

The measured spectra can be reconstructed very well with the derived single species spectra (example: **Fig. 6.13**).

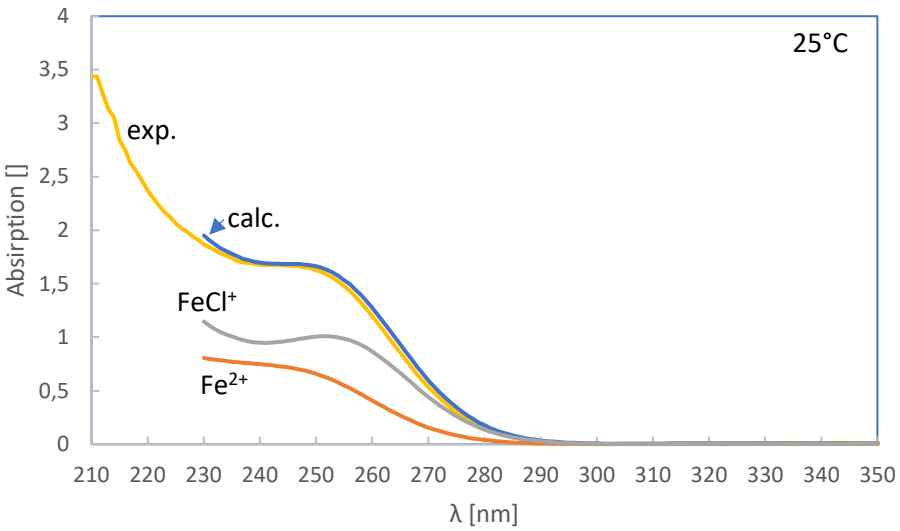

Fig. 6.13 Measured and reconstructed spectrum of the solution NaCl-20 (6.1 mol/kg NaCl) at 25°C

Based on the individual species spectra, the species distribution could now be calculated. For 25 and 80°C the results are shown in Fig. 6.14 and Fig. 6.15. They demonstrate that at 25°C the first species dominates to about 7 mol/kg. Afterwards, the second complex prevails. A third complex is observed at chloride concentrations above 8 mol/kg. At about 10 mol/kg chloride the second complex shows its concentration maximum. At

about 13 mol/kg the third complex dominates. While the first appearance of the two chloro complexes is characterized by a slow concentration increase, the disappearance of the free Fe^{2+} and the first complex is quite abrupt. Normally, a slow run-out would be expected. Instead, the calculated concentration quickly drops to zero. Probably, this does not correspond with reality. Rather, it can be assumed that the calculated single spectra of the following species (2 and 3) contain spectral components of the respective previous species. Because of the strong overlapping of the three species a mathematical separation is difficult (see discussion above).

At 80°C, the formation of the first complex starts earlier. Its maximum is observed at about 8 mol/kg. The second complex is already detectible around 3 mol/kg. Its calculated relative concentration reaches its maximum exactly at the highest LiCl concentration. This is most probably a mathematical artefact and the last measured spectrum is still a mixture of two species.

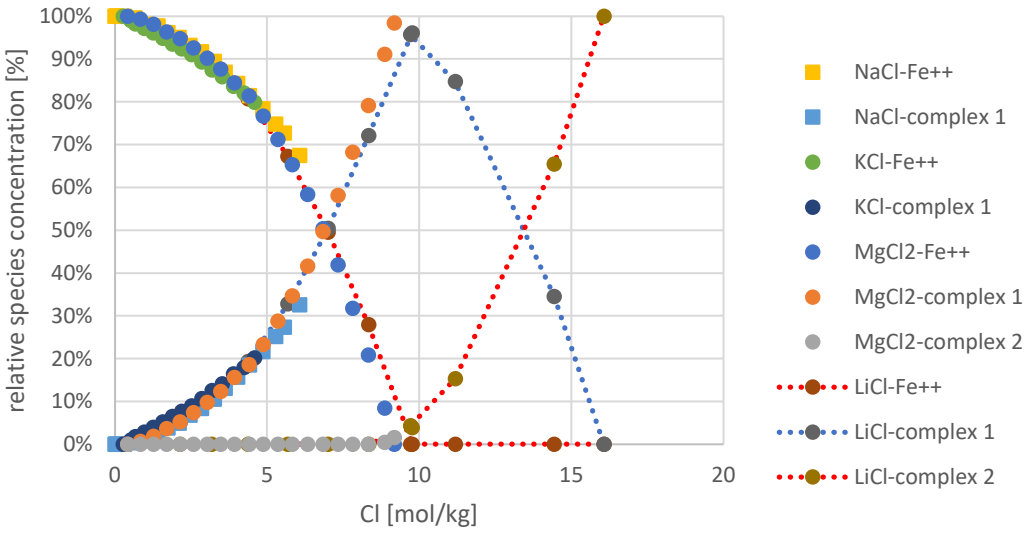

Fig. 6.14 Distribution of Fe(II) species in NaCl, KCl, LiCl, and $MgCl_2$ solutions at 25°C.

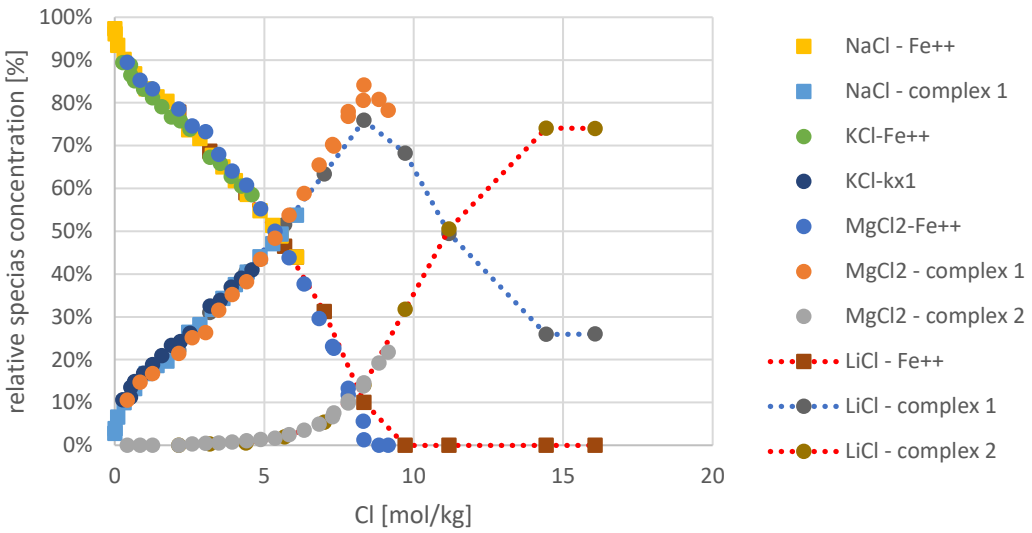

Fig. 6.15 Distribution of Fe(II) species in NaCl, KCl, LiCl, and $MgCl_2$ solutions at 80°C.

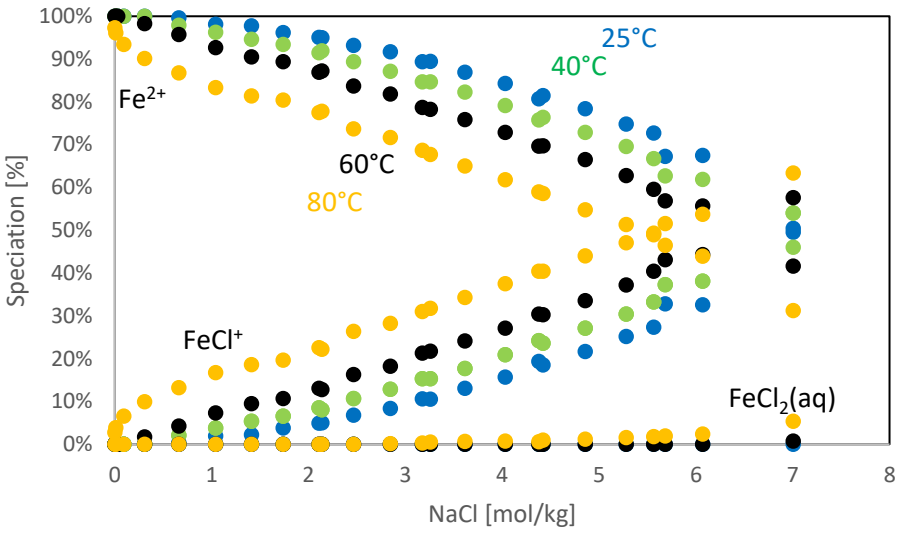

Fig. 6.16 Speciation of Fe(II) between 0 and 8 mol/kg Cl in NaCl and LiCl solutions at 25, 40, 60 and 80°C.

First of all, the spectra and the relative species concentrations tell nothing about the nature of the second and third species. Nevertheless, their relationship can be evaluated by a rough thermodynamic calculation. For this purpose, a hypothesis is made that the second species is the complex $FeCl^+$. For the free cation Fe^{2+}, it is assumed that its activity coefficients in chloride solutions correspond to those of Ca^{2+}. This assumption is justified because the water activity of $FeCl_2$ and $CaCl_2$ are almost identical at

concentrations up to 2 mol/kg (**Fig. 6.17**). At higher chloride concentrations the water activities of $FeCl_2$ decreases slower than those of $CaCl_2$. This is consistent with the observation that the complex formation becomes more important for Fe(II) than with Ca with the result that the number of dissolved ions is decreasing slower with Ca. For the ion pairs Ca^{2+}/ Cl^- and consequently Fe^{2+}/ Cl^- the THEREDA model is applied. This assumption cannot be proven now, but at least the model is plausible to a certain degree. For $FeCl^+$, in the absence of reliable models, it is assumed that its activity coefficients can be described as the similarly heavy cation Rb^+. For this purpose, a preliminary model is used[2]. On this basis, the activity coefficients for Fe^{2+}, $FeCl^+$ and Cl^- were calculated for all solutions except LiCl, for which the necessary ternary interaction coefficients are not available. In addition, since it is questionable whether the spectral separation at high chloride concentrations yields correct species distributions, this step is not necessary. If the activity ratio log a_{FeCl+}/ a_{Fe2+} is plotted against log a_{Cl}, a slope of -1 is obtained as expected.

The second complex was identified similarly but only at a later stage. As there were at 25°C only two measurements In NaCl, KCl and $MgCl_2$ solutions where the second complex occurred, a preliminary evaluation was performed for the solutions at 80°C. Again, Pitzer coefficients for Fe^{2+}/ Cl^- were adopted from Ca^{2+}/ Cl^-. A Pitzer model was established for $FeCl^+$. The hypothesis was tested that $FeCl_2$(aq) was the second complex. It was assumed that the activity coefficients of $FeCl_2$(aq) were equal to unity. For the evaluation, only those solutions were selected that contained at least 5% of the second complex. This applied to nine $MgCl_2$ solutions with a chloride concentration between 6.8 and 9.1 mol/kg. The calculated equilibrium constant for the reaction

$FeCl^+ + Cl^- \rightarrow FeCl_2(aq)$

was constant for all considered solutions, thus confirming the hypothesis. This observation is consistent with the results of Testemale et al. (2009) who have shown by X-ray absorption spectroscopy (XANES) that a species with tetragonal symmetry like $FeCl_4^{2-}$ or $FeCl_3^-$ can be observed only at much higher temperatures (>300°C).

[2] This model is being developed as part of the THEREDA project by T. Scharge (GRS). As it is used only for a first approximation of the complex formation constant but not further on, it is not documented here.

In contrast to that, Liu et al. (2007) concluded from their XANES spectra that the complex $FeCl_4^{2-}$ starts to form at about 6 mol/kg even at 25°C. They relied on the complex formation constants for FeCl+ and $FeCl_2$(aq) from Zhao and Pan (2001). Based on UV spectroscopic measurements, they assigned the tetrahedral complex $FeCl_4^{2-}$ to the (moving) Peak around 265 nm and concluded that this complex occurs in significant concentrations already at 60°C. According to Vogel Koplitz et al. (1987) $FeCl_4^{2-}$ is detectable already at 25°C and 6 mol/kg LiCl in D_2O.

Other spectroscopic investigations of Fe(II) chloro complexation worked with considerably lower chloride concentrations and did not find complexes beyond $FeCl_2$(aq) (Susak and Crerar 1985, Heinrich and Seward 1990, Palmer and Hyde 1993)

In our measurements, even at 80°C and 16.1 mol/kg LiCl there is no indication of a third complex species beyond $FeCl_2$(aq).

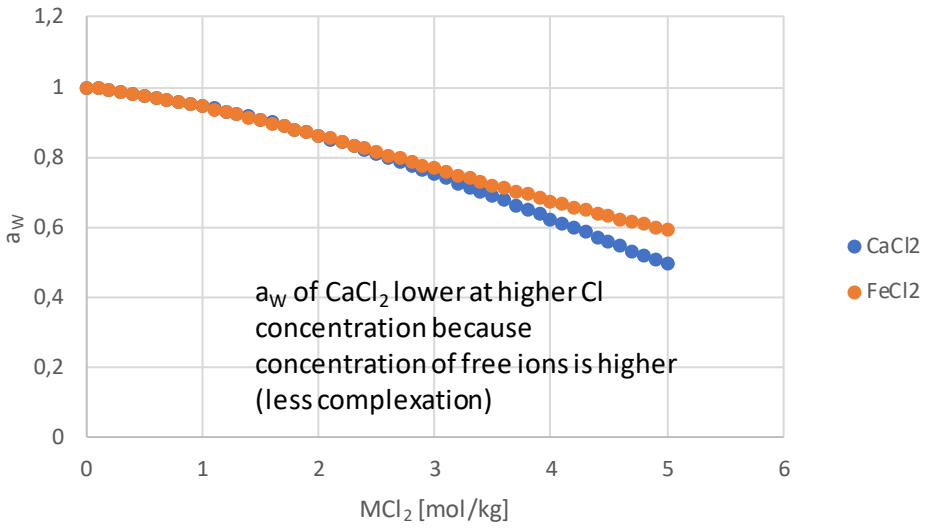

Fig. 6.17 Water activity of $FeCl_2$ and $CaCl_2$ at 25°C

6.5 Determination of ion interaction coefficients and complex formation constants

Based on the assumptions regarding the activity coefficients of Fe^{2+} and $FeCl^+$, a complex formation constant for the reaction

$Fe^{2+} + Cl^- \rightarrow FeCl^+$

was estimated at 25°C. For the aqueous solutions of NaCl, KCl and $MgCl_2$, it amounted to approximately log β_1=-0.9. As all measuring solutions contained perchlorate it was necessary to include model parameters for the interaction of perchlorate with the major ions and iron species. These were taken from May et al. (2011), Hagemann et al. (2015) and other sources (Tab. 6.1). For the ternary system $MgCl_2$-$Mg(ClO_4)_2$-H_2O neither interaction parameters nor experimental data were available. It was assumed that the system obeys the Zdanovskii rule (straight isoactivity lines) so that ternary interaction parameters could be calculated from a plot of synthetic data between two solutions of equal water activity (4 m $MgCl_2$ and 4.71 m $Mg(ClO_4)_2$).

Neither interaction coefficients nor thermodynamic data for $Fe(ClO_4)_2$ solutions were available. In lack of other options, it was assumed the interaction coefficients for $Ca(ClO_4)_2$ apply to $Fe(ClO_4)_2$ as well. The situation was even more complicated for the interaction between $FeCl^+$ and ClO_4^-. No suitable analogue was found and no experimental data that could be applied to our situation. Instead, the parameters $\beta^{(0)}$ and $\beta^{(1)}$ were estimated using the method of Simoes et al. (2016). The method works exclusively based on charge and ionic radius and provides reasonable estimation for Pitzer coefficients. In the first step, the ionic radius of $FeCl^+$ had to be estimated. Using the method in Simoes et al. (2017) we calculated 1.71 Å. This resulted in the interaction coefficients shown in Tab. 6.1. Although this guess may be rough the effect of low perchlorate concentrations (max. 0.1 mol/kg) on the activity coefficient of $FeCl^+$ is rather low as other ions are present in much greater concentration when the complex occurs.

Using the program Wotan (Hagemann et al. 2015), Pitzer interaction coefficients for $FeCl^+$ in NaCl, KCl and $MgCl_2$ solutions were calculated (**Tab. 6.2**). It was not possible to determine the parameter $C^{\varphi}_{FeCl+\ Cl-}$ next to $\Psi_{FeCl+\ Mn+\ Cl-}$ or $\theta_{FeCl+\ Mn+}$ in combination with to $\beta^{(0)}$ and $\beta^{(1)}$, because these parameters correlate in solutions with Fe(II) as trace element. In the same way, it was not possible to optimize the interaction parameters for Fe^{2+}, Cl^- although this would be highly desirable. Making the activity coefficients for this ion pair variable directly causes new mathematical correlations that would make the optimization very unstable.

In the following step, the complexing constant β_1 was varied and the parameters optimized again until the error sum of squares became minimal. This occurred at log β_1 = -1.33. However, the final binary interaction coefficient $\beta^{(1)}$ has a negative value (about -1.7) and the calculated activity coefficient of $FeCl^+$ was often lower than that of Fe^{2+}. Principally, it is possible to select a different combination of complex formation

constant and interaction coefficients that still performs well in predicting the observed experimental properties. But there is no way to select the 'right' combination without arbitrary assumptions.

The calculated complex formation constant at 25°C differs significantly from previously published constants. A selection of published values is shown in **Tab. 6.3**. For a more comprehensive overview, one might refer to the NEA review on iron (Lemire et al. 2013). Interestingly, the authors of the NEA review were confronted with the same challenge. Using the isopiestic measurements of $FeCl_2$ solutions by Moog et al. (2004) they derived a complex formation constant of $\log \beta_1 = -2.05$. We strongly object the idea of deriving speciation and species activity coefficients from a single colligative solution property (here, water activity, the same problem occurs with potentiometric measurements at high ionic strengths) because fatal correlation between the derived complex formation constants and ion interaction coefficients is inevitable. Without spectroscopic data on speciation, it is not possible to establish a sound chemical model that is the necessary basis for deriving a thermodynamic model that described the activity of the occurring species.

But the outlined procedure shows that the formation of weak complexes at high ionic strengths can be described by different sets of complex formation constants in combination with a certain ion activity model. Therefore, our value of $\log \beta_1 = -1.33$ is not out of range, but just one flavour in a field of possibilities.

Only in two solutions with high $MgCl_2$ concentration $FeCl_2$(aq) was detected. The complex occurred in a region where the spectra deconvolution is difficult because of spectral pollution of single species spectra. Our evaluation is only preliminary and leads to a formation constant of about $\log K_2 = -3.9$ ($\log \beta_2 = -5.2$) if the activity coefficients of $FeCl_2$(aq) are assumed to be unity. The value needs to be confirmed by additional measurements and evaluation of data at 40 to 80°C.

Tab. 6.1 Pitzer interaction coefficients considered as given (25°C)

Ion pair/ triple	$\beta^{(0)}$	$\beta^{(1)}$	C^{φ}	θ	Ψ	Source
Na^+ ClO_4^-	0.05704	0.2801	-0.0007192			1
Mg^{2+} ClO_4^-	0.4961	2.009	0.003387			4
$Fe(ClO_4)_2$	0.4638	1.7616	-0.00070598			2
Cl^- ClO_4^-				0.04731		1
Na^+ Cl^- ClO_4^-					-0.007384	1
Mg^{2+} Cl^- ClO_4^-					-0.01285	5
Fe^{2+} Cl^-	0.3065	1.708	0.002224			3
Na^+ Fe^{2+} Cl^-				0.05813	-0.001095	3
K^+ Fe^{2+} Cl^-				0.1156	-0.04319	3
Mg^{2+} Fe^{2+} Cl^-				-0.01803	-0.01178	3

Sources: 1:Hagemann et al. (2015), 2: This work, based on coefficients for $Ca(ClO_4)$ in May et al. (2011), 3: This work, parameters for Ca^{2+} in the THEREDA database, 4: May et al. (2011), 5: This work, based on artificial date (Zdanovskii plot),

Tab. 6.2 Determined Pitzer interaction coefficients (25°C)

Parameter	value	α
$\beta^{(0)}$ ($FeCl^+$, Cl^-)	0.239429	
$\beta^{(1)}$ ($FeCl^+$, Cl^-)	-1.72777	$\alpha^{(1)}$ ($FeCl^+$, Cl^-)=2
Ψ ($FeCl^+$, Na^+, Cl^-)	-0.00287987	
Ψ ($FeCl^+$, K^+, Cl^-)	-0.0430964	
Ψ ($FeCl^+$, Mg^{2+}, Cl^-)	-0.0313789	

Tab. 6.3 Complex formation constant β_1 for the reaction $Fe^{2+} + Cl^- \rightarrow FeCl^+$ at 25°C

log β_1	Analytical method	Activity model	Source
-0.125	UV	Extended Debye-Hückel	Palmer and Hyde (1993)
-0.16	UV	HKF	Heinrich and Seward (1990)
-0.425	UV	Pitzer	Zhao and Pan (2001)
-0.506	NIR	Pitzer	Zhao and Pan (2001)
-0.366	UV, NIR	Pitzer, average	Zhao and Pan (2001)
-0.5		HKF	Testemale et al. (2009) from Zhao and Pan (2001)
-1.33	UV	Pitzer	This work

The ion interaction parameters allow a reliable calculation of the speciation in the considered concentration range. Only at the highest $MgCl_2$ concentrations, there is a small deviation (Fig. 6.18, Fig. 6.19). At discussed above, the species spectra of $FeCl^+$, and possibly $FeCl_2(aq)$ probably include spectral features of Fe^{2+} and $FeCl^+$, respectively. Using the derived thermodynamic speciation model, it should be possible to adjust the species concentration matrix in the evolving factor analysis process to remove or at least to minimize the spectral pollution of single species spectra. This would be an iterative process that needs to be implemented in the program WOTAN.

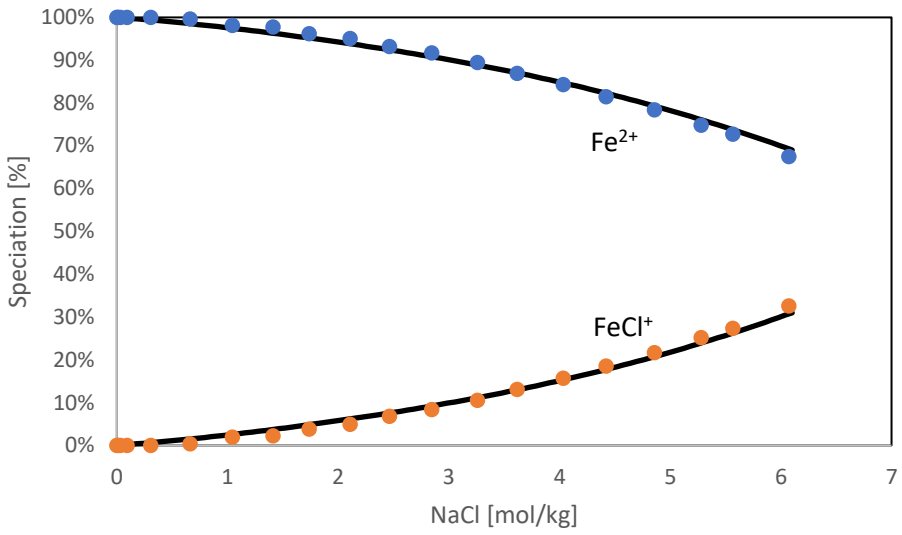

Fig. 6.18 Speciation of Fe(II) in NaCl solutions at 25°C

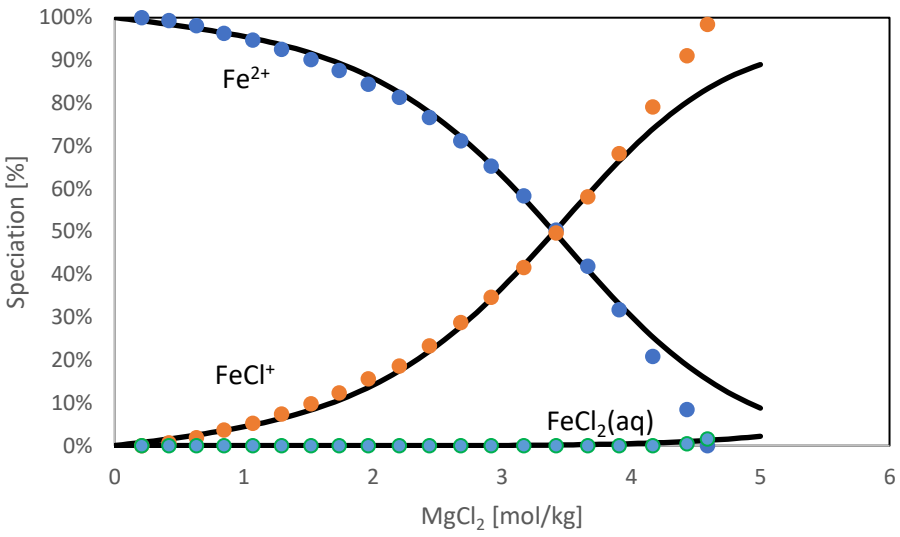

Fig. 6.19 Speciation of Fe(II) in $MgCl_2$ solutions at 25°C

The next step was to test the parameter set with binary aqueous solutions of $FeCl_2$. In this system, specific interactions between different iron species (Fe^{2+} and $FeCl^+$) may occur. No information is available on the speciation in pure $FeCl_2$ solutions so that in the first approach no such interactions could be considered. Water activities were calculated up to a total iron concentration of 5.1 mol/kg. They were recalculated into apparent osmotic coefficients[3] to allow for a simple comparison with literature values. Apparent os

Up to a concentration of 4 mol/kg calculated and experimental values correspond surprisingly well. At higher iron concentrations, a gap occurs. But even the at highest concentration the difference is only 0.08 in ϕ (Fig. 6.20). According to the calculation, in nearly saturated $FeCl_2$ solutions almost only $FeCl^+$ occurs so that specific interactions between $FeCl^+$ and Fe^{2+} cannot be the cause of the deviations. Rather, the interaction coefficients between $FeCl^+$ and Cl^+ need to be adjusted. Further work will be necessary to determine the speciation of iron(II) in binary solutions, but for the time being the model is sufficiently satisfactory.

Based on the current model and a saturation concentration of 5.11 mol/kg (Moog and Hagemann 2004) a solubility constant of log K = 2.91 was determined for $FeCl_2 \cdot 4H_2O$.

[3] Apparent osmotic coefficients are calculated from water activities by assuming full dissociation of $FeCl_2$.The real osmotic coefficients would consider the actual speciation that is a-prior unknown for vapor pressure measurements.

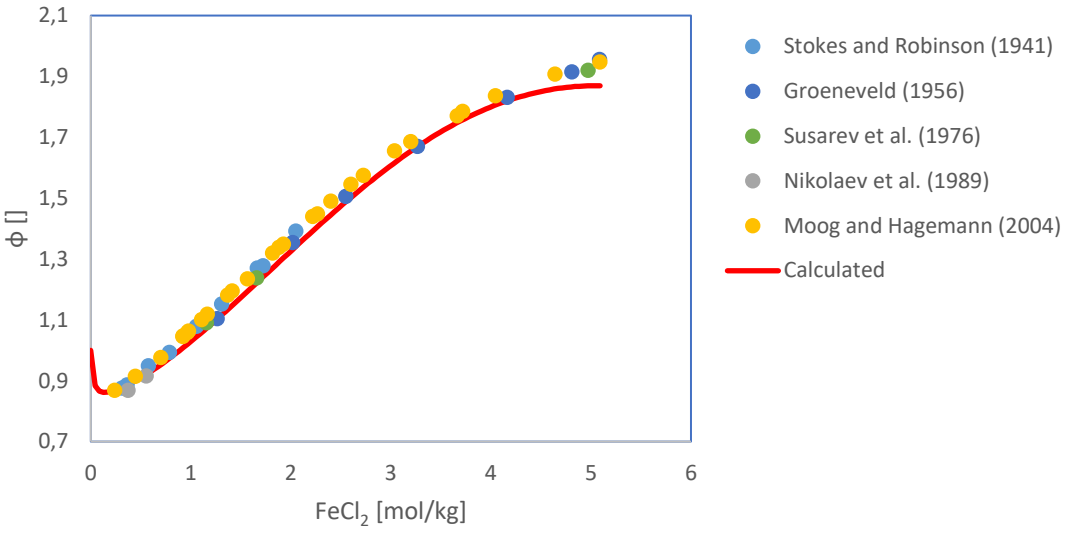

Fig. 6.20 Calculated and literature values for the apparent osmotic coefficient of $FeCl_2$ solutions at 25°C.

In the next step the phase equilibria in saturated solution systems $FeCl_2$-NaCl-H_2O and $FeCl_2$-KCl-H_2O were evaluated. For this purpose, Geochemist's Workbench was used. Although no additional parameters were determined and Fe(II) is no longer only a trace component in these systems, experiment and modelling are in a good agreement up to highest concentrations. In the system $FeCl_2$-NaCl-H_2O experimental and calculated solubilities agree perfectly (Fig. 6.21). In the system $FeCl_2$-KCl-H_2O, the agreement was very good up to 2 mol/kg $FeCl_2$. At higher $FeCl_2$ concentrations the calculated values were slightly lower (Fig. 6.22). This applied to the sylvite as well as to the $FeCl_2 \cdot 4H_2O$ branch of the solubility system. Consequently, the calculated invariant point KCl(cr)/ $FeCl_2 \cdot 4H_2O$(cr)/ saturated solution lies in some distance to the experimental values. On the other hand, Moog and Hagemann (2004) could not calculate the invariant point at all because the predicted branches of sylvite and $FeCl_2 \cdot 4H_2O$ did not cross. In this regard, the new dataset elaborated in this study is more robust.

The unusual value for $\beta^{(1)}$ ($FeCl^+$, Cl^-) shows that some further work is necessary to produce a model that is in line with other observations in chloride systems. Due to the weak spectral absorptivity of Fe(II) species, it is possible to investigate concentrated $FeCl_2$ solutions as well. Such measurements would allow to include water activity and solubility measurements in the evaluation. This would also open an independent way to estimate the ion interaction coefficients of free Fe^{2+}.

Because of these considerations, we decided not to further evaluate the measurements at 40, 60, 80°C.

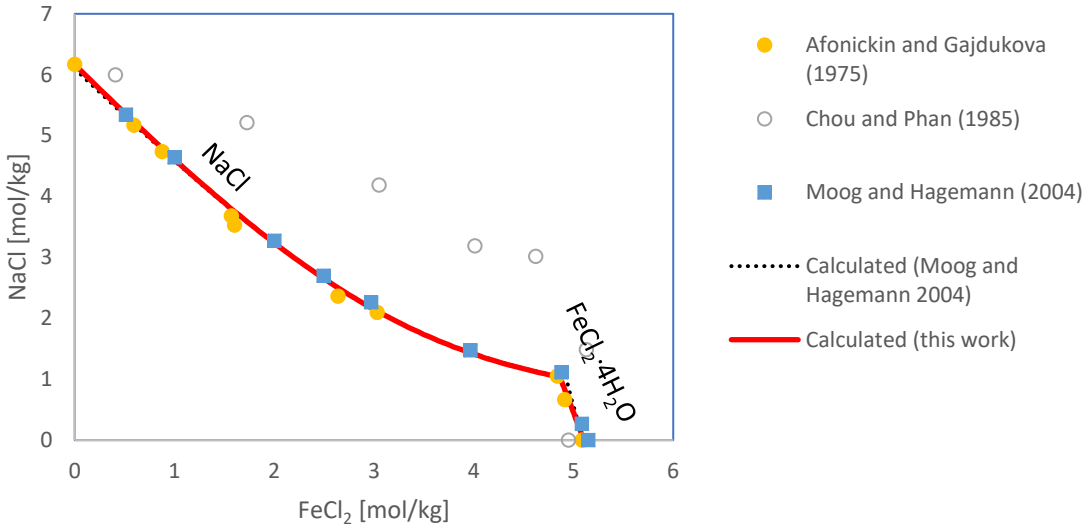

Fig. 6.21 Phase equilibria in the system $FeCl_2$-NaCl-H_2O at 25°C

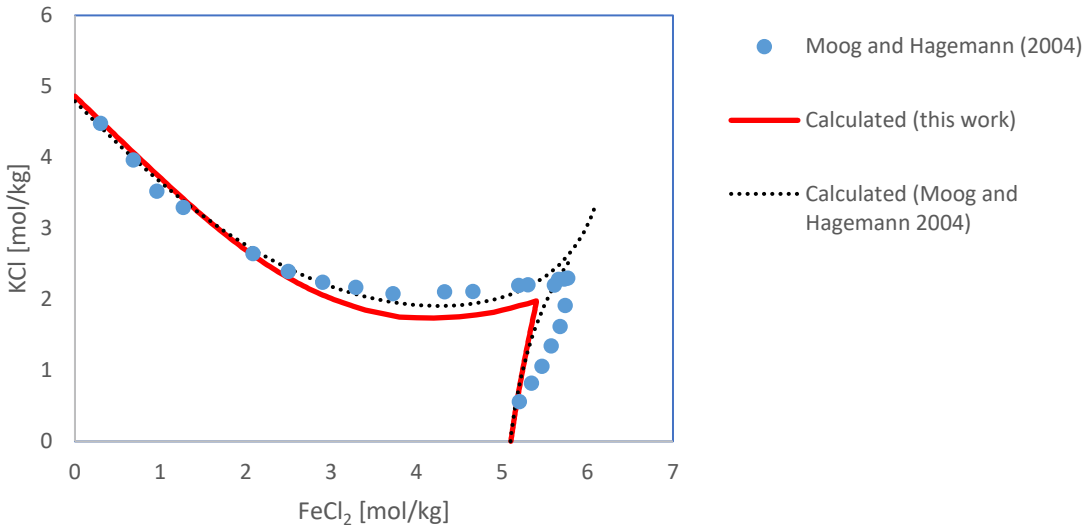

Fig. 6.22 Phase equilibria in the system $FeCl_2$-KCl-H_2O at 25°C

7 Summary and conclusions

The redox state in the near-field of a repository has a significant impact on the solubility of radionuclides. It is usually expressed as the redox potential, which is determined by potentiometric measurement with a cell consisting of a platinum electrode and a silver, silver chloride reference electrode. However, in saline solutions, these measurements lead to systematic deviations that cannot be quantified by thermodynamic means. Based on previous work, a two-step computational method was developed which allows to convert the primary potentiometric measurement into a concentration ratio of two redox-sensitive species and then into an alternative measure of the redox status.

The method was derived from systematic measurements of the redox potential in mixed solutions of hexacyanoferrate (II) and hexacyanoferrate (III) in solutions of the salts NaCl and $MgCl_2$. This allowed an empirical relationship to be established between the redox potential, the salt concentration (NaCl or $MgCl_2$) and the known mixing ratio of the hexacyanoferrate. This relationship can also be applied to solutions that do not contain hexacyanoferrate but other redox-sensitive substances. The calculated mixing ratio of the hexacyanoferrate is already an alternative measure for the redox state. However, the ratio is rather unusual and may be converted into a more common measure. The negative logarithm of the partial pressure of oxygen pO_2, for example, is suitable for this purpose.

The conversion from the mixing ratio to the oxygen partial pressure requires, in addition to the measurable hydrogen concentration (pcH), a model to describe the activity coefficients of hexacyanoferrate ions in NaCl and $MgCl_2$ solutions. For this purpose, literature data were collected and evaluated, but for all relevant binary and ternary systems, additional data were necessary. For these systems, notably $Na_4Fe(CN)_4$-H_2O, $Na_3Fe(CN)_6$-H_2O, $Mg_2Fe(CN)_6$-H_2O, $Mg_3[Fe(CN)_6]_2$-H_2O, $Na_4Fe(CN)_4$-NaCl-H_2O, $Na_3Fe(CN)_6$-NaCl-H_2O, $Mg_2Fe(CN)_6$-$MgCl_2$-H_2O, $Mg_3[Fe(CN)_6]_2$-$MgCl_2$-H_2O isopiestic measurements were performed to obtain vapour pressure data at 25, 40 and 60°C. Some solubility measurements were performed at 25, 40 and 60°C. The measurements, in combination with literature data, served as a basis to derive a Pitzer model for binary and ternary systems. For systems with sodium hexacyanoferrates, this model can reliably describe the activity coefficients. For magnesium-containing systems, this is only partially possible. Apparently, a strong complex formation between Mg^{2+} and hexacyanoferrates had a significant effect.

This effect was particularly strong between Mg^{2+} and $Fe(CN)_6^{4-}$. As a consequence, the binary system $Mg_2Fe(CN)_6$-H_2O was difficult to describe and the ternary system $Mg_2Fe(CN)_6$-$MgCl_2$-H_2O could be represented by the model only in parts only to a limited extent. Here, either further measurements are necessary to quantitatively describe the complex formation or investigations with another redox pair in which the difficulties mentioned do not occur.

Under strongly reducing conditions, such as those that occur during corrosion of steel in the final layer, dissolved iron practically only occurs in the oxidation state +II. From earlier work, it was known that concentrated chloride solutions lead to complex formation between Fe^{2+} and Cl^-. This was probably one of the reasons why the modelling of solubility systems such as KCl-$FeCl_2$-H_2O was not satisfactory so far. A model for the quantitative description of the complex formation of Fe^{2+} with chloride in solutions of NaCl, KCl and $MgCl_2$ was missing until now. UV-spectrophotometric measurements were performed to investigate the complex formation in these solutions as well as in LiCl solutions at 25 to 80°C. The spectra obtained were deconvoluted into single-species spectra by a factor analysis method. At the same time, the concentrations of individual species were determined. It was found that at 25°C and a chloride concentration of about 1 mol/kg the first complex became significant. The composition $FeCl^+$ could be assigned to this complex. A second complex could be detected at chloride concentrations higher than 8 mol/kg. It was identified to be $FeCl_2$(aq). Further complexes could not be detected up to a chloride concentration of 16 mol/kg (in LiCl solutions) even at 80°C.

For the complex $FeCl^{+,}$ a formation constant and Pitzer coefficients for the interaction with the ions Cl^-, Na^+, K^+ and Mg^{2+} were derived at 25°C. With their help, it was possible to describe the observed speciation very well for most of the chloride concentration range. Small deviations at the highest chloride concentrations were an indication that the calculated single species spectra for $FeCl^+$ (and possibly for $FeCl_2$(aq) as well) probably contained spectral features of the preceding species Fe^{2+} and $FeCl^+$, respectively, as well. Some adjustments for factor analysis process are proposed to eliminate or at least to reduce the spectral ‘pollution’ of single species spectra.

The model was then applied to describe the osmotic coefficients of pure $FeCl_2$ solutions (up to 5 mol/kg) and solubilities in the systems NaCl-$FeCl_2$-H_2O and KCl-$FeCl_2$-H_2O. Although the iron concentrations occurring in these systems are much higher than in the photometric measurements and interactions between different iron species become relevant, the agreement between calculated and observed solubilities is surprisingly good.

Although the performance of the model was satisfactory, the unusual value of one ion interaction coefficient for $FeCl^+$ and the deviation of the calculated complex formation constant from literature values showed that the model should be treated with some care. Additional scientific efforts are needed to improve the spectra deconvolution procedure and to reveal the Fe(II) speciation in solutions with higher iron concentrations. This would open a way for an independent estimation of ion interaction coefficients for Fe^{2+}, $FeCl^+$ and possibly $FeCl_2(aq)$ that cannot be determined from solutions where Fe(II) is only a trace component.

Similar measurements were conducted for Fe(II) in sulphate solutions but even in solutions of highest sulphate concentrations, the spectra changed very little so that it was not possible to quantify the complexation.

8 References

Adie, R. H. (1891) On the osmotic pressure of salts in solution. J. Chem. Soc. 59, p. 344–372.

Akerlof, G. (1937) A study of the composition of the liquid phase in aqueous systems containing strong electrolytes of higher valence types as solid phases. J. Phys. Chem. 41, p. 1053–1076.

Aruga, R. (1982) Solute-solvent interactions in the association of hexacyanoferrate(III) with group II A cations. A calorimetric study. Can. J. Chem. 60, p. 1828–1831.

Bedford, T. G. (1910) The depression of freezing point in very dilute aqueous solutions. Phil. Trans. Royal. Soc. A (London) 83, p. 454–461.

Berkeley, E. o.; Hartley, E. G. J.; Stephenson (1916) Further determinations of direct osmotic pressures. Proc. Royal Soc. (London) A 92, p. 477–492.

Berkeley, E. o.; Hartley, E. G. J.; Stephenson, J. (1909) On the osmotic pressures of aqueous solutions of calcium ferrocyanide. Part II. Weak solutions. Phil. Trans. Royal. Soc. (London) 209, p. 319–336.

Bette, A. (1837) Ueber einige Cyanverbindungen. Liebigs Ann. 23, p. 115–132.

Bischofer, B.; Hagemann, S.; Altmaier, M.; Banik, N.; Bosbach, D., Bracke, G.; Brendler, V. et al. (2016) Behaviour of long-lived fission and activation products in the near-field of a nuclear waste repository and the possibilities of their retention (GRS-Bericht, 374).

Bovalini, E.; Fabris, E. (1933) Il sistema ternario $K_4Fe(CN)_6$+K_2SO_4+H_2O. Gazz. Chim. Ital. 63, p. 338–344.

Bovalini, E.; Fabris, E. (1937) Tensione del vapor d'acqua del ferrocianuro potassico idrato e delle sue soluzioni sature a varie temperature. Gazz. Chim. It. 67, p. 802–807.

Bretti, C.; Foti, C.; Porcino, N. (2006) SIT parameters for 1:1 electrolytes and correlation with Pitzer coefficients. J. Solution Chem. 35, p. 1401–1415.

Capone, S.; Robertis, A. d.; Sammartano, S.; Rigano, C. (1986) Studies on hexacyanoferrate(II) complexes. Formation constants for alkali metal, ammonium and calcium(II) complexes at different temperatures and ionic strengths in aqueous solution. Thermochim. Acta 102, p. 1–14.

Cappellina, F.; Bubani, B. (1954) Ricerche sull´acqua di cristallizzanzione nei ferrocianuri di metalli alcalini ed alcalino-terrosi. Atti Acad. Sci. Istituto Bologna Classe Sci. F 11 (4), p. 76–96.

Cohen, S. R.; Plane, R. A. (1957) The Association of ferrocyanide Ions with various cations. J. Phys. Chem. 61 (8), p. 1096–1100.

Conroy, J. T. (1898) The composition and solubility of sodium ferrocyanide. J. Soc. Chem. Ind. 17, p. 103–106.

Crozes, X.; Blanc, P.; Cote, G.; Moisy, P. (2012) Acid–base properties of the $Fe(CN)_6^{3-}$ / $Fe(CN)_6^{4-}$ redox couple in the presence of various background mineral acids and salts. J. Solution Chem. 41 (3), p. 503–515.

Dehury, S. D.; Talukdar, M.; Dash, U. N. (2012) Studies on ion association and solvation of multi-charged electrolytes (potassium ferricyanide and ferrocyanide) in aqueous and aqueous D-fructose mixtures at different temperatures. J. Chem. Pharm. Res. 4, p. 1619–1624.

Domingo, P. L.; García, B.; Leal, J. M. (1990) Acid–base behaviour of the ferricyanide ion in perchloric acid media. Spectrophotometric and kinetic study. Can. J. Chem. 68 (2), p. 228–235.

Eaton, W.; George, P.; Hanania, G. I. H. (1967) Thermodynamic aspects of the potassium hexacyanoferrate(III)-(II) system I. Ion association. J. Phys. Chem. 71, p. 2016–2021.

Fabris, E. (1921) Solubilità in acqua del ferrocianuro potassico Curvaghiaccio e punto crioidratico. Gazz. Chim. It. 51 II, p. 374–380.

Fabris, E. (1931) Indagini relative as un eventuale punto di trasformazione del ferrocianuro potassico. Gazz. Chim. Ital. 61, p. 527–537.

Fabris, E. (1932) Ulteriori indagini sulla solubilità del ferrocianuro di potassico. Gazz. Chim. Ital. 62, p. 909–912.

Farrow, M. (1926) The solubilities of sodium, potassium, and calcium ferrocyanides. Part I. J. Chem. Soc. 129, p. 49–55.

Farrow, M. (1927) The system calcium ferrocyanide-sodium ferrocyanide-water. Part II. J. Chem. Soc., p. 1153–1158.

Fleysher, N. A.; Osokoreva, N. A. (1935a) Izuchenie rastvorimosti v sisteme $Na_4Fe(CN)_6$ - NaCl - H_2O pri t=80°. Sb. Tr. Inst. Prikl. Chim. 26, p. 38–47.

Fleysher, N. A.; Osokoreva, N. A. (1935b) Soljanye ravnovesiya v vodnych rastvorach zhelezistosinerodistovo, chloristogo, uglekislogo i sernokislogo natriya pri t=25°. Sb. Tr. Inst. Prikl. Chim. 26, p. 23–38.

Friend, J. A. N.; Smirles, W. N. (1928) The solubility of potassium ferricyanide in water between 0° and 100°. J. Chem. Soc., p. 2242–2245.

Friend, J. A. N.; Townley, J. E.; Vallance, R. H. (1929) The solubility of sodium ferricyanide in water between 0° and 104°. J. Chem. Soc., p. 2326–2330.

Gampp, H.; Maeder, M.; Meyer, C. J. (1986) Calculation of equilibrium constants from multiwavelength spectroscopic data - IV. Model-free least squares refinement by use of evolving factor analysis. Talanta 33, p. 943–951.

Gibby, C. W.; Monk, C. B. (1952) The dissociation constants of the alkaline earth ferricyanides. Trans. Faraday Soc. 48, p. 632.

Guthrie, F. (1878) On salt solutions and attached water. Phil. Mag. J. Sci. [5] 6, p. 35–44.

Hagemann, S. (2012) Entwicklung eines thermodynamischen Modells für Zink, Blei und Cadmium in salinaren Lösungen. GRS-Bericht 219.

Hagemann, S.; Bischofer, B.; Scharge, T. (2014) Entwicklung von Methoden und Modellen zur Bestimmung des Redoxpotentials salinarer Lösungen. GRS-Bericht 260.

Hagemann, S.; Moog, H. C.; Herbert, H.-J. (2012) Rückhaltung und thermodynamische Modellierung von Iod und Selen in hochsalinaren Lösungen. GRS-Bericht 245, p. 167.

Hagemann, S.; Schönwiese, D.; Scharge, T. (2015) Werkzeuge und Daten für die Geochemische Modellierung - Thermodynamische Daten für Schwefelspezies und Hintergrundsalze sowie Tools zur Unsicherheitsanalyse. GRS-Bericht 373.

Hanania, G. I. H.; Irvine, D. H.; Eaton, W. A. (1967) Thermodynamic aspects of the potassium hexacyanoferrate(III)-(II) system. II. Reduction potential. J. Phys. Chem. 71, p. 2022–2030.

Harkins, W. D.; Pearce, W. T. (1916) The effect of salts upon the solubility of other salts. VIIIb. The solubility relations of some extremely soluble salts. J. Am. Chem. Soc. 38, p. 2714–2717.

Haung, H. -H. (1989) Estimation of Pitzer's ion interaction parameters for electrolytes involved in complex formation using a chemical equilibrium model. J. Solution Chem. 18 (11), 1069-.

Hedwig, G. R.; Watson, I. D. (1981) A microcalorimetric study of the association of hexacyanoferrate(II) ions with calcium and magnesium ions in aqueous solution. J. Solution Chem. 40, 411-418, 596-597.

Heinrich, C. A.; Seward, T. M. (1990) A spectrophotometric study of aqueous iron (II) chloride complexing from 25 to 200°C. Geochim. Cosmochim. Acta 54, p. 2207–2221.

Hepler, L. G.; Sweet, J. R.; Jesser, R. A. (1960) Thermodynamics of aqueous ferricyanide, ferrocyanide and cobalticyanide ions. J. Am. Chem. Soc. 82, p. 304–306.

Hummel, W.; Berner, U.; Curti, E. (2002) NAGRA / PSI Chemical Thermodynamic Data Base 01/01. Nagra, Technical Report 02 (16).

Jackman, F. A.; Lister, M. W. (1975) The association of hexacyanoferrate(II) ions and group IIA cations. J. Solution Chem. 4, p. 1023–1031.

James, J. C.; Monk, C. B. (1950) The conductivities of potassium and lanthanum cobalticyandes and ferricyanides. Trans. Faraday Soc. 46, p. 1041.

Jiménez-Gallegos, J.; Roque, J.; Yee-Madeira, H.; Reguera, E. (2012) Mg3[M(CN)6]2·xH2O with M = Fe, Co: Synthesis, crystal structure, and hydrogen sorption. Z. Anorg. Allg. Chem. 638 (7-8), p. 1146–1150.

Jones, H. C. (1906) Die annähernde Zusammensetzung der Hydrate, welche von verschiedenen Elektrolyten in wässriger Lösung gebildet werden. Z. Phys. Chem. 55, p. 385–434.

Jordan, J.; Ewing, G. J. (1962) The Protonation of hexacyanoferrates. Inorg. Chem. 1, p. 587–591.

Katila, T.; Leskelä, M.; Niinistö, L.; Riski, K. J.; Valkonen, J.; Ylä-Jääski, J. (1980) Crystal structure and Mössbauer measurements of monoclinic sodium hexacyanoferrate(III) dihydrate. J. Solid State Chem. 35 (3), p. 341–346.

Kistiakowsky, W. (1890) Die wässerigen Lösungen von Doppelsalzen. Z. Phys. Chem. 6, p. 97–120.

Klenk, H.; Griffith, A.; Huthmacher, K.; Itzel, H.; Knorre, H.; Voigt, C.; Weiberg, O. (1987) Cyano compounds, inorganic (Ullmann's Encyclopedia of industrial chemistry 5th ed, A8), 159-p.

Kolthoff, I. M.; Tomiscek, W. J. (1935) The oxidation potential of the system potassium ferrocyanide-potassium ferricyanide at various ionic strengths. J. Phys. Chem. 39, p. 945–954.

Krulic, D.; Fatouros, N.; Khoshtariya, D. E. (1998) Kinetic data for the hexacyanoferrate (II)/(III) couple on platinum electrode in various chlorides of monovalent cations. J. Chem. Phys. 95, p. 497–512.

Kunze, N. (2004) Vorkommen, Speziesverteilung und Transportverhalten von Cyaniden im Grundwasser des Testfeldes Süd (Diss. Univ. Heidelberg).

Laliberté, M.; Cooper, W. E. (2004) Model for Calculating the Density of Aqueous Electrolyte Solutions. J. Chem. Eng. Data 49 (5), p. 1141–1151.

Lange, E.; Miederer, W. (1956) Integrale Verdünnungswärmen wäßriger Lösungen von K_3FeCy_6, K_4FeCy_6 und $NiSO_4$ bei 25°C. Z. Elektrochem. 60, p. 34–36.

Lange, E.; Secrest, D. (1957) Integrale Lösungswärmen wäßriger Lösungen von $Na_3Fe(CN)_6$ bei 25°C. Z. Elektrochem. 61, p. 280–281.

Langer, E.; Miederer, W. (1956) Integrale Verdünnungswärmen wäßriger Lösungen von $La(NO_3)_3$, $Ba_3(FeCy_6)_2$,Mg_2FeCy_6 und $LaFeCy_6$. Z. Elektrochem. 60, p. 362–364.

Lemire, R. J.; Berner, U.; Musikas, C. (2013) Chemical Thermodynamics of iron Part I (Chemical Thermodynamics, 13a), 1082p.

Lemire, R. J.; Lister, M. W. (1976) Conductivity measurements and relative association constants of some 3. 1 electrolytes. J. Solution Chem. 5 (3), p. 171–181.

Liu, W.; Etschmann, B.; Foran, G.; Shelley, M.; Brugger, J. (2007) Deriving formation constants for aqueous metal complexes from XANES spectra: Zn2+ and Fe2+ chloride complexes in hypersaline solutions. Am. Mineral. 92 (5-6), p. 761–770.

Malatesta, F.; Giacomelli, A.; Zamboni, R. (1994) Activity coefficients of electrolytes from the emf of liquid membrane cells. III: $LaCl_3$, $K_3Fe(CN)_6$, and $LaFe(CN)_6$. J. Solution Chem. 23, p. 11–36.

Malatesta, F.; Giacomelli, A.; Zamboni, R. (1996) Activity coefficients from the emf of liquid membrane cells V. Alkaline earth hexacyanoferrates(III) in aqueous solutions at 25°C. J. Solution Chem. 25, p. 61–73.

Masłowska, J. (1967) Mieszane kompleksy żelaza(III). IV. Badanie układu $Fe(ClO_4)_3$-NaBr-Na_2SO_4-H_2O. Roczn. Chem. 43, p. 1857–1866.

May, P. M.; Rowland, D.; Hefter, G. (2011) A generic and updatable Pitzer characterization of aqueous binary electrolyte solutions at 1 bar and 25°C. J. Chem. Eng. Data 56, p. 5066–5077.

Mironov, V. E.; Rutkovskii, Y. I. (1966) Ferricyanide complexes of sodium, potassium, cesium, magnesium, strontium, and barium. Zh. Neorg. Khim. 11, p. 1792–1797.

Moog, H. C.; Hagemann, S. (2004) Thermodynamische Modellierung hochsalinarer Lösungen. GRS-Bericht 195.

Moog, H. C.; Hagemann, S.; Rumyantsev, A. V. (2004) Isopiestic Investigation of the Systems $FeCl_2$ –(Na, K, Mg, Ca)Cl_n –H_2O at 298.15 K. Z. Phys. Chem. 218, p. 1063–1087.

Neumark, H. R. (1944) Electrostatic preparation of sodium ferricyanides. Anmeldenr: US 2,353,782.

Nordstrom, D. K. (1977) Thermochemical redox equilibria of ZoBell's solution. Geochim. Cosmochim. Acta 41, p. 1835–1841.

Noyes, A. A.; Johnston, J. (1909) The conductivity and ionization of polyionic salts. J. Am. Chem. Soc. 31, p. 987–1010.

Palmer, D. A.; Hyde, K. E. (1993) An experimental determination of ferrous chloride and acetate complexation in aqueous solutions to 300°C. Geochim. Cosmochim. Acta 57, p. 1393–1408.

Pitzer, K. S. (1991) Activity coefficients in electrolyte solutions. 2nd ed: CRC Press, Boca raton.

Regner, A.; Baley, J. (1957) Löslichkeitsdiagramm des Systems $K_3[Fe(CN)_6]$-$K_4[Fe(CN)_6]$-H_2O. Coll. Czech. Chem. Comm. 22, p. 1684.

Reindel, F. (1867) Ueber einige Ferrocyanid- und Ferrocyanür-Verbindungen. J. Prakt. Chem. 102 (1), p. 43–46.

Robertis, A. d.; Rigano, C.; Sammartano, S. (1984) Studies on hexacyanoferrate(II) complexes. Potentiometric determination of protonation constants in Li^+, Na^+, K^+, NH_4^+ and Ca^{2+} chloride media and K^+ formations constants, in aqueous solution at 25°C, using H^+-glass and potassium ion selective electrodes. Ann. Chim. (Rome) 74, p. 33–39.

Robertson, C.; La Mer, V. K. (1931) A critical study of precision cryoscopy: the freezing-point depressions of potassium cobalticyanide and potassium ferricyanide. J. Phys. Chem. 35, p. 1953–1984.

Robinson, R. A. (1937) The Osmotic and Activity Coefficient Data of Some Aqueous Salt Solutions from Vapor Pressure Measurements. J. Am. Chem. Soc. 59, p. 84–90.

Robinson, R. A.; Levien, B. J. (1946) The vapour pressures of potassium ferricyanide and thorium nitrate solutions at 25°C. Trans. Roy. Soc. New Zeal. 76, p. 295–299.

Romankiw, L. A.; Chou, I. M. (1983) Densities of Aqueous NaCl, KCl, $MgCl_2$, and $CaCl_2$ binary solutions in the concentration range 0.5-6.1 m at 25, 30, 35, 40, and 45 °C. J. Chem. Eng. Data 28, p. 300–305.

Rutkovskii, Y. I.; Mironov, V. E. (1967) Stability constants of the hexacyanoferrate(III) association complexes of alkali and alkaline earth metals. Russ. J. Inorg. Chem. 12, p. 1739–1741.

Silvester, L. F.; Rock, P. A. (1973) Activity coefficients of $Na_4Fe(CN)_6$ in water and in $Na_4Fe(CN)_6$(aq) + NaCl(aq) solutions at 25°c. J. Chem. Eng. Data 18, p. 314–316.

Simoes, M. C.; Hughes, K. J.; Ingham, D. B.; Ma, L.; Pourkashanian, M. (2016) Estimation of the Pitzer Parameters for 1–1, 2–1, 3–1, 4–1, and 2–2 Single Electrolytes at 25 °C. J. Chem. Eng. Data 61 (7), p. 2536–2554.

Simoes, M. C.; Hughes, K. J.; Ingham, D. B.; Ma, L.; Pourkashanian, M. (2017) Estimation of the thermochemical tadii and ionic volumes of vomplex ions. Inorg. Chem. 56 (13), p. 7566–7573.

Stefánsson, A. (2007) Iron(III) hydrolysis and solubility at 25°C. Env. Sci. Tech. 41, p. 6117–6123.

Susak, N. J.; Crerar, D. A. (1985) Spectra and coordination changes of transition metals in hydrothermal solutions: implications for ore genesis. Geochim. Cosmochim. Acta 49, p. 555–564.

Tanaka, N.; Kobayashi, Y.; Kamada, M. (1966) Infrared spectroscopic study on ion association of hexacyanoferrate(III) and hexacyanoferrate(II) ions. Bull. Chem. Soc. Jpn. 39 (10), p. 2187–2190.

Testemale, D.; Brugger, J.; Liu, W. (2009) In-situ X-ray absorption study of iron(II) speciation in brines up to supercritical conditions. Chem. Geol. 264, p. 295–310.

Tettamanzi, A. (1933) La solubilità dei ferrocianuri di potassio e di sodio nelle soluzioni acquose di ammoniaca. Gazz. Chim. Ital. 63, p. 575–579.

Vallance, R. H. (1922) The solubility of potassium ferrocyanide. Chem. News 125, p. 7.

Vallance, R. H. (1927) The solubility of potassium ferrocyanide in water at temperatures up to 25° 130, p. 1328–1334.

Vogel Koplitz, L.; McClure, D. S.; Crerar, D. A. (1987) Spectroscopic study of chloroion(II) complexes in LiCl-DCl-D_2O solutions. Inorg. Chem. 26, p. 308–313.

Wagner, W.; Pruss, A. (2002) The IAPWS Formulation 1995 for the Thermodynamic Properties of Ordinary Water Substance for General and Scientific Use. J. Phys. Chem. Ref. Data 31, p. 387–535.

Williams, H. E. (1948) Cyanogen compounds. Their chemistry, detection and estimation. 2nd ed: Edward Arnold & Co, London.

Zhao, R.; Pan, P. (2001) A spectrophotometric study of Fe(II)-chloride complexes in aqueous solutions from 10 to 100°C. Can. J. Chem. 79, p. 131–144.

List of tables

List of figures

9 Annex

9.1 Isopiestic measurements

Tab. 9.1 Water activities of $Na_4Fe(CN)_6$ solutions

T [°C]	Vessel/ Weighing	$Na_4Fe(CN)_6$ [mol/kg]	NaCl [mol/kg]	a_W	ϕ
25	30 / 4	0.100	0.167	0.99444	0.6213
25	29 / 3	0.160	0.261	0.99137	0.6002
25	20 / 2	0.215	0.342	0.98871	0.5866
25	19 / 1	0.307	0.477	0.98430	0.5730
25	18 / 2	0.419	0.639	0.97891	0.5648
25	16 / 1	0.460	0.699	0.97693	0.5634
25	15 / 1	0.527	0.799	0.97359	0.5637
25	14 / 3	0.586	0.889	0.97057	0.5660
40	30 / 6	0.100	0.173	0.99425	0.6403
40	29 / 4	0.158	0.265	0.99125	0.6172
40	20 / 3	0.213	0.346	0.98859	0.5974
40	19 / 3	0.309	0.492	0.98377	0.5886
40	18 / 3	0.415	0.651	0.97845	0.5835
40	16 / 2	0.459	0.719	0.97619	0.5828
40	18 / 4	0.474	0.740	0.97548	0.5810
40	15 / 2	0.522	0.816	0.97291	0.5846
40	14 / 2	0.574	0.898	0.97013	0.5867
60	30 / 7	0.108	0.186	0.99383	0.6349
60	29 / 7	0.170	0.286	0.99056	0.6210
60	20 / 4	0.218	0.359	0.98816	0.6063
60	19 / 5	0.321	0.516	0.98299	0.5931
60	18 / 5	0.466	0.738	0.97553	0.5906
60	16 / 3	0.475	0.758	0.97485	0.5946
60	15 / 3	0.536	0.857	0.97148	0.5991

Tab. 9.2 Water activities of $Na_3Fe(CN)_6$ solutions - I

T [°C]	Vessel/ Weighing	$Na_3Fe(CN)_6$ [mol/kg]	NaCl [mol/kg]	$CaCl_2$ [mol/kg]	a_w	ϕ
25	1 / 1	2.317	5.194		0.79792	1.3520
25	2 / 1	2.162	4.767		0.81736	1.2946
25	3 / 1	1.894	4.042		0.84938	1.1961
25	4 / 1	1.724	3.591		0.86862	1.1340
25	5 / 1	1.485	2.975		0.89384	1.0490
25	6 / 1	1.281	2.475		0.91347	0.9806
25	11 / 1	0.734	1.279		0.95719	0.8278
25	13 / 1	0.558	0.943		0.96872	0.7901
25	15 / 1	0.480	0.801		0.97352	0.7765
25	17 / 1	0.422	0.699		0.97693	0.7681
25	19 / 1	0.293	0.478		0.98423	0.7518
25	20 / 2	0.211	0.344		0.98866	0.7482
25	21 / 1	2.624		2.937	0.75780	1.4665
25	22 / 2	2.814		3.138	0.73320	1.5302
25	23 / 1	3.133		3.463	0.69254	1.6275
25	24 / 2	2.942		3.207	0.72462	1.5194
25	25 / 2	1.046	1.895		0.93522	0.8882
25	29 / 3	0.163	0.261		0.99137	0.7398
25	30 / 4	0.103	0.167		0.99444	0.7481

Tab. 9.3 Water activities of $Na_3Fe(CN)_6$ solutions - II

T [°C]	Vessel/ Weighing	$Na_3Fe(CN)_6$ [mol/kg]	NaCl [mol/kg]	$CaCl_2$ [mol/kg]	a_w	ϕ
40	1 / 3	2.301	5.130		0.80019	1.3441
40	2 / 4	2.184	4.816		0.81434	1.3051
40	3 / 4	1.856	3.936		0.85294	1.1891
40	4 / 4	1.728	3.603		0.86711	1.1452
40	5 / 2	1.482	2.983		0.89263	1.0635
40	6 / 2	1.288	2.511		0.91130	1.0005
40	11 / 2	0.732	1.290		0.95654	0.8426
40	13 / 2	0.562	0.963		0.96790	0.8049
40	15 / 2	0.484	0.818		0.97285	0.7899
40	17 / 3	0.416	0.698		0.97689	0.7803
40	17 / 4	0.436	0.727		0.97592	0.7759
40	19 / 3	0.299	0.494		0.98371	0.7615
40	20 / 3	0.213	0.347		0.98854	0.7524
40	21 / 3	2.316		2.629	0.79791	1.3527
40	22 / 3	2.496		2.822	0.77631	1.4080
40	23 / 3	2.755		3.099	0.74437	1.4871
40	24 / 3	2.946		3.245	0.72705	1.5017
40	25 / 3	1.054	1.934		0.93327	0.9093
40	29 / 4	0.164	0.265		0.99125	0.7448
40	30 / 6	0.108	0.173		0.99425	0.7443

Tab. 9.4 Water activities of $Na_3Fe(CN)_6$ solutions - III

T [°C]	Vessel/ Weighing	$Na_3Fe(CN)_6$ [mol/kg]	NaCl [mol/kg]	$CaCl_2$ [mol/kg]	a_w	ϕ
60	1 / 5	2.357	5.221		0.79695	1.3366
60	2 / 5	2.334	5.193		0.79819	1.3401
60	3 / 5	1.979	4.242		0.83980	1.2242
60	4 / 5	1.807	3.792		0.85897	1.1675
60	5 / 3	1.558	3.121		0.88672	1.0706
60	6 / 3	1.406	2.785		0.90022	1.0374
60	11 / 3	0.748	1.314		0.95559	0.8425
60	13 / 3	0.575	0.985		0.96710	0.8077
60	15 / 3	0.503	0.859		0.97141	0.8001
60	17 / 5	0.434	0.726		0.97595	0.7788
60	19 / 5	0.321	0.518		0.98293	0.7435
60	20 / 4	0.227	0.361		0.98812	0.7302
60	21 / 4	2.069		2.385	0.82916	1.2568
60	22 / 4	2.405		2.759	0.79026	1.3581
60	24 / 4	2.871		3.150	0.74695	1.4104
60	25 / 4	1.130	2.092		0.92712	0.9290
60	25 / 5	1.200	2.231		0.92182	0.9411
60	29 / 7	0.178	0.286		0.99058	0.7396
60	30 / 7	0.115	0.186		0.99385	0.7442

Tab. 9.5 Water activities of $K_4Fe(CN)_6$ solutions - I

T [°C]	Vessel/ Weighing	$K_4Fe(CN)_6$ [mol/kg]	NaCl [mol/kg]	a_w	ϕ
25	12 / 2	0.771	1.013	0.96635	0.4928
25	13 / 1	0.716	0.943	0.96872	0.4925
25	14 / 3	0.672	0.891	0.97050	0.4946
25	15 / 1	0.602	0.801	0.97352	0.4948
25	16 / 1	0.520	0.701	0.97688	0.4991
25	17 / 1	0.518	0.699	0.97693	0.5004
25	18 / 2	0.473	0.642	0.97883	0.5025
25	19 / 1	0.342	0.478	0.98423	0.5162
25	20 / 2	0.236	0.344	0.98866	0.5355
25	29 / 3	0.172	0.261	0.99137	0.5595
25	30 / 4	0.104	0.167	0.99444	0.5961
40	12 / 3	0.754	1.030	0.96559	0.5153
40	13 / 2	0.703	0.963	0.96790	0.5150
40	14 / 2	0.655	0.900	0.97005	0.5152
40	15 / 2	0.593	0.818	0.97285	0.5154
40	16 / 2	0.518	0.720	0.97614	0.5173
40	17 / 3	0.500	0.698	0.97689	0.5187
40	17 / 4	0.520	0.727	0.97592	0.5203
40	18 / 3	0.464	0.654	0.97836	0.5238
40	18 / 4	0.534	0.743	0.97538	0.5181
40	19 / 3	0.343	0.494	0.98371	0.5319
40	20 / 3	0.234	0.347	0.98854	0.5472
40	29 / 4	0.172	0.265	0.99125	0.5676
40	30 / 6	0.107	0.173	0.99425	0.5976

Tab. 9.6 Water activities of $K_4Fe(CN)_6$ solutions - II

T [°C]	Vessel/ Weighing	$K_4Fe(CN)_6$ [mol/kg]	NaCl [mol/kg]	a_w	ϕ
60	12 / 4	0.759	1.076	0.96394	0.5370
60	13 / 3	**0.698**	0.985	0.96710	0.5321
60	15 / 3	0.606	0.859	0.97141	0.5316
60	16 / 3	0.533	0.760	0.97479	0.5316
60	17 / 5	0.504	0.726	0.97595	0.5361
60	18 / 5	0.510	0.741	0.97543	0.5417
60	19 / 5	0.349	0.518	0.98293	0.5480
60	20 / 4	0.235	0.361	0.98812	0.5645
60	29 / 7	0.181	0.286	0.99058	0.5804
60	30 / 7	0.111	0.186	0.99385	0.6150

Tab. 9.7 Water activities of $K_3Fe(CN)_6$ solutions - I

T [°C]	Vessel/ Weighing	$K_3Fe(CN)_6$ [mol/kg]	NaCl [mol/kg]	a_w	ϕ
25	7 / 1	1.518	2.316	0.91955	0.7667
25	8 / 1	1.364	2.062	0.92909	0.7482
25	9 / 1	1.128	1.680	0.94304	0.7217
25	10 / 1	1.012	1.497	0.94954	0.7102
25	11 / 1	0.871	1.279	0.95719	0.6973
25	12 / 2	0.693	1.013	0.96635	0.6850
25	14 / 3	0.611	0.891	0.97050	0.6807
25	16 / 1	0.479	0.701	0.97688	0.6773
25	18 / 2	0.438	0.642	0.97883	0.6783
25	20 / 2	0.230	0.344	0.98866	0.6881
25	29 / 3	0.172	0.261	0.99137	0.6993
25	30 / 4	0.108	0.167	0.99444	0.7178
40	7 / 2	1.496	2.344	0.91777	0.7960
40	8 / 2	1.307	2.023	0.92993	0.7713
40	9 / 2	1.079	1.650	0.94368	0.7457
40	10 / 2	0.977	1.481	0.94977	0.7318
40	11 / 2	0.853	1.290	0.95654	0.7227
40	12 / 3	0.687	1.030	0.96559	0.7075
40	14 / 2	0.601	0.900	0.97005	0.7016
40	16 / 2	0.482	0.720	0.97614	0.6949
40	18 / 3	0.436	0.654	0.97836	0.6955
40	18 / 4	0.502	0.743	0.97538	0.6891
40	20 / 3	0.229	0.347	0.98854	0.6990
40	29 / 4	0.172	0.265	0.99125	0.7073
40	30 / 6	0.111	0.173	0.99425	0.7237

Tab. 9.8 Water activities of $K_3Fe(CN)_6$ solutions - II

T [°C]	Vessel/ Weighing	$K_3Fe(CN)_6$ [mol/kg]	NaCl [mol/kg]	a_w	ϕ
60	7 / 3	1.499	2.392	0.91566	0.8155
60	8 / 3	1.321	2.084	0.92740	0.7920
60	9 / 3	1.042	1.628	0.94432	0.7630
60	10 / 3	0.977	1.510	0.94859	0.7500
60	11 / 3	**0.887**	1.314	0.95559	0.7109
60	12 / 4	0.715	1.076	0.96394	0.7128
60	18 / 5	0.494	0.741	0.97543	0.6994
60	20 / 4	0.239	0.361	0.98812	0.6928
60	29 / 7	0.194	0.286	0.99058	0.6775
60	30 / 7	0.123	0.186	0.99385	0.6980

Tab. 9.9 Water activities of $Mg_2Fe(CN)_6$ solutions - I

T [°C]	Vessel/ Weighing	$Mg_2Fe(CN)_6$ [mol/kg]	NaCl [mol/kg]	a_w	ϕ
25	9 / 1	1.152	1.680	0.94304	0.9416
25	10 / 1	1.085	1.497	0.94954	0.8829
25	11 / 1	0.997	1.279	0.95719	0.8118
25	12 / 2	0.878	1.013	0.96635	0.7214
25	13 / 1	0.844	0.943	0.96872	0.6971
25	14 / 3	0.819	0.891	0.97050	0.6765
25	15 / 1	0.766	0.801	0.97352	0.6479
25	16 / 1	0.713	0.701	0.97688	0.6073
25	17 / 1	0.706	0.699	0.97693	0.6115
25	18 / 2	0.670	0.642	0.97883	0.5912
25	19 / 1	0.553	0.478	0.98423	0.5321
25	20 / 2	0.436	0.344	0.98866	0.4839
25	29 / 3	0.349	0.261	0.99137	0.4600
25	30 / 4	0.234	0.167	0.99444	0.4406
40	9 / 2	1.179	1.650	0.94368	0.9096
40	10 / 2	1.116	1.481	0.94977	0.8542
40	11 / 2	1.036	1.290	0.95654	0.7935
40	12 / 3	0.917	1.030	0.96559	0.7067
40	13 / 2	0.882	0.963	0.96790	0.6844
40	14 / 2	0.851	0.900	0.97005	0.6607
40	15 / 2	0.802	0.818	0.97285	0.6352
40	16 / 2	0.750	0.720	0.97614	0.5960
40	17 / 3	0.728	0.698	0.97689	0.5940
40	17 / 4	0.751	0.727	0.97592	0.6007
40	18 / 3	0.696	0.654	0.97836	0.5812
40	18 / 4	0.767	0.743	0.97538	0.6014
40	19 / 3	0.583	0.494	0.98371	0.5215
40	20 / 3	0.453	0.347	0.98854	0.4706
40	29 / 4	0.365	0.265	0.99125	0.4461
40	30 / 6	0.252	0.173	0.99425	0.4240

Tab. 9.10 Water activities of $Mg_2Fe(CN)_6$ solutions - II

T [°C]	Vessel/ Weighing	$Mg_2Fe(CN)_6$ [mol/kg]	NaCl [mol/kg]	a_w	ϕ
60	9 / 3	1.266	1.628	0.94432	0.8373
60	10 / 3	1.225	1.510	0.94859	0.7971
60	11 / 3	1.155	1.314	0.95559	0.7276
60	12 / 4	1.022	1.076	0.96394	0.6647
60	13 / 3	0.970	0.985	0.96710	0.6379
60	15 / 3	0.898	0.859	0.97141	0.5974
60	17 / 5	**0.816**	0.726	0.97595	0.5523
60	18 / 5	0.873	0.741	0.97543	0.5273
60	19 / 5	0.727	0.518	0.98293	0.4386
60	20 / 4	0.555	0.361	0.98812	0.3982
60	29 / 7	0.470	0.286	0.99058	0.3726
60	30 / 7	0.315	0.186	0.99385	0.3628

Tab. 9.11 Water activities of $Mg_3[Fe(CN)_6]_2$ solutions-I

T [°C]	Vessel/ Weighing	$Mg_3[Fe(CN)_6]_2$ [mol/kg]	NaCl [mol/kg]	a_w	ϕ
25	7 / 1	0.636	2.316	0.91955	1.4630
25	8 / 1	0.593	2.062	0.92909	1.3776
25	17 / 1	0.299	0.699	0.97693	0.8673
25	18 / 2	0.282	0.642	0.97883	0.8424
25	19 / 1	0.230	0.478	0.98423	0.7684
25	20 / 2	0.179	0.344	0.98866	0.7059
25	26 / 2	0.583	2.014	0.93087	1.3645
25	27 / 1	0.522	1.680	0.94302	1.2484
25	28 / 1	0.394	1.069	0.96443	1.0206
25	29 / 3	0.143	0.261	0.99137	0.6705
25	30 / 4	0.098	0.167	0.99444	0.6307
40	7 / 2	0.656	2.344	0.91777	1.4511
40	8 / 2	0.600	2.023	0.92993	1.3449
40	17 / 3	0.304	0.698	0.97689	0.8526
40	17 / 4	0.315	0.727	0.97592	0.8594
40	18 / 3	0.291	0.654	0.97836	0.8350
40	18 / 4	0.320	0.743	0.97538	0.8639
40	19 / 3	0.239	0.494	0.98371	0.7632
40	20 / 3	0.184	0.347	0.98854	0.6961
40	26 / 3	0.596	2.012	0.93037	1.3447
40	26 / 4	0.616	2.095	0.92726	1.3619
40	27 / 2	0.533	1.680	0.94258	1.2312
40	28 / 2	0.403	1.071	0.96419	1.0057
40	29 / 4	0.148	0.265	0.99125	0.6609
40	30 / 6	0.103	0.173	0.99425	0.6193

Tab. 9.12 Water activities of $Mg_3[Fe(CN)_6]_2$ solutions-II

T [°C]	Vessel/ Weighing	$Mg_3[Fe(CN)_6]_2$ [mol/kg]	NaCl [mol/kg]	a_w	ϕ
60	7 / 3	0.695	2.392	0.91566	1.4067
60	8 / 3	0.638	2.084	0.92740	1.3119
60	17 / 5	0.332	0.726	0.97595	0.8152
60	18 / 5	0.343	0.741	0.97543	0.8048
60	19 / 5	0.271	0.518	0.98293	0.7051
60	20 / 4	0.205	0.361	0.98812	0.6480
60	26 / 5	0.672	2.219	0.92227	1.3359
60	27 / 4	0.569	1.706	0.94145	1.1778
60	28 / 4	0.465	1.201	0.95960	0.9846
60	29 / 7	0.171	0.286	0.99058	0.6143
60	30 / 7	0.117	0.186	0.99385	0.5862

Tab. 9.13 Isoactive concentrations of mixed Na3Fe(CN)6-NaCl solutions at 25 to 60°C - I

T [°C]	$(Na.K)_3Fe(CN)_6$ [mol/kg]	NaCl [mol/kg]	Na [mol/kg]	K [mol/kg]	aW	phi
25	2.052	0	6.033	0.122	0.8243	1.307
25	1.906	0.3393	5.944	0.113	0.8243	1.292
25	1.782	0.6284	5.868	0.106	0.8243	1.279
25	1.643	0.9519	5.784	0.0976	0.8243	1.265
25	1.492	1.302	5.690	0.0886	0.8243	1.251
25	1.362	1.597	5.603	0.0809	0.8243	1.241
25	1.218	1.925	5.506	0.0723	0.8243	1.230
25	1.086	2.220	5.414	0.0645	0.8243	1.221
25	0.9416	2.547	5.316	0.0559	0.8243	1.211
25	0.8072	2.848	5.222	0.0480	0.8243	1.202
25	0.6678	3.154	5.118	0.0397	0.8243	1.194
25	0.5335	3.451	5.020	0.0317	0.8243	1.187
25	0.4013	3.740	4.920	0.0238	0.8243	1.181
25	0.2677	4.033	4.820	0.0159	0.8243	1.174
25	0.1387	4.312	4.720	0.0082	0.8243	1.168
25	0	4.615	4.615	0	0.8243	1.162
25	0	4.613	4.613	0	0.8243	1.163
25	0	4.612	4.612	0	0.8243	1.163

Tab. 9.14 Isoactive concentrations of mixed Na3Fe(CN)6-NaCl solutions at 25 to 60°C - II

T [°C]	$(Na.K)_3Fe(CN)_6$ [mol/kg]	NaCl [mol/kg]	NaCl medium [mol/kg]	Na [mol/kg]	K [mol/kg]	aW	phi
40	2.036	0		5.988	0.121	0.8251	1.310
40	1.894	0.3371		5.905	0.112	0.8251	1.294
40	1.770	0.6242		5.829	0.105	0.8251	1.282
40	1.631	0.9447		5.740	0.0969	0.8251	1.269
40	1.481	1.292		5.646	0.0880	0.8251	1.255
40	1.352	1.585		5.561	0.0803	0.8251	1.244
40	1.209	1.912		5.469	0.0718	0.8251	1.232
40	1.078	2.203		5.373	0.0640	0.8251	1.224
40	0.9346	2.528		5.276	0.0555	0.8251	1.214
40	0.8005	2.825		5.179	0.0476	0.8251	1.206
40	0.6621	3.128		5.075	0.0393	0.8251	1.199
40	0.5287	3.419		4.974	0.0314	0.8251	1.192
40	0.3978	3.706		4.876	0.0236	0.8251	1.185
40	0.2655	3.999		4.780	0.0158	0.8251	1.178
40	0.1376	4.276		4.680	0.00817	0.8251	1.173
40	0	4.577		4.577	0	0.8251	1.166
40	0	4.576		4.576	0	0.8251	1.166
40	0	4.573	4.5756	4.573	0	0.8251	1.167

Tab. 9.15 Isoactive concentrations of mixed Na3Fe(CN)6-NaCl solutions at 25 to 60°C - III

T [°C]	$(Na.K)_3Fe(CN)_6$ [mol/kg]	NaCl [mol/kg]	Na [mol/kg]	K [mol/kg]	aW	phi
60	2.082	0	6.122	0.124	0.8219	1.307
60	1.934	0.3443	6.031	0.115	0.8219	1.292
60	1.796	0.6333	5.914	0.107	0.8219	1.288
60	1.662	0.9630	5.851	0.0987	0.8219	1.270
60	1.508	1.316	5.751	0.0896	0.8219	1.256
60	1.372	1.608	5.644	0.0815	0.8219	1.251
60	1.231	1.946	5.566	0.0731	0.8219	1.235
60	1.095	2.238	5.457	0.0650	0.8219	1.229
60	0.9510	2.572	5.369	0.0565	0.8219	1.217
60	0.8141	2.872	5.266	0.0484	0.8219	1.209
60	0.6732	3.180	5.160	0.0400	0.8219	1.203
60	0.5377	3.478	5.059	0.0319	0.8219	1.195
60	0.4047	3.771	4.960	0.0240	0.8219	1.188
60	0.2699	4.065	4.858	0.0160	0.8219	1.182
60	0.1398	4.346	4.757	0.00831	0.8219	1.177
60	0	4.651	4.651	0	0.8219	1.170
60	0	4.655	4.655	0	0.8219	1.169
60	0	4.656	4.656	0	0.8219	1.169
60	2.276	0	6.694	0.135	0.8113	1.275
60	2.096	0.3731	6.537	0.125	0.8113	1.271
60	1.926	0.6791	6.342	0.114	0.8113	1.281
60	1.793	1.039	6.311	0.107	0.8113	1.255
60	1.614	1.409	6.156	0.0959	0.8113	1.251
60	1.447	1.695	5.949	0.0859	0.8113	1.265
60	1.310	2.072	5.926	0.0778	0.8113	1.237
60	1.153	2.357	5.748	0.0685	0.8113	1.245
60	1.007	2.723	5.683	0.0598	0.8113	1.225
60	0.8547	3.016	5.529	0.0508	0.8113	1.228
60	0.7085	3.347	5.430	0.0421	0.8113	1.218
60	0.5647	3.653	5.313	0.0335	0.8113	1.214
60	0.4267	3.976	5.231	0.0253	0.8113	1.202
60	0.2847	4.289	5.126	0.0169	0.8113	1.195
60	0.1475	4.584	5.017	0.00876	0.8113	1.190
60	0	4.897	4.897	0	0.8113	1.185
60	0	4.893	4.893	0	0.8113	1.186
60	0	4.899	4.899	0	0.8113	1.185

Tab. 9.16 Isoactive concentrations of mixed Na3Fe(CN)6-NaCl solutions at 25 to 60°C - IV

T [°C]	$(Na.K)_3Fe(CN)_6$ [mol/kg]	NaCl [mol/kg]	Na [mol/kg]	K [mol/kg]	aW	phi
40	2.290	0	6.733	0.136	0.8102	1.276
40	2.106	0.3749	6.568	0.125	0.8102	1.273
40	1.934	0.6820	6.369	0.115	0.8102	1.284
40	1.801	1.043	6.339	0.107	0.8102	1.257
40	1.621	1.415	6.181	0.0963	0.8102	1.254
40	1.452	1.702	5.971	0.0863	0.8102	1.268
40	1.314	2.078	5.942	0.0781	0.8102	1.241
40	1.157	2.365	5.769	0.0687	0.8102	1.248
40	1.010	2.733	5.704	0.0600	0.8102	1.229
40	0.8575	3.025	5.547	0.0509	0.8102	1.232
40	0.7114	3.360	5.452	0.0423	0.8102	1.221
40	0.5667	3.666	5.332	0.0337	0.8102	1.217
40	0.4281	3.988	5.247	0.0254	0.8102	1.206
40	0.2856	4.303	5.143	0.0170	0.8102	1.198
40	0.1477	4.591	5.025	0.00877	0.8102	1.195
40	0	4.907	4.907	0	0.8102	1.190
40	0	4.911	4.911	0	0.8102	1.189
40	0	4.907	4.907	0	0.8102	1.190

9.2 pH Measurements in salt solutions

Tab. 9.17 Results of the pH measurements in NaCl solutions at 25°C

No.	NaCl [mol/kg]	HCl [mol/kg]	pH_{obs}	ΔpH
1	0	0.001004	3.014	-0.016
2	0.294	0.000996	3.002	0.000
3	0.598	0.000994	2.965	0.038
4	0.999	0.000998	2.898	0.102
5	1.498	0.000990	2.820	0.184
6	2.000	0.000988	2.737	0.268
7	2.496	0.000999	2.643	0.357
8	2.990	0.001002	2.556	0.443
9	3.493	0.000998	2.463	0.538
10	3.987	0.001002	2.361	0.638
12	4.981	0.000995	2.194	0.808
13	5.479	0.000995	2.106	0.896
14	5.950	0.000994	2.021	0.982

Tab. 9.18 Results of the pH measurements in NaCl solutions at 40°C

No.	NaCl [mol/kg]	HCl [mol/kg]	pH_{obs}	ΔpH
1	0	0.001004	3.014	-0.016
2	0.294	0.000996	3.003	-0.001
3	0.598	0.000994	2.963	0.040
4	0.999	0.000998	2.900	0.101
5	1.498	0.000990	2.832	0.172
6	2.000	0.000988	2.746	0.259
7	2.496	0.000999	2.656	0.344
8	2.990	0.001002	2.574	0.425
9	3.493	0.000998	2.490	0.511
10	3.987	0.001002	2.403	0.596
12	4.981	0.000995	2.243	0.759
13	5.479	0.000995	2.151	0.852
14	5.950	0.000994	2.075	0.928

Tab. 9.19 Results of the pH measurements in NaCl solutions at 60°C

No.	NaCl [mol/kg]	HCl [mol/kg]	pH_{obs}	ΔpH
1	0	0.001004	3.015	-0.017
2	0.294	0.000996	3.009	-0.007
3	0.598	0.000994	2.982	0.021
4	0.999	0.000998	2.932	0.069
5	1.498	0.000990	2.856	0.148
6	2.000	0.000988	2.782	0.223
7	2.496	0.000999	2.706	0.294
8	2.990	0.001002	2.632	0.367
9	3.493	0.000998	2.556	0.444
10	3.987	0.001002	2.470	0.529
12	4.981	0.000995	2.326	0.676
13	5.479	0.000995	2.247	0.755
14	5.950	0.000994	2.170	0.832

Tab. 9.20 Results of the pH measurements in $MgCl_2$ solutions at 25°C

No.	$MgCl_2$ [mol/kg]	HCl [mol/kg]	pH_{obs}	ΔpH
1	0	0.001001	3.015	-0.016
2	0.300	0.001004	2.901	0.097
3	0.600	0.001000	2.784	0.216
4	1.000	0.000998	2.581	0.420
5	1.501	0.000992	2.338	0.665
6	2.001	0.000998	2.070	0.931
7	2.501	0.001001	1.797	1.202
8	2.998	0.000996	1.520	1.481
9	3.505	0.001002	1.228	1.771
10	4.000	0.000999	0.952	2.048
11	4.499	0.001001	0.667	2.333
12	4.990	0.000999	0.389	2.611
13	5.426	0.000994	0.148	2.855

Tab. 9.21 Results of the pH measurements in $MgCl_2$ solutions at 40°C

No.	$MgCl_2$ [mol/kg]	HCl [mol/kg]	pH_{obs}	ΔpH
1	0	0.001001	3.016	-0.016
2	0.300	0.001004	2.899	0.099
3	0.600	0.001000	2.769	0.231
4	1.000	0.000998	2.567	0.434
5	1.501	0.000992	2.329	0.674
6	2.001	0.000998	2.071	0.930
7	2.501	0.001001	1.816	1.184
8	2.998	0.000996	1.548	1.454
9	3.505	0.001002	1.272	1.727
10	4.000	0.000999	1.017	1.984
11	4.499	0.001001	0.736	2.264
12	4.990	0.000999	0.471	2.529
13	5.426	0.000994	0.248	2.754

Tab. 9.22 Results of the pH measurements in $MgCl_2$ solutions at 60°C

No.	$MgCl_2$ [mol/kg]	HCl [mol/kg]	pH_{obs}	ΔpH
1	0	0.001001	3.016	-0.017
2	0.300	0.001004	2.927	0.072
3	0.600	0.001000	2.817	0.183
4	1.000	0.000998	2.636	0.365
5	1.501	0.000992	2.422	0.582
6	2.001	0.000998	2.183	0.818
7	2.501	0.001001	1.946	1.054
8	2.998	0.000996	1.701	1.301
9	3.505	0.001002	1.446	1.553
10	4.000	0.000999	1.211	1.790
11	4.499	0.001001	0.940	2.060
12	4.990	0.000999	0.699	2.301
13	5.426	0.000994	0.461	2.542

9.3 Redox measurements in salt solutions

Tab. 9.23 Standard half-cell potentials of Ag.AgCl reference electrode with 3M KCl filling (Metrohm. supplementary information)

T [°C]	E0 [mV]
0	224.2
10	217.4
20	210.5
25	207
30	203.4
40	196.1
50	188.4
60	180.3
70	172.1
80	163.1
90	153.3
95	148.1

Tab. 9.24 Composition of NaCl solutions used for the measurement of the redox potential

No.	Na^+	Cl^-	$Fe(CN)_6^{4-}$	$Fe(CN)_6^{3-}$	K^+	HPO_4^{2-}	$H_2PO_4^-$
	[mol/kg]	[mol/kg]	[mol/kg]	[mol/kg]	[mol/kg]	[mol/kg]	[mol/kg]
1	0.00047267	0	0.00460	0.00560	0.0354	0.000236	0.000236
2	0.308	0.307	0.00412	0.00461	0.0305	0.000247	0.000247
3	0.408	0.407	0.00442	0.00472	0.0321	0.000242	0.000242
4	0.833	0.832	0.00440	0.00481	0.0323	0.000241	0.000241
5	1.368	1.368	0.00451	0.00449	0.0318	0.000242	0.000242
6	2.035	2.035	0.00441	0.00471	0.0320	0.000232	0.000232
7	2.435	2.434	0.00431	0.00493	0.0322	0.000241	0.000241
8	2.739	2.738	0.00442	0.00472	0.0321	0.000247	0.000247
9	3.411	3.411	0.00442	0.00484	0.0324	0.000238	0.000238
10	3.887	3.886	0.00440	0.00481	0.0323	0.000246	0.000246
11	4.076	4.076	0.00448	0.00479	0.0325	0.000235	0.000235
12	4.866	4.865	0.00441	0.00471	0.0320	0.000242	0.000242
13	5.439	5.439	0.00482	0.00505	0.0346	0.000237	0.000237
14	5.868	5.867	0.00452	0.00483	0.0328	0.000247	0.000247

Tab. 9.25 Composition of $MgCl_2$ solutions used for the measurement of the redox potential (1st set of solutions)

No.	$MgCl_2$	$Fe(CN)_6^{4-}$	$Fe(CN)_6^{3-}$	K^+	Na^+	HPO_4^{2-}	$H_2PO_4^-$
	[mol/kg]	[mol/kg]	[mol/kg]	[mol/kg]	[mol/kg]	[mol/kg]	[mol/kg]
1	0	0.00356	0.00300	0.0235	0.000494	0.000247	0.000247
2	0.284	0.00372	0.00341	0.0254	0.000474	0.000237	0.000237
3	0.570	0.00355	0.00349	0.0249	0.000473	0.000237	0.000237
4	0.957	0.00353	0.00347	0.0248	0.000482	0.000241	0.000241
5	1.400	0.00354	0.00331	0.0244	0.000472	0.000236	0.000236
6	1.865	0.00353	0.00339	0.0245	0.000470	0.000235	0.000235
7	2.324	0.00353	0.00354	0.0250	0.000498	0.000249	0.000249
8	2.786	0.00361	0.00338	0.0248	0.000469	0.000235	0.000235
9	3.241	0.00351	0.00320	0.0239	0.000468	0.000234	0.000234
10	3.718	0.00353	0.00338	0.0245	0.000489	0.000245	0.000245
11	4.152	0.00350	0.00360	0.0251	0.000476	0.000238	0.000238
12	4.607	0.00334	0.00335	0.0237	0.000513	0.000257	0.000257
13	5.058	0.00349	0.00335	0.0243	0.000465	0.000233	0.000233
14	5.329	0.00357	0.00335	0.0245	0.000455	0.000228	0.000228

Tab. 9.26 Composition of $MgCl_2$ solutions used for the measurement of the redox potential (2nd set of solutions)

No.	$MgCl_2$	$Fe(CN)_6^{4-}$	$Fe(CN)_6^{3-}$	K^+	Na^+	HPO_4^{2-}	$H_2PO_4^-$
	[mol/kg]	[mol/kg]	[mol/kg]	[mol/kg]	[mol/kg]	[mol/kg]	[mol/kg]
1	0	0.00367	0.00356	0.0256	0.000455	0.000228	0.000228
2	0.266	0.00367	0.00356	0.0256	0.000455	0.000227	0.000227
3	0.532	0.00367	0.00355	0.0256	0.000454	0.000227	0.000227
4	0.880	0.00366	0.00355	0.0255	0.000454	0.000227	0.000227
5	1.317	0.00366	0.00354	0.0255	0.000453	0.000227	0.000227
6	1.755	0.00365	0.00354	0.0254	0.000452	0.000226	0.000226
7	2.190	0.00364	0.00353	0.0254	0.000451	0.000226	0.000226
8	2.618	0.00364	0.00353	0.0254	0.000451	0.000226	0.000226
9	3.141	0.00224	0.00217	0.0157	0.000462	0.000231	0.000231
10	3.642	0.00114	0.00110	0.00811	0.000470	0.000235	0.000235
11	4.183	0.000291	0.000282	0.00225	0.000480	0.000240	0.000240
12	4.668	0.000115	0.000112	0.00103	0.000475	0.000238	0.000238
13	5.106	0.000116	0.000113	0.00104	0.000480	0.000240	0.000240
14	5.372	0.000116	0.000112	0.00104	0.000478	0.000239	0.000239

Tab. 9.27 Composition of mixed NaCl-$MgCl_2$ solutions used for the measurement of the redox potential

No.	Mg	Na^+	Cl-	$Fe(CN)_6^{4-}$	$Fe(CN)_6^{3-}$	K^+	HPO_4^{2-}	$H_2PO_4^-$
	[mol/kg]	[mol/kg]	[mol/kg]	[mol/kg]	[mol/kg]	[mol/kg]	[mol/kg]	[mol/kg]
1	0	5.311	5.311	0.00368	0.00356	0.0256	0.000228	0.000228
2	0.2778	4.868	5.423	0.00367	0.00356	0.0256	0.000228	0.000228
3	0.5550	4.392	5.502	0.00367	0.00355	0.0256	0.000227	0.000227
4	0.9236	3.760	5.607	0.00366	0.00355	0.0255	0.000227	0.000227
5	1.384	2.752	5.520	0.00366	0.00354	0.0255	0.000227	0.000227
6	1.895	2.152	5.942	0.00226	0.00219	0.0158	0.000233	0.000233
7	2.356	1.597	6.310	0.00225	0.00218	0.0157	0.000232	0.000232
8	2.835	1.025	6.694	0.00225	0.00218	0.0158	0.000232	0.000232
9	3.296	0.6388	7.230	0.00168	0.00163	0.0119	0.000231	0.000231
10	3.857	0.4247	8.138	0.000919	0.000890	0.00658	0.000237	0.000237
11	4.399	0.2685	9.066	0.000233	0.000226	0.00185	0.000240	0.000240
12	4.887	0.1658	9.939	0.000116	0.000113	0.00104	0.000240	0.000240
13	5.374	0.1002	10.849	0.000116	0.000113	0.00104	0.000240	0.000240
14	5.663	0.0667	11.392	0.000116	0.000113	0.00104	0.000240	0.000240

Tab. 9.28 Results of the redox potential measurements in NaCl solutions at 25°C

No.	T [°C]	pHobs	pcH (calc.)$^-$	E_{obs} [mV]	Eh_{obs} [mV]	ΔEh [mV]
1	25.0	7.003	6.943	196.5	403.4	43.4
2	25.0	6.619	6.577	229.6	436.5	78.7
3	25.0	6.519	6.490	235.6	442.5	85.9
4	25.0	6.280	6.314	252.1	459.0	101.8
5	25.0	6.084	6.207	266.2	473.1	118.3
6	25.0	5.866	6.104	280.1	487.0	130.4
7	25.0	5.885	6.194	287.3	494.2	135.8
8	25.0	5.703	6.066	292.2	499.1	142.5
9	25.0	5.532	6.016	302.3	509.2	152.0
10	25.0	5.574	6.143	308.3	515.2	158.0
11	25.0	5.410	6.013	310.8	517.7	161.0
12	-	-	-	-		
13	25.0	5.160	6.011	326.3	533.2	177.0
14	25.1	5.242	6.171	330.4	537.3	182.5

Tab. 9.29 Results of the redox potential measurements in NaCl solutions at 40°C

No.	T [°C]	pH_{obs}	pcH (calc.)$^{-}$	E_{obs} [mV]	Eh_{obs} [mV]	ΔEh [mV]
1	40.1	7.130	7.130	176.6	372.6	53.0
2	40.1	6.674	6.674	211.1	407.1	89.8
3	40	6.495	6.495	216.6	412.7	96.3
4	39.9	6.400	6.400	234.3	430.5	113.2
5	40	6.227	6.227	248.7	444.8	130.3
6	40	6.035	6.035	262.9	459.0	142.6
7	40.1	5.974	5.974	269.8	465.8	147.8
8	40.1	5.867	5.867	275.3	471.3	155.2
9	40	5.719	5.719	285.7	481.8	164.8
10	40	5.681	5.681	291.4	487.5	170.5
11	40	5.616	5.616	294.4	490.5	174.1
12	40	5.619	5.619	303.4	499.5	183.1
13	40	5.402	5.402	310.4	506.5	190.6
14	39.9	5.394	5.394	314	510.2	195.3

Tab. 9.30 Results of the redox potential measurements in NaCl solutions at 60°C

No.	T [°C]	pH_{obs}	pcH (calc.)$^{-}$	E_{obs} [mV]	Eh_{obs} [mV]	ΔEh [mV]
1	60.0	7.037	7.009	138.7	319.2	52.8
2	60.1	6.548	6.541	175.3	355.7	92.0
3	60.0	6.386	6.392	180.7	361.2	98.5
4	60.1	6.261	6.322	200.1	380.5	117.5
5	60.0	6.104	6.242	215	395.5	134.9
6	60.0	5.920	6.157	230.1	410.6	147.9
7	59.9	5.855	6.152	237.2	417.8	152.9
8	60.0	5.758	6.102	242.7	423.2	160.5
9	60.1	5.624	6.072	253.3	433.7	170.7
10	60.0	5.583	6.103	259.6	440.1	176.8
11	60.0	5.520	6.069	262.8	443.3	180.6
12	60.0	5.515	6.187	272.3	452.8	190.1
13	60.0	5.321	6.083	279.5	460.0	197.9
14	59.9	5.315	6.142	283.2	463.8	202.7

Tab. 9.31 Results of the redox potential measurements in $MgCl_2$ solutions at 25°C (1st series)

No.	T [°C]	pH_{obs}	pcH (calc.)$^-$	E_{obs} [mV]	Eh_{obs} [mV]	ΔEh [mV]
1	25.1	6.901	6.860	203.6	410.5	51.3
2	25.1	5.644	5.697	283	489.9	132.9
3	25.1	5.309	5.504	305.1	512.0	156.8
4	25.1	4.979	5.378	328	534.9	179.6
5	25	4.633	5.271	350.4	557.3	200.6
6	25	4.313	5.204	372.1	579.0	223.0
7	25	4.024	5.165	392.8	599.7	244.9
8	25	3.750	5.145	411	617.9	261.3
9	25	3.511	5.155	430.6	637.5	280.2
10	25.1	3.137	5.044	487.9	694.8	338.96
11	25.1	2.894	5.040	515.6	722.5	368.5
12	24.9	2.663	5.059	561.6	768.6	413.5
13	25	2.430	5.075	595.3	802.2	446.2
14	25	2.242	5.037	612.1	819.0	462.4

Tab. 9.32 Results of the redox potential measurements in $MgCl_2$ solutions at 25°C (2nd series)

No.	T [°C]	pH_{obs}	pcH (calc.)$^-$	E_{obs} [mV]	Eh_{obs} [mV]	ΔEh [mV]
1	25	6.820	6.778	193.4	400.3	44.5
2	25	5.621	5.667	278.8	485.7	129.9
3	25	5.296	5.475	299.8	506.7	150.9
4	25	4.977	5.340	320.8	527.7	171.9
5	25	4.659	5.259	342.2	549.1	193.3
6	25	4.353	5.193	363.8	570.7	214.9
7	25	4.073	5.152	383.3	590.2	234.4
8	25.1	3.822	5.137	402	608.9	253.3
9	25.1	3.493	5.095	423.4	630.3	274.7
10	25	3.264	5.141	442.7	649.6	293.8
11	25	2.903	5.079	460.9	667.8	312.0
12	25.1	2.670	5.115	476	682.9	327.3
13	25.1	2.335	5.024	489.1	696.0	340.4
14	25.1	2.343	5.180	496.3	703.2	347.6

Tab. 9.33 Results of the redox potential measurements in $MgCl_2$ solutions at 40°C

No.	T [°C]	pH_{obs}	pcH (calc.)$^-$	E_{obs} [mV]	Eh_{obs} [mV]	ΔEh [mV]
1	40.1	6.734	6.705	167.5	363.5	48.3
2	40.0	5.647	5.714	258.1	454.2	138.7
3	40.0	5.365	5.563	280.1	476.2	160.7
4	40.0	5.081	5.457	302.1	498.2	182.7
5	40.0	4.801	5.404	324.3	520.4	204.9
6	40.0	4.544	5.377	346.6	542.7	227.2
7	40.1	4.323	5.385	366.6	562.6	247.4
8	40.1	4.121	5.410	386.1	582.1	266.9
9	40.0	3.706	5.268	408.3	604.4	288.9
10	40.1	3.409	5.234	428.2	624.2	309.0
11	40.1	2.946	5.057	446.5	642.5	327.3
12	40.1	2.667	5.034	461.8	657.8	342.6
13	40.1	2.342	4.943	473.4	669.4	354.2
14	40.1	2.358	5.100	480.5	676.5	362.2

Tab. 9.34 Results of the redox potential measurements in $MgCl_2$ solutions at 60°C (1s series)

No.	T [°C]	pH_{obs}	pcH (calc.)$^-$	E_{obs} [mV]	Eh_{obs} [mV]	ΔEh [mV]
1	60.1	6.901	6.860	288.5	468.9	203.5
2	59.9	5.644	5.680	243.8	424.4	160.9
3	59.9	5.309	5.470	265.2	445.8	184.2
4	59.9	4.979	5.321	289.8	470.4	208.8
5	60.1	4.633	5.186	314.9	495.3	232.9
6	60.1	4.313	5.090	337.3	517.7	256.0
7	60.1	4.024	5.024	359.4	539.8	279.5
8	60.1	3.750	4.975	384.14	564.5	302.2
9	60	3.511	4.957	402.2	582.7	319.8

Tab. 9.35 Results of the redox potential measurements in $MgCl_2$ solutions at 60°C (2nd series)

No.	T [°C]	pH_{obs}	pcH (calc.)$^-$	E_{obs} [mV]	Eh_{obs} [mV]	ΔEh [mV]
1	60	6.384	6.342	147.9	328.4	66.7
2	60	5.696	5.726	231.1	411.6	149.9
3	60.1	5.453	5.599	255.2	435.6	174.2
4	60.1	5.219	5.529	278.9	459.3	197.9
5	60	5.029	5.548	303.7	484.2	222.5
6	60	4.762	5.494	325.5	506.0	244.3
7	60	4.597	5.542	347.3	527.8	266.1
8	60	4.447	5.602	368.9	549.4	287.7
9	60.1	4.121	5.530	392.2	572.6	311.2
10	60.1	3.931	5.584	412.2	592.6	331.2
11	60.1	3.411	5.329	432	612.4	351.0
12	60.1	3.035	5.193	446.3	626.7	365.3
13	60	2.816	5.191	459.7	640.2	378.5
14	60.1	2.906	5.412	464.6	645.0	383.6

Tab. 9.36 Results of the redox potential measurements in mixed NaCl/$MgCl_2$ solutions at 25°C

No.	T [°C]	pH_{obs}	pcH (calc.)$^-$	E_{obs} [mV]	Eh_{obs} [mV]	ΔEh [mV]
1	25.1	5.488	6.363	324.5	531.4	177.5
2	24.9	5.097	6.036	333.4	540.3	186.0
3	25.1	4.865	5.861	342.1	549.0	195.1
4	25.1	4.748	5.818	353.1	560.0	206.1
5	25.1	4.577	5.698	363.4	570.3	216.4
6	25.1	4.164	5.435	380.7	587.6	233.7
7	25.1	4.082	5.488	397.3	604.2	250.3
8	25.1	3.757	5.301	410.3	617.2	263.3
9	25.1	3.647	5.359	424.2	631.1	277.2
10	25.1	3.240	5.199	441.3	648.2	294.3
11	25.1	2.930	5.141	458.4	665.3	311.4
12	25.1	2.711	5.160	471.2	678.1	324.2
13	25.1	2.519	5.206	482.3	689.2	335.3
14	25.1	2.395	5.228	488.3	695.2	341.3

Tab. 9.37 Results of the redox potential measurements in mixed NaCl/$MgCl_2$ solutions at 40°C

No.	T [°C]	pH_{obs}	pcH (calc.)$^-$	E_{obs} [mV]	Eh_{obs} [mV]	ΔEh [mV]
1	40.1	5.536	6.422	302	498.0	184.5
2	40.1	5.125	6.069	311.5	507.5	194.0
3	40.1	4.903	5.899	321.2	517.2	203.7
4	39.9	4.793	5.857	333.5	529.7	215.7
5	40.0	4.649	5.756	344.7	540.8	227.0
6	40.0	4.252	5.502	363.1	559.2	245.4
7	40.0	4.106	5.484	380.5	576.6	262.8
8	40.0	3.838	5.347	394.4	590.5	276.7
9	40.0	3.713	5.381	409.1	605.2	291.4
10	40.1	3.301	5.205	427	623.0	309.5
11	40.1	2.968	5.114	443.9	639.9	326.4
12	40.0	2.732	5.104	457.2	653.3	339.5
13	40.1	2.553	5.152	469.1	665.1	351.6
14	40.1	2.433	5.171	475.7	671.7	358.2

Tab. 9.38 Results of the redox potential measurements in mixed NaCl/$MgCl_2$ solutions at 60°C

No.	T [°C]	pH_{obs}	pcH (calc.)$^-$	E_{obs} [mV]	Eh_{obs} [mV]	ΔEh [mV]
1	60.1	5.593	6.467	272.2	452.6	193.0
2	60.1	5.072	5.993	282.6	463.0	203.4
3	60.1	4.812	5.774	293.3	473.7	214.1
4	60.1	4.613	5.629	306.5	486.9	227.3
5	60.0	4.442	5.481	318.5	499.0	239.1
6	60.0	4.104	5.264	338.3	518.8	258.9
7	60.1	3.948	5.217	357.1	537.5	277.9
8	60.1	3.708	5.087	372.9	553.3	293.7
9	60.2	3.609	5.129	388.1	568.4	309.1
10	60.0	3.242	4.977	407.7	588.2	328.3
11	60.0	2.924	4.880	428.4	608.9	349.0
12	60.1	2.728	4.893	444.1	624.5	364.9
13	60.1	2.557	4.932	457.5	637.9	378.3
14	60.1	2.426	4.930	465.5	645.9	386.3

9.4 Solubility measurements

Tab. 9.39 Solubility in the system NaCl-$Na_4Fe(CN)_6$-H_2O at 25°C

NaCl [mol/kg]	**$Na_4Fe(CN)_6$ [mol/kg]**	**Solid phase**
0.000	0.699	$Na_4Fe(CN)_6 \cdot 10H_2O$
0.601	0.500	$Na_4Fe(CN)_6 \cdot 10H_2O$
1.21	0.337	$Na_4Fe(CN)_6 \cdot 10H_2O$
1.82	0.219	$Na_4Fe(CN)_6 \cdot 10H_2O$
2.40	0.143	$Na_4Fe(CN)_6 \cdot 10H_2O$
2.96	0.108	$Na_4Fe(CN)_6 \cdot 10H_2O$
3.60	0.0592	$Na_4Fe(CN)_6 \cdot 10H_2O$
4.15	0.0428	$Na_4Fe(CN)_6 \cdot 10H_2O$
4.66	0.0308	$Na_4Fe(CN)_6 \cdot 10H_2O$
5.23	0.0230	$Na_4Fe(CN)_6 \cdot 10H_2O$
5.80	0.0174	$Na_4Fe(CN)_6 \cdot 10H_2O$
5.98	0.0160	$Na_4Fe(CN)_6 \cdot 10H_2O$

Tab. 9.40 Solubility in the system NaCl-$Na_4Fe(CN)_6$-H_2O at 40°C

NaCl [mol/kg]	**$Na_4Fe(CN)_6$ [mol/kg]**	**Solid phase**
0	0.909	$Na_4Fe(CN)_6 \cdot 10H_2O$
0.615	0.704	$Na_4Fe(CN)_6 \cdot 10H_2O$
1.46	0.462	$Na_4Fe(CN)_6 \cdot 10H_2O$
2.12	0.320	$Na_4Fe(CN)_6 \cdot 10H_2O$
2.91	0.201	$Na_4Fe(CN)_6 \cdot 10H_2O$
3.55	0.138	$Na_4Fe(CN)_6 \cdot 10H_2O$
4.05	0.0961	$Na_4Fe(CN)_6 \cdot 10H_2O$
4.67	0.0713	$Na_4Fe(CN)_6 \cdot 10H_2O$
5.05	0.0587	$Na_4Fe(CN)_6 \cdot 10H_2O$
5.37	0.0482	$Na_4Fe(CN)_6 \cdot 10H_2O$
5.65	0.0625	$Na_4Fe(CN)_6 \cdot 10H_2O$
5.81	0.0424	$Na_4Fe(CN)_6 \cdot 10H_2O$
5.92	0.0430	$Na_4Fe(CN)_6 \cdot 10H_2O$ + NaCl
6.22	0	NaCl
2.16	0.352	$Na_4Fe(CN)_6 \cdot 10H_2O$
3.10	0.199	$Na_4Fe(CN)_6 \cdot 10H_2O$
3.92	0.130	$Na_4Fe(CN)_6 \cdot 10H_2O$
4.75	0.0719	$Na_4Fe(CN)_6 \cdot 10H_2O$ + white solid
4.89	0.0667	$Na_4Fe(CN)_6 \cdot 10H_2O$ + white solid

Tab. 9.41 Solubility in the system NaCl-$Na_4Fe(CN)_6$-H_2O at 60°C

NaCl [mol/kg]	**$Na_4Fe(CN)_6$ [mol/kg]**	**Solid phase**
2.46	0.619	$Na_4Fe(CN)_6 \cdot 10H_2O$
3.67	0.392	$Na_4Fe(CN)_6 \cdot 10H_2O$
4.76	0.225	$Na_4Fe(CN)_6 \cdot 10H_2O$ + white solid
4.83	0.240	$Na_4Fe(CN)_6 \cdot 10H_2O$ +white solid
4.84	0.234	$Na_4Fe(CN)_6 \cdot 10H_2O$ +white solid

Tab. 9.42 Solubility in the system KCl-$K_4Fe(CN)_6$-H_2O at 25°C

KCl [mol/kg]	$K_4Fe(CN)_6$ [mol/kg]	Solid phase
0.515	0.682	$K_4Fe(CN)_6.3H_2O$
1.03	0.523	$K_4Fe(CN)_6.3H_2O$
1.54	0.405	$K_4Fe(CN)_6.3H_2O$
2.06	0.299	$K_4Fe(CN)_6.3H_2O$
2.58	0.239	$K_4Fe(CN)_6.3H_2O$
3.11	0.177	$K_4Fe(CN)_6.3H_2O$
3.63	0.138	$K_4Fe(CN)_6.3H_2O$
4.16	0.106	$K_4Fe(CN)_6.3H_2O$
4.68	0.0860	$K_4Fe(CN)_6.3H_2O$
4.69	0.0835	$K_4Fe(CN)_6.3H_2O$ + KCl

Tab. 9.43 Solubility in the system $MgCl_2$-$Mg_4Fe(CN)_6$-H_2O at 25°C

Liquid		Wet Solid		H_2O [mol.-%]	Solid phase
$MgCl_2$ [mol/kg]	$Mg_2Fe(CN)_6$ [mol/kg]	$MgCl_2$ [mol.-%]	$Mg_2Fe(CN)_6$ [mol.-%]		
0	1.38	0.0%	4.47%	95.5%	$Mg_2Fe(CN)_6 \cdot 11H_2O$
0.737	0.941	0.857%	4.50%	94.6%	$Mg_2Fe(CN)_6 \cdot 11H_2O$
1.280	0.633	1.43%	3.67%	94.9%	$Mg_2Fe(CN)_6 \cdot 11H_2O$
1.841	0.371	1.89%	3.79%	94.3%	$Mg_2Fe(CN)_6 \cdot 11H_2O$
2.401	0.195	2.57%	3.35%	94.1%	$Mg_2Fe(CN)_6 \cdot 11H_2O$
2.874	0.0112	6.26%	5.14%	88.6%	$xMgCl_2.Mg_2Fe(CN)_6 \cdot yH_2O$
3.163	0.00649	5.61%	2.98%	91.4%	$3MgCl_2.Mg_2Fe(CN)_6 \cdot 23H_2O$
3.770	0.00146	6.07%	2.65%	91.3%	$3MgCl_2.Mg_2Fe(CN)_6 \cdot 23H_2O$
4.226	0.000513	6.33%	1.96%	91.7%	$3MgCl_2.Mg_2Fe(CN)_6 \cdot 23H_2O$
4.879	*0.000162*	*6.75%*	*1.92%*	*91.3%*	$3MgCl_2.Mg_2Fe(CN)_6 \cdot 23H_2O$
5.432	*0.0000971*	*7.44%*	*1.99%*	*90.6%*	$3MgCl_2.Mg_2Fe(CN)_6 \cdot 23H_2O$
5.627	0.00216	7.76%	2.11%	90.1%	$3MgCl_2.Mg_2Fe(CN)_6 \cdot 23H_2O$
3.778	*0.000763*	6.66%	1.84%	91.5%	$3MgCl_2.Mg_2Fe(CN)_6 \cdot 23H_2O$
4.187	0.000271	6.63%	1.77%	91.6%	$3MgCl_2.Mg_2Fe(CN)_6 \cdot 23H_2O$
4.682	0.000108	6.98%	1.99%	91.0%	$3MgCl_2.Mg_2Fe(CN)_6 \cdot 23H_2O$
5.137	0.0000415	7.61%	2.09%	90.3%	$3MgCl_2.Mg_2Fe(CN)_6 \cdot 23H_2O$
5.723	0.0000553	7.86%	2.14%	90.0%	$3MgCl_2.Mg_2Fe(CN)_6 \cdot 23H_2O$

Tab. 9.44 Solubility in the system NaCl-$Na_3Fe(CN)_6$-H_2O at 25°C

Liquid [mol/kg]					Wet Solid [mol-%]				
K	**Na**	**Cl**	**Fe(CN)6**	**K/ (Na+K) [mol-%]**	**K**	**Na**	**Cl**	**$Fe(CN)_6$**	**K/ (Na+K)**
0.1710	11.42	0	3.865	1.5%	5.8%	32.0%	0.0%	12.6%	15.3%
0.1132	11.50	0.662	3.651	1.0%	5.9%	35.6%	1.1%	13.5%	14.2%
0.1730	10.52	1.977	2.904	1.6%	8.3%	31.6%	4.0%	12.0%	20.8%
0.1917	10.21	2.313	2.697	1.8%	9.9%	29.0%	6.8%	10.7%	25.4%
0.0885	11.18	2.608	2.886	0.8%	6.6%	36.5%	3.4%	13.3%	15.4%
0.0988	10.54	3.827	2.269	0.9%	6.8%	36.1%	3.2%	13.2%	15.8%
0.0912	10.28	4.099	2.090	0.9%	6.9%	37.9%	4.5%	13.5%	15.5%
0.1560	9.612	4.283	1.828	1.6%	0.1%	47.2%	46.6%	0.2%	0.2%*
0.1397	8.288	4.715	1.238	1.7%	0.1%	48.9%	48.8%	0.1%	0.1%*
0.1052	8.229	5.949	0.795	1.3%	0.0%	47.2%	47.1%	0.0%	0.0%*
0.0297	7.782	6.073	0.580	0.4%	0.0%	30.1%	30.1%	0.0%	0.0%*
0.0180	7.296	6.748	0.189	0.2%	0.0%	43.0%	42.9%	0.0%	0.0%*
solid phase: $(Na.K)_3Fe(CN)_6 \cdot 2H_2O$ or NaCl (*)									

Tab. 9.45 Solubility in the system KCl-$K_3Fe(CN)_6$-H_2O at 25°C; solid phase: $K_3Fe(CN)_6$ in all batches

KCl [mol/kg]	**$K_3Fe(CN)_6$ [mol/kg]**
0.502	1.339
1.001	1.200
1.504	1.038
2.002	0.886
2.502	0.757
2.998	0.654
3.502	0.530
3.999	0.459
4.499	0.388

Tab. 9.46 Solubility in the system $MgCl_2$-$Mg_3[Fe(CN)_6]_2$-H_2O at 25°C; solid phase: $Mg_3[Fe(CN)_6]_2 \cdot 11H_2O$ in all batches

$MgCl_2$ [mol/kg]	**$Mg_3[Fe(CN)_6]_2$ [mol/kg]**
0	0.8782
0.5886	0.6880
1.132	0.5324
1.658	0.3945
2.217	0.2529
2.765	0.1400
3.276	0.06793
3.692	0.03069
4.175	0.01141
4.956	0.005243
5.405	0.002700
5.862	0.001835

9.5 Spectrophotometric determination of Fe(II) speciation in chloride media

9.5.1 Measurements at 25°C

Tab. 9.47 Speciation of Fe(II) in NaCl solutions at 25°C

No.	NaCl	$Fe(ClO_4)_2$	$HClO_4$	Fe^{2+}	$FeCl^+$	$FeCl_2(aq)$
	[mol/kg]	[mol/kg]	[mol/kg]	[%]	[%]	[%]
1	0	0.0500	0.00101	100%	0%	0%
2	0.00952	0.0499	0.00101	100%	0%	0%
3	0.0304	0.0496	0.00101	100%	0%	0%
4	0.0933	0.0500	0.00101	100%	0%	0%
5	0.307	0.0502	0.00101	100%	0%	0%
6	0.661	0.0505	0.00102	100%	0%	0%
7	1.04	0.0508	0.00103	98%	2%	0%
8	1.41	0.0511	0.00104	98%	2%	0%
9	1.74	0.0514	0.00105	96%	4%	0%
10	2.11	0.0517	0.00105	95%	5%	0%
11	2.46	0.0519	0.00106	93%	7%	0%
12	2.84	0.0523	0.00107	92%	8%	0%
13	3.26	0.0526	0.00108	89%	11%	0%
14	3.62	0.0529	0.00109	87%	13%	0%
15	4.03	0.0532	0.00110	84%	16%	0%
16	4.42	0.0535	0.00111	81%	19%	0%
17	4.86	0.0539	0.00112	78%	22%	0%
18	5.28	0.0542	0.00113	75%	25%	0%
19	5.56	0.0544	0.00113	73%	27%	0%
20	6.07	0.0548	0.00114	67%	33%	0%

Tab. 9.48 Speciation of Fe(II) in LiCl solutions at 25°C

No.	LiCl	$Fe(ClO_4)_2$	$HClO_4$	$Mg(ClO_4)_2$	Fe^{2+}	$FeCl^+$	$FeCl_2(aq)$
	[mol/kg]	[mol/kg]	[mol/kg]	[mol/kg]	[%]	[%]	[%]
1	2.14	0.0521	0.00105	-	95%	5%	0%
2	3.18	0.0532	0.00107	-	89%	11%	0%
3	4.38	0.0544	0.00110	-	81%	19%	0%
4	5.68	0.0557	0.00113	-	67%	33%	0%
5	7.00	0.0571	0.00116	-	50%	50%	0%
6	8.33	0.0584	0.00119	-	28%	72%	0%
7	9.77	0.0599	0.00122	-	0%	96%	4%
12	9.71	0.0356	0.00121	0.0153	0%	96%	4%
13	11.18	0.0335	0.00124	0.0179	0%	85%	15%
14	14.43	0.0286	0.00131	0.0206	0%	35%	65%
15	16.07	0.0262	0.00134	0.0267	0%	0%	100%

Tab. 9.49 Speciation of Fe(II) in $MgCl_2$ solutions at 25°C

No.	$MgCl_2$	$Fe(ClO_4)_2$	$HClO_4$	Fe^{2+}	$FeCl^+$	$FeCl_2(aq)$
	[mol/kg]	[mol/kg]	[mol/kg]	[%]	[%]	[%]
1	0.207	0.0502	0.000248	100%	0%	0%
2	0.419	0.0504	0.000247	99%	1%	0%
3	0.631	0.0507	0.000247	98%	2%	0%
4	0.846	0.0509	0.000246	96%	4%	0%
5	1.07	0.0512	0.000246	95%	5%	0%
6	1.29	0.0514	0.000246	93%	7%	0%
7	1.52	0.0517	0.000246	90%	10%	0%
8	1.74	0.0519	0.000247	88%	12%	0%
9	1.96	0.0521	0.000247	84%	16%	0%
10	2.20	0.0524	0.000246	81%	19%	0%
11	2.44	0.0527	0.000247	77%	23%	0%
12	2.68	0.0529	0.000246	71%	29%	0%
13	2.91	0.0532	0.000247	65%	35%	0%
14	3.17	0.0535	0.000247	58%	42%	0%
15	3.42	0.0538	0.000247	50%	50%	0%
16	3.66	0.0540	0.000247	42%	58%	0%
17	3.90	0.0543	0.000246	32%	68%	0%
18	4.17	0.0546	0.000247	21%	79%	0%
19	4.43	0.0549	0.000247	8%	91%	0%
20	4.59	0.0551	0.000245	0%	98%	2%

Tab. 9.50 Speciation of Fe(II) in KCl solutions at 25°C

No.	KCl	$Fe(ClO_4)_2$	$HClO_4$	Fe^{2+}	$FeCl^+$	$FeCl_2(aq)$
	[mol/kg]	[mol/kg]	[mol/kg]	[%]	[%]	[%]
1	0.168	0.0497	0.00101	100%	0%	0%
2	0.416	0.0501	0.00102	99%	1%	0%
3	0.556	0.0504	0.00102	98%	2%	0%
4	0.854	0.0509	0.00103	97%	3%	0%
5	1.15	0.0514	0.00104	96%	4%	0%
6	1.46	0.0519	0.00105	95%	5%	0%
7	1.78	0.0524	0.00106	94%	6%	0%
8	2.09	0.0529	0.00107	92%	8%	0%
9	2.41	0.0534	0.00108	91%	9%	0%
10	2.74	0.0540	0.00109	89%	11%	0%
11	3.07	0.0545	0.00110	87%	13%	0%
12	3.42	0.0551	0.00111	86%	14%	0%
13	3.78	0.0557	0.00113	84%	16%	0%
14	4.12	0.0563	0.00114	82%	18%	0%
15	4.48	0.0569	0.00115	80%	20%	0%
16	0.426	0.0502	0.00102	99%	1%	0%
17	0.561	0.0504	0.00102	98%	2%	0%

9.5.2 Measurements at 40°C

Tab. 9.51 Speciation of Fe(II) in NaCl solutions at 40°C

No.	NaCl	$Fe(ClO_4)_2$	$HClO_4$	Fe^{2+}	$FeCl^+$	$FeCl_2(aq)$
	[mol/kg]	[mol/kg]	[mol/kg]	[%]	[%]	[%]
1	0	0.0500	0.00101	100%	0%	0%
2	0.00952	0.0499	0.00101	100%	0%	0%
3	0.0304	0.0496	0.00101	100%	0%	0%
4	0.0933	0.0500	0.00101	100%	0%	0%
5	0.307	0.0502	0.00101	100%	0%	0%
6	0.661	0.0505	0.00102	98%	2%	0%
7	1.04	0.0508	0.00103	96%	4%	0%
8	1.41	0.0511	0.00104	95%	5%	0%
9	1.74	0.0514	0.00105	93%	7%	0%
10	2.11	0.0517	0.00105	91%	9%	0%
11	2.46	0.0519	0.00106	89%	11%	0%
12	2.84	0.0523	0.00107	87%	13%	0%
13	3.26	0.0526	0.00108	85%	15%	0%
14	3.62	0.0529	0.00109	82%	18%	0%
15	4.03	0.0532	0.00110	79%	21%	0%
16	4.42	0.0535	0.00111	76%	24%	0%
17	4.86	0.0539	0.00112	73%	27%	0%
18	5.28	0.0542	0.00113	70%	30%	0%
19	5.56	0.0544	0.00113	67%	33%	0%
20	6.07	0.0548	0.00114	62%	38%	0%

Tab. 9.52 Speciation of Fe(II) in LiCl solutions at 40°C

No.	LiCl	$Fe(ClO_4)_2$	$HClO_4$	$Mg(ClO_4)_2$	Fe^{2+}	$FeCl^+$	$FeCl_2(aq)$
	[mol/kg]	[mol/kg]	[mol/kg]	[mol/kg]	[%]	[%]	[%]
1	2.14	0.0521	0.00105	-	92%	8%	0%
2	3.18	0.0532	0.00107	-	85%	15%	0%
3	4.38	0.0544	0.00110	-	76%	24%	0%
4	5.68	0.0557	0.00113	-	63%	37%	0%
5	7.00	0.0571	0.00116	-	46%	54%	0%
6	8.33	0.0584	0.00119	-	25%	74%	1%
7	9.77	0.0599	0.00122	-	0%	94%	6%
12	9.71	0.0356	0.00121	0.0153	0%	92%	8%
13	11.18	0.0335	0.00124	0.0179	0%	77%	23%
14	14.43	0.0286	0.00131	0.0206	0%	24%	76%
15	16.07	0.0262	0.00134	0.0267	0%	0%	100%

Tab. 9.53 Speciation of Fe(II) in $MgCl_2$ solutions at 40°C

No.	$MgCl_2$	$Fe(ClO_4)_2$	$HClO_4$	Fe^{2+}	$FeCl^+$	$FeCl_2(aq)$
	[mol/kg]	[mol/kg]	[mol/kg]	[%]	[%]	[%]
1	0.207	0.0502	0.000248	100%	0%	0%
2	0.419	0.0504	0.000247	97%	3%	0%
3	0.631	0.0507	0.000247	96%	4%	0%
4	0.846	0.0509	0.000246	93%	7%	0%
5	1.07	0.0512	0.000246	91%	9%	0%
6	1.29	0.0514	0.000246	89%	11%	0%
7	1.52	0.0517	0.000246	86%	14%	0%
8	1.74	0.0519	0.000247	83%	17%	0%
9	1.96	0.0521	0.000247	79%	21%	0%
10	2.20	0.0524	0.000246	76%	24%	0%
11	2.44	0.0527	0.000247	72%	28%	0%
13	2.91	0.0532	0.000247	61%	39%	0%
14	3.17	0.0535	0.000247	54%	46%	0%
15	3.42	0.0538	0.000247	46%	54%	0%
16	3.66	0.0540	0.000247	38%	62%	0%
17	3.90	0.0543	0.000246	28%	72%	0%
18	4.17	0.0546	0.000247	16%	83%	1%
19	4.43	0.0549	0.000247	3%	94%	3%
20	4.59	0.0551	0.000245	0%	96%	4%

Tab. 9.54 Speciation of Fe(II) in KCl solutions at 40°C

No.	KCl	$Fe(ClO_4)_2$	$HClO_4$	Fe^{2+}	$FeCl^+$	$FeCl_2(aq)$
	[mol/kg]	[mol/kg]	[mol/kg]	[%]	[%]	[%]
1	0.168	0.0497	0.00101	100%	0%	0%
2	0.416	0.0501	0.00102	98%	2%	0%
3	0.556	0.0504	0.00102	96%	4%	0%
4	0.854	0.0509	0.00103	95%	5%	0%
5	1.15	0.0514	0.00104	93%	7%	0%
6	1.46	0.0519	0.00105	91%	9%	0%
7	1.78	0.0524	0.00106	90%	10%	0%
8	2.09	0.0529	0.00107	89%	11%	0%
9	2.41	0.0534	0.00108	87%	13%	0%
10	2.74	0.0540	0.00109	85%	15%	0%
11	3.07	0.0545	0.00110	83%	17%	0%
12	3.42	0.0551	0.00111	82%	18%	0%
13	3.78	0.0557	0.00113	79%	21%	0%
14	4.12	0.0563	0.00114	77%	23%	0%
15	4.48	0.0569	0.00115	75%	25%	0%
16	0.426	0.0502	0.00102	97%	3%	0%
17	0.561	0.0504	0.00102	96%	4%	0%

9.5.3 Measurements at 60°C

Tab. 9.55 Speciation of Fe(II) in NaCl solutions at 60°C

No.	NaCl	$Fe(ClO_4)_2$	$HClO_4$	Fe^{2+}	$FeCl^+$	$FeCl_2(aq)$
	[mol/kg]	[mol/kg]	[mol/kg]	[%]	[%]	[%]
1	0	0.0500	0.00101	100%	0%	0%
2	0.00952	0.0499	0.00101	100%	0%	0%
3	0.0304	0.0496	0.00101	100%	0%	0%
5	0.307	0.0502	0.00101	98%	2%	0%
6	0.661	0.0505	0.00102	96%	4%	0%
7	1.04	0.0508	0.00103	93%	7%	0%
8	1.41	0.0511	0.00104	90%	10%	0%
9	1.74	0.0514	0.00105	89%	11%	0%
10	2.11	0.0517	0.00105	87%	13%	0%
11	2.46	0.0519	0.00106	84%	16%	0%
12	2.84	0.0523	0.00107	82%	18%	0%
13	3.26	0.0526	0.00108	78%	22%	0%
14	3.62	0.0529	0.00109	76%	24%	0%
15	4.03	0.0532	0.00110	73%	27%	0%
16	4.42	0.0535	0.00111	70%	30%	0%
17	4.86	0.0539	0.00112	66%	34%	0%
18	5.28	0.0542	0.00113	63%	37%	0%
19	5.56	0.0544	0.00113	60%	40%	0%
20	6.07	0.0548	0.00114	56%	44%	0%

Tab. 9.56 Speciation of Fe(II) in LiCl solutions at 60°C

No.	LiCl	$Fe(ClO_4)_2$	$HClO_4$	$Mg(ClO_4)_2$	Fe^{2+}	$FeCl^+$	$FeCl_2(aq)$
	[mol/kg]	[mol/kg]	[mol/kg]	[mol/kg]	[%]	[%]	[%]
1	2.14	0.0521	0.00105	-	87%	13%	0%
2	3.18	0.0532	0.00107	-	79%	21%	0%
3	4.38	0.0544	0.00110	-	70%	30%	0%
4	5.68	0.0557	0.00113	-	57%	43%	0%
5	7.00	0.0571	0.00116	-	42%	58%	1%
6	8.33	0.0584	0.00119	-	22%	73%	6%
7	9.77	0.0599	0.00122	-	0%	86%	14%
12	9.71	0.0356	0.00121	0.0153	0%	80%	20%
13	11.18	0.0335	0.00124	0.0179	0%	60%	40%
14	14.43	0.0286	0.00131	0.0206	0%	21%	79%
15	16.07	0.0262	0.00134	0.0267	0%	2%	98%

Tab. 9.57 Speciation of Fe(II) in $MgCl_2$ solutions at 60°C

No.	$MgCl_2$	$Fe(ClO_4)_2$	$HClO_4$	Fe^{2+}	$FeCl^+$	$FeCl_2(aq)$
	[mol/kg]	[mol/kg]	[mol/kg]	[%]	[%]	[%]
1	0.207	0.0502	0.000248	98%	2%	0%
2	0.419	0.0504	0.000247	95%	5%	0%
3	0.631	0.0507	0.000247	92%	8%	0%
4	0.846	0.0509	0.000246	92%	8%	0%
5	1.07	0.0512	0.000246	87%	13%	0%
6	1.29	0.0514	0.000246	84%	16%	0%
7	1.52	0.0517	0.000246	81%	19%	0%
8	1.74	0.0519	0.000247	78%	22%	0%
9	1.96	0.0521	0.000247	74%	26%	0%
10	2.20	0.0524	0.000246	71%	29%	0%
11	2.44	0.0527	0.000247	66%	34%	0%
12	2.68	0.0529	0.000246	61%	39%	0%
13	2.91	0.0532	0.000247	55%	45%	0%
14	3.17	0.0535	0.000247	48%	51%	0%
15	3.42	0.0538	0.000247	41%	59%	1%
16	3.66	0.0540	0.000247	32%	66%	1%
17	3.90	0.0543	0.000246	23%	74%	2%
18	4.17	0.0546	0.000247	12%	83%	5%
19	4.43	0.0549	0.000247	0%	91%	9%
20	4.59	0.0551	0.000245	0%	90%	10%

Tab. 9.58 Speciation of Fe(II) in KCl solutions at 60°C

No.	KCl	$Fe(ClO_4)_2$	$HClO_4$	Fe^{2+}	$FeCl^+$	$FeCl_2(aq)$
	[mol/kg]	[mol/kg]	[mol/kg]	[%]	[%]	[%]
1	0.168	0.0497	0.00101	97%	3%	0%
2	0.416	0.0501	0.00102	96%	4%	0%
3	0.556	0.0504	0.00102	93%	7%	0%
4	0.854	0.0509	0.00103	91%	9%	0%
5	1.15	0.0514	0.00104	89%	11%	0%
6	1.46	0.0519	0.00105	88%	12%	0%
7	1.78	0.0524	0.00106	85%	15%	0%
8	2.09	0.0529	0.00107	85%	15%	0%
9	2.41	0.0534	0.00108	83%	17%	0%
10	2.74	0.0540	0.00109	82%	18%	0%
11	3.07	0.0545	0.00110	78%	22%	0%
12	3.42	0.0551	0.00111	76%	24%	0%
13	3.78	0.0557	0.00113	73%	27%	0%
14	4.12	0.0563	0.00114	71%	29%	0%
15	4.48	0.0569	0.00115	69%	31%	0%
16	0.426	0.0502	0.00102	94%	6%	0%
17	0.561	0.0504	0.00102	93%	7%	0%

9.5.4 Measurements at 80°C

Tab. 9.59 Speciation of Fe(II) in NaCl solutions at 80°C

No.	NaCl	$Fe(ClO_4)_2$	$HClO_4$	Fe^{2+}	$FeCl^+$	$FeCl_2(aq)$
	[mol/kg]	[mol/kg]	[mol/kg]	[%]	[%]	[%]
1	0	0.0500	0.00101	97%	3%	0%
2	0.00952	0.0499	0.00101	96%	4%	0%
4	0.0933	0.0500	0.00101	93%	7%	0%
5	0.307	0.0502	0.00101	90%	10%	0%
6	0.661	0.0505	0.00102	87%	13%	0%
7	1.04	0.0508	0.00103	83%	17%	0%
8	1.41	0.0511	0.00104	81%	19%	0%
9	1.74	0.0514	0.00105	80%	20%	0%
10	2.11	0.0517	0.00105	77%	23%	0%
11	2.46	0.0519	0.00106	74%	26%	0%
12	2.84	0.0523	0.00107	72%	28%	0%
13	3.26	0.0526	0.00108	68%	32%	1%
14	3.62	0.0529	0.00109	65%	34%	1%
15	4.03	0.0532	0.00110	62%	37%	1%
16	4.42	0.0535	0.00111	59%	40%	1%
17	4.86	0.0539	0.00112	55%	44%	1%
18	5.28	0.0542	0.00113	51%	47%	2%
19	5.56	0.0544	0.00113	49%	49%	2%
20	6.07	0.0548	0.00114	44%	54%	2%

Tab. 9.60 Speciation of Fe(II) in LiCl solutions at 80°C

No.	LiCl	$Fe(ClO_4)_2$	$HClO_4$	$Mg(ClO_4)_2$	Fe^{2+}	$FeCl^+$	$FeCl_2(aq)$
	[mol/kg]	[mol/kg]	[mol/kg]	[mol/kg]	[%]	[%]	[%]
1	2.14	0.0521	0.00105	-	78%	22%	0%
2	3.18	0.0532	0.00107	-	69%	31%	0%
3	4.38	0.0544	0.00110	-	59%	40%	1%
4	5.68	0.0557	0.00113	-	46%	52%	2%
5	7.00	0.0571	0.00116	-	31%	63%	5%
6	8.33	0.0584	0.00119	-	10%	76%	14%
12	9.71	0.0356	0.00121	0.0153	0%	68%	32%
13	11.18	0.0335	0.00124	0.0179	0%	50%	50%
14	14.43	0.0286	0.00131	0.0206	0%	26%	74%
15	16.07	0.0262	0.00134	0.0267	0%	26%	74%

Tab. 9.61 Speciation of Fe(II) in $MgCl_2$ solutions at 80°C

No.	$MgCl_2$	$Fe(ClO_4)_2$	$HClO_4$	Fe^{2+}	$FeCl^+$	$FeCl_2$(aq)
	[mol/kg]	[mol/kg]	[mol/kg]	[%]	[%]	[%]
1	0.207	0.0502	0.000248	89%	11%	0%
2	0.419	0.0504	0.000247	85%	15%	0%
3	0.631	0.0507	0.000247	83%	17%	0%
5	1.07	0.0512	0.000246	79%	21%	0%
6	1.29	0.0514	0.000246	75%	25%	0%
7	1.52	0.0517	0.000246	73%	26%	0%
8	1.74	0.0519	0.000247	68%	32%	1%
9	1.96	0.0521	0.000247	64%	35%	1%
10	2.20	0.0524	0.000246	61%	38%	1%
11	2.44	0.0527	0.000247	55%	43%	1%
12	2.68	0.0529	0.000246	50%	48%	2%
13	2.91	0.0532	0.000247	44%	54%	2%
14	3.17	0.0535	0.000247	38%	59%	4%
15	3.42	0.0538	0.000247	30%	65%	5%
16	3.66	0.0540	0.000247	23%	70%	8%
17	3.90	0.0543	0.000246	12%	78%	10%
18	4.17	0.0546	0.000247	1%	84%	15%
21	3.66	0.0296	0.00110	23%	70%	7%
22	3.92	0.0281	0.00111	13%	77%	10%
23	4.18	0.0267	0.00112	6%	81%	14%
24	4.44	0.0252	0.00113	0%	81%	19%
25	4.60	0.0243	0.00113	0%	78%	22%

Tab. 9.62 Speciation of Fe(II) in KCl solutions at 80°C

No.	KCl	$Fe(ClO_4)_2$	$HClO_4$	Fe^{2+}	$FeCl^+$	$FeCl_2(aq)$
	[mol/kg]	[mol/kg]	[mol/kg]	[%]	[%]	[%]
1	0.168	0.0497	0.00101	89%	11%	0%
2	0.416	0.0501	0.00102	89%	11%	0%
3	0.556	0.0504	0.00102	85%	15%	0%
4	0.854	0.0509	0.00103	83%	17%	0%
5	1.15	0.0514	0.00104	81%	19%	0%
6	1.46	0.0519	0.00105	79%	21%	0%
7	1.78	0.0524	0.00106	77%	23%	0%
8	2.09	0.0529	0.00107	76%	24%	0%
9	2.41	0.0534	0.00108	74%	26%	0%
10	2.74	0.0540	0.00109	67%	33%	0%
11	3.07	0.0545	0.00110	66%	34%	0%
12	3.42	0.0551	0.00111	63%	37%	0%
13	3.78	0.0557	0.00113	61%	39%	0%
14	4.12	0.0563	0.00114	58%	41%	1%
15	4.48	0.0569	0.00115	86%	14%	0%
16	0.426	0.0502	0.00102	85%	15%	0%
17	0.561	0.0504	0.00102	89%	11%	0%

TEILBERICHT C

Arbeiten des PSI-LES

Der von PSI-LES an KIT-INE übermittelte Bericht zu den durchgeführten Arbeiten innerhalb von ThermAc (inklusive der Verlängerungsphase) ist nachfolgend dargestellt.

ThermAc project final report

PSI contribution

G. D. Miron[1], D. A. Kulik[1], T. Thoenen[1]

[1] Paul Scherrer Institut, LES, Forschungsstrasse 111, 5232 Villigen PSI, Switzerland

Summary

ThermAc is a joint project ("Verbundprojekt") on aquatic actinide chemistry and thermodynamics at elevated temperature conditions financed by the German Federal Ministry of Education and Research that started in March 2015 and ended in April 2020. The general objective of the ThermAc project was to extend the chemical understanding and available thermodynamic database for actinides, long-lived fission products and relevant matrix elements in aquatic systems to elevated temperatures (using a combination of experiments, estimation methods, and quantum chemical calculations).

The contribution of PSI LES (Laboratory for Waste Management) to ThermAc consists of two complementary parts:

1. Evaluation and systematic application of the isocoulombic estimation method for the extrapolation of equilibrium constants to higher temperatures.
2. Revision and extension of the existing PMATCHC software for the management of internally consistent thermodynamic datasets.

Work at LES was centered mainly on the application and testing of the isocoulombic estimation method for the solid solution – aqueous solution system (Ba, Sr, Ra)SO4(s)–H2O(l); on validating the applicability of various alternative isocoulombic reactions to estimate $\log K_T^\circ$ values of aqueous complexation reactions for lanthanides and actinides to elevated temperatures; and on the development of parts of a ThermoEcos integrated software framework for managing, estimating, and calculating thermodynamic data as a function of pressure and temperature: the C++ library ThermoFun for temperature corrections of thermodynamic data, the ThermoHub database for storing thermodynamic data, and the ThermoMatch code for managing thermodynamic data in the database and in exported files.

In the first part of the report, we present an overview of the development of the software tools and their main functionality and applications. In the second part, we present a systematic evaluation of the use of isocoulombic reactions for extrapolating equilibrium constants to higher temperatures with focus on actinides and lanthanides complexation. This was greatly simplified and accelerated using the dedicated software and database for fast and accurate generation of reactions and calculation of their effects.

1. Software for managing thermodynamic data

The reliability of results of (geo)chemical modeling largely depends on the flexibility, accuracy and consistency of thermodynamic models and their input data. Alternative chemical thermodynamic databases exist for various areas of application (aquatic systems, petrology, cement, waste), but they cannot be easily compared or combined. This situation calls for the creation of automated tools and workflows to generate and maintain internally consistent thermodynamic datasets.

The ThermoEcos ecosystem is an open-source framework under continuous development, consisting of code tools and databases for storing, managing, processing, and delivering thermodynamic data. It provides users and modeling codes with a unified access to thermodynamic data. Tools for which development started within the ThermAc prject are (**Figure 1**): (1) ThermoHub database server which provides efficient and traceable storage and management of thermodynamic data; (2) ThermoMatch client and code (formerly called PMATCHC and later PMATCH++) for editing, managing, importing and exporting thermodynamic data stored in ThermoHub and thermodynamic data conversions between substances and reactions; (3) ThermoFun, a C++ library for retrieving standard state thermodynamic properties of chemical substances and reactions from the ThermoHub database, with conversion from reference temperature (298.15 K) and pressure (1 bar = 105 Pa) to the temperature and pressure of interest.

Software development was carried out by G.D. Miron (and D. Kulik as software architect) in close collaboration with our IT consultant Svitlana V. Dmytrieva (Cosylab) who was funded by ThermAc. The ThermoHub server was set up and is maintained by Congineer GmbH Switzerland as in-kind contribution. Work on these software tools has started during the ThermAc project, but their development continues and is foreseen to continue in future projects.

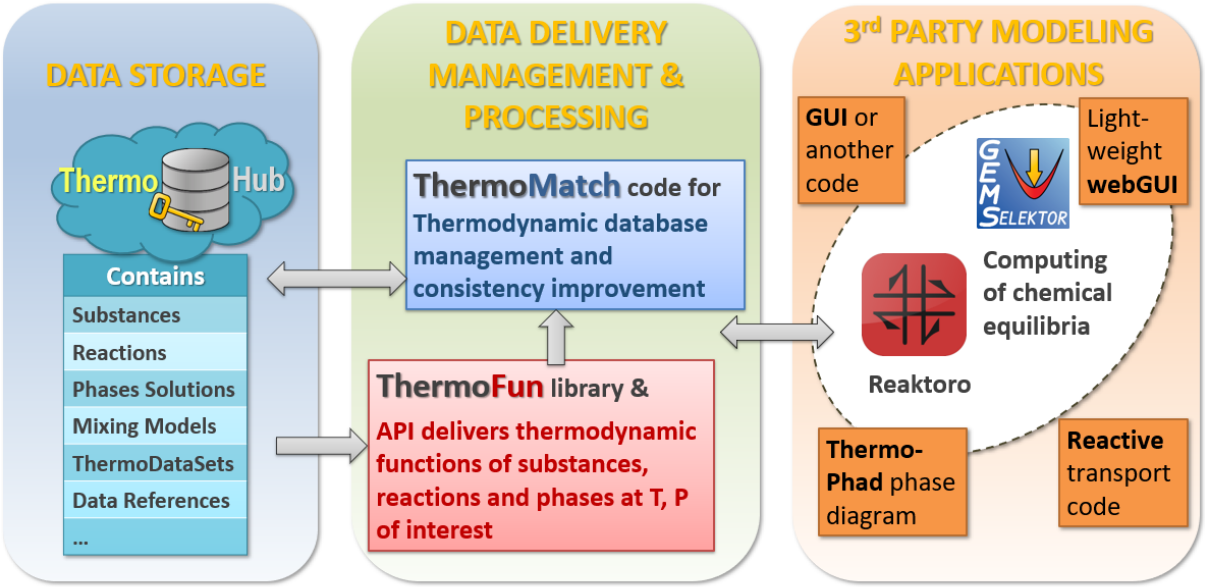

Figure 1. *Data-centric integration of the software tools and codes developed in the ThermAc project. Arrows show the directions of data flow. More details can be found at https://thermohub.org.*

1.1. ThermoHub

ThermoHub is a database server hub multi-format database for storing various types of thermodynamic data and thermodynamic datasets. It uses a flexible JSON format that allows the storage of structured, hierarchical, and often incomplete thermodynamic and other chemical data. ThermoHub employs a property graph database allowing for complete traceability of the data using graph links between data source documents (references) and any data field in stored data documents. A graph layer can be independently added on top of the individual data types, representing different links between records (e.g. links to data source records).

The ThermoHub *property graph database* (Kulik, Miron, Thoenen, in preparation) consists of two types of structured data objects:

- **Vertices** (or nodes): Contain data as nested JSON documents
- **Edges** (or links): Connect two vertices, are directed (inbound or outbound) and contain data as key-value pairs

Vertices "know" nothing about the edges; any number of edges of the same or different types can be connected to a vertex. Each vertex has at least one inbound or outbound edge (no isolated vertices).

Thermodynamic entities such as reactions, interaction parameters, phases, LMA reaction sets, GEM thermodynamic data sets, or data source references can all be represented, traversed, extracted and processed as property graphs created in the graph database after importing/adding the data as vertices.

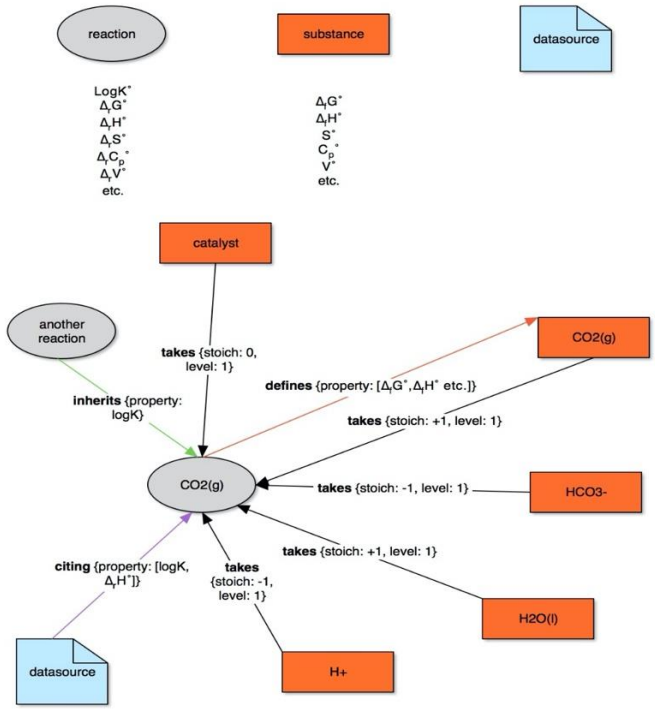

Figure 2. *Representation of the chemical reaction $HCO_3^- + H^+ \rightleftharpoons CO_{2(g)} + H_2O_{(l)}$ as a property graph.*

Figure 2 shows how chemical reactions are represented in a property graph, taking the reaction

$$HCO_3^- + H^+ \rightleftharpoons CO_2(g) + H_2O(l)$$

as an example, for which three types of vertices can be distinguished:

- **substance vertex**: Contains thermodynamic data such as Δ_fG°, Δ_fH°, S°, Cp°, V°, etc. for a specific aqueous species, liquid, gas, or solid substance
- **reaction vertex:** Contains thermodynamic data such as log K°, Δ_rG°, Δ_rH°, Δ_rS°, Δ_rCp°, Δ_rV°, etc. for a specific reaction among different substances
- **datasource vertex:** Contains bibliographic data for a specific datasource or reference

The reaction involves four types of edges, the directions of which represent the flow of information:

- **“takes” edge:** Connects the vertex of a substance involved in a reaction with the corresponding reaction vertex, the “takes” edge contains the stoichiometric coefficient of the substance in the reaction (negative for reactants, positive for products and zero for catalysts)
- **“defines” edge:** Connects the reaction vertex with the vertex of a substance whose thermodynamic properties are defined by those of the reaction and the other substances involved in the reaction, information on which properties are defined are contained in the edge
- **“inherits” edge:** Connects a reaction (or substance) vertex with another reaction or (substance) which inherits one or more thermodynamic properties from the first reaction (or substance), e.g., thermodynamic data for americium species are often "inherited" from the corresponding curium species
- **“citing” edge:** Connects a datasource vertex with a reaction or substance vertex which contains data from that datasource. Information on the referenced data is stored in the edge

This property graph structure is convenient for the automatic generation of isocoulombic reactions among specific substances to extrapolate equilibrium constants to higher temperatures (see Section 1.2.3).

Several other data structures are in use in ThermoHub. These are needed to describe the thermodynamic data of a solution phase such as the vertex types: Phase (data for phases), InteractionModel (data for solution models) and Interaction (data for interactions between different substances).

An important data structure of vertex type is the ThermoDataSet which is a collection of thermodynamic data for substances and/or reactions linked through edges to the ThermoDataSet vertex. This entity defines what researchers would refer to as a thermodynamic database (e.g. slop98, PSI/Nagra database). Several ThermoDataSets (well-known thermodynamic databases) are already available in ThermoHub (Table 1), and several others will be uploaded. New ThermoDataSets can be put together by thermodynamic database experts in GEM (Gibbs energy based) or LMA (reaction based) formats.

Table 1. *Currently available ready to use ThermoDataSets in the remote ThermoHub server. The database is periodically extended with new ThermoDataSets.*

Database (references)	**Application field**
psinagra-12-07 (Hummel et al., 2002; Thoenen et al., 2014)	radioactive waste disposal
slop98-inorganic and slop98-organic (Shock et al., 1997; Sverjensky et al., 1997)	aqueous geothermal systems (revised SUPCRT92)
cemdata18 (Lothenbach et al., 2019)	suitable for cement systems
Heracles (PSI Heracles)	modeling of U and fission products
mines16 (https://geoinfo.nmt.edu/tdb/)	modeling magmatic-hydrothermal ore forming processes
aq17 (Miron et al., 2017)	modeling fluid rock interaction at hydrothermal conditions (major elements)
slop16 (GEOPIG)	aqueous geothermal systems (organic and inorganic, updated to slop98)

1.2. ThermoMatch

ThermoHub data can be managed using the **ThermoMatch** graphical user interface (GUI) client module. ThermoMatch provides various methods for maintaining, editing, importing and backing up data, as well as functionality to define and keep scripts for importing/exporting thermodynamic databases from/to foreign format files (e.g. slop.dat, phreeqc, json-thereda, csv, etc.). ThermoMatch is also a platform for consistency checks, and it provides simple data aggregation tools for the automatic generation of reactions and particularly of isocoulombic reactions. These applications allow fast and easy conversion of substance-based datasets (for GEM - Gibbs Energy Minimization) into reaction-based databases (for LMA - Law of Mass action codes), and help investigating the extrapolation capabilities of isocoulombic reactions. Workflows for consistency checks can be developed for performing checks within a thermodynamic dataset (e.g. properties consistent with thermodynamic relationships) or between datasets (e.g. consistency of the reaction properties with those of reactants from different databases).

ThermoMatch can be used to:

- Create, read, update, and delete (CRUD) operations for maintaining the ThermoHub database.
- Import 3rd party thermodynamic databases from foreign format files (e.g. slop.dat, phreeqc, json, csv, etc.), and extending existing ones with new substances and reactions.
- Generate LMA (Law of Mass Action) reaction-based style databases from substance-based GEM (Gibbs Energy Minimization) style databases using the automatic reaction generator module.
- Combine reactions into isocoulombic/isoelectric reactions, useful for extrapolating reaction properties at elevated temperatures when no or little experimental data is available.

1.2.1. Import/Export

An important step in developing the new framework for managing thermodynamic data was to import the available data for chemical elements and substances from various existing (exported) formats into the new ThermoHub database. ThermoMatch uses the JsonIO and JsonUI libraries for managing structured data, allowing the import of thermodynamic data from “foreign” file types (e.g., text, JSON, YAML, XML) and formats (e.g. key-value, tabulated data, structured data).

To import data from “foreign” files into the data object model (DOM - describes the structure of the stored data in the database), it is necessary to create a format description file. This file contains a list of matches that connect the data blocks from the imported file with the place in the DOM where this data should be stored. The format file can be created and edited in a JsonUI data widget (**Figure 3**) or with a text editor and saved in a JSON file or in the database. Having such a format files makes it easy and efficient to automatically import thermodynamic data stored in different formats, opening the way for ThermoMatch and ThermoHub to become a “universal hub” for retrieving, storing, importing, exporting and managing thermodynamic data.

Several import scripts for database files of major geochemical software tools are used in ThermoMatch to import from formats such as: csv (table format exported from excel), slop (SUPCRT), json-thereda, GEM-Selektor, phreeqc, etc.

This is essential for accessing various sources of thermodynamic data and storing them in one place. This makes it easier to compare different databases or to evaluate different temperature and pressure correction methods and extrapolation methods such as using isocoulombic reactions.

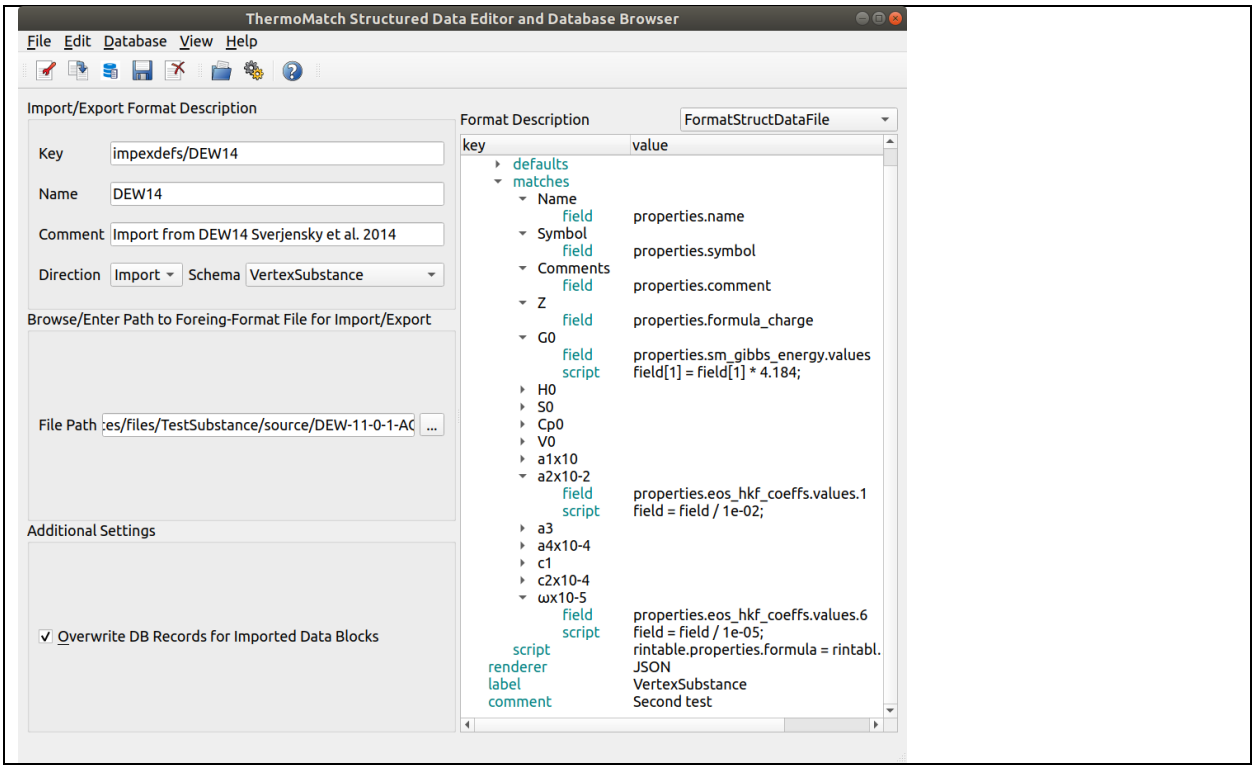

Figure 3. *Import script in JsonUI widgets describing the foreign format, matching the fields from the foreign format (e.g. "Z") with the path in the ThermoHub data structure (e.g. "properties.formula_charge").*

The data present in the ThermoHub database can also be exported into many other formats. The simplest possibility is to export the selected data or a ThermoDataSet into a table format or a simplified JSON format that contains only the fields that are important for the user or for a specific application (e.g. ready for publication table with thermodynamic data for selected substances). More complex export functionality and scripts are available for exporting data into foreign formats of widely used geochemical modeling software (e.g. GEM-Selektor and phreeqc, **Figure 4**).

The import/export capability of ThermoMatch can be easily extended to accommodate many other foreign formats.

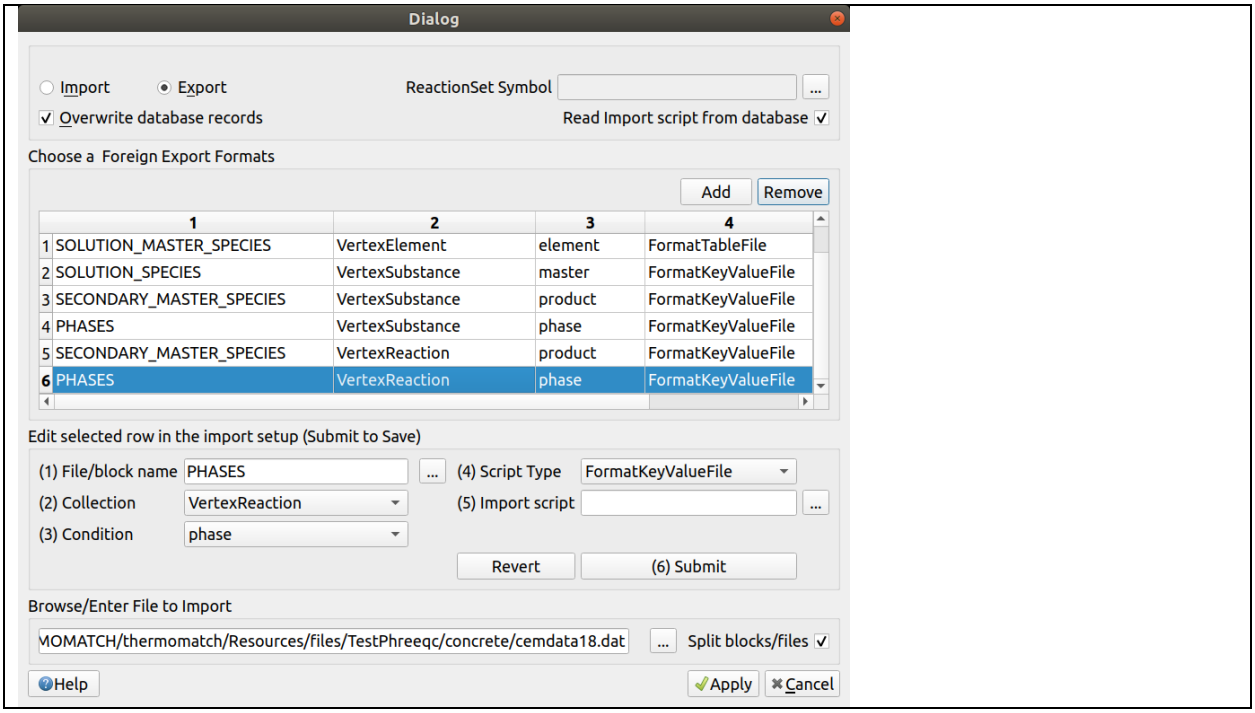

Figure 4. *Export widget for producing phreeqc.dat database files. Different sections from the phreeqc database (1st column) are connected with data types present from ThermoHub (second column).*

1.2.2. Algorithm for generating reactions

An algorithm for generating reactions was developed in ThermoMatch and can be used through the reaction generator widget. The algorithm uses the Chemical Reaction Stoichiometry (CRS) method (Missen and Smith, 1998) to generate a set of reactions for product species in terms of master species. We can consider a system with M elements and N substances (M master species, N-M product species). For example: C, O, H, (e-) as elements and HCO_3^-, OH^-, H^+, CO_3^{2-}, $CO_{2(aq)}$ as substances with HCO_3^-, OH^-, H^+ selected as masters species. We write the formula matrix A (M rows, N columns), in which each column

represents the ordered elemental composition of a substance (formula vector) (**Table 2**). Using row operations (addition/subtraction) and column interchange (if necessary), a unit matrix is created in the upper left part of matrix A. For our simple example, we perform the following matrix operations:

row(3) – row(2)

row(2) – 3*row(1)

row(3) + 2*row(1)

row(4) – row(1) – row(2) + row(3)

These operations lead to **A***, the unit matrix form of **A** (**Table 3**). Each column to the right of the unit matrix in **A*** contains the stoichiometric coefficients of the reaction leading to the respective product species (column header). In our example, the last two columns in A* are the desired reactions:

HCO_3^- - H^+ = CO_3^{2-}

HCO_3^- -OH^- = CO_2(aq)

Table 2. *Formula matrix **A**.*

	HCO_3^-	OH^-	H^+	CO_3^{2-}	CO_2(aq)
C	1	0	0	1	1
O	3	1	0	3	2
H	1	1	1	0	0
e^-	-1	-1	1	-2	0

Table 3. *Reaction matrix **A**** *(row-reduced form of **A**)*

	HCO_3^-	*OH^-*	*H^+*	*CO_3^{2-}*	*CO_2(aq)*
HCO_3^-	*1*	*0*	*0*	*1*	*1*
OH^-	*0*	*1*	*0*	*0*	*-1*
H^+	*0*	*0*	*1*	*-1*	*0*
e^-	*0*	*0*	*0*	*0*	*0*

The system in the above example can be described using 3 master species and 2 independent reactions, while the electron does not have to be explicitly defined.

The “row-reduce” algorithm described by (Missen and Smith, 1998) was also implemented in the reaction generator module. The reaction generator module is operated via a simple graphical widget. After selecting the source thermodynamic dataset (e.g. PSI/Nagra database, (Hummel et al., 2002;

Thoenen et al., 2014)) and the chemical elements of the chemical system to be considered, a list of all feasible species is produced, and the user may choose the desired master species ('M') from the list. With a mouse click, the list of reactions is then generated for all remaining product (dependent, 'D') species (**Figure 5**). The generated reactions can then be saved in the database. This allows the user to generate various types of reactions that can be later combined into isocoulombic reactions (see section 1.2.3), and to further investigate how their properties can be more accurately extrapolated to different conditions (e.g. at different temperatures, see section 2).

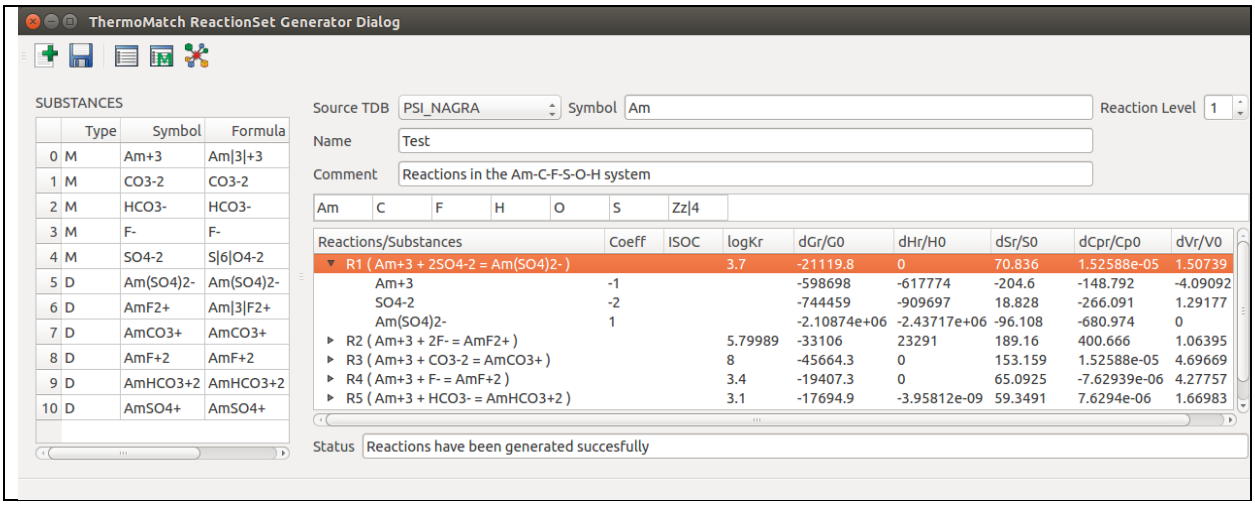

Figure 5. *The ReactionSet generator widget.*

Application: generating an LMA database from GEMS dataset

One important application of the reaction generator is to use it for creating LMA type reaction sets out of GEM type databases that contain standard thermodynamic data for substances, but not for reactions between them. This operation was automated by extending and using the ThermoMatch, our new innovative tool for managing TDBs both for substances (GEM format) and reactions (LMA format).

For example, the new Cemdata18 thermodynamic database (TDB) was developed for the GEM (Gibbs Energy Minimization) format, which includes standard-state thermodynamic properties of cement-relevant substances and some aqueous complexes. Details on the development of Cemdata18 can be found in (Lothenbach et al., 2019).

The database was imported into ThermoMatch using an import script from the GEM-Selektor foreign format. For generating the LMA style reactions for product species, the following aqueous "master" species were selected, based on their generic predominance: Ca^{+2}, Mg^{+2}, Sr^{+2}, Na^{+}, K^{+}, H^{+}, CO_3^{-2}, SO_4^{-2}, Cl^{-}, NO_3^{-}, AlO_2^{-}, FeO_2^{-}, SiO_2^{0}, H_2O^{0}. For all the "product" species in the Cemdata18 database, the formation reactions were automatically generated, and their standard properties at 25 °C and 1 bar were calculated. The generated reactions were then saved as an LMA type ThermoDataSet and then exported into a PHREEQC *.dat file using an export script developed for this purpose (Lothenbach et al., 2019; Miron et al., 2018). This provided the PHREEQC modeler community with the latest development

related to the thermodynamics of cementitious materials. It also shows the potential of innovative tools such as ThermoMatch for supplying relevant TDBs of improved quality and consistency in various formats in a semi-automatic, less error-prone way, to embrace as broad circles of specialists as possible.

1.2.3. Algorithm for generating isocoulombic/isoelectric reactions

An isocoulombic reaction has the same number and type of charged species on both sides of the reaction while for an isoelectric reaction the total amount of charge (positive or negative) of the reactants is equal to the total amount of charge of the products (see section 2). Therefore, the isocoulombic reactions are a subset of the set of isoelectric reactions.

Isocoulombic and isoelectric reactions can be created by linear combination of non-isocoulombic reactions. For example, two reactions that have the same charge pattern (map) can be linearly combined into an isocoulombic reaction (Simmler, 2012):

	Reaction	Charge pattern {"charge type": coefficient}
(1)	$UO_2^{+2} + CO_3^{-2} = UO_2CO_{3(aq)}$	{"+2": -1, "-2": -1}
+ (2)	$CaCO_{3(cr)} = Ca^{+2} + CO_3^{-2}$	{"+2": 1, "-2": 1}
	$CaCO_{3(cr)} + UO_2^{+2} + CO_3^{-2} = Ca^{+2} + UO_2CO_{3(aq)} + CO_3^{-2}$	{"+2": 0, "-2": 0}
	$CaCO_{3(cr)} + UO_2^{+2} = Ca^{+2} + UO_2CO_{3(aq)}$	{"+2": 0}

Using the principle of reaction charge pattern, an algorithm that generates all possible isocoulombic reactions from a list of reactions for two or more combinations was developed (Miron, Kulik, Thoenen, in preparation). The list of reactions is separated into two groups: the investigated reactions (i.e. the reactions to be made isocoulombic), and the model reactions (the reactions that are combined with the investigated ones to produce isocoulombic reactions). For each investigated reaction, the algorithm starts a recursive loop through all the model reactions and looks in the charge pattern for a charge in the model reaction that can cancel out a charge present in the investigated reaction. This allows to test all possible combinations with one or more model reactions for each investigated reaction. At the end, only the resulting combined reactions that have all their charges in the charge pattern with zero coefficient are kept as isocoulombic reactions.

An additional module implemented in ThermoMatch is the Isocoulombic Reaction Generator, aimed at compiling all possible reactions with the same-charge species on both sides. This module is useful for performing systematic investigations into using isocoulombic reactions to predict their standard thermodynamic properties at elevated temperatures, where little or no experimental data are available (see section 2). The module comes as a graphical widget, where the user can select a list of reactions to be investigated and a list of model reactions, and generate all possible isocoulombic reactions (**Figure 6**). With the use of the ThermoFun library, the standard properties of isocoulombic reactions are calculated at elevated temperatures using one-term, two-term or van't Hoff, and three-term extrapolations (see Appendix A). The properties of model reactions are also calculated using ThermoFun, based on the methods and their respective coefficients set in their database records or based on the properties of the

reactants that take part in the reactions. Predicted effects of the investigated reaction are retrieved at each temperature and pressure point from the calculated properties of the model reaction and from those of the isocoulombic reaction. In addition, the properties of the reaction defined species present in the isocoulombic reaction are also calculated from the properties of the isocoulombic reaction and the rest of the reactants participating in the reaction (provided that their properties and a method for extrapolating them is defined). The predictions from the generated isocoulombic reactions can then be plotted, and their quality can be checked within desired temperature and pressure intervals.

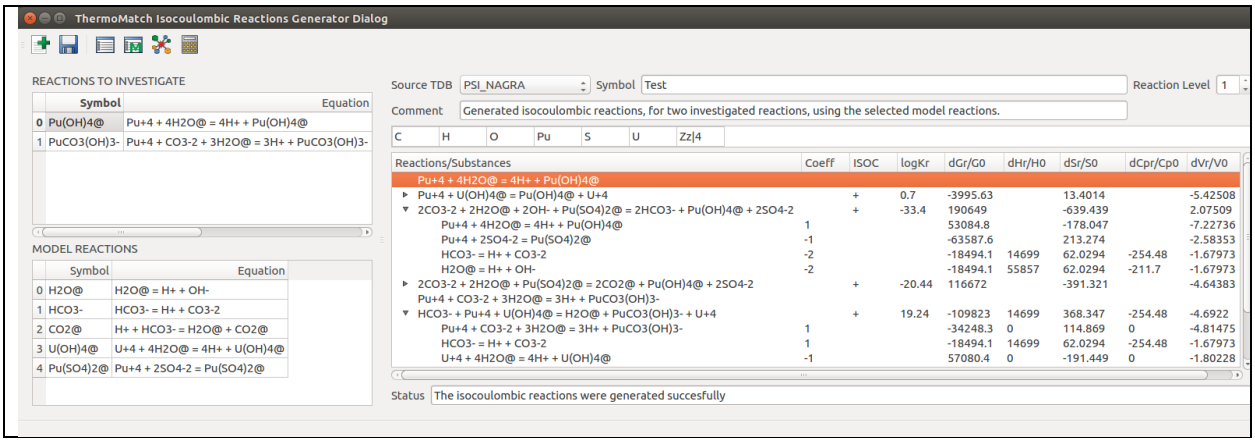

Figure 6. *Isocoulombic reaction generator widget.*

1.3. ThermoFun

ThermoFun (Thermodynamic Functions) is a universal open-source client that delivers thermodynamic properties of substances and reactions at temperature and pressure of interest. ThermoFun solves the problem of having hard-coded methods or databases specific to one modeling code by separating the input data, the EoS parameters, and the thermodynamic functions, and delivering the thermodynamic data to any C/C++ or Python code, in principle.

The ThermoFun library contains a collection of models and Equations of State (EoS) for temperature-pressure corrections of standard thermodynamic functions for: solid, aqueous, gaseous, and melt components (see Table 4 for current implementations).

The code architecture was developed such that new thermodynamic functions and methods can be implemented as modules or “slots”, thus making it possible at any time to extend the library with additional thermodynamic methods or equations of state developed in the future.

ThermoFun can automatically pull the required standard thermodynamic data from the remote ThermoHub server, or from the user-provided local JSON files. These data represent records of substances and reactions containing reference thermodynamic properties and assigned T-P correction methods with their respective coefficients, that are connected through property graph links to a thermodynamic dataset (ThermoDataSet), see section 1.1.

ThermoFun has two main modes of calculating standard molar properties of substances and reactions. This depends on the available data and the existing relations between the substance and reaction records in the database.

The first and default calculation mode allows to use the method that is specified in the respective substance or reaction record (e.g. the record Ca^{2+} can have the T-P correction method specified as "HKF") to perform temperature and pressure corrections to the standard state properties.

The second calculation mode uses the graph links between the records in the database. For example, the properties of a reaction can be calculated from the properties of all reactants participating in the reaction, which, in turn, are corrected for temperature and pressure with their own specified correction method. The properties of a substance can also be calculated from the properties of a reaction and the properties of all other reactants participating in the reaction. Such a substance is linked to a reaction through an edge of type "defines" that signifies that its properties are defined by the linked reaction. More complex combinations are possible with records that have their properties calculated using their own methods and others using the assigned graph links. To do this, ThermoFun uses a recursive algorithm that starts from the deepest level, where the properties of all records can be independently calculated, and travels through the graph up to the selected record (Miron, Kulik, Leal, Thoenen, in prep.).

The library can be used by third-party codes (written in C++ or Python) that require standard state thermodynamic properties in calculations (e.g. equilibrium solvers, phase diagram plotters). This is possible through the C++ or Python application programming interface (API) of ThermoFun, which can be used for single or batch calculations (Figure 7).

ThermoFun uses the automatic differentiation scheme developed in Reaktoro (http://reaktoro.org) for some of the implemented models. This means that, besides the calculated values of the respective thermodynamic properties, the library API can provide their first- and second-order derivatives with respect to temperature and pressure. This can significantly accelerate calculations of geochemical equilibria using the Reaktoro GEM and LMA algorithms (Leal et al., 2017, 2016). In addition, the automatic differentiation is used in ThermoFun to compute the error propagation from the input reference properties through the T and P correction method to the calculated properties at the desired T and P.

For fast investigation, tabulation, or examination of thermodynamic data, ThermoFun offers the possibility of using a graphical widget (ThermoFunGUI) for tabulating thermodynamic properties of substances. Using the widget, the user can select a desired thermodynamic dataset (ThermoDataSet), filter the data by chemical elements, select a list of substances or reactions, define a list of T and P points, and select standard thermodynamic properties to be calculated (**Figure 8**). Results are written into a comma-separated values (CSV) file that can be viewed and plotted using the "Results" button, or imported into any commercial spreadsheet software.

A

```cpp
#include "Thermofun/ThermoFun.h"
using namespace std;

int main()
{
  // Create the engine object using a database file in JSON format
  // Examples of such files can be found in /Resources/databases/ folder or can be
  // retrieved from ThermoHub database using ThermoHubClient
  ThermoFun::Engine engine("aq17-thermofun.json");

  double T       = 398.15; double P = 1e7; // in K and Pa

  auto propAl    = engine.thermoPropertiesSubstance(T, P, "Al+3");

  // extracting values from results for the Gibbs energy
  double G0      = propAl.gibbs_energy.val; // value
  double G0dT    = propAl.gibbs_energy.ddt; // derivative with T = -S0
  double G0error = propAl.gibbs_energy.err; // propagated error

  return 0;
}
```

B

```cpp
#include "Thermofun/ThermoFun.h"
using namespace std;

int main()
{
    ThermoFun::Batch batch("aq17-thermofun.json");

    batch.setPropertiesUnits({"temperature", "pressure"},{"degC","bar"});
    batch.setTemperatureIncrement(0, 200, 25);
    batch.setPressureIncrement(100, 1000, 50);

    batch.thermoPropertiesSubstance({"Al+3", "OH-", "SiO2@"},
                                    {"gibbs_energy","entropy", "volume", "enthalpy"},
                                   ).toCSV("results.csv");
    return 0;
}
```

Figure 7. *Example of using the ThermoFun library to calculate the thermodynamic properties of a substance (A) using the ThermoEngine (API) or doing batch calculations for a list of substances at several P and T (B) using the ThermoBatch (API).*

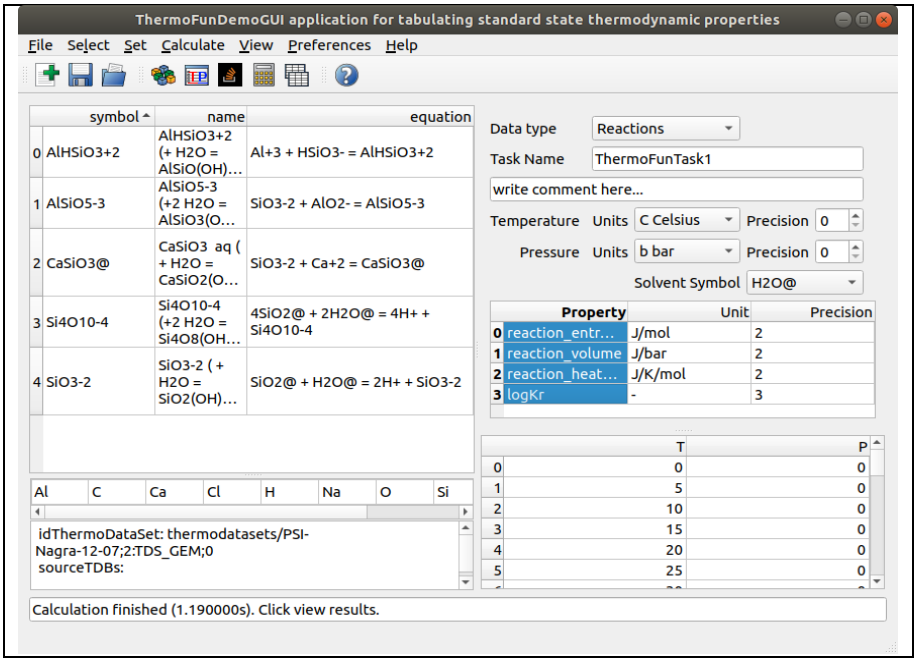

Figure 8. *ThermoFunGUI with selected reactions, selected properties to calculate and T-P points list.*

1.3.1. Methods and EoS

In ThermoFun, several popular Equations of State (EOS) and temperature and pressure correction models for substances are implemented (Table 4). These include the IAWPS95 (Wagner and Pruß, 2002) and ZHANG AND DUAN (2005) EOS for water. The latter, together with the newly implemented model for calculating the dielectric properties of H_2O and the revised HKF model (Sverjensky et al., 2014) allows for calculating the properties of aqueous ions and complexes at pressures beyond the previous 5 kbar limit of the HKF model (Tanger and Helgeson, 1988). The library allows different combinations of the available models for correcting the standard state thermodynamic properties. For example, it is possible to combine the standard state properties of H_2O calculated with the IAWPS95 EOS, the dielectric permittivity calculated using the empirical fit of Sverjensky et al. (2014), and the revised parameters for the HKF model (Sverjensky et al., 2014), to calculate the reference properties of ions and aqueous species at a given temperature and pressure.

Table 4. *Methods and equations of state (EOS) currently implemented in ThermoFun*

Substances	Reactions
Heat Capacity integration Cp = f(T)	Δ_rCp = f(T); Δ_rG = f(T); logK = f(T); Δ_rV = f(T);
Molar volume integration V = f(P,T)	Marshall-Franck density model, (Marshall and Franck, 1983; Mesmer et al., 1991)
Birch-Murnaghan, Cp and V integration (Birch, 1947; Holland and Powell, 1998; Murnaghan, 1944)	Modified Ryzhenko-Bryzgalin (MRB) model (Ryzhenko et al., 1985)
Helgeson-Kirkham-Flowers (HKF) (Tanger and Helgeson, 1988)	Dolejs-Manning density model (Dolejš and Manning, 2010)
Akinfiev-Diamond (Akinfiev and Diamond, 2003) nonelectrolyte model	Temperature extrapolations
Churakov-Gottschalk fluid EoS (Churakov and Gottschalk, 2003)	One term (logK = const. when Δ_rH = 0)
Peng-Robinson fluid EoS (Peng and Robinson, 1976)	One term (Δ_rH = Δ_rG const. when Δ_rS = 0)
Peng-Robinson-Stryjek-Vera fluid EoS (Stryjek and Vera, 1986)	Two term (Van't Hoff, Δ_rCp = 0)
Compensated Redlich-Kwong fluid EoS (Holland and Powell, 1991; Redlich and Kwong, 1949)	Three term (Δ_rCp = const.)
Soave-Redlich-Kwong fluid EoS (Soave, 1972)	
Holland and Powell (1998) density model for aqueous species	
Anderson (1991) density model for aqueous species	
H_2O EoS	H_2O Dielectric constant
Haar-Gallagher-Kell (Haar et al., 1984)	Johnson and Norton (1992)
IAPWS Formulation (1995) (Wagner and Pruß, 2002)	Fernandez et al. (1997)
Zhang & Duan (Zhang and Duan, 2005)	Sverjensky et al. (2014)

For calculating the properties of reactions, extrapolation methods such as one-, two-, and three-term extrapolations are available. In addition, the properties of reactions can also be calculated as a function of temperature and pressure using a density model, provided the model coefficients for the desired reaction are available. Density models describe the change in $\log K^{\circ}_{TP}$ as a function of the water solvent density.

All these methods are based on different physical concepts and have a certain range of applicability and accuracy. ThermoFun makes it possible to test their performance against each other, against other estimation methods such as using isocoulombic reactions, or use them to calculate the properties of model reactions used to construct isocoulombic reactions.

Application: Impact of using different thermodynamic and electrostatic models on the calculated properties of solutes with the HKF EoS

The Helgeson-Kirkham-Flowers (HKF) equation of state (EoS) model (Tanger and Helgeson, 1988) is extensively used in geochemistry to calculate standard state thermodynamic properties of aqueous ions and complexes in wide ranges of temperature and pressure. The HKF EoS uses the dielectric constant of the solvent which is formulated as a function of the solvent density. Several models for calculating thermodynamic and electrostatic properties of water have been developed (Dolejš, 2013; Miron et al., 2019). Existing implementations of the HKF EoS largely come with hardcoded models for water solvent properties, making it difficult to use different and more recent formulations for calculating water solvent properties. Due to its modular structure, ThermoFun library makes it easy to use any combination of EoS and methods for calculating the standard state thermodynamic properties of solutes and solvents.

This aspect was used by (Miron et al., 2019) to test the performance of commonly used thermodynamic and electrostatic models and asses the discrepancies in the calculated water solvent properties, and its derivatives, in the framework of the Helgeson-Kirkham-Flowers model. The results of the investigation showed that there is a good agreement between the investigated models for calculating the volumetric properties of water, with discrepancies not exceeding 0.2 log units for reactions (Figure 9 A). On the other hand, models for calculating the dielectric constant produce increasingly different values above 500 °C, which can lead to discrepancies larger than 2 log units (Figure 9 B). This will have an impact when modeling magmatic-hydrothermal systems or when using the HKF model to retrieve standard state data from solubility experiments at elevated temperatures (the uncertainity in the calculated dielectric constant will be propagated to the standard state properties).

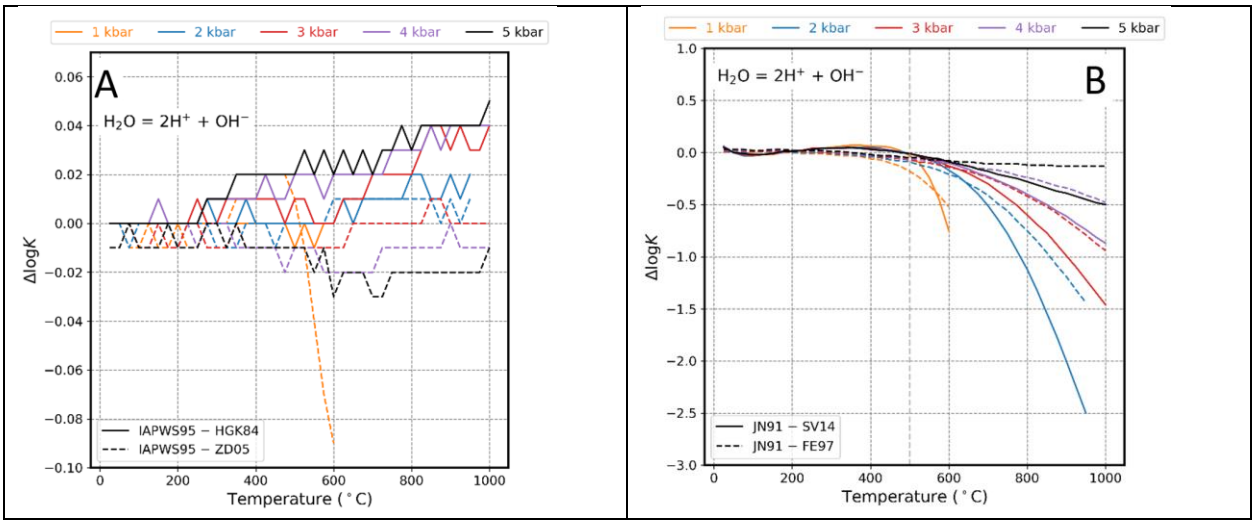

Figure 9. *Differences in logK values of the water dissociation reaction, obtained from: (A) different thermodynamic models for calculating water volumetric properties, full lines -- difference between IAPWS95* (Wagner and Pruß, 2002) *and HGK84* (Haar et al., 1984)*, and dashed lines -- between IAPWS95 and ZD05* (Zhang and Duan, 2005)*; (B) different models for calculating water dielectric properties, full lines -- difference between JN91*(Johnson and Norton, 1991) *and SV14* (Sverjensky et al., 2014)*, and dashed lines -- between JN91 and FE97, using IAPWS95 for water volumetric properties.*

2. Isocoulombic estimations

2.1 Motivation

A large part of the thermodynamic data for safety relevant radionuclides was obtained at room temperature and is restricted in most cases to values for log K˚(25˚C) (see Fig. 10 for the data from the PSI/Nagra TDB 12/07, Thoenen et al. 2014) which is insufficient to warrant extrapolation to higher temperatures. This lack of data is also evident by looking at the speciation of radionuclides in the Opalinus Clay reference porewater, where species with insufficient thermodynamic data (only log K˚(25˚C) known) predominate (see Table 5).

It is clearly not possible to obtain this large amount of missing data within a realistic time and cost frame without resorting to estimation methods, one of which is the isocoulombic estimation method (see, e.g., Gu et al., 1994; Lindsay, 1980; Puigdomenech et al., 1997) Miron et al. (2020).

Table 5. *Speciation of some safety relevant radionuclides in the Opalinus Clay reference porewater (data from Thoenen et al. 2014). Only log K˚(25˚C) is known for species marked in red, which is insufficient for calculating the speciation at higher temperatures.*

Element	Species	%		Element	Species	%
Ni	Ni^{2+}	72		Np	Np(OH)4	100
	$NiSO_4$(aq)	23		Pu	*PuSiO(OH)3+2*	39
	$NiCl^+$	4			*PuCO3+*	33
Se	HSe^-	59			PuSO4+	11
	Se_4^{2-}	38			*PuCO3(OH)3-*	4
	Se_3^{2-}	3			Pu(SO4)2-	3
Zr	$Zr(OH)_4$(aq)	100			Pu+3	3
Tc	$TcO(OH)_2$(aq)	91			*Pu(CO3)2-*	3
	$TcCO_3(OH)_2$(aq)	9			PuOH+2	1
Th	$Th(OH)_2(CO_3)_2^{2-}$	3			*PuCl+2*	1
	$Th(OH)_4$(aq)	27		Am	AmSiO(OH)3+2	47
U	$CaUO_2(CO_3)_3^{2-}$	80			AmCO3+	39
	$Ca_2UO_2(CO_3)_3$(aq)	8			Am+3	4
	$MgUO_2(CO_3)_3^{2-}$	5			Am(CO3)2-	4
	$UO_2(CO_3)_3^{4-}$	5			AmSO4+	3
	$UCO_3(OH)_3^-$	1			AmHCO3+2	2

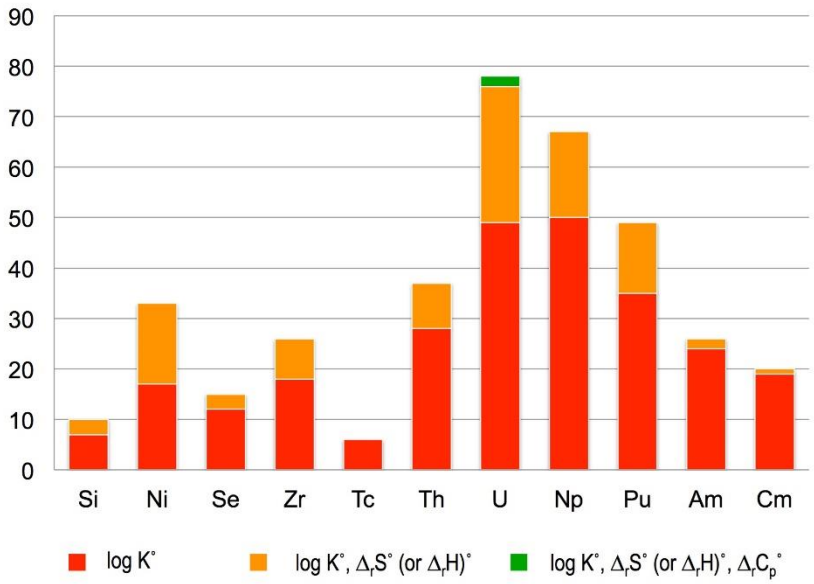

Figure 10. *Histogram of the number of aqueous species present in the PSI/Nagra TDB 12/07 (Thoenen et al. 2014). The numbers of species for which only log K˚(25˚C) is known are marked in red, those for which additionally $\Delta_rS^\circ(25^\circ C)$ or $\Delta_rH^\circ(25^\circ C)$ are known are marked in orange. Only for a single species (marked in green) are values known for log K˚(25˚C), $\Delta_rS^\circ(25^\circ C)$ or $\Delta_rH^\circ(25^\circ C)$, and $\Delta_rCp(25^\circ C)$.*

2.2. Thermodynamic basics

The general expression for the isobaric temperature dependence of the equilibrium constant K˚ of a reaction is given by

$$\log_{10}K^\circ(T) = \frac{T_0}{T}\log_{10}K^\circ(T_0) + \left(1-\frac{T_0}{T}\right)\frac{\Delta_r S^\circ_m(T_0)}{R\ln(10)} - \frac{1}{RT\ln(10)}\int_{T_0}^{T}\Delta_r C^\circ_{p,m}dT + \frac{1}{R\ln(10)}\int_{T_0}^{T}\Delta_r C^\circ_{p,m}d\ln T$$

where T is the temperature of interest, T_0 the reference temperature (usually 298.15 K or 25˚C), $\Delta_r S_m^\circ$ the standard molar entropy of reaction, $\Delta_r C_{p,m}^\circ$ the standard molar isobaric heat capacity of reaction, and R the gas constant (see Appendix A for a derivation). If information on the temperature dependence of $\Delta_r C_{p,m}$ is missing, it is often assumed that $\Delta_r C_{p,m}$ is constant over the temperature interval under consideration, leading to the ***3-term approximation*** (see Appendix A for details)

$$\log_{10}K^\circ(T) = \frac{T_0}{T}\log_{10}K^\circ(T_0) + \left(1-\frac{T_0}{T}\right)\frac{\Delta_r S^\circ_m(T_0)}{R\ln(10)} - \left(1-\frac{T_0}{T}+\ln\frac{T_0}{T}\right)\frac{\Delta_r C^\circ_{p,m}(T_0)}{R\ln(10)}$$

Assuming that $\Delta_r C^\circ_{p,m}(T_0)$ is not only constant but also equal to zero results in the ***2-term approximation*** (van't Hoff)

$$\log_{10}K^\circ(T) = \frac{T_0}{T}\log_{10}K^\circ(T_0) + \left(1-\frac{T_0}{T}\right)\frac{\Delta_r S^\circ_m(T_0)}{R\ln(10)}$$

If $\Delta_r S^\circ_m(T_0)$ is also assumed to be equal to zero, one finally obtains the ***1-term approximation (type A)***

$$\log_{10}K^\circ(T) = \frac{T_0}{T}\log_{10}K^\circ(T_0)$$

Note that all of these reactions may also be expressed in terms of $\Delta_r H^\circ_m$ (see Appendix A for details). In that case, the corresponding ***1-term approximation (type B)*** is

$$\log_{10}K^\circ(T) = \log_{10}K^\circ(T_0)$$

The 3-, 2-, and 1-term approximations are not generally applicable. However, it is often possible to use them for isocoulombic and, to a much lesser extent, for isoelectric reactions, both of which will be discussed in the following section.

2.3. Isocoulombic estimation method

In **isocoulombic** reactions equal numbers of like-charged species appear on both sides of the reaction, as in

$$HPO_4^{2-} + HSO_4^- \rightleftharpoons H_2PO_4^- + SO_4^{2-}$$

while in **isoelectric** reactions the sum of positive or negative charges is equal on both sides of a reaction as in

$$Ni^{2+} + H_2O(l) \rightleftharpoons Ni(OH)^{+} + H^{+}$$

The fundamental assumption of the isocoulombic principle is that in aqueous electrolyte solutions the interaction of solutes with the solvent are mainly of electrostatic nature and that the thermodynamic properties of like charged species have similar responses to changes in temperature and ionic strength (Gu et al., 1994). When equal numbers of like-charged species appear on both sides of a reaction, the temperature dependencies of like-charged species are similar and tend to cancel, leading to a nearly constant heat capacity of reaction (advocating the use of the 3-term approximation). In a seminal paper, Lindsay (1980) gave numerous examples of isocoulombic reactions where the heat capacities of reaction are not only nearly constant but also close to zero, such that the 2-term approximation can be safely applied. GU et al. (1994) argued that since the change in entropy is closely related to the solute-solvent interaction (and thus to the charge of the ion), isocoulombic reactions should not only balance the heat capacities but also the entropies, leading to both heat capacities and entropies of reaction close to zero. In such a case, the 1-term A approximation could be used.

In order to apply the isocoulombic estimation method to a general (non-isocoulombic) reaction, it is necessary to have another reaction at hand (called model reaction by some authors, e.g., Wood and Samson, 1998) whose variation of thermodynamic parameters over the required temperature range is well-known and which can be combined with the general reaction in such a way that an isocoulombic reaction is formed.

Take for example the formation reaction of bicarbonate

$$CO_2(aq) + H_2O(l) = HCO_3^{-} + H^{+}$$

whose $\log_{10}K$ was determined at saturation pressure up to 300˚C. The values for $\log_{10}K^{\circ}$(25˚C), -6.35, Δ_rS°(25˚C), -91.2 J mol^{-1} K^{-1}, and Δ_rCp°(25˚C), -338 J mol^{-1} K^{-1} determined by Patterson et al. (1982) can be used to apply the 1-term, 2-term, and 3-term approximations for this non-isocoulombic reaction. As shown in Fig. 2.2, the 1-term A approximation overestimates the experimentally determined $\log_{10}K$(100˚C) by 1.2 log units, the 2-term approximation by 0.3 log units and the 3-term approximation by only -0.13 log units. The respective deviations at 300˚C are 5.2, 2.9, and -0.15 log units.

It is evident that the 1-term A approximation is inadequate for extrapolating values of $\log_{10}K$ even to temperatures in the close vicinity of room temperature, while the 2-term approximation works well up to about 120˚C and the 3-term approximation all the way up to 300˚C.

These approximations can be significantly improved by considering an isocoulombic variant of the bicarbonate-forming reaction

$$CO_2(aq) + OH^{-} = HCO_3^{-}$$

which is formed from $CO_2(aq) + H_2O(l) \rightleftharpoons HCO_3^{-} + H^{+}$ by adding the model reaction $H^{+} + OH^{-} \rightleftharpoons H_2O(l)$.

Combining the values of $\log_{10}K^{\circ}$(25˚C), Δ_rS°(25˚C), and Δ_rCp°(25˚C) for the non-isocoulombic reaction with those for the model reaction (13.993, 80.67 J mol^{-1} K^{-1}, and 231.38 J mol^{-1} K^{-1}, resp., from Busey and Mesmer, 1978) leads to the corresponding values for the isocoulombic reaction. It is clear from Fig. 2.2 that both the 1-term A and the 2-term approximations allow the extrapolation of $\log_{10}K$ to temperatures well above 100˚C, while there is negligible deviation of the 3-term estimations from experimental data at all temperatures.

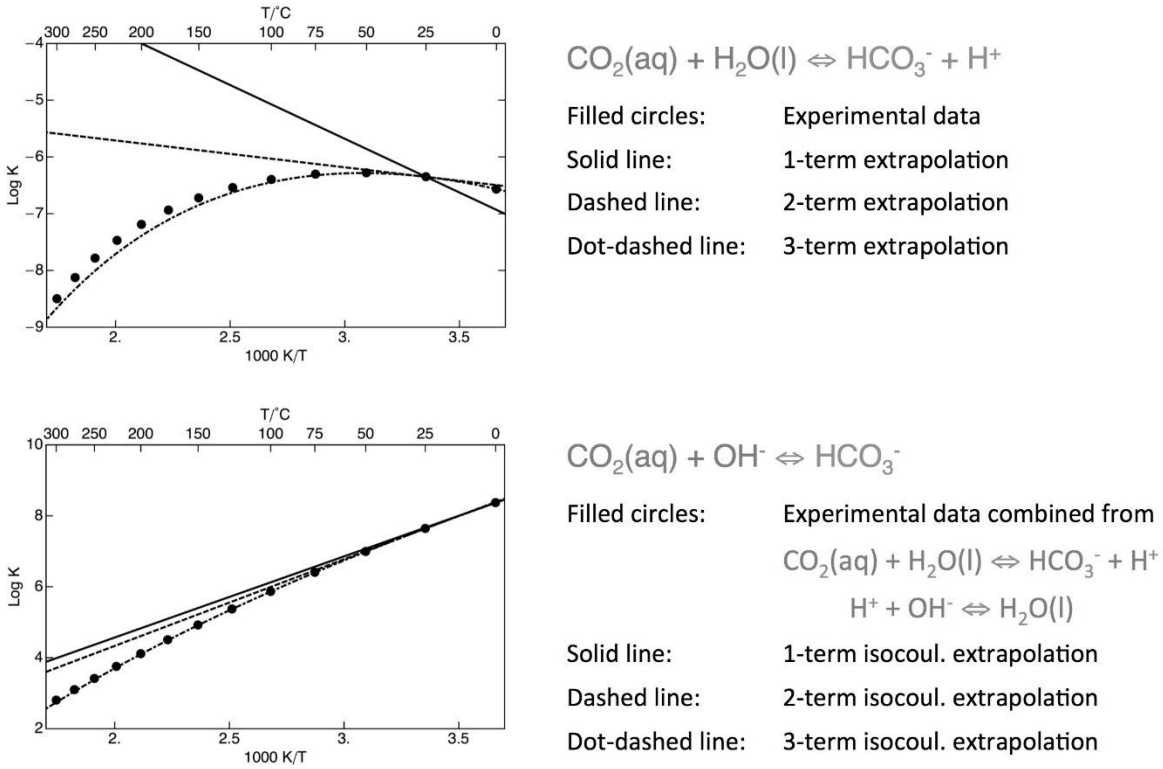

Figure 11. *Comparison of temperature extrapolations using the 1-term A, 2-term, and 3-term estimates for isocoulombic (below) and non-isocoulombic formulations (above) of the formation reaction of the bicarbonate anion. Experimental data for $CO_2(aq) + H_2O(l) = HCO_3^- + H^+$ from Patterson et al. (1982) and for $H^+ + OH^- = H_2O(l)$ from Busey and Mesmer (1978).*

2.4. Systematic evaluation of the use of isocoulombic/isoelectric reactions for logK temperature extrapolations

The lanthanide and actinide systems are of interest in fields such as radioactive waste disposal, REE ore deposits, etc. and their properties tend to vary gradually along the series. While new experimental data are gradually becoming available they are not yet sufficient to cover the large number of species, especially concerning their stability at elevated temperature. The isocoulombic method is a suitable option when limited data is available. This is specifically important for reactions that have only values for the equilibrium constant at ambient conditions. Extrapolating the properties of an isocoulombic reaction guarantees that the error due to the unknown reaction properties (setting entropy/enthalpy and/or heat capacity of reaction to zero) is smaller compared with the error introduced by using the direct complexation or dissolution reaction for extrapolating properties.

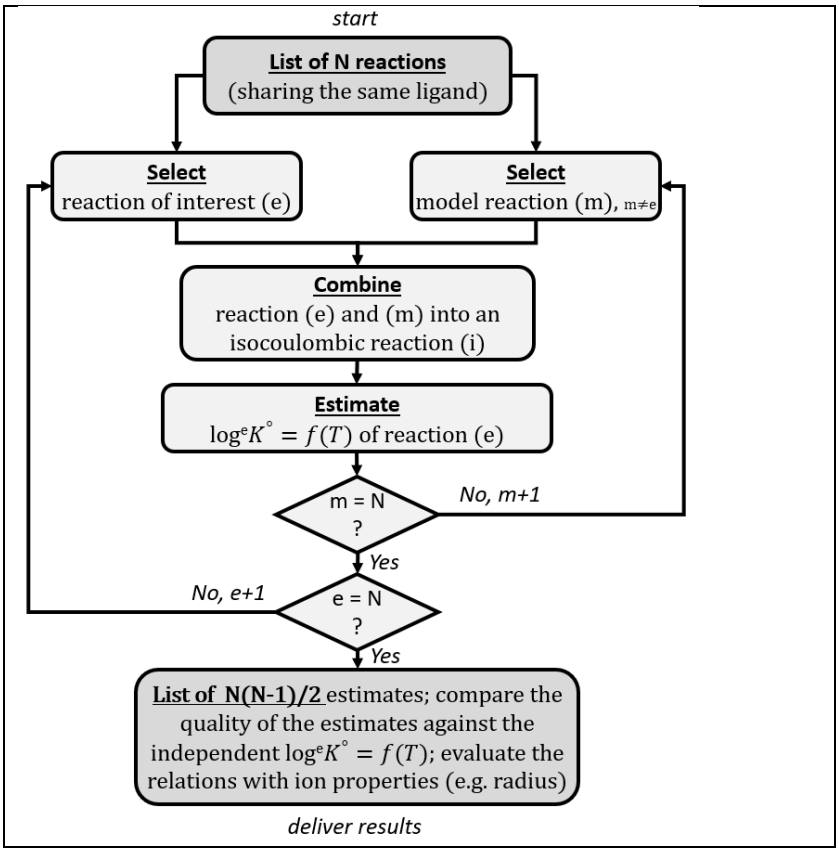

Figure 12. *Flow-chart* (Miron et al., 2020) *of a procedure for the systematic evaluation of $log K_T^\circ$ temperature trends by generating all possible isocoulombic combinations from a list of selected reactions and testing the quality of the $log^e K_T^\circ$ estimates.*

Details on the systematic evaluation are described in Miron et al. (2020). The authors present an extensive application of the (established) isocoulombic method on existing datasets for lanthanide and actinide speciation using a new methodology consisting of: automatically generating reactions, combining them into isocoulombic reactions and doing a systematic evaluation and validation of temperature extrapolations against independent experimental data. This allows to create all possible alternative reactions and identify criteria for choosing the optimal ones that produce the most accurate extrapolations. The methodology is shown in the flowchart (**Figure 12**) and was streamlined using the dedicated database and tools for efficient processing and generating reactions (see section 1). This methodology is applied to the lanthanide and actinide series, taking advantage of new experimental data, to establish principles for generating isocoulombic reactions that produce the best temperature extrapolations, especially since many complexation data is limited to ambient conditions.

For the systematic investigation of the isocoulombic method to temperature extrapolations, thermodynamic data for substances and reactions were collected from different sources and published databases (e.g. Guillaumont et al., 2003; Haas et al., 1995; Lemire et al., 2001; Migdisov et al., 2009; Thoenen et al., 2014, and references therin). To use the isocoulombic method, the thermodynamic data needs to be in the form of reactions. From the collected substances, reactions were created using the reaction generator (see section 1.2.2) and saved in the database. These could be then combined into isocoulombic reactions.

For a dataset of selected reactions, the isocoulombic reactions are automatically generated by considering all possible combinations. These are then used for estimations using the one-, two-, or three-term extrapolations, as if we had only a limited amount of data (**Figure 12**). The quality of the estimates is then determined by comparing them with a set of independent experimental, $\log^{e} K_T^{\circ}$ values (some measurements retrieved in the ThermAc) for the reaction of interest (Miron et al., 2020).

To identify criteria for choosing the optimal isocoulombic reactions, data on trivalent lanthanide La(III) fluoride and chloride aqueous complexes from Migdisov et al. (2009) was used as a learning dataset. This dataset contains high quality temperature data for many lanthanide complexes. For the "blind testing", we excluded La, Eu, and Tm from the full Ln(III) dataset; the remaining species and their reactions were used as a "learning stage" dataset. All complexation reactions with chloride and fluoride were generated and their standard properties of reaction were calculated from standard properties of reactants and products. Next, we considered all possible combinations between the fluoride complexation reactions to generate isocoulombic reactions (Figure 12, row 3). For each combination of two reactions, one reaction was considered the investigated reaction (with assumed unknown temperature trend) and the other the model reaction (with known temperature trend). The $\log^{e} K_T^{\circ}$ were estimated from the $\log^{i} K_T^{\circ}$ of the isocoulombic reaction extrapolated using the one-, two-, or three-term extrapolations and the $\log^{m} K_T^{\circ}$ of the model reaction calculated using the HKF model. The quality of estimated $\log^{e} K_T^{\circ}$ was compared with values calculated from the HKF model parameters reported by Migdisov et al. (2009).

The main observations from the learning datasets was that the smaller the difference in the hydrated ionic radii between the lanthanide ion present in the reaction of interest and the ion in the model reaction the better the estimate (**Figure 13**). Another observation is that the $\log^{e} K_T^{\circ}$ estimates from the one-term extrapolation of the $\log^{i} K_T^{\circ}$ have average deviations smaller than 0.3 log units for the investigated 0 to 250 ℃ temperature interval.

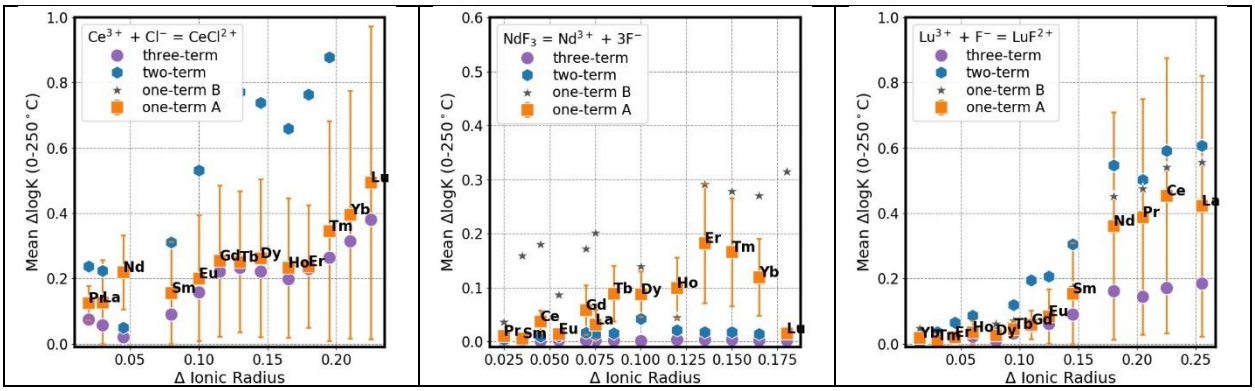

Figure 13. *Mean of the differences between the $\log K_T^{\circ}$ values of the displayed reactions of interest calculated using the HKF model (properties of reactants, based on experimental data) and the $\log^{e} K_T^{\circ}$ values estimated using one-term A, one-term B, two-, and three-term extrapolations for a temperature interval from 0 to 250 ℃ with a 5 ℃ step plotted against the difference in the ionic radius between the La(III) ion in the reaction of interest and the ion in the model reaction (marked on each data-point). For the one-term A extrapolation, the standard deviation is also shown. Ionic radii values taken from* D'Angelo et al. (2011)*.*

Based on the relation between the quality of the estimates and the difference in the ionic radii the standard property effects of reaction at elevated temperatures for La, Eu, and Tm fluoride complexation reactions previously excluded from the learning dataset can be estimated reasonably well (**Figure 14** A). This was done assuming that only their $\log K^{\circ}_{25\,^{\circ}C}$ is known. As seen in **Figure 14** B, the values estimated using the one-term A extrapolation and model reactions having more different ionic radii leads to significant deviations from the experimental trend.

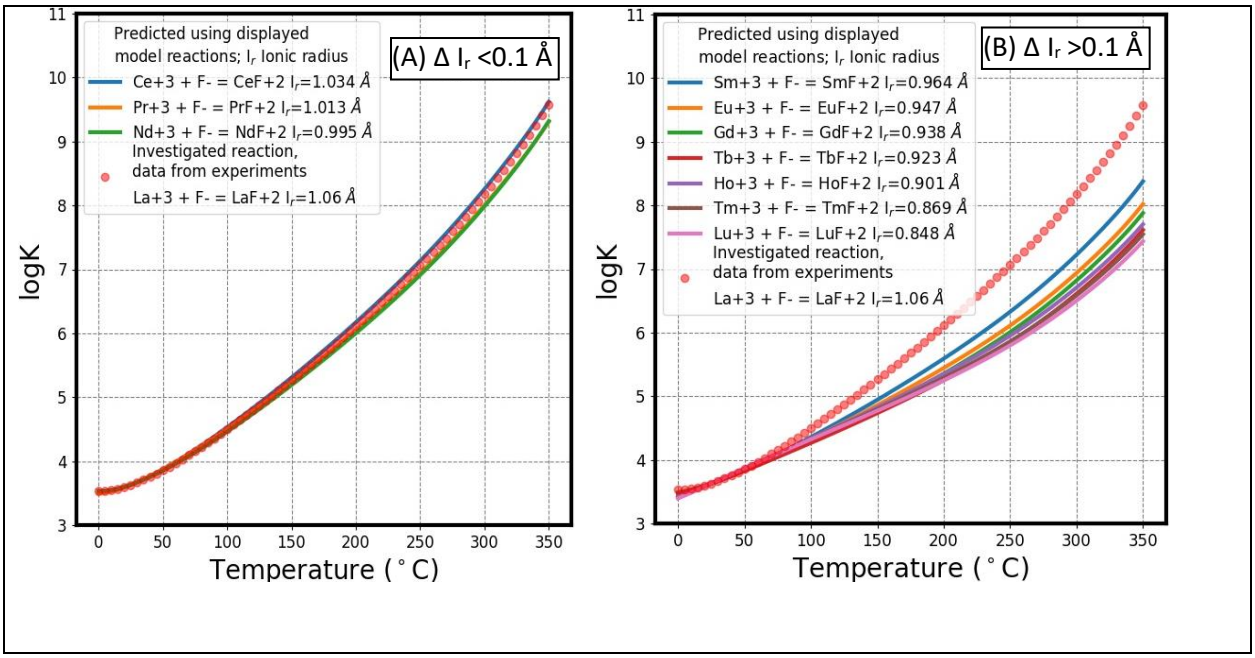

Figure 14. *Experimentally-based $\log K^{\circ}_{T}$ of the LaF+2 formation reaction (red circles) and values estimated using the one-term A extrapolation of $\log {}^{i}K^{\circ}_{T}$ of isocoulombic reactions resulted from combining the LaF+2 formation reaction with the model reactions shown (colored curves): (A) For model reactions of Ln(III) cations having hydrated ionic radii similar to that of La+3 (< 0.1 Å). (B) For model reactions of Ln(III) cations having ionic radii different from that of La+3 (> 0.1 Å).*

Because Ln(III) and An(III) have almost identical hydrated ionic radii (D'Angelo et al., 2013) the properties of complexation reactions as a function of temperature can be estimated from temperature data available in one or the other element group (used as model reactions).

The same methodology was applied in the case of actinide complexation (whit less extensive elevated temperature data available) (**Figure 15**) (Miron et al., 2020). The main focus is on cases where the thermodynamic properties for both model reaction and the reaction of interest are known, and experimental values for $\log {}^{e}K^{\circ}_{T}$ are also available in order to validate the isocoulombic method and to provide guidelines for choosing the model reactions that are expected to result in the best estimates. The results show that similar actinides and lanthanides (based on the ionic radius and solvation properties) can be used as analogues for the temperature dependence and, when combined into isocoulombic reactions, the temperature dependence can be calculated just using the $\log K^{\circ}_{298}$. This is of great importance for closing the existing gaps and thereby enhancing the applicability of thermodynamic

calculations of chemical equilibria, until new experimental data on the temperature trends of complexation reactions become available.

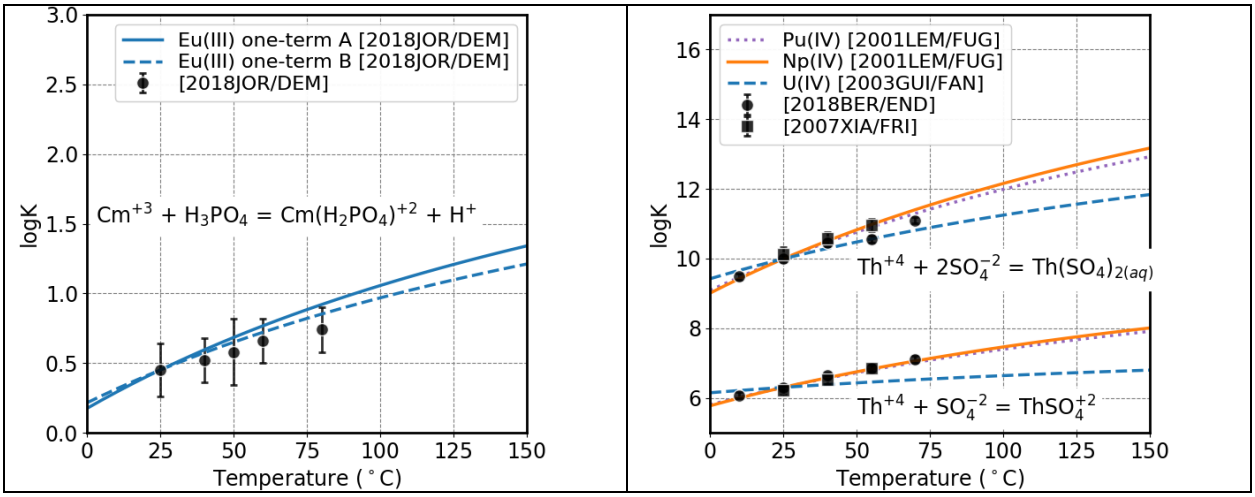

Figure 15. *Independent experimental data points (symbols) compared with estimated* $log K_T^\circ$ *(lines) for the displayed reactions using isocoulombic reactions constructed with analogue model reactions of the elements in the legend. Experimental data from* (Di Bernardo et al., 2018; Jordan et al., 2018; Xia et al., 2007) *and data for model reactions from* (Guillaumont et al., 2003; Jordan et al., 2018; Lemire et al., 2001).

Finally, for using the isocoulombic method to estimate the thermodynamic properties for reactions with unknown temperature dependence, a three-step methodology is recommended (Miron et al., 2020): "(Step 1) seek for the "best" available model reaction in order to construct an isocoulombic exchange reaction; (Step 2) extrapolate $\log^{i}K_T^\circ$ of the isocoulombic reaction using the appropriate one-, two-, or three-term extrapolation method depending on the availability of thermodynamic data; and (Step 3) estimate $\log^{e}K_T^\circ$ of the reaction of interest as a function of temperature, or retrieve the standard-state thermodynamic properties of the substance of interest at *T* and T_{298}. "

2.5. Application and test of the isocoulombic estimation method for the solid solution – aqueous solution system (Ba, Sr, Ra)SO_4(s)–H_2O(l)

Isocoulombic extrapolations were used along with other predictions and correlations to elaborate on consistency of the thermodynamic dataset for (Ba,Sr,Ra)SO4 aqueous – solid solution systems, applicable for a wide temperature range from 0 to 300 °C. (collaboration of D. Kulik with V. Vinograd, FZJ, (Vinograd et al., 2018a, 2018b)).

In the first part of this work, we used literature data and several prediction and correlation methods to obtain an internally consistent thermodynamic dataset for the solids $BaSO_4$,cr (baryte), $SrSO_4$,cr (celestine), $PbSO_4$,cr (anglesite) and $RaSO_4$,cr, compatible with the PSI/Nagra TDB 12/07 (Thoenen et al., 2014)in the GEMS version (http://gems.web.psi.ch), and valid for temperature corrections in the range 0 to 300˚C (Tables 6,7).

Table 6. *The "tCp" dataset for standard thermodynamic properties of MSO_4,cr solids (from Vinograd et al. 2018a,b). Units: J/bar; kJ/mol; J/K/mol.*

Solid	V^o_{298}	G^o_{298}	H^o_{298}	S^o_{298}	Cp^o_{298}
$CaSO_4$	4.59	-1321.97	-1434.15	107.4	101.2
$SrSO_4$	4.63	-1346.14	-1457.76	123.4	100.3
$PbSO_4$	4.80	-813.10	-919.95	148.5	104.3
$BaSO_4$	5.21	-1362.15	-1473.15	132.2	101.7
$RaSO_4$	5.54	-1364.52	-1475.96	**139.3**	**102.5**

Table 7. *Cp=f(T) polynomial coefficients for the "tCp" dataset for MSO_4,cr solids*

Solid	a_0	a_1 (*T)	a_2 (/T^2)	a_3 (/$T^{0.5}$)	a_4 (*T^2)	T_{max}, C	References
$CaSO_4$	372.8	-0.1574	1.695e6	-4330.8	7.99e-5	827	RH95
$SrSO_4$	77.96	0.08831	-1.213e6	189.0	-1.449e-5	827	VK
$PbSO_4$	46.83	0.1278	1.724e6	0	0	827	RH95
$BaSO_4$	224.6	-0.07395	-1.17e6	-1587	4.784e-5	827	VK
$RaSO_4$	225.4	-0.07395	-1.17e6	-1587	4.784e-5	600	VK

References: RH95 (Robie and Hemingway, 1995); VK: Vinograd et al. (2018a, 2018b).

This dataset with the coefficients of the heat capacity function $C_p^o = f(T)$ was used to calculate the standard reaction properties of the dissolution reactions, labelled as (R), MSO_4,cr = $M^{2+} + SO_4^{2-}$, with M = (Sr, Pb, Ba, Ra), forming the "R3" thermodynamic dataset (see Table 8). The standard reaction properties of the isocoulombic exchange reactions, labelled as (I), $M1SO_4$,cr + $M2^{2+}$ = $M2SO_4$,cr + $M1^{2+}$ were calculated by combining the reaction properties of the appropriate dissolution reactions from the dataset "R3", thus resulting in the "I3" dataset. For example, the (I) reaction $BaSO_4$,cr + Ra^{2+} = $RaSO_4$,cr + Ba^{2+} is the difference of the (R) reactions $BaSO_4$,cr = $Ba^{2+} + SO_4^{2-}$ and $RaSO_4$,cr = $Ra^{2+} + SO_4^{2-}$; hence, any property of the (I) reaction is equal to the difference of the respective properties of the two (R) reactions, for instance $\log_{10}K_{(I),Ba\text{-}Ra} = \log_{10}K_{Ba} - \log_{10}K_{Ra}$.

By means of GEM-Selektor (DComp, ReacDC and RTparm modules), we compared the applicability of dissolution reactions (R) and isocoulombic reactions (I) to simple temperature approximations of the thermodynamic properties of MSO_4 crystalline solids. Such approximations have the form

$$\log_{10}K_T = 0.4343\ (A - B/T + C\ \ln T)$$

with $A = (\Delta_r S^o_{298} - (1+\ln(298.15))\Delta_r C_p^o{}_{298})/R$, $B = (\Delta_r H^o_{298} - 298.15 \cdot \Delta_r C_p^o{}_{298})/R$, and $C = \Delta_r C_p^o{}_{298}/R$, where R = 8.31451 J/mol is the universal gas constant and 298.15 K the reference temperature (see also Section 2.2). Two-term approximation means that the heat capacity effect of reaction, $\Delta_r C_p^o{}_{298}$, is set to zero, and one-term approximation - that both $\Delta_r C_p^o{}_{298}$ and $\Delta_r S^o_{298}$ are set to zero. From the $\log_{10}K$ value at the temperature of interest T, the standard Gibbs energy of the solid (e.g. $RaSO_4$,cr), needed for GEMS model calculations, can be found by using $\Delta_r G^o_T = -(RT \log_{10}K)/0.4343$ and the standard Gibbs energies at T of the other substances involved in the reaction.

Table 8. *Dataset "R3" (based on the "tCp" dataset, Table 7) for MSO_4,cr = $M^{2+} + SO_4^{2-}$ (from Vinograd et al. 2018a,b). Units: J/bar; kJ/mol; J/K/mol.*

Solid	$\log_{10}K^o_{298}$	$\Delta_r V^o_{298}$	$\Delta_r G^o_{298}$	$\Delta_r H^o_{298}$	$\Delta_r S^o_{298}$	$\Delta_r Cp^o_{298}$
$CaSO_4$	-4.33	-5.15	24.72	-18.53	-145.1	-398.2
$SrSO_4$	-6.63	-5.11	37.84	-0.88	-129.9	-412.1
$PbSO_4$	-7.84	-5.10	44.75	11.33	-112.1	-423.1
$BaSO_4$	-9.97	-5.21	56.91	25.98	-103.7	-418.8
$RaSO_4$	-10.26	-5.50	58.56	38.74	-66.51	-428.1

In Fig. 16, the predictions from three-term T extrapolations for $\log_{10}K_T$ using the "R3" dataset are shown in comparison with those of (Brown et al., 2015) and some experimental data. As seen in this figure, three-term extrapolations for dissolution reactions provide rather accurate descriptions of MSO_4,cr solubility at temperatures at least below 250˚C. All curves have maxima that shift to higher temperatures in the sequence Ca – Sr – Pb – Ba – Ra. Note that the curves for $RaSO_4$,cr and $BaSO_4$,cr cross at ca. 70˚C, and that at higher temperatures, radium sulphate becomes more soluble than baryte. Also the logK differences between all sulphate solids get smaller with increasing temperature.

Applicability ranges of different temperature approximations using reaction effects from Table 8 are shown in Fig. 17 as differences to the standard Gibbs energy $G^o_T(RaSO_4,cr)$ directly computed from the "tCp" dataset by heat capacity integration (assuming that this "tCp" dataset is the most accurate). We note that R1 and R2 (notation: Rn, with n = 1, 2, 3, refers to the n-term extrapolation of a dissolution reaction) extrapolations are inaccurate, except in a narrow region around the reference temperature 298.15 K, clearly because of neglecting the very large heat capacity (and entropy) effects of the dissolution reactions. The R3 approximation is good up to 350 K, then it slightly overestimates the stability of $RaSO_4$,cr up to 500-550 K, and becomes inaccurate above 550-560 K. However, I2 and I3 (notation: In, with n = 1, 2, 3, refers to the n-term extrapolation of an isocoulombic reaction) extrapolations remain accurate in the whole temperature range, which means that the heat capacity effect of the isocoulombic reactions is insignificant and can be ignored. The I1 extrapolation becomes inaccurate already above 340 K because of neglecting the (still significant) entropy effect.

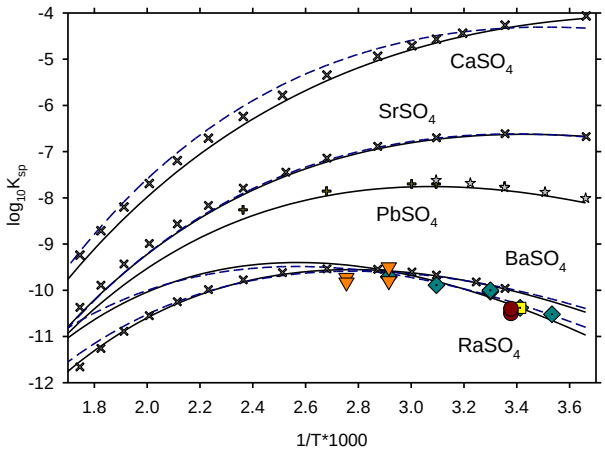

Figure 16. *Solubility products of MSO_4 solids vs inverse temperature (K). Solid curves: our predictions from the R3 dataset (Table 8); dashed curves: predictions using Brown et al. (2015); colored scattered symbols: experimental data for $RaSO_4$,cr – circles and triangles: from solubility of (Ba,Ra)SO_4, Brandt et al.* (2015)*; Vinograd et al. (2018a,b); – diamonds and squares: from solubility of pure $RaSO_4$,cr, Hedström* (2013)*and Nikitin & Tolmatscheff* (1933)*. Crosses are the interpolated MSO_4,cr solubility data from Raju & Atkinson* (1988, 1990, 1989) *and Howell et al.* (1992)*; pluses and asterisks – solubility data for $PbSO_4$,cr* (Helgeson, 1969; Khodakovsky et al., 1966)*.*

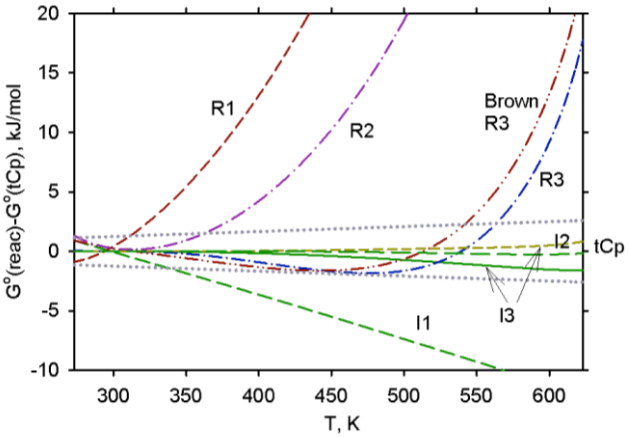

Figure 17. *Comparison of differences of G^o_T($RaSO_4$,cr) obtained by various T approximations of (R) and (I) reactions from G^o_T($RaSO_4$,cr) calculated directly using the "tCp" dataset. Digits after 'R' or 'I' mean: 3 – three-term; 2 – two-term with $\Delta_r C_p^o{}_{298}$ set to 0; 1 – one-term with both $\Delta_r C_p^o{}_{298}$ and $\Delta_r S^o_{298}$ set to 0; Brown R3 - three-term approximation using parameters from Brown et al. (2015) instead of those from Table 8. Dotted lines show uncertainty intervals of ±0.5 $log_{10}K$ units. I1, I2, I3 curves are obtained from the reaction $RaSO_4$,cr + Ba^{+2} = $BaSO_4$,cr + Ra^{+2}, except the short-dash I3 curve derived from the reaction $RaSO_4$,cr + Pb^{+2} = $PbSO_4$,cr + Ra^{+2}.*

We conclude that two-term (Van't Hoff) temperature approximations of isocoulombic reactions in the solid solution – aqueous solution system (Sr,Ba,Ra)SO_4(cr) – H_2O(l) are safe to use in the range from 0˚C to 300˚C because the very large $\Delta_r Cp^o_{298}$ effects of (R) reactions (see Table 8) due to ion hydration essentially cancel out in (I) reactions. The entropy effects $\Delta_r S^o_{298}$ are less similar and do not compensate well even in (I) reactions, so the one-term approximation is not very appropriate.

In the second part of this study (Vinograd et al. 2018a,b), atomistic methods were used to re-evaluate parameters of mixing in the ternary (Sr,Ba,Ra)SO_4 solid solution system, leading to a regular model of mixing with binary interaction parameters given in Table 9 and zero ternary parameter. This model of mixing, together with the "tCp" thermodynamic dataset and the PSI/Nagra TDB 12/07, was used in GEM-Selektor simulations of SS-AS systems firstly involving a binary (Ba,Ra)SO_4 phase to test temperature trends of radium retention in baryte (a widely recognized repository-relevant issue).

In addition, a ternary (Sr,Ba,Ra)SO_4 phase was employed to investigate the impact of adding Sr to baryte on the retention of radium at various temperatures. This scenario is of interest because natural barytes, e.g., such as found in the Opalinus Clay, have various contents of Sr, and the porewater in clayrock appears to be saturated with respect to celestine. Process simulations were conducted using parent systems composed of 1 kg of H_2O, 0.1 mol of NaCl, $5 \cdot 10^{-6}$ mol $RaCl_2$, 0.1 g of dry air, and either 0.5 g or 5.0 g $BaSO_4$ initially. The SUPCRT extended Debye-Hückel aqueous activity model was used.

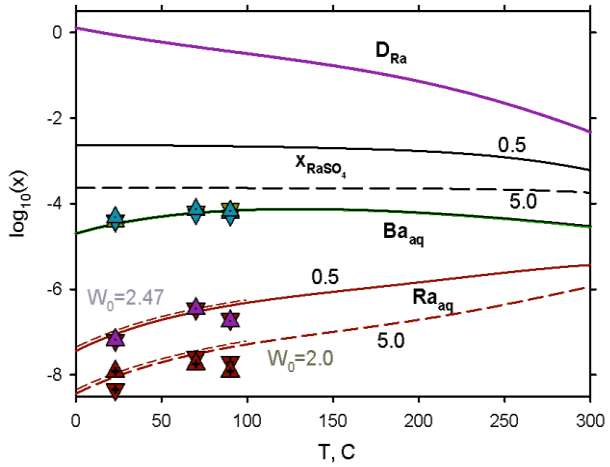

***Figure 18**. Temperature variations of mole fraction x_{RaSO_4} in solid, fractionation coefficient D_{Ra}, dissolved aqueous Ba_{aq} and Ra_{aq} (log molal) in the equilibrium SS-AS system. Solid curves: W_0 = 2.0 kJ/mol, solid/water ratio S/W = 0.5 g/kg; medium dashed: W_0 = 2.0 kJ/mol, S/W = 5.0 g/kg. Short-dashed curves show the shifts if W_0 = 2.47 kJ/mol is used (Table 9). Triangles correspond to recrystallization experiments from (Brandt et al. 2015; Vinograd et al. 2018a,b).*

***Table 9.** Binary interaction parameters of a regular mixing model for the ternary (Sr,Ba,Ra)SO_4 solid solution system evaluated using atomistic methods (Vinograd et al. 2018a,b). The ternary interaction parameter is zero.*

W_0	Value (kJ/mol)
W_{BaRa}	2.47 ± 0.5
W_{BaSr}	4.95 ± 0.5
W_{SrRa}	17.5 ± 1.5

In the case of the binary SS system, only temperature was changed (at two S/W ratios). The fit to experimental data was found slightly better when a lower W_0 = 2.0 kJ/mol parameter was used. Overall, it is clear that the most efficient immobilization of radium in solid solution with baryte happens at lower temperatures and higher S/W ratios – the latter produce a stronger "dilution effect" for Ra in solid solution. At 125˚C, the mobility of radium will be ca. 10 times higher than at 25˚C (all other parameters kept constant). The Ra-Ba fractionation coefficient in the solid D_{Ra} is the ratio of two distribution ratios:

$$Kd(\mathrm{Ra}) = n_{ss}(\mathrm{Ra})/n_{ss}(\mathrm{S})/m_{aq}(\mathrm{Ra});\ \ Kd(\mathrm{Ba}) = n_{ss}(\mathrm{Ba})/n_{ss}(\mathrm{S})/m_{aq}(\mathrm{Ba});\ \ D_{\mathrm{Ra}} = Kd(\mathrm{Ra})\ /Kd(\mathrm{Ba})$$

where n_{ss} is the amount of element in solid solution phase(s) and m_{aq} is its molality in the aqueous phase. As seen in Fig. 19, D_{Ra} decreases with temperature by two orders of magnitude.

In systems with the ternary solid solution (with interaction parameters from Table 9), the same initial recipes were used as before (at S/W = 0.5 g/kg or 5.0 g/kg $BaSO_4$). During the process calculations, the composition of solid solution was changed by stepwise addition of $SrSO_4$ (starting from $1 \cdot 10^{-6}$ mol) and subtraction of $BaSO_4$ such that the mass of the solid phase remained constant at the given S/W ratio. Simulations were performed at several temperatures, as shown in Fig. 19.

At both S/W ratios, the addition of $SrSO_4$ to baryte results in a much stronger retention of radium, especially at low temperatures, the strongest at 7-10% of Sr end member (Fig. 19 A, B, and D). In comparison with the binary (Ba,Ra)SO_4 – H_2O system at the same S/W ratio, the addition of 5-10% Sr results in an about 9-11 times lower aqueous Ra_{aq} concentration; this effect becomes much weaker at increasing temperature. As seen in Fig. 19 B, this is because the common anion effect, due to a much higher aqueous concentration of sulphate at higher Sr contents in the solid solution, decreases the equilibrium aqueous solubility of both Ba and Ra, adding to the dilution effect of Ra in the solid solution. In the Opalinus clayrock, natural diagenetic Ba-Sr sulphate cements contain 22% to 90% Sr and fibrolytic baryte along shear planes 2 to 12 % Sr (Lerouge et al., 2014). In the Callovo-Oxfordian clayrock, rare diagenetic barite contains up to 19% Sr and more abundant celestine contains 7 to 16% Ba (Lerouge et al., 2011). In both clayrocks, the porewater is assumed saturated with respect to celestine (as seen in Fig. 19 D, this corresponds to the presence of celestine with less than 10-12% Ba).

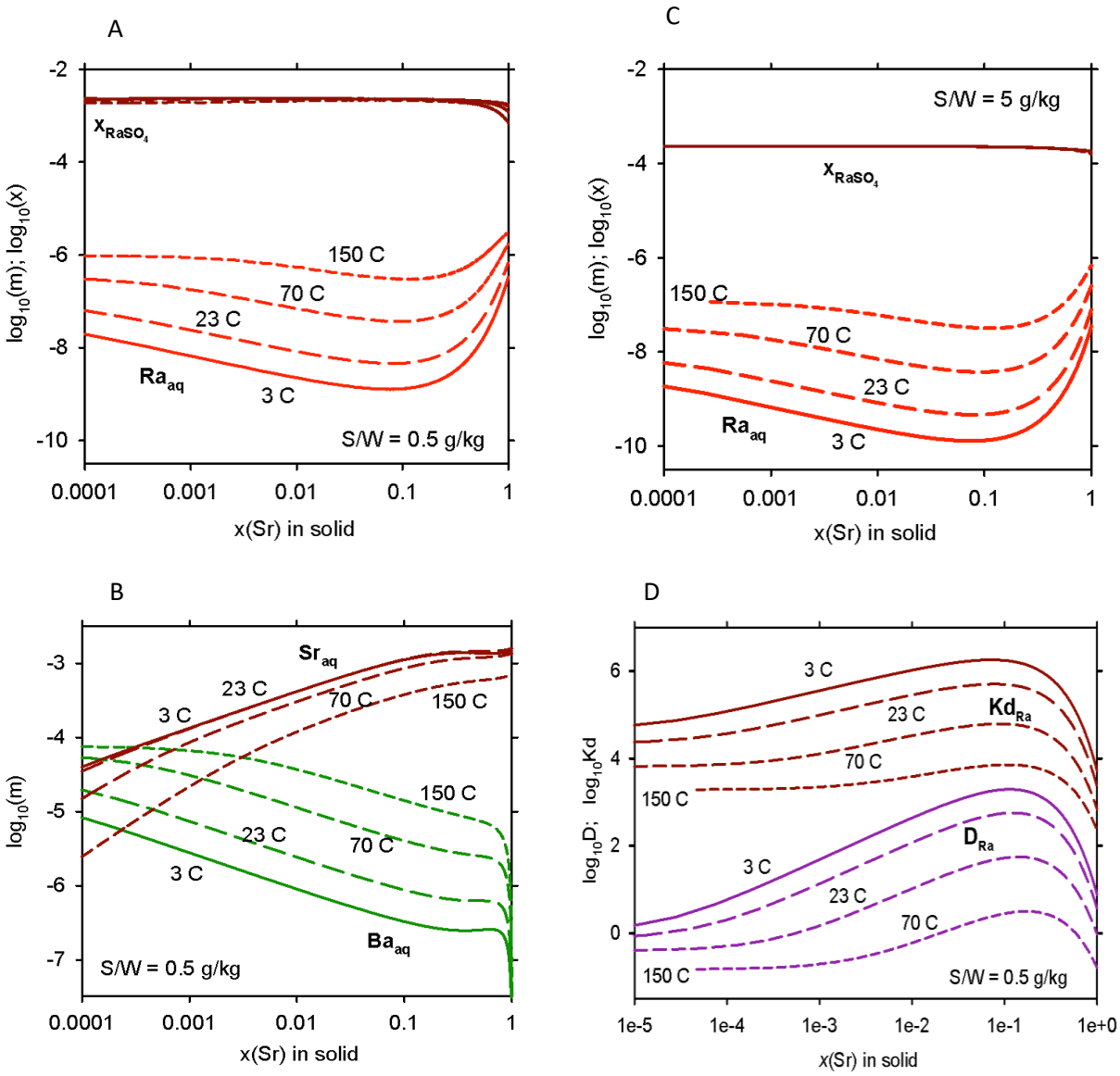

Figure 19. *The impact of Sr content in the ternary non-ideal (Sr,Ba,Ra)SO_4 solid solution onto Ra uptake at $5 \cdot 10^{-6}$ m $RaCl_2$, constant S/W mass ratios of 0.5and 5.0 g/kg, and different temperatures at 1 bar (150˚C at saturated vapour pressure). See text for explanations.*

Such predictions of equilibrium Ra retention in non-ideal ternary (Ba,Sr,Ra)SO_4 solid solutions can only be calculated using GEM algorithms (advanced LMA codes can only solve speciation involving binary or ideal solid solutions, (Reed, 1982)). Indeed, our results are more realistic than those involving pure (Sr-free) baryte, hence comprising a more general and favourable case for considering disposal safety.

Publications

Miron, G.D., Kulik, D.A., Thoenen, T., 2020. Generating isocoulombic reactions as a tool for systematic evaluation of temperature trends of thermodynamic properties: Application to aquocomplexes of lanthanides and actinides. Geochim. Cosmochim. Acta 286, 119–142

Miron, G.D., Leal, A.M.M., Yapparova, A., 2019. Thermodynamic Properties of Aqueous Species Calculated Using the HKF Model: How Do Different Thermodynamic and Electrostatic Models for Solvent Water Affect Calculated Aqueous Properties? Geofluids 2019, 1–24.

Lothenbach, B., Kulik, D.A., Matschei, T., Balonis, M., Baquerizo, L., Dilnesa, B., Miron, G.D., Myers, R.J., 2019. Cemdata18: A chemical thermodynamic database for hydrated Portland cements and alkali-activated materials. Cem. Concr. Res. 115, 472–506.

Vinograd, V.L., Kulik, D.A., Brandt, F., Klinkenberg, M., Weber, J., Winkler, B., Bosbach, D. (2018a): Thermodynamics of the solid solution - aqueous solution system (Ba,Sr,Ra)SO4 + H2O: I. The effect of strontium content on radium uptake by barite. Applied Geochemistry 89, 59-74.

Vinograd, V.L., Kulik, D.A., Brandt, F., Klinkenberg, M., Weber, J., Winkler, B., Bosbach, D. (2018b): Thermodynamics of the solid solution - aqueous solution system (Ba,Sr,Ra)SO4 + H2O: II. Radium retention in barite-type minerals at elevated temperatures. Applied Geochemistry 93, 190-208.

Participation in conferences

Miron, G.D., Kulik, D.A., Thoenen, T. Estimating temperature dependence of Ln and An complexes using isocoulombic reactions. Goldschmidt 18-23 August 2019, Barcelona, Spain. (invited talk).

Miron, G.D., Kulik, D.A., Thoenen, T. Estimating the temperature dependence of Ln and An complexes using isocoulombic reactions. HiTAC 3 27 June 2019, Karlsruhe, Germany.

Miron, G. D., Kulik, D. A., Lothenbach B. A PHREEQC version of Cemdata'18 generated using ThermoMatch. CASH 2 workshop 12 March 2018, EMPA Dübendorf, Switzerland.

References

Akinfiev, N.N., Diamond, L.W., 2003. Thermodynamic description of aqueous nonelectrolytes at infinite dilution over a wide range of state parameters. Geochim. Cosmochim. Acta 67, 613–629. https://doi.org/10.1016/S0016-7037(02)01141-9

Anderson, G.M., Castet, S., Schott, J., Mesmer, R.E., 1991. The density model for estimation of thermodynamic parameters of reactions at high temperatures and pressures. Geochim. Cosmochim. Acta 55, 1769–1779. https://doi.org/10.1016/0016-7037(91)90022-W

Birch, F., 1947. Finite elastic strain of cubic crystals. Phys. Rev. 71, 809–824.

https://doi.org/10.1103/PhysRev.71.809

Brandt, F., Curti, E., Klinkenberg, M., Rozov, K., Bosbach, D., 2015. Replacement of barite by a (Ba,Ra)SO4 solid solution at close-to-equilibrium conditions: A combined experimental and theoretical study. Geochim. Cosmochim. Acta 155, 1–15. https://doi.org/10.1016/j.gca.2015.01.016

Brown, P.L., Ekberg, C., Ramebäck, H., Hedström, H., Matyskin, A., 2015. Solubility of Radium and Strontium Sulfate across the Temperature Range of 0 to 300°C, in: Uranium - Past and Future Challenges. Springer International Publishing, pp. 553–564. https://doi.org/10.1007/978-3-319-11059-2_63

Busey, R.H., Mesmer, R.E., 1978. Thermodynamic Quantities for the Ionization of Water in Sodium Chloride Media to 300 °C. J. Chem. Eng. Data 23, 175–176. https://doi.org/10.1021/je60077a025

Churakov, S. V., Gottschalk, M., 2003. Perturbation theory based equation of state for polar molecular fluids: II. Fluid mixtures. Geochim. Cosmochim. Acta 67, 2415–2425. https://doi.org/10.1016/S0016-7037(02)01348-0

D'Angelo, P., Martelli, F., Spezia, R., Filipponi, A., Denecke, M.A., 2013. Hydration Properties and Ionic Radii of Actinide(III) Ions in Aqueous Solution. Inorg. Chem. 52, 10318–10324. https://doi.org/10.1021/ic400678u

D'Angelo, P., Zitolo, A., Migliorati, V., Chillemi, G., Duvail, M., Vitorge, P., Abadie, S., Spezia, R., 2011. Revised Ionic Radii of Lanthanoid(III) Ions in Aqueous Solution. Inorg. Chem. 50, 4572–4579. https://doi.org/10.1021/ic200260r

Di Bernardo, P., Endrizzi, F., Melchior, A., Zhang, Z., Zanonato, P.L., Rao, L., 2018. Complexation of Th(IV) with sulfate in aqueous solution at 10–70 °C. J. Chem. Thermodyn. 116, 273–278. https://doi.org/10.1016/j.jct.2017.09.025

Dolejš, D., 2013. Thermodynamics of Aqueous Species at High Temperatures and Pressures: Equations of State and Transport Theory. Rev. Mineral. Geochemistry 76, 35–79. https://doi.org/10.2138/rmg.2013.76.3

Dolejš, D., Manning, C.E., 2010. Thermodynamic Model for Mineral Solubility in Aqueous Fluids: Theory, Calibration and Application to Model Fluid-Flow Systems. Front. Geofluids 20–40. https://doi.org/10.1002/9781444394900.ch3

Gu, Y., Gammons, C.H., Bloom, M.S., 1994. A one-term extrapolation method for estimating equilibrium constants of aqueous reactions at elevated temperatures. Geochim. Cosmochim. Acta 58, 3545–3560. https://doi.org/10.1016/0016-7037(94)90149-X

Guillaumont, R., Fanghänel, T., Neck, V., Fuger, J., Palmer, D.A., Grenthe, I., Rand, M.H., 2003. Update on the chemical thermodynamics of uranium, neptunium, plutonium, americium and technetium. Chemical Thermodynamics 5, NEA OECD. Elsevier, 919 pp.

Haar, L., Gallagher, J.G., Kell, G.S., 1984. NBS/NRC Steam Tables. Hemisphere Pub., Washington, D. C.

Haas, J.R., Shock, E.L., Sassani, D.C., 1995. Rare earth elements in hydrothermal systems: Estimates of standard partial molal thermodynamic properties of aqueous complexes of the rare earth elements at high pressures and temperatures. Geochim. Cosmochim. Acta 59, 4329–4350. https://doi.org/10.1016/0016-7037(95)00314-P

Hedström, H., 2013. Radium Sulphate and Its Co-precipitation Behaviour with Barium and Strontium. Chalmers University of Technology.

Helgeson, H.C., 1969. Thermodynamics of hydrothermal systems at elevated temperatures and pressures. Am. J. Sci. 267, 729–804. https://doi.org/10.2475/ajs.267.7.729

Holland, T., Powell, R., 1991. A Compensated-Redlich-Kwong (CORK) equation for volumes and fugacities of CO2 and H2O in the range 1 bar to 50 kbar and 100-1600 C. Contrib. to Mineral. Petrol. 109, 265–273. https://doi.org/10.1007/BF00306484

Holland, T.J.B., Powell, R., 1998. An internally consistent thermodynamic data set for phases of petrological interest. J. Metamorph. Geol. 16, 309–343. https://doi.org/10.1111/j.1525-1314.1998.00140.x

Howell, R.D., Raju, K., Atkinson, G., 1992. Thermodynamics of "Scale" Mineral Solubilities 4. Experimental Measurements of SrSO4(s) in H2O and aqueous NaCl from 25 to 250 °C And from 1 to 500 bar. J. Chem. Eng. Data 37, 464–469. https://doi.org/10.1021/je00008a020

Hummel, W., Berner, U., Curti, E., Pearson, F.J., Thoenen, T., 2002. Nagra/PSI Chemical Thermodynamic Data Base 01/01. Radiochim. Acta 90, 805–813. https://doi.org/10.1524/ract.2002.90.9-11_2002.805

Johnson, J.W., Norton, D., 1991. Critical phenomena in hydrothermal systems: state, thermodynamic, electrostatic, and transport properties of H2O in the critical region. Am. J. Sci. 291, 541–648. https://doi.org/10.2475/ajs.291.6.541

Jordan, N., Demnitz, M., Lösch, H., Starke, S., Brendler, V., Huittinen, N., 2018. Complexation of Trivalent Lanthanides (Eu) and Actinides (Cm) with Aqueous Phosphates at Elevated Temperatures. Inorg. Chem. 57, 7015–7024. https://doi.org/10.1021/acs.inorgchem.8b00647

Khodakovsky, I.L., Mishin, I.V., Zhogina, V.V., 1966. About temperature dependence ofsolubility constants and some limits on the chemical composition of hydrothermalsolutions. Geokhimiya 7, 861–866.

Leal, A.M.M., Kulik, D.A., Kosakowski, G., Saar, M.O., 2016. Computational methods for reactive transport modeling: An extended law of mass-action, xLMA, method for multiphase equilibrium calculations. Adv. Water Resour. 96, 405–422. https://doi.org/10.1016/j.advwatres.2016.08.008

Leal, A.M.M., Kulik, D.A., Smith, W.R., Saar, M.O., 2017. An overview of computational methods for chemical equilibrium and kinetic calculations for geochemical and reactive transport modeling. Pure Appl. Chem. 89, 597–643. https://doi.org/10.1515/pac-2016-1107

Lemire, R.J., Fuger, J., Spahiu, K., Sullivan, J.C., Nitsche, H., Ullman, W.J., Potter, P., Vitorge, P., Rand, M.H., Wanner, H., Rydberg, J., 2001. Chemical Thermodynamics of Neptunium and Plutonium. Chem. Thermodyn. 4, NEA OECD. Elsevier, 845 pp.

Lerouge, C., Grangeon, S., Claret, F., Gaucher, E., Blanc, P., Guerrot, C., Flehoc, C., Wille, G., Mazurek, M., 2014. Mineralogical and isotopic record of diagenesis from the Opalinus Clay formation at Benken, Switzerland: Implications for the modeling of pore-water chemistry in a clay formation. Clays Clay Miner. 62, 286–312. https://doi.org/10.1346/CCMN.2014.0620404

Lerouge, C., Grangeon, S., Gaucher, E.C., Tournassat, C., Agrinier, P., Guerrot, C., Widory, D., Fléhoc, C., Wille, G., Ramboz, C., Vinsot, A., Buschaert, S., 2011. Mineralogical and isotopic record of biotic

and abiotic diagenesis of the Callovian-Oxfordian clayey formation of Bure (France). Geochim. Cosmochim. Acta 75, 2633–2663. https://doi.org/10.1016/j.gca.2011.02.025

Lindsay, W.T., 1980. Estimation of Concentration Quotients for Ionic Equilibria in High Temperature Water: The Model Substance Approach, in: Proceedings of the 41st International Water Conference, Pittsburgh, PA (USA). Engineers Society of Western Pennsylvania., pp. 284–294.

Lothenbach, B., Kulik, D.A., Matschei, T., Balonis, M., Baquerizo, L., Dilnesa, B., Miron, G.D., Myers, R.J., 2019. Cemdata18: A chemical thermodynamic database for hydrated Portland cements and alkali-activated materials. Cem. Concr. Res. 115, 472–506. https://doi.org/10.1016/j.cemconres.2018.04.018

Marshall, W.L., Franck, E.U., 1983. Ion product of water substance, 0-1000 °C, 1-10,000 bars New International Formulation and its background. J. Phys. Chem. Ref. Data 10, 295–304. https://doi.org/10.1063/1.555643

Mesmer, R.E., Palmer, D.A., Simonson, J.M., 1991. Ion association at high temperatures and pressures., in: Pitzer, K.S. (Ed.), Activity Coefficients in Electrolyte Solutions. CRC Press, Boston.

Migdisov, A., Williams-Jones, A.E., Wagner, T., 2009. An experimental study of the solubility and speciation of the Rare Earth Elements (III) in fluoride- and chloride-bearing aqueous solutions at temperatures up to 300 °C. Geochim. Cosmochim. Acta 73, 7087–7109. https://doi.org/10.1016/j.gca.2009.08.023

Miron, G.D., Kulik, D.A., Lothenbach, B., 2018. A PHREEQC version of CEMDATA'18 generated using ThermoMatch, in: Calcium-Silicate Hydrates Containing Aluminium: C-A-S-H II. Dübendorf, Switzerland.

Miron, G.D., Kulik, D.A., Thoenen, T., 2020. Generating isocoulombic reactions as a tool for systematic evaluation of temperature trends of thermodynamic properties: Application to aquocomplexes of lanthanides and actinides. Geochim. Cosmochim. Acta 286, 119–142. https://doi.org/10.1016/j.gca.2020.07.020

Miron, G.D., Leal, A.M.M., Yapparova, A., 2019. Thermodynamic Properties of Aqueous Species Calculated Using the HKF Model: How Do Different Thermodynamic and Electrostatic Models for Solvent Water Affect Calculated Aqueous Properties? Geofluids 2019, 1–24. https://doi.org/10.1155/2019/5750390

Miron, G.D., Wagner, T., Kulik, D.A., Lothenbach, B., 2017. An internally consistent thermodynamic dataset for aqueous species in the system Ca-Mg-Na-K-Al-Si-O-H-C-Cl to 800 °C and 5 kbar. Am. J. Sci. 317, 755–806. https://doi.org/10.2475/07.2017.01

Missen, R.W., Smith, W.R., 1998. Chemical Reaction Stoichiometry (CRS): A Tutorial. Downloaded from www.chemical-stoichiometry.net/tutorial.htm.

Murnaghan, F.D., 1944. The Compressibility of Media under Extreme Pressures. Proc. Natl. Acad. Sci. 30, 244–247. https://doi.org/10.1073/pnas.30.9.244

Nikitin, B., Tolmatscheff, P., 1933. Article on the validity of mass effect law. II. Quantitative determination of solubility of radium-sulfate in sodium-sulfate solutions and in water. Z. Phys. Chem. A – Chem. Thermodyn. Kinet. Elektrochem. Eig. 167, 260–272.

Patterson, C.S., Slocum, G.H., Busey, R.H., Mesmer, R.E., 1982. Carbonate equilibria in hydrothermal

systems: First ionization of carbonic acid in NaCl media to 300°C. Geochim. Cosmochim. Acta 46, 1653–1663. https://doi.org/10.1016/0016-7037(82)90320-9

Peng, D.Y., Robinson, D.B., 1976. A New Two-Constant Equation of State. Ind. Eng. Chem. Fundam. 15, 59–64. https://doi.org/10.1021/i160057a011

Puigdomenech, I., Plyasunov, A., Rard, J.A., Grenthe, I., 1997. Temperature Corrections to Thermodynamic data and Enthalpy Calculations, In: Puigdomenech, I. & Grenthe, I. (eds.): Modelling in Aquatic Chemistry. NEA OECD, Paris, 427–493.

Raju, K., Atkinson, G., 1988. Thermodynamics of "Scale" Mineral Solubilities. 1. BaSO4(s) in H2O and Aqueous NaCl. J. Chem. Eng. Data 33, 490–495. https://doi.org/10.1021/je00054a029

Raju, K.U.G., Atkinson, G., 1990. The Thermodynamics of "Scale" Mineral Solubilities. 3. Calcium Sulfate in Aqueous NaCl. J. Chem. Eng. Data 35, 361–367. https://doi.org/10.1021/je00061a038

Raju, K.U.G., Atkinson, G., 1989. Thermodynamics of "Scale" Mineral Solubilities. 2. SrSO4(s) in Aqueous NaCl. J. Chem. Eng. Data 34, 361–364. https://doi.org/10.1021/je00057a028

Redlich, O., Kwong, J.N.S., 1949. On the thermodynamics of solutions. V. An equation of state. Fugacities of gaseous solutions. Chem. Rev. 44, 233–244. https://doi.org/10.1021/cr60137a013

Reed, M.H., 1982. Calculation of multicomponent chemical equilibria and reaction processes in systems involving minerals, gases and an aqueous phase. Geochim. Cosmochim. Acta 46, 513–528. https://doi.org/10.1016/0016-7037(82)90155-7

Robie, R., Hemingway, B.S., 1995. Thermodynamic Properties of Minerals and Related Substances at 298.15K and 1 Bar. U.S. Geol. Surv. Bull.

Ryzhenko, B.N., Bryzgalin, O. V., Artamkina, I.Y., Spasennykh, M.Y., Shapkin, A.I., 1985. An electrostatic model for the electrolytic dissociation of inorganic substances dissolved in water. Geochemistry Int. 22, 138-144.

Shock, E.L., Sassani, D.C., Willis, M., Sverjensky, D.A., 1997. Inorganic species in geologic fluids: Correlations among standard molal thermodynamic properties of aqueous ions and hydroxide complexes. Geochim. Cosmochim. Acta 61, 907–950. https://doi.org/10.1016/S0016-7037(96)00339-0

Simmler, M., 2012. Can the isocoulombic approach fill data gaps in the PSI/Nagra thermodynamic database? AN-44-12-09. PSI Villigen.

Soave, G., 1972. Equilibrium constants from a modified Redlich-Kwong equation of state. Chem. Eng. Sci. 27, 1197–1203. https://doi.org/10.1016/0009-2509(72)80096-4

Stryjek, R., Vera, J.H., 1986. PRSV: An improved peng—Robinson equation of state for pure compounds and mixtures. Can. J. Chem. Eng. 64, 323–333. https://doi.org/10.1002/cjce.5450640224

Sverjensky, D.A., Harrison, B., Azzolini, D., 2014. Water in the deep Earth: The dielectric constant and the solubilities of quartz and corundum to 60 kb and 1200 °C. Geochim. Cosmochim. Acta 129, 125–145. https://doi.org/10.1016/J.GCA.2013.12.019

Sverjensky, D.A., Shock, E.L., Helgeson, H.C., 1997. Prediction of the thermodynamic properties of aqueous metal complexes to 1000°C and 5 kb. Geochim. Cosmochim. Acta. 61, 1359-1412. https://doi.org/10.1016/S0016-7037(97)00009-4

Tanger, J.C., Helgeson, H.C., 1988. Calculation of the thermodynamic and transport properties of aqueous species at high pressures and temperatures; revised equations of state for the standard partial molal properties of ions and electrolytes. Am. J. Sci. 288, 19–98. https://doi.org/10.2475/ajs.288.1.19

Thoenen, T., Hummel, W., Berner, U.R., Curti, E., 2014. The PSI / Nagra Chemical Thermodynamic Database 12 / 07. PSI Bericht Nr. 14-04, 417pp.

Vinograd, V.L., Kulik, D.A., Brandt, F., Klinkenberg, M., Weber, J., Winkler, B., Bosbach, D., 2018a. Thermodynamics of the solid solution - Aqueous solution system (Ba,Sr,Ra)SO4 + H2O: I. The effect of strontium content on radium uptake by barite. Appl. Geochemistry 89, 59–74. https://doi.org/10.1016/j.apgeochem.2017.11.009

Vinograd, V.L., Kulik, D.A., Brandt, F., Klinkenberg, M., Weber, J., Winkler, B., Bosbach, D., 2018b. Thermodynamics of the solid solution - Aqueous solution system (Ba,Sr,Ra)SO4 + H2O: II. Radium retention in barite-type minerals at elevated temperatures. Appl. Geochemistry 93, 190–208. https://doi.org/10.1016/j.apgeochem.2017.10.019

Wagner, W., Pruß, A., 2002. The IAPWS Formulation 1995 for the Thermodynamic Properties of Ordinary Water Substance for General and Scientific Use. J. Phys. Chem. Ref. Data 31, 387–535. https://doi.org/10.1063/1.1461829

Wood, S.A., Samson, I.M., 1998. Solubility of Ore Minerals and Complexation of Ore Metals in Hydrothermal Solutions. Tech. Hydrothermal Ore Depos. Geol. https://doi.org/10.5382/Rev.10.02

Xia, Y.X., Friese, J.I., Moore, D.A., Bachelor, P.P., Rao, L., 2007. Complexation of plutonium(IV) with sulfate at variable temperatures. J. Radioanal. Nucl. Chem. 274, 79–86. https://doi.org/10.1007/s10967-006-6907-z

Zhang, Z., Duan, Z., 2005. Prediction of the PVT properties of water over wide range of temperatures and pressures from molecular dynamics simulation. Phys. Earth Planet. Inter. 149, 335–354. https://doi.org/10.1016/j.pepi.2004.11.003

Appendix A: Derivation of the temperature extrapolation equations

Glossary of symbols

$\Delta_r C^\circ_{p,m}$	Standard molar isobaric heat capacity effect of reaction
$\Delta_r G^\circ_m$	Standard molar Gibbs free energy effect of reaction
$\Delta_r H^\circ_m$	Standard molar enthalpy effect of reaction
$\Delta_r S^\circ_m$	Standard molar entropy effect of reaction
T	Temperature, absolute
T_0	Reference temperature
ln	Natural logarithm
$\log_{10}$	Decimal logarithm
K°	Equilibrium constant

The standard molar Gibbs free energy change of reaction at temperature T is defined by

$$\Delta_r G^\circ_m(T) = \Delta_r H^\circ_m(T) - T\Delta_r S^\circ_m(T) \quad \text{(A1)}$$

The rate of change of the standard molar enthalpy of reaction with temperature at constant pressure is given by

$$\left(\frac{\partial \Delta_r H^\circ_m}{\partial T}\right)_p = \Delta_r C^\circ_{p,m} \quad \text{(A2)}$$

and that of the standard molar entropy of reaction by

$$\left(\frac{\partial \Delta_r S^\circ_m}{\partial T}\right)_p = \frac{\Delta_r C^\circ_{p,m}}{T} \quad \text{(A3)}$$

Integration of eq. (A2) leads to

$$\Delta_r H^\circ_m(T) = \Delta_r H^\circ_m(T_0) + \int_{T_0}^{T} \Delta_r C^\circ_{p,m} dT \quad \text{(A4)}$$

and integration of eq. (A3) to

$$\Delta_r S^\circ_m(T) = \Delta_r S^\circ_m(T_0) + \int_{T_0}^{T} \frac{\Delta_r C^\circ_{p,m}}{T} dT \quad \text{(A5)}$$

which is equivalent to

$$\Delta_r S^\circ_m(T) = \Delta_r S^\circ_m(T_0) + \int_{T_0}^{T} \Delta_r C^\circ_{p,m} d\ln T \quad \text{(A6)}$$

Inserting eqs. (A4) and (A6) into eq. (A1) and rearranging terms results in

$$\Delta_r G^\circ_m(T) = \Delta_r H^\circ_m(T_0) - T\,\Delta_r S^\circ_m(T_0) + \int_{T_0}^{T} \Delta_r C^\circ_{p,m} dT - T\int_{T_0}^{T} \Delta_r C^\circ_{p,m} d\ln T \quad \text{(A7)}$$

From eq. (A1) follows (replacing T by T_0)

$$\Delta_r H^\circ_m(T_0) = \Delta_r G^\circ_m(T_0) + T_0 \Delta_r S^\circ_m(T_0) \quad \text{(A8)}$$

Inserting eq. (A8) into eq. (A7) leads to a general expression for the temperature dependence of the standard molar Gibbs free energy of reaction

$$\Delta_r G^\circ_m(T) = \Delta_r G^\circ_m(T_0) - (T - T_0)\,\Delta_r S^\circ_m(T_0) + \int_{T_0}^{T} \Delta_r C^\circ_{p,m} dT - T\int_{T_0}^{T} \Delta_r C^\circ_{p,m} d\ln T \quad \text{(A9)}$$

An equivalent expression can be obtained by replacing $\Delta_r S^\circ_m(T_0)$ with

$$\Delta_r S^\circ_m(T_0) = \frac{\Delta_r H^\circ_m(T_0) - \Delta_r G^\circ_m(T_0)}{T_0} \quad \text{(A10)}$$

which follows from eq. (A8). Thus

$$\Delta_r G^\circ_m(T) = \frac{T}{T_0}\,\Delta_r G^\circ_m(T_0) + \left(1 - \frac{T}{T_0}\right)\Delta_r H^\circ_m(T_0) + \int_{T_0}^{T} \Delta_r C^\circ_{p,m} dT - T\int_{T_0}^{T} \Delta_r C^\circ_{p,m} d\ln T \quad \text{(A11)}$$

Similar expressions for the temperature dependence of the equilibrium constant can be obtained by inserting

$$\Delta_r G^\circ_m(T) = -RT\ln K^\circ(T) = -RT\ln(10)\log_{10} K^\circ(T) \quad \text{(A12)}$$

into eqs. (A9) and (A11), resulting in

$$\log_{10} K^\circ(T) = \frac{T_0}{T}\log_{10} K^\circ(T_0) + \left(1 - \frac{T_0}{T}\right)\frac{\Delta_r S^\circ_m(T_0)}{R\ln(10)} - \frac{1}{RT\ln(10)}\int_{T_0}^{T} \Delta_r C^\circ_{p,m} dT + \frac{1}{R\ln(10)}\int_{T_0}^{T} \Delta_r C^\circ_{p,m} d\ln T \quad \text{(A13)}$$

and

$$\log_{10} K^\circ(T) = \log_{10} K^\circ(T_0) - \left(\frac{1}{T} - \frac{1}{T_0}\right)\frac{\Delta_r H^\circ_m(T_0)}{R\ln(10)} - \frac{1}{RT\ln(10)}\int_{T_0}^{T} \Delta_r C^\circ_{p,m} dT + \frac{1}{R\ln(10)}\int_{T_0}^{T} \Delta_r C^\circ_{p,m} d\ln T \quad \text{(A14)}$$

If $\Delta_r C^\circ_{p,m}$ is assumed to be constant over the considered temperature interval, the integrals in the expressions above can be evaluated as follows:

$$\int_{T_0}^{T} \Delta_r C^\circ_{p,m} dT = (T - T_0)\,\Delta_r C^\circ_{p,m}(T_0) \quad \text{(A15)}$$

$$\int_{T_0}^{T} \Delta_r C^\circ_{p,m} d\ln T = \ln\frac{T}{T_0}\,\Delta_r C^\circ_{p,m}(T_0) \quad \text{(A16)}$$

Inserting these equations into eqs. (A13) and (A14) leads to the 3-term temperature extrapolation equations

$$\log_{10}K^{\circ}(T) = \frac{T_0}{T}\log_{10}K^{\circ}(T_0) + \left(1 - \frac{T_0}{T}\right)\frac{\Delta_r S^{\circ}_m(T_0)}{R\ln(10)} - \left(1 - \frac{T_0}{T} + \ln\frac{T_0}{T}\right)\frac{\Delta_r C^{\circ}_{p,m}(T_0)}{R\ln(10)} \quad \text{(A17)}$$

and

$$\log_{10}K^{\circ}(T) = \log_{10}K^{\circ}(T_0) - \left(\frac{1}{T} - \frac{1}{T_0}\right)\frac{\Delta_r H^{\circ}_m(T_0)}{R\ln(10)} - \left(1 - \frac{T_0}{T} + \ln\frac{T_0}{T}\right)\frac{\Delta_r C^{\circ}_{p,m}(T_0)}{R\ln(10)} \quad \text{(A18)}$$

If it is assumed that $\Delta_r C^{\circ}_{p,m} = 0$, eqs. (A17) and (A18) are reduced to the 2-term temperature extrapolation equations

$$\log_{10}K^{\circ}(T) = \frac{T_0}{T}\log_{10}K^{\circ}(T_0) + \left(1 - \frac{T_0}{T}\right)\frac{\Delta_r S^{\circ}_m(T_0)}{R\ln(10)} \quad \text{(A19)}$$

and

$$\log_{10}K^{\circ}(T) = \log_{10}K^{\circ}(T_0) - \left(\frac{1}{T} - \frac{1}{T_0}\right)\frac{\Delta_r H^{\circ}_m(T_0)}{R\ln(10)} \quad \text{(A20)}$$

The 1-term temperature extrapolation equations

$$\log_{10}K^{\circ}(T) = \frac{T_0}{T}\log_{10}K^{\circ}(T_0) \quad \text{(A21)}$$

and

$$\log_{10}K^{\circ}(T) = \log_{10}K^{\circ}(T_0) \quad \text{(A22)}$$

are finally obtained by assuming that either $\Delta_r S^{\circ}_m(T_0) = 0$, equation (A21), or $\Delta_r H^{\circ}_m(T_0) = 0$, equation (A22).

TEILBERICHT D

Arbeiten von Amphos[21]

Der von Amphos[21] an KIT-INE übermittelte Bericht zu den durchgeführten Arbeiten innerhalb von ThermAc (inklusive der Verlängerungsphase) ist nachfolgend dargestellt.

SPONSORED BY THE
Federal Ministry of Education and Research

AMPHOS 21
SCIENTIFIC AND STRATEGIC ENVIRONMENTAL CONSULTING

KIT
Karlsruhe Institute of Technology

ThermAc project: Thermodynamics and speciation of actinides at elevated temperatures.

Estimation methods and comparison with the experimental data generated within ThermAc.

E. Colàs.

March 2020

SPONSORED BY THE

This work has been supported by ThermAc project, funded by the German Federal Ministry for Education and Research (BMBF),

Amphos21 was subcontracted to KIT-INE

In bibliography, this report will be cited as follows:

E. Colàs, (2020) ThermAc project: Thermodynamics and speciation of actinides at elevated temperatures. Estimation methods and comparison with the experimental data generated within ThermAc. Amphos 21 report vs0.

Amphos 21 Consulting S.L.

Pg. de García Faria, 49-51, 08019 Barcelona (Spain)

+34 935 830 500

www.amphos21.com

Prepared by	Reviewed by	Validated by
		
E. Colàs	D. García	L. Duro

Index

1 Introduction

The disposal of high-level waste glass or spent nuclear fuel leads to elevated temperatures in the nearfield and the surrounding host rock of a radioactive waste repository. The temperature evolution will depend on many parameters, such as the type of waste and its thermal loading, the canister material, the engineered barriers, the type of host rock or the overall design of the repository itself. Consequently, the performance assessment of a repository for heat generating waste will have well-defined scenarios including those periods of time for which the thermal peaks are expected to occur in the different engineered and natural barriers. For these scenarios, sufficient knowledge on the processes influenced by elevated temperatures is needed.

Nevertheless, aqueous and solid chemistry and geochemistry of radionuclides has been mostly studied at room temperature, mainly because performing experiments at temperatures different than 25°C is not straightforward and requires dedicated efforts and specific equipment. Takin into account the wide variety of elements and conditions for which data are needed, approaching the problem only from the experimental point of view would not be realistic. Therefore, besides experimental investigations, estimation methodologies are also required to cover the experimental gaps.

In this context, the aim of the present work is to evaluate different estimation algorithms in order to expand the available thermodynamic data for actinides, long-lived fission products and relevant matrix elements in aquatic systems at temperatures higher than 25°C, using the methodology outlined in Figure 1-1. The final goal is to verify the accuracy of the different estimation methodologies and provide a solid basis for its application by comparing the results of the estimations with the experimental data generated within the project.

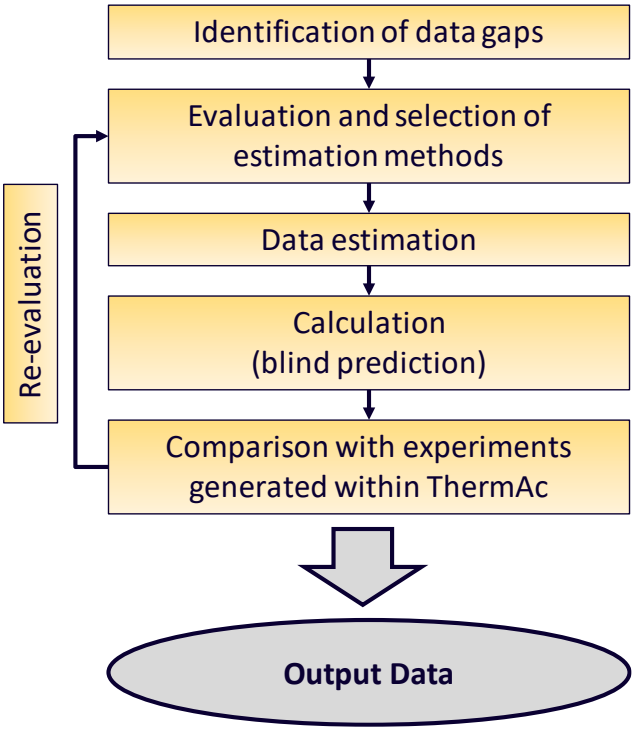

Figure 1-1. *Summary of the methodology to fill in data gaps.*

The systems of main interest are both aqueous species and solid compounds for trivalent lanthanides and actinides (such as Nd(III), Cm(III) or Eu(III)), Np(V), U(VI) and Th(IV). Besides hydrolysis, aqueous species and solid oxides and hydroxides, other ligands to be considered are chloride, sulphate, carbonate and phosphate. Even though peak temperatures can reach 200ºC (depending on the repository system), estimations are focused in the temperature range up to 90ºC and low or moderate ionic strengths, where most reliable results could be obtained.

2 Estimation methods

Reliable experimental data related to temperature effects are scarce, due to the inherent difficulties in the experimental designs and interpretations. To overcome this disadvantage, different estimation methodologies have been reported by different authors. The procedures are diverse; different approaches have been proposed for aqueous species (section 2.1) and solid compounds (section 2.2). More detailed information on relevant estimation methods is provided in Appendix A.

2.1 Aqueous species

For aqueous species, most of the available methods use correlations between entropies of analogous complexes and parameters such as crystallographic radii, molar volumes and mass, electrical charge, etc.

Langmuir (1978) empirically found that, for a given element, the entropies of aqueous complexes reasonably correlate with the charge (z) of the complexes. *Baes and Mesmer (1981)* suggested a dependency of the entropy of the hydrolysis reaction on the stability constant of the stepwise hydrolysis and the z/d ratio, where z is the charge of the cation and d is the interatomic distance between the cation and the oxygen atom in the complex. *Shock et al. (1997)* established correlations among experimental standard molal entropies of an aqueous hydroxide complex and the standard molal entropy of the corresponding cation ("SºCation"). *Sverjensky et al. (1997)* suggested a correlation between entropy of reaction and standard molal entropies of the cation and the ligand.

The correlations were built up in the publications with the data available in that moment, leading to specific equations. In some cases, those equations can be built up again and/or extended using as a basis new and updated values or different species (chemically similar to the species for which the entropy has to be estimated).

Information on those methods is provided in the sections below and in Appendix A.

2.1.1 Correlations based on Baes & Mesmer approach

The approach described by Baes and Mesmer (1981) is based on a correlation among the dependency on the entropy of the stepwise hydrolysis reaction and the charge of the species; an example proposed by the authors is shown in Figure 2-1. Details and original equations are provided in Table 6-8.

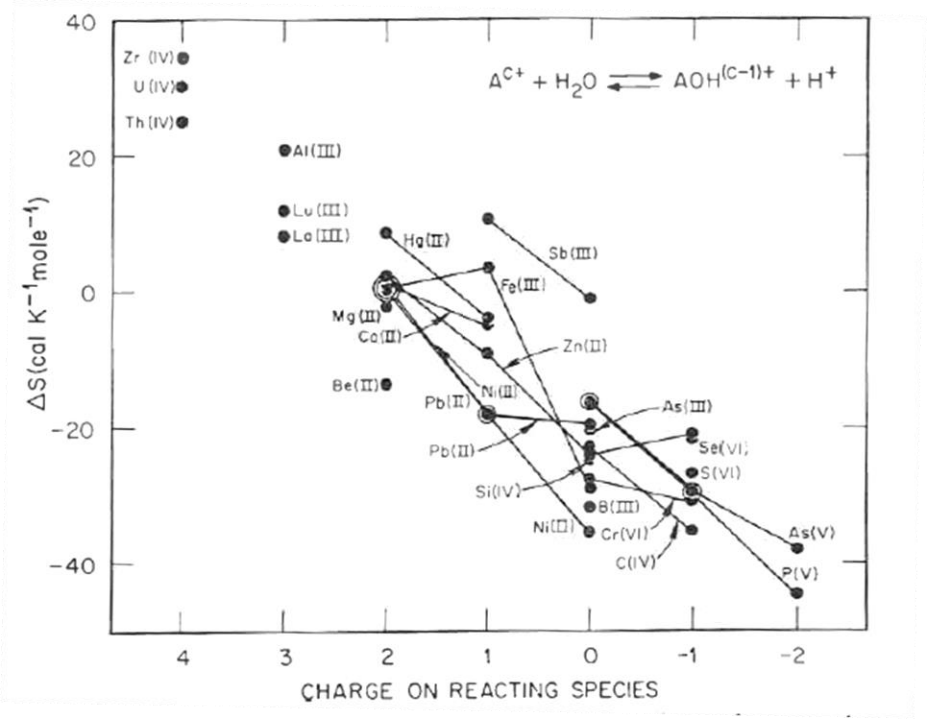

Figure 2-1. *Correlation of the entropy of stepwise hydrolysis with the charge of the reacting species, from Baes and Mesmer (1981). All species involve water, hydroxide ion, or oxide ion as ligands. The points connected by line stand for stepwise hydrolysis.*

We have tested this approach using available experimental data for the hydrolysis of elements such as Al(III), Ni(II), U(IV), Th(IV), U(VI), etc... ThermoChimie database version 9b (www.thermochimie-tdb.com; Giffaut et al. 2014 ; Grivé et al. 2015) has been used as a source of information; in the database, the results of the NEA-TDB project are used as a primary data source for many radionuclides. Only those values coming from experimental sources have been used in the correlations. Results are shown in Figure 2-2.

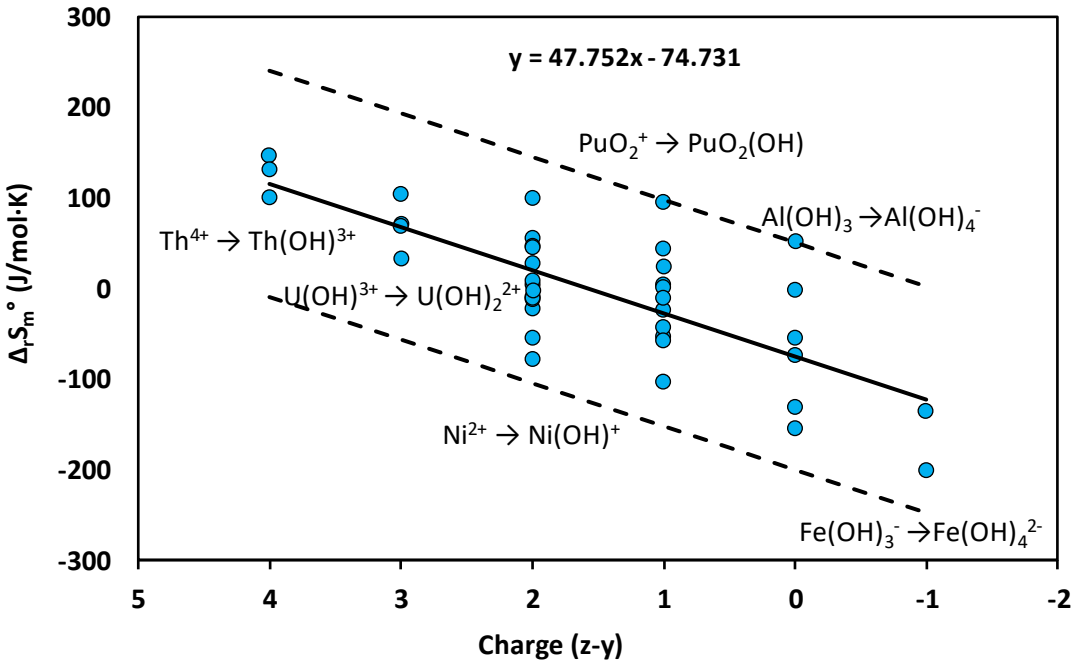

Figure 2-2. *Correlation between $\Delta_r S_m^o$ and charge of the species for different stepwise hydrolysis reactions. Blue circles are experimental data available for the stepwise hydrolysis of different metals and radionuclides; labels indicate some examples. The line represents the fitting of the available experimental data.*

2.1.2 Correlations based on Langmuir approach

Langmuir (1978) suggested that the entropies of uranium aqueous complexes reasonably correlate with the charge (z) of the complexes, following the 4th degree polynomial equation (Figure 2-3). The approach proposed by Langmuir was later applied by Lemire and Tremaine (1980), Lemire (1984) and Lemire and Garisto (1989) (among others) to estimate the entropies of some Pu and Np hydroxides.

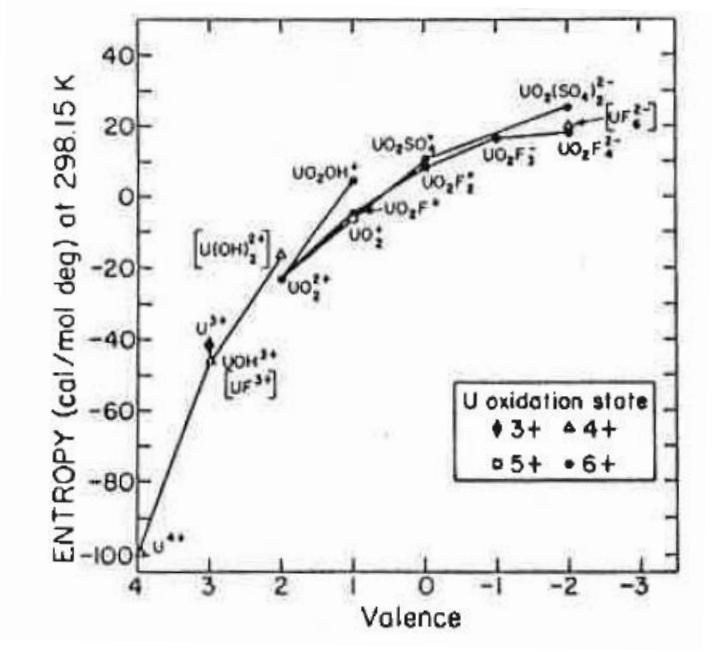

Figure 2-3. *Entropy vs valence for some uranium ions and complexes, as reported in Langmuir (1978). The line represents the fit to the 4th degree polynomial* S_m^0 *(cal/mol deg) = 8.3 – 10.55Z – 2.17Z² + 0.05Z³ – 0.13Z⁴.*

A similar correlation has been built up in present work using updated values; available experimental entropy data for mononuclear uranium species (Figure 2-4) and neptunium species (Figure 2-5) available in ThermoChimie version 9b and the NEA-TDB have been used in the correlations.

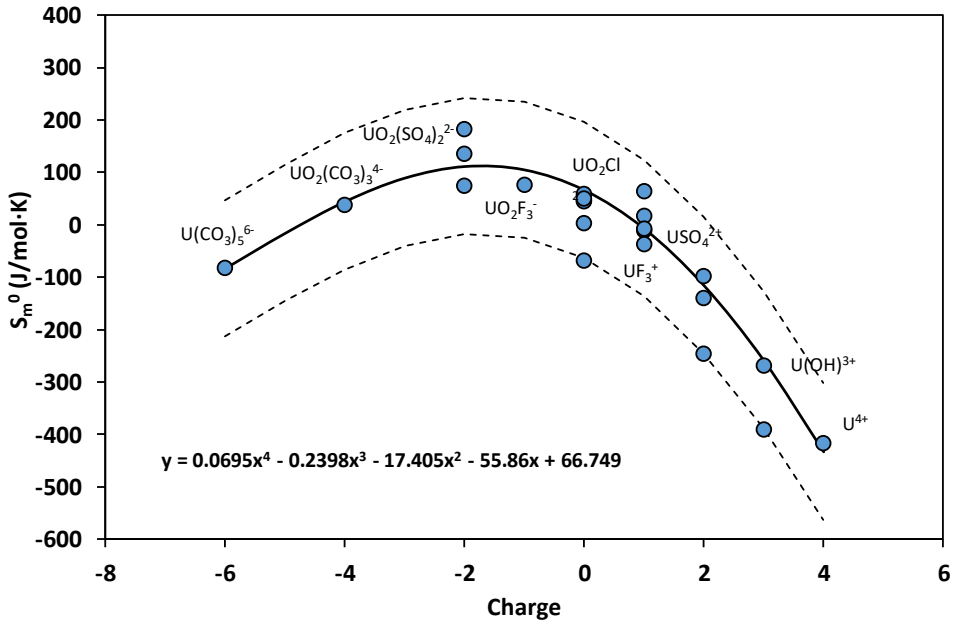

Figure 2-4. *Langmuir-type correlation between $S_m°$ and charge calculated in present work with uranium data. Blue circles are experimental data available for different uranium species; labels indicate some examples. The line represents the fitting of the available experimental data using a 4th degree polynomial.*

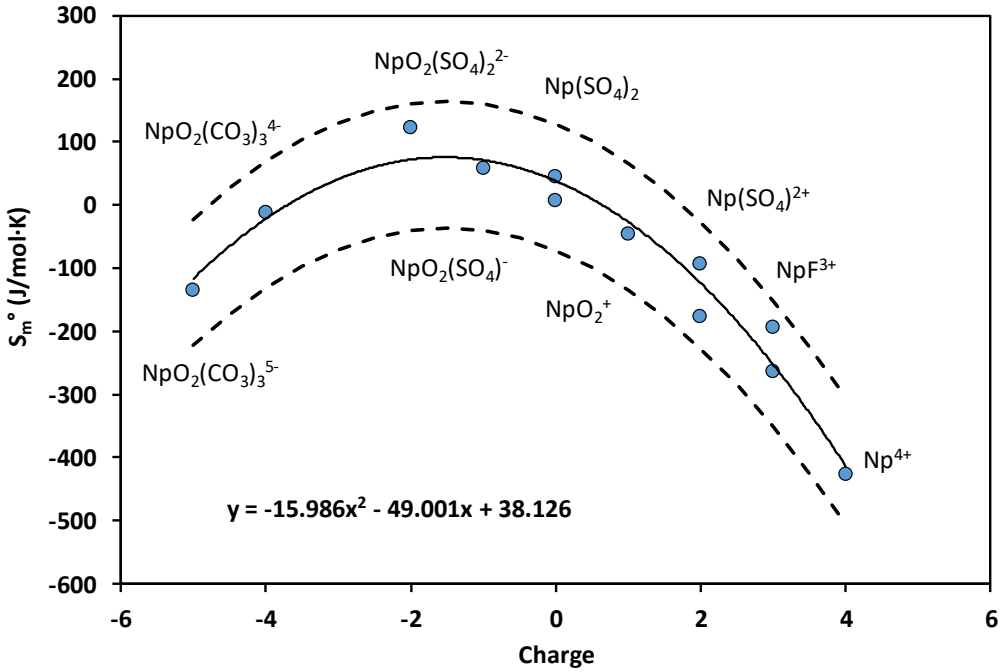

Figure 2-5. *Langmuir-type correlation between $S_m°$ and charge calculated in present work with neptunium data. Blue circles are experimental data available for different neptunium species; labels indicate some examples. The line represents the fitting of the available experimental data.*

Langmuir and Herman (1980) also provided rough estimates for monomeric complexes of thorium. The original graph reported in Langmuir and Herman (1980) for estimating entropy values of Thorium species is provided in Figure 2-6. No anionic species are included in the graph; thus, this curve may not be adequate to estimate entropy values of anionic thorium species.

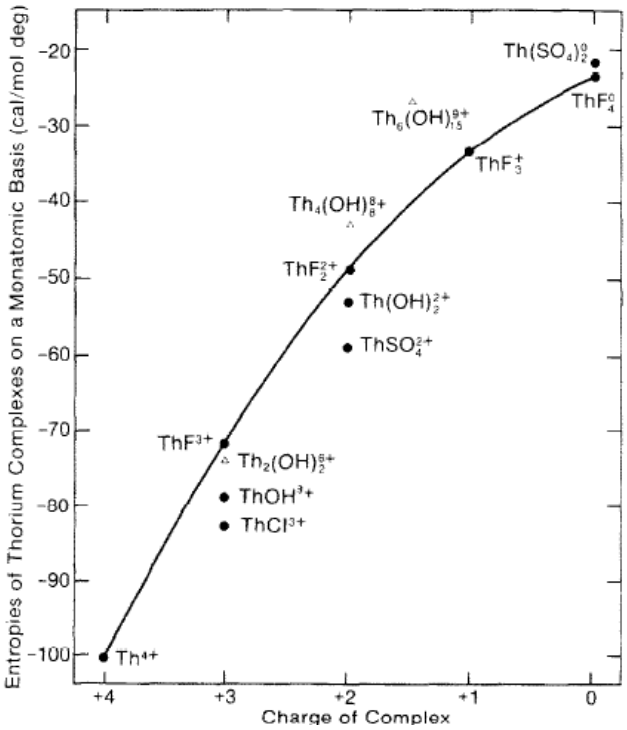

Figure 2-6. *Entropy vs valence for some thorium ions and complexes, as reported in Langmuir and Herman (1980). Entropy units are cal/mol deg.*

Although with a rather limited theoretical basis, it can be shown that available experimental entropies for lanthanide and actinide aqueous complexes follow a defined parabolic trend when represented versus the charge of the complex (Figure 2-7). This correlation was previously reported in Duro et al (2012).

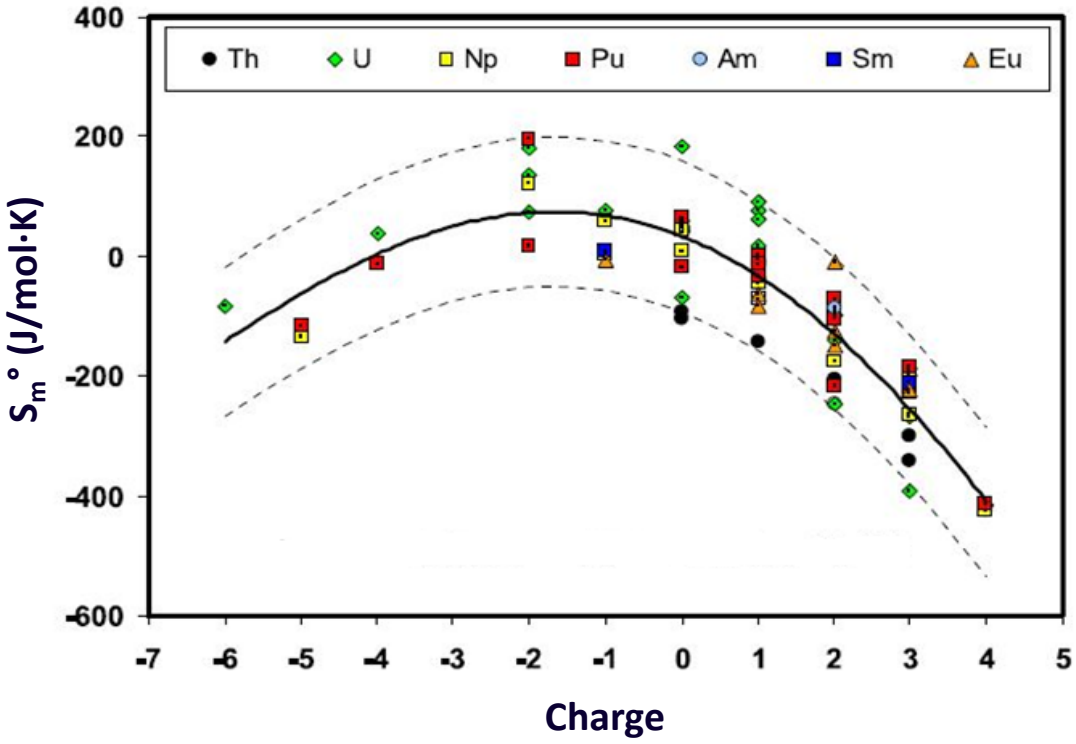

Figure 2-7. *Relationship between experimental entropies for lanthanide and actinide aqueous complexes and the charge of the complex, from Duro et al. (2012). Entropy units are J/mol K.*

2.1.3 **Shock et al. (1997) approach**

Shock et al. (1997) suggested a correlation between standard molal entropies S^o_m of an aqueous hydroxide complex and the standard molal entropy of the corresponding cation; an example is shown in Figure 2-8. The correlation was dependent on both the charge of the complex and the degree of hydrolysis (first, second, third or fourth hydrolysis). The main drawback of this approach is that it needs a significant amount of experimental data, as different equations are built up for each case (section 6.10) . As the amount of data for radionuclides is very limited, only a limited amount of radionuclide experimental values are included in the correlations.

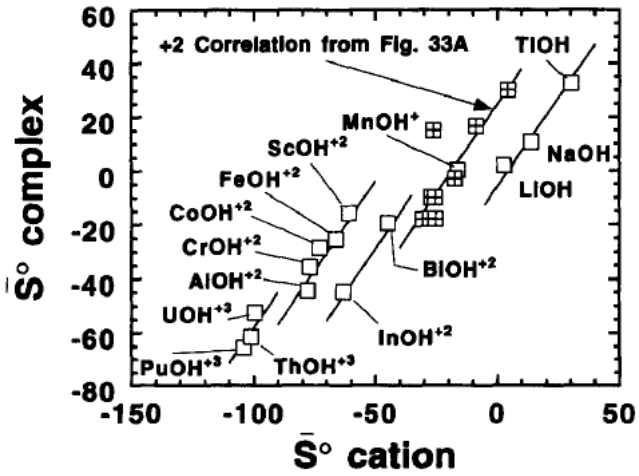

Figure 2-8. *Plot showing the charge dependence in the correlation among $S°_m$ of first hydroxide complex of different cations and the $S°_m$ of the corresponding cation, from Shock et al. (1997). Entropy units are cal/mol·K.*

2.1.4 Sverjensky et al. (1997) approach

Sverjensky et al. (1997) suggested a correlation between the entropy of reaction, $\Delta_r S_m°$, and the molar entropies $S_m°$ of the cation and the ligand. The equations described in the original publication are applicable to halides, sulphates and a limited number of carbonates for monovalent and some divalent or trivalent cations (see Table 6-11). A limited number of data for radionuclides were included in the original correlations.

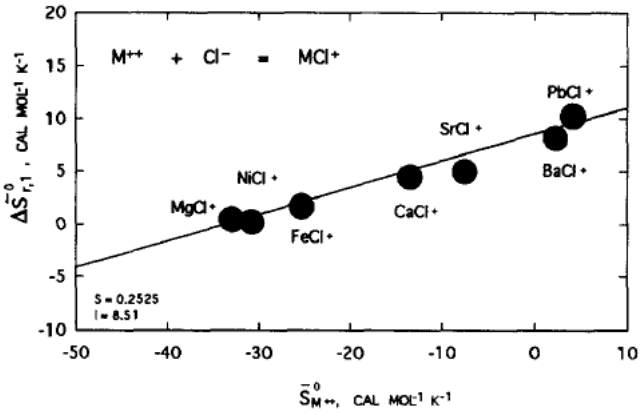

Figure 2-9. *Correlation of $\Delta_r S_m°$(for the reaction corresponding to addition of a monovalent ligand to a divalent cation) with the standard partial molar entropy of the cation, from Sverjensky et al. (1997). Entropy units are cal/mol·K.*

2.2 Solid compounds

Methods to estimate the enthalpy or entropy data of solid compounds are limited. Most of them are based on empirical observations and usually focused on specific groups of elements.

One of the most widespread approaches for the estimation of entropies is the methodology developed by Latimer (Latimer, 1951; Latimer, 1952). The method described in Latimer (1951, 1952) to estimate the entropy of a solid salt is based on adding ionic contributions of the negative and positive ions. The calculated entropies may vary significantly depending on the exact set of parameters used in the calculations.

Although Latimer initially devised the method for ionic compounds, Mills (Mills, 1974) demonstrated its applicability to estimate entropies of non-ionic compounds from the analysis of experimental data for approximately 300 solids. The coefficients used in the algorithm where further revised by Naumov et al. (1974), and Langmuir (1978) modified later some parameters to estimate entropies of solid compounds containing the UO_2^{2+} moiety. Contributions of the ions are also reported in Grenthe et al. (1992); those set of parameters, summarized in Figure 2-10, have been used in several calculations in the present work.

There is a lack of knowledge on the applicability of these estimation procedures for amorphous solid compounds.

Anion	Average cation charge			
	+1	+2	+3	+4
OH^-	30.5	19.2	17.5	(19.2)
O^{2-}	8.4	2.5	2.1	1.3
F^-	23.0	17.6	16.1	20.1
Cl^-	43.9	32.6	29.3	33.1
Br^-	56.1	45.2	41.8	49.8
I^-	63.2	54.4	55.2	51.0
IO_3^-	104.6	(92)		
CO_3^{2-}	64.9	49.4		
NO_3^-	90.8	73.2		
SO_3^{2-}	83.3	62.3	50.2	(46)[a]
SO_4^{2-}	92.9	67.8	57.3	(50)
PO_4^{3-}	79.5	62.8	57.3	(50)[a]
PO_3^-	66.9	54.0	(50.0)	(48)[a]
HPO_4^-	87.9	72.4	66.9	(63)
H_2O	44.7			
UO_2^{2+}[b]	94.7			
U[c]	66.9			

(a) Estimated in the present review.
(b) Treated as a dipositive ion for the purpose of selecting anion contributions.
(c) For uranium compounds not containing $U^{VI}O_2$.

Figure 2-10. *Contributions to entropies of solids to be used with the Latimer approach, as reported in Grenthe et al. (1992). Most of these values were originally extracted from Naumov et al. (1971).*

3 Validation: comparison with data generated in ThermAc

Most estimation methods allow to calculate missing entropy (S_m^o or $\Delta_r S_m^o$) data; results of those estimations are provided in the form of tables in section 7. Once the missing entropy data have been estimated, the values of the enthalpy of reaction ($\Delta_r H_m°$) can be internally calculated using Eq. 1. $\Delta_r H_m°$ is then dependant not only on the estimated entropy values, but also on the log *K*° values used for the internal calculations.

$$\Delta_r G_m^0 = \Delta_r H_m^0 - T\Delta_r S_m^0 \qquad \textit{Eq. 1}$$

When the molar enthalpy of reaction ($\Delta_r H_m^0$) has been calculated, the van't Hoff equation (Eq. 2) is applied to obtain the stability constants (log K_T) at different temperatures studied.

van't Hoff

$$\log K_{T,P_r} = \log K_{T_r,P_r} + \frac{\Delta H_r^\circ}{R \ln 10}\left(\frac{1}{T_r} - \frac{1}{T}\right) \qquad \textit{Eq. 2}$$

Those values will be then compared with the experimental results obtained by the ThermAc partners using different experimental approaches, such as solubility studies (e.g. Endrizzi et al. 2018) or TRLFS experiments (e.g. Skerencak-Fech et al. 2014). Results of those comparisons are provided in the sections below.

3.1 Nd(III)-Hydrolysis

The solubility of $Nd(OH)_3$(cr) in NaCl media at temperatures up to 80°C was studied by KIT-INE in the context of ThermAc; part of these data are under publication.

In order to estimate missing entropy data for aqueous neodymium hydroxides and chlorides, four different approaches were applied:

- The Langmuir approach, using the equations reported in Duro et al. (2012) (section 2.1.2).
- The Baes and Mesmer approach, using the equations updated in present work (section 2.1.1).
- The original equations from Shock et al. (1997) (section 6.10).
- The original equations from Sverjensky et al. (1997) (section 6.11).

In order to estimate missing entropy data for the solid neodymium hydroxide, two different approaches were applied:

- Latimer's approach (with the numerical values reported in Grenthe et al. 1992, see section 2.2).
- Konings (2001) approach (section 6.13).

The different tests performed are summarized in Table 3-1. The estimated values, together with the stability constants used in the calculations, are summarized in Table 7-1.

Table 3-1. *Summary of tests applied in the calculations for $Nd(OH)_3(cr)$ solubility.*

	Aqueous	**Solid**
Test A	12DUR/GRI	51LAT
Test B	97SHO/SAS & 97SVE/SHO	51LAT
Test C	81BAE/MES & 97SVE/SHO	51LAT
Test D	12DUR/GRI	01KON

As shown in Figure 3-1, results obtained using the Shock et al. (1997) approach (test B) are different from those calculated with Langmuir (1978) or Baes and Mesmer (1981) approaches, especially at pH values higher than 8. However, no reliable experimental data are available above this pH (Figure 3-2).

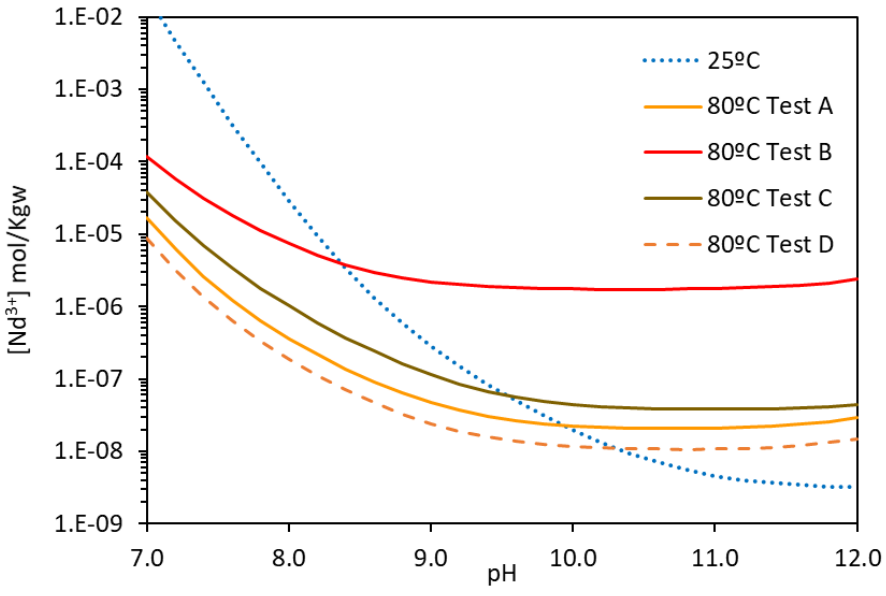

Figure 3-1. *Calculated solubility for $Nd(OH)_3(cr)$ at 0.5M NaCl at 25°C (blue line) and at 80°C (orange, brown and red lines) with the different approaches described in the text.*

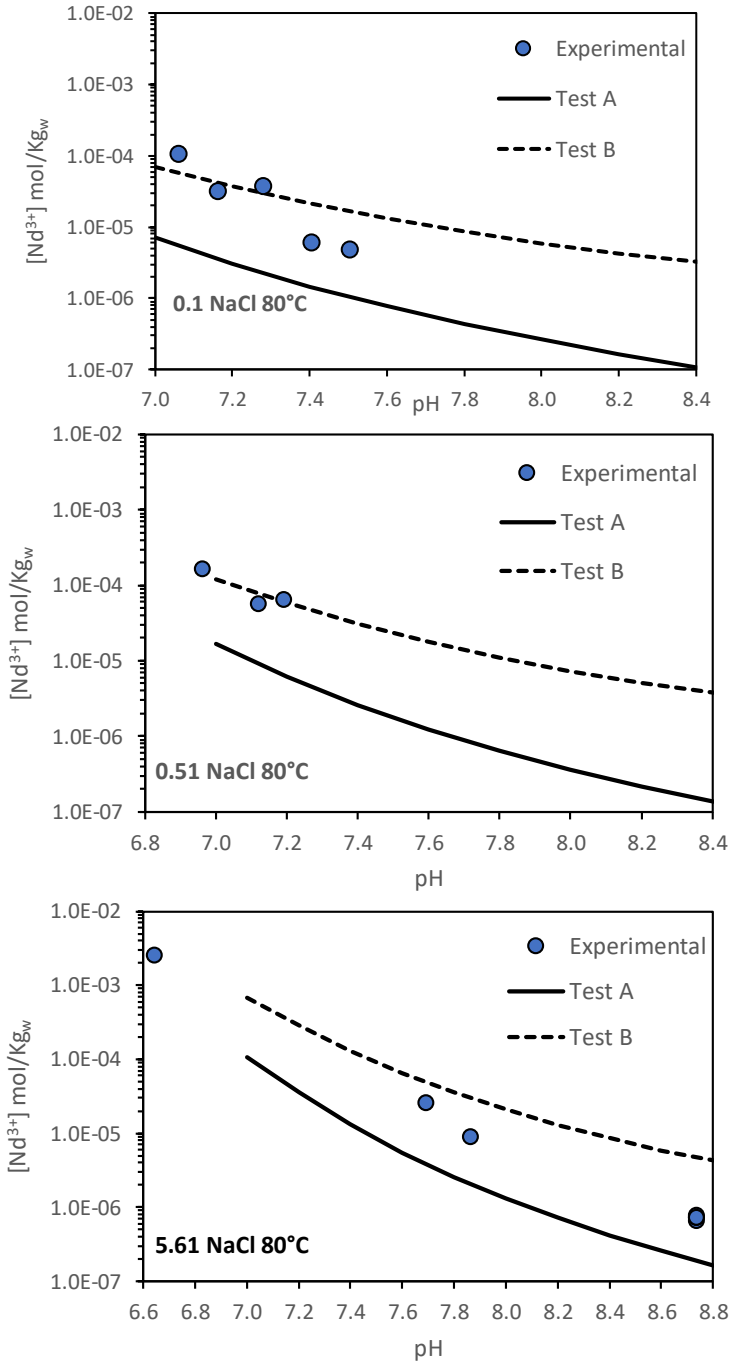

Figure 3-2. *Solubility for $Nd(OH)_3(cr)$ at 80°C, at different ionic strengths. Symbols: experimental data. Lines: calculated values with approaches "A" and "B" described in the text.*

3.2 Cm(III)-Hydrolysis

The possible formation of $Cm(OH)_4^-$ species in the alkaline pH range was investigated using Time-resolved Laser-induced Fluorescence Spectroscopy (TRLFS) by the University of

Heidelberg and KIT-INE at temperatures up to 80°C and ionic strengths up to 5 m. In the TRLFS results, strong evidences of the formation of $Cm(OH)_4^-$ species are not seen. Specifically, the concentration of this species in the sample is calculated to be below 10^{-11} m.

In order to estimate the missing entropy data for aqueous curium hydroxides, two different approaches were applied:

- The Langmuir approach, using the equations reported in Duro et al. (2012) (section 2.1.2).
- The original equations from Shock et al. (1997) (section 6.10).

The possible precipitation of curium hydroxide solids in the experiments was also evaluated. In order to estimate missing entropy data for the solid, the Latimer's approach (with the numerical values reported in Grenthe et al. 1992, see section 2.2) was applied.

The tests performed are summarized in Table 3-2. The estimated values, together with the stability constants used in the calculations, are summarized in Table 7-2.

Table 3-2. *Summary of tests applied in the calculations for $Nd(OH)_3(cr)$ solubility.*

	Aqueous	**Solid**
Test A	12DUR/GRI	51LAT
Test B	97SHO/SAS	51LAT

Using the estimated values, calculations indicate that the contribution of the species $Cm(OH)_4^-$ under the hyperalkaline conditions and 25 and 80°C of the experiments may vary between 58% and 25% (depending on the method used and of the temperature) and that total $Cm(OH)_4^-$ amount is above 10^{-11} m. An example for 1m NaCl is shown in Figure 3-3.

The estimated values are not in agreement with the TRLFS results. Nevertheless, calculations also indicate that a solid may precipitate in the experiments (solid bars in Figure 3-3); this is a handicap in order to ensure that the comparisons between experimental data and calculations are accurate.

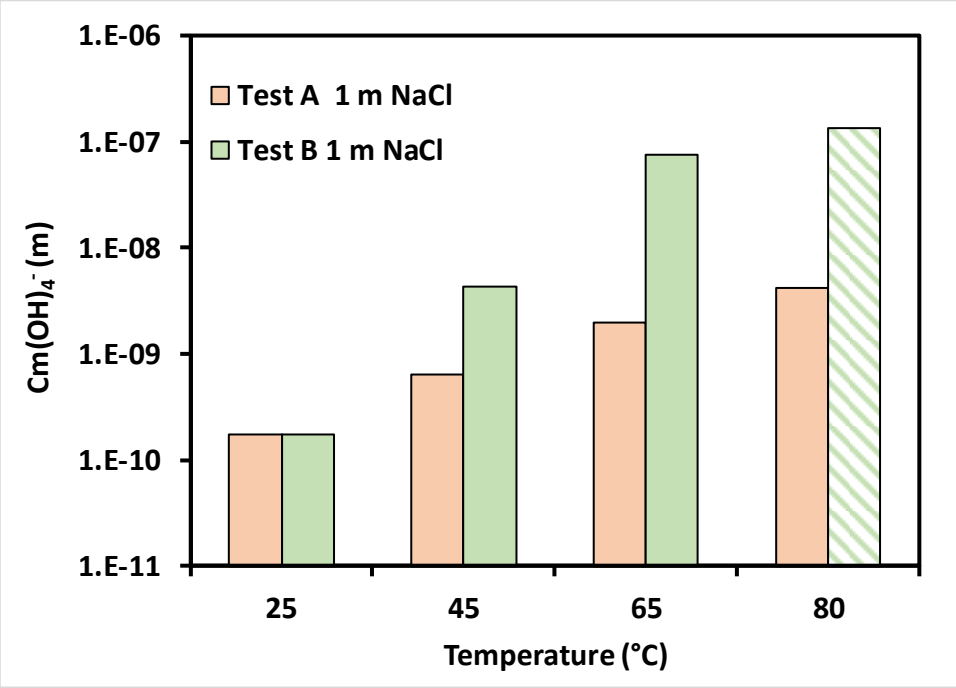

Figure 3-3. *Calculated $Cm(OH)_4^-$ molality at different temperatures, estimated with the approaches "A" (orange columns) and "B" (green columns) described in the text. Solid bars indicate those cases for which precipitation of $Cm(OH)_3(s)$ is expected according to the calculations.*

3.3 Cm(III)-Chloride

Data for Cm-Cl formation, specifically for Reaction 3-1, was generated by University of Heidelberg and KIT-INE (Skerencak-Fech et al. 2014, Koke et al. 2019). log β°_2(T) values for Reaction 3-1 were determined by TRLFS in different ionic media, and $\Delta_r H_m^\circ$ and $\Delta_r S_m^\circ$ were determined by fitting the temperature dependency of the stability constant using the Van't Hoff equation.

$$Cm^{3+} + 2Cl^- \leftrightarrow CmCl_2^+ \quad \textbf{\textit{Reaction 3-1}}$$

In order to estimate entropy data for $CmCl_2^+$, the Langmuir approach, using the equations reported in Duro et al. (2012) (section 2.1.2), has been applied[1]. The estimated values, together with the stability constants used in the calculations, are summarized in Table 7-3.

As explained before, once the missing entropy data have been estimated, the values of the enthalpy of reaction ($\Delta_r H_m°$) are dependant not only on the estimated entropy values, but also on the log *K*° values used for the internal calculations. The comparison shown in Figure 3-4 uses the log *K*° values Skerencak-Fech et al. (2014) (this is, log *K*° = -0.81±0.35 for Reaction 3-1) in the calculations.

As shown in Figure 3-4, the estimated values do not provide an accurate result. The reason for this disagreement is not clear; it may be related to the fact that $CmCl_2^+$ is a weak complex (-1<log *K*°<1), and thus, its associated thermodynamic data are very sensitive to small variations in the calculations. The large uncertainty associated to the estimated values may be a handicap in those cases.

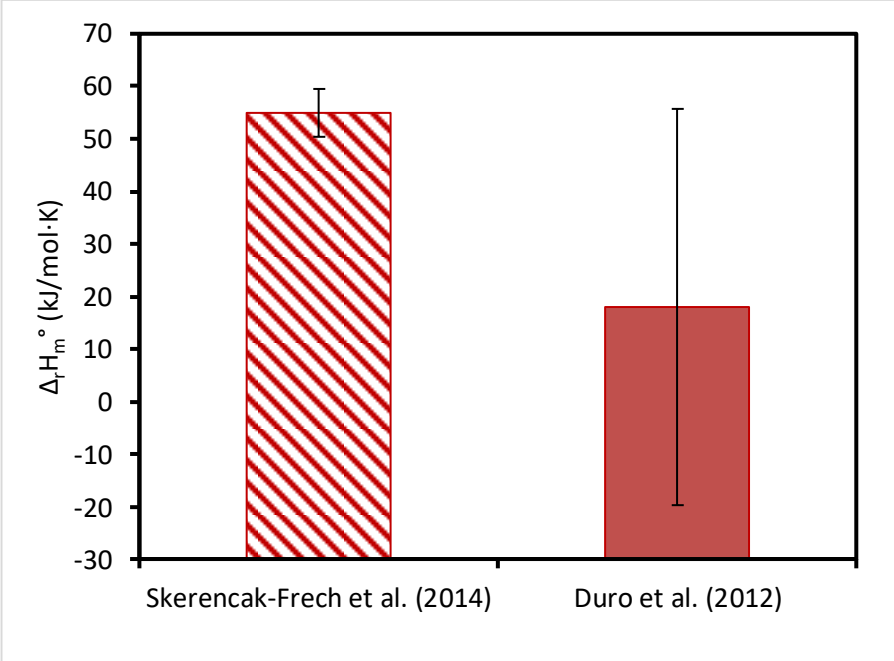

[1] Sverjensky et al. (1997) approach is also applicable, but it requires data for the formation of $CmCl^{2+}$, not available in the publication discussed above.

Figure 3-4. *$\Delta_r H_m°$ values for $CmCl_2^+$ formation. Experimental value from Skerencak-Fech et al. (2014) (dashed bar) is compared with estimated value using Duro et al. (2012) approach (solid bar).*

3.4 Ln(III)-Phosphate

The complexation of Eu(III) and Cm(III) with aqueous phosphates was investigated by HZDR using laser-induced luminescence spectroscopy (Jordan et al. 2018). The experiments showed that upon increasing the temperature (25−80 °C), the formation of both $EuH_2PO_4^{2+}$ and $CmH_2PO_4^{2+}$ (Reaction 3-2 and Reaction 3-3) were favoured. Using the van't Hoff equation, $\Delta_r H_m°$ and $\Delta_r S_m°$ values were derived.

$$Eu^{3+} + H_2PO^{4-} \leftrightarrow EuH_2PO_4^{2+} \qquad \textbf{\textit{Reaction 3-2}}$$

$$Cm^{3+} + H_2PO^{4-} \leftrightarrow CmH_2PO_4^{2+} \qquad \textbf{\textit{Reaction 3-3}}$$

Langmuir (1979) (section 6.6) summarized different approaches in order to estimate missing thermodynamic data. Two of the approaches suggested in Langmuir (1979), applicable to estimation of entropy data for aqueous fluorides, sulphates and phosphates, were tested:

- The simple electrostatic model (section 6.6)
- The Fuoss model (section 6.6)

The methods are based on the correlation between the Gibbs energy of reaction or the entropies of reaction and z^+z^-/d, were z is the charge of the metal or the ligand and d is the distance between the cation and the ligand in the complex. Thus, the approaches suggested can be used to estimate both the log K^o at 25°C and the temperature dependence of the stability constants.

The estimated stability and entropy values were used to calculate the corresponding enthalpy of reaction values (Table 7-6 and Table 7-4 in the appendix). With those data, the results shown in Figure 3-5 and Figure 3-6 were obtained.

As seen in Figure 3-5, the electrostatic model suggested by Langmuir (1979) allows to estimate log $K°$ values (stability constants) that are similar to the experimental data obtained by Jordan et al. (2018), which provides an indication of the suitability of this approach. On the contrary, the Fuoss model does not allow a reasonable prediction of the stability values.

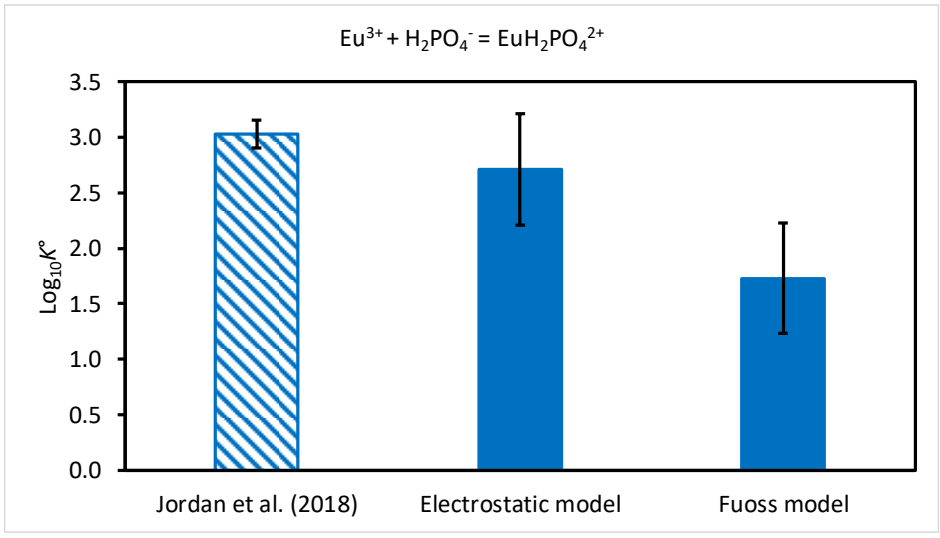

(a)

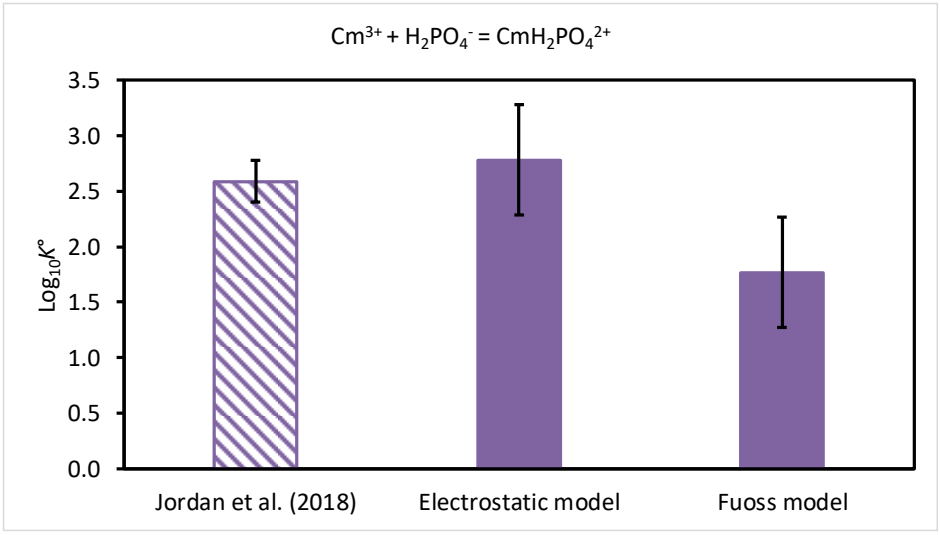

(b)

Figure 3-5. *Stability constants for (a) $EuH_2PO_4^{2+}$ and (b) $CmH_2PO_4^{2+}$. Experimental values (dashed bars) are compared with estimated values (solid bars) using the electrostatic model or the Fuoss model.*

Even if results for the estimation of stability constants are reasonable, the electrostatic and Fuoss models may have a limited application to estimate the effect of temperature on trivalent phosphate complexes, as seen in Figure 3-6. This may be related to the lack of adequate experimental data for the phosphate system in order to calibrate the model.

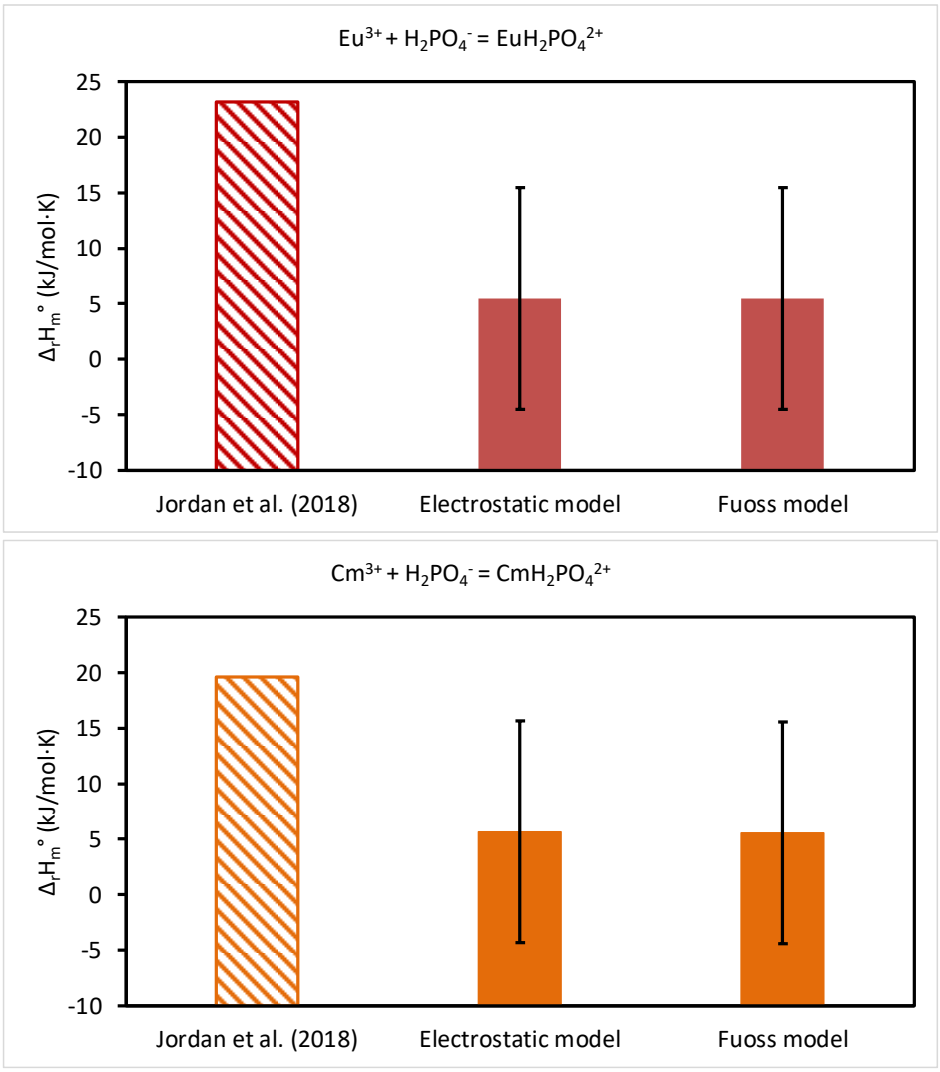

Figure 3-6. *Enthalpy of reaction for (a) $EuH_2PO_4^{2+}$ and (b) $CmH_2PO_4^{2+}$ (b). Experimental values (dashed bars) are compared with estimated values (solid bars) using the electrostatic model or the Fuoss model.*

Additional studies by HZDR deal with the formation of $Cm(H_2PO_4)_2^+$ and $Cm(HPO_4)^+$ and the effect of temperature on those species. However, it is not clear how the simple electrostatic model or the Fuoss model could be extended to 1:2 complexes. Furthermore, the application of the simple electrostatic model or the Fuoss model to $Eu(HPO_4)^+$ or $Cm(HPO_4)^+$ complexes is limited due to the lack of data for HPO_4^{2-} radii in the literature.

3.5 Np(V)-Sulphate

Np(V)-sulphate formation was studied up to 85°C by University of Heidelberg and KIT-INE (Maiwald et al. 2018) using absorption spectroscopy. A single complex species ($NpO_2(SO_4)^-$)

was identified by peak deconvolution of the absorption spectra. Fitting the data according to the integrated Van`t Hoff equation yielded $\Delta_r H_m°$ and $\Delta_r S_m°$ values for Reaction 3-4.

Enthalpy data for $NpO_2(SO_4)^-$ were also available in Guillaumont et al. (2003) and Xia et al. (2006); those data have been used for comparison purposes.

$$NpO_2^+ + SO_4^{2-} \leftrightarrow NpO_2(SO_4)^- \qquad \textbf{\textit{Reaction 3-4}}$$

In order to estimate entropy data for $NpO_2(SO_4)^-$, two different approaches were applied:

- The Langmuir approach, using the equations updated in present work (section 2.1.2).
- The original equations from Sverjensky et al. (1997) (section 6.11).

The estimated entropy values were used to calculate the corresponding enthalpy of reaction values, as shown in Table 7-7. With those data, the results shown in Figure 3-7 were obtained. The results obtained with the Langmuir approach agree reasonably well with the experimental data.

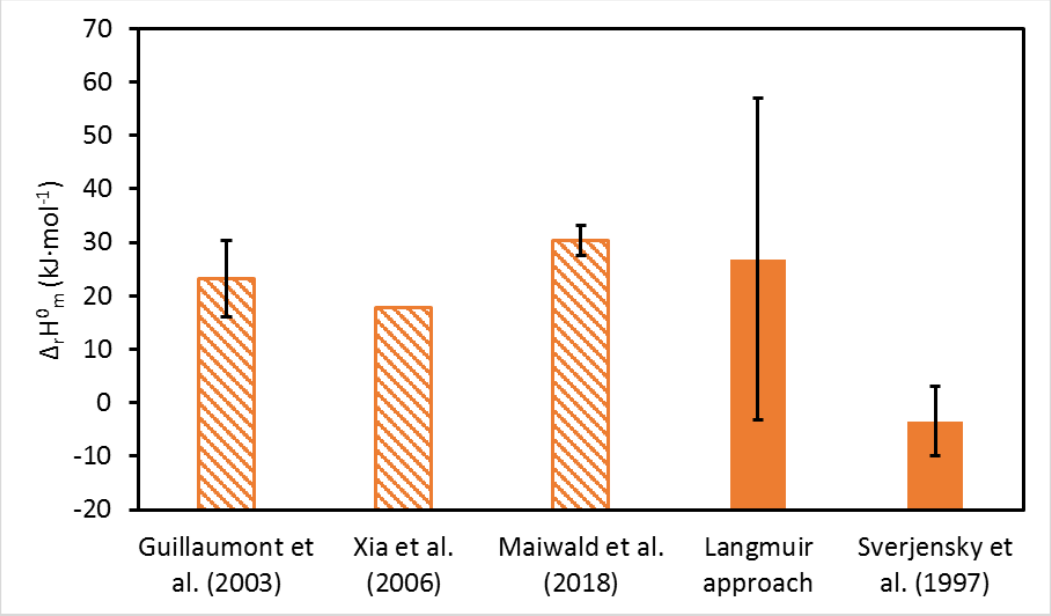

Figure 3-7. *Enthalpy of reaction for $NpO_2(SO_4)^-$. Experimental values (dashed bars) are compared with estimated values (solid bars).*

3.6 U(VI)-Hydrolysis

The solubility of uranium in NaCl media at temperatures up to 80°C was studied by KIT-INE in the context of ThermAc; part of these experimental data are published in Endrizzi et al. (2018). Two different solids (schoepite and sodium uranate) were used as starting materials in the experiments at acidic or alkaline pH values, respectively.

In order to estimate missing entropy data for aqueous species such as $UO_2(OH)_3^-$ and $UO_2(OH)_4^{2-}$, the Langmuir approach, using the equations updated in present work, was applied (section 2.1.2).

Solubility and enthalpy data for sodium uranate used in the calculations are the ones reported in Endrizzi et al. (2018). Entropy data for schoepite was estimated using the Latimer's approach (with the numerical values reported in Grenthe et al. 1992, see section 2.2). The estimated values, together with the stability constants used in the calculations, are summarized in Table 7-8.

The comparison between estimated data and experimental results, summarized in Figure 3-8, is satisfactory; the Langmuir approach seems to provide adequate results for this system.

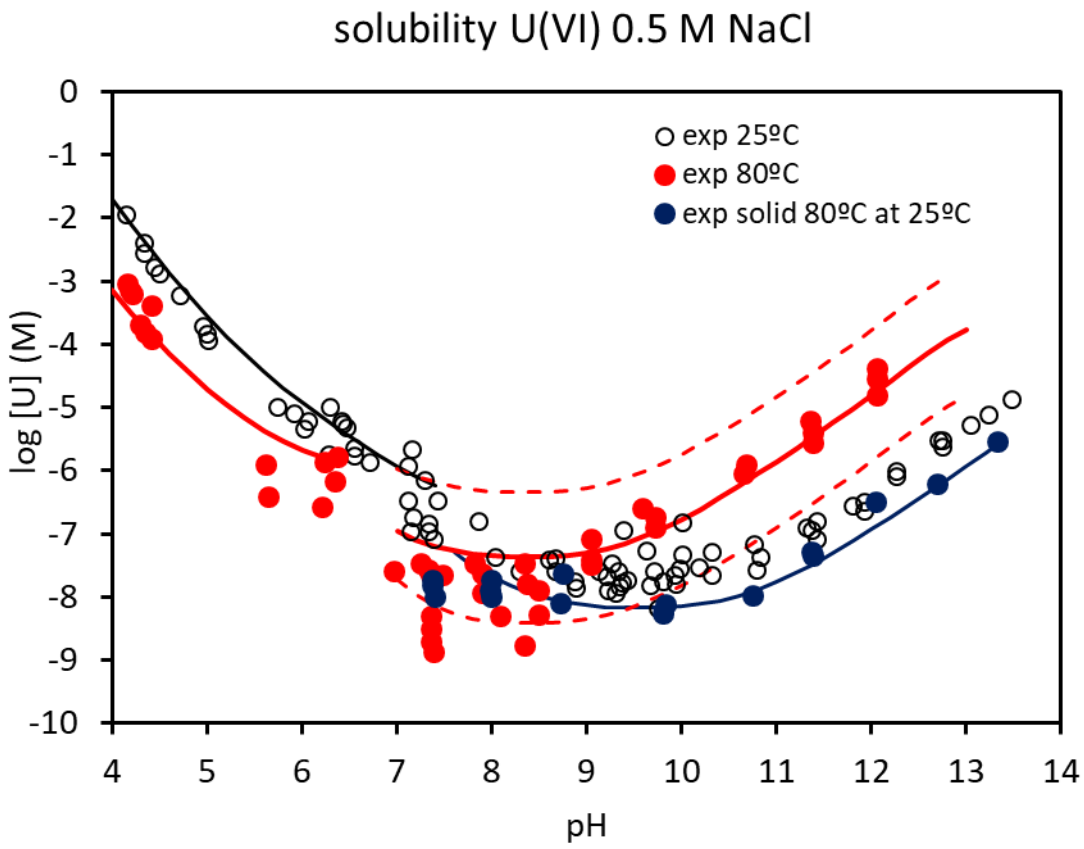

Figure 3-8. *Solubility for schoepite (below pH 7) and sodium uranate (above pH 7) at different temperatures. Black symbols: Solubility data at 25°C from Altmaier et al. (2017). Blue symbols: Solubility data at 25°C from Endrizzi et al. (2018); this solid had been previously equilibrated at 80°C to exclude effects related to crystallinity changes. Red symbols: Solubility data at 80°C from Endrizzi et al. (2018). Symbols correspond to the experimental data generated by KIT-INE; lines are modelling results using the estimations described in the text.*

3.7 Th(IV)-OH-carbonate

The chemistry of Th(IV) at elevated temperatures, and specifically the ternary system Th(IV)-OH-CO_3, is being experimentally investigated at KIT-INE.

Several Th(IV)-OH-CO_3 species can be expected in neutral to alkaline solutions of low to high carbonate concentrations at room temperature (Altmaier et al. 2005). The most likely species are identified as black and grey fields in Figure 3-9.

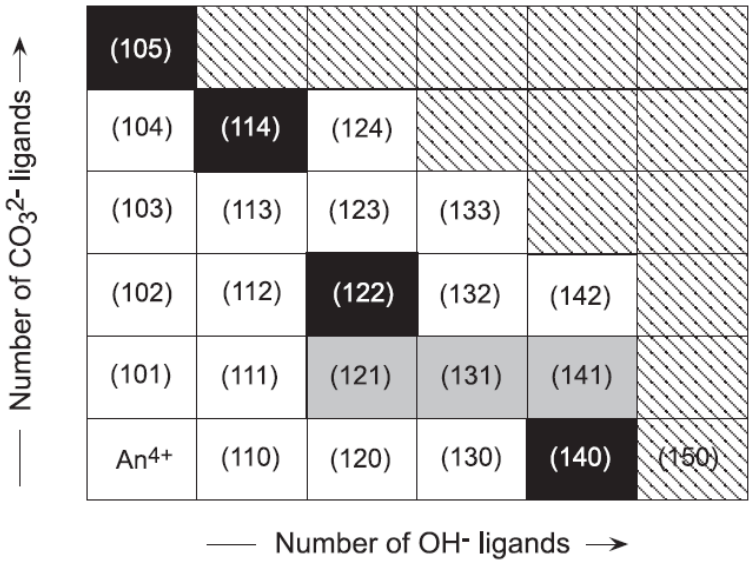

Figure 3-9. *Possible mononuclear thorium carbonate complexes (1yz) = $An(OH)_y(CO_3)_z^{4-y-2z}$, as reported in Altmaier et al. (2005). Black fields indicate the most important species in neutral and alkaline solutions of low to high carbonate concentration at room temperature. Grey fields indicate further Th(IV) complexes quantified in Altmaier et al. (2005).*

As discussed in section 2.1.2, Langmuir and Herman (1980) provided rough estimates for monomeric complexes of thorium. However, no anionic species were included in the correlation, so it is difficult to extrapolate the curve proposed by the authors to Th-OH-CO_3 species. Thus, we have preferred the approach described in Duro et al (2012), because the correlation includes negatively charged complexes such as the limiting complex $U(CO_3)_5^{6-}$, for which experimental enthalpy data was available in Grenthe et al. (1984). Nevertheless, it does not include any ternary complexes, due to the lack of literature data. The estimated values for the aqueous complexes are provided in

Table 7-9.

When solubility experiments are performed, it is necessary to estimate the enthalpy for the thorium (hydr)oxide solid. As a preliminary approach, we have used the Latimer's method (Latimer 1951), where the entropy is calculated adding empirically estimated ionic contributions for the anion ("OH^-" or "O^{2-}"), the cation ("Th^{4+}") and the number of water molecules ("H_2O") in the solid. Thus, using this approach, the entropy will depend on the exact formula of the compound, which may be difficult to determine in the case of amorphous solids. Using different formulas for the same stability constant provides a preliminary evaluation of the uncertainty associated to the calculation. The estimated values are provided in Table 7-10.

Estimations can be used for preliminary calculations/blind predictions. Once the experimental data are ready, a closer comparison of the experimental versus estimated data will be performed in order to evaluate the accuracy of the estimated values.

4 Conclusions

Different numerical approaches to estimate entropy values have been tested by comparing the results of the estimations with the experimental data generated within the project (Table 4-1).

Estimations based on the Langmuir approach (this is, correlations among standard molar entropy of the complexes and its charge) have provided satisfactory results for U(VI) hydrolysis and Np(V) sulphate systems. The Langmuir approach is simple to apply, extensive and easily extended to several elements and ligands not considered in the initial Langmuir's work. Furthermore, it was initially developed for actinides; this is an advantage over other approaches, such as the one suggested by Shock et al. (1997), for which the correlations where build up mainly with major elements data.

Langmuir's approach main drawback is the large uncertainty associated to the entropy calculations. This may be a handicap when accurate predictions are needed, for example in those cases where thermodynamic data are very sensitive to small variations in the calculations.

On the other hand, the comparison among the different methods evaluated (Langmuir 1978; Baes and Mesmer 1981; Shock et al. 1997; Sverjensky et al. 1997; etc) does not allow to clearly establish clear trends. As not all methods can be applied to all systems, it is difficult to identify if one of the methods systematically overestimates or underestimates the experimental results.

Table 4-1. *Summary of the systems studied and the estimation methods applied in present work for aqueous species.*

	Hydrolysis	Chloride	Sulphate	Carbonate	Phosphate
Nd(III)	Langmuir approach (1) Baes & Mesmer (1981) Shock et al. (1997)				
Cm(III)	Langmuir approach (1) Shock et al. (1997)	Langmuir approach (1) Sverjensky et al. (1997)			(3)
Eu(III)					(3)
Np(V)			**Langmuir approach (2)**		
U(VI)	**Langmuir approach(2)**				
Th(IV)				Langmuir approach(1)?	

(1) Langmuir approach, using the equation reported in Duro et al. (2012)
(2) Langmuir approach, using equations updated in present work
(3) The electrostatic model suggested by Langmuir (1979) allows to successfully estimate stability constants, but the results for enthalpy are not accurate
? The accuracy of the estimation method will be evaluated once the experimental values are available.

In the case of solids, estimations based on the Latimer approach, have provided satisfactory results for U(VI) oxides. Once the experimental data for the Th-CO_3 system will be ready, a closer comparison of the experimental versus estimated data will provide further insights on the accuracy of these estimations.

As demonstrated in the case of the thorium-carbonate system, the use of the different estimation approaches has a clear impact in order to improve the design of the experiments. Estimations can be used for preliminary calculations and blind predictions, which allows to reduce the number of experiments needed to obtain reliable data and to focus the efforts in those conditions where temperature is expected to have a more significant impact.

Furthermore, the comparison of the estimated and experimental data allows to increase the confidence in different estimation approaches, specifically in those based on Langmuir (1978) for aqueous species and Latimer (1951) for solid phases. These type of exercises are of utmost importance when fill in data gaps for actinides, long-lived fission products and relevant matrix elements in aquatic systems at temperatures higher than 25°C. Covering those gaps will helps the redefiniton of safety margins under repository conditions, using less conservative and more realistic approches in the calculations.

5 References

Altmaier, M., Brendler, V., Bosbach, D., Kienzler, B., Marquardt, C., Neck, V. and Richter, A. 2004. Sichtung, Zusammenstellung und Bewertung von Daten zur geochemischen Modellierung, Forschungszentrum Karlsruhe, Report FZK-INE 002/04.

Altmaier, M., Neck, V., Müller, R., & Fanghänel, T. 2005. Solubility of $ThO_2 \cdot xH_2O$ (am) in carbonate solution and the formation of ternary Th (IV) hydroxide-carbonate complexes. Radiochimica Acta, 93(2), 83-92.

Altmaier, M., Yalçıntaş, E., Gaona, X., Neck, V., Müller, R., Schlieker, M., Fanghänel, T., 2017. Solubility of U(VI) in chloride solutions. I. The stable oxides/hydroxides in NaCl systems, solubility products, hydrolysis constants and SIT coefficients. The Journal of Chemical Thermodynamics 114, 2–13.

Baes Jr, C. F. and Mesmer, R. E. 1981. Thermodynamics of cation hydrolysis. Am. J. Sci. 281(7), 935-962.

Baes, C. F., and Mesmer, R. E. 1976. Hydrolysis of cations. John Wiley & Sons, New York, London.

Cobble, J. W. 1953. Empirical considerations of entropy. II. The entropies of inorganic complex ions. The Journal of Chemical Physics, 21(9), 1446-1450.

Cox, J. D., Wagman, D. D. and Medvedev, V. A. 1989. CODATA key values for thermodynamics, Hemisphere Pub. Corp.

Diakonov, I. I., Ragnarsdottir, K. V. and Tagirov, B. R. 1998. Standard thermodynamic properties and heat capacity equations or rare earth hydroxides: II. Ce(III)-, Pr-, Sm-, Eu(III)-, Gd-, Tb-, Dy-, Ho-, Er-, Tm-, Yb- and Y-hydroxides. Comparison of thermochemical and solubility data. Chem. Geol., 151 327-347.

Duro, L., Grivé, M., Colàs, E., Gaona, X. and Richard, L. 2012. TDB for elevated temperature conditions using entropy estimations. In: Proceedings of the International Workshops ABC-Salt (II) and HiTAC 2011. Altmaier, M., Bube, C., Kienzler, B., Metz, V., Reed, D.T. (Eds.). KIT Scientific reports Nr. KIT-SR 7625.

Endrizzi, F., Gaona, X., Fernandes, M. M., Baeyens, B., & Altmaier, M. (2018). Solubility and hydrolysis of U (VI) in 0.5 mol/kg NaCl solutions at T= 22 and 80°C. The Journal of Chemical Thermodynamics, 120, 45-53.

Giffaut, E., Grivé, M., Blanc, P., Vieillard, P., Colàs, E., Gailhanou, H., Gaboreau, S., Marty, N., Madé, B., & Duro, L. 2014. Andra thermodynamic database for performance assessment: ThermoChimie. Applied Geochemistry, 49, 225–236.

Grenthe, I., Fuger, J., Konings, R. J. M., Lemire, R. J., Muller, A. B., Nguyen-Trung, C. and Wanner, H. 1992. Chemical thermodynamics Vol. 1: Chemical thermodynamics of uranium, NEA North Holland Elsevier Science Publishers B. V., Amsterdam, The Netherlands.

Grivé, M., Duro, L., Colàs, E., & Giffaut, E. 2015. Thermodynamic data selection applied to radionuclides and chemotoxic elements: An overview of the ThermoChimie-TDB. Applied Geochemistry, 55, 85-94.

Guillaumont, R., Fanghänel, T., Fuger, J., Grenthe, I., Neck, V., Palmer, D. and Rand, M. 2003. Chemical thermodynamics Vol. 5: Update on the chemical thermodynamics of uranium, neptunium, plutonium, americium and technetium, NEA North Holland Elsevier Science Publishers B. V., Amsterdam, The Netherlands.

Haas, J. R., Shock, E. L., & Sassani, D. C. 1995. Rare earth elements in hydrothermal systems: estimates of standard partial molal thermodynamic properties of aqueous complexes of the rare earth elements at high pressures and temperatures. Geochimica et Cosmochimica Acta, 59(21), 4329-4350.

Helgeson, H. C. 1978. Summary and critique of the thermodynamic properties of rock-forming minerals. American Journal of Science, 278, 229.

Johnson, J. W., Oelkers, E. H. and Helgeson, H. C. 1992. SUPCRT92: A software package for calculating the standard molal thermodynamic properties of minerals, gases, aqueous species, and reactions from 1 to 5000 bar and 0 to 1000ºC. Computers & Geosciences, 18, 899-947.

Jordan, N., Demnitz, M., Lösch, H., Starke, S., Brendler, V., and Huittinen, N. 2018. Complexation of trivalent lanthanides (Eu) and actinides (Cm) with aqueous phosphates at elevated temperatures. Inorganic chemistry, 57(12), 7015-7024.

Koke, C., Skerencak-Frech, A., & Panak, P. J. 2019. Thermodynamics of the complexation of curium (III) with chloride in alkali and alkali earth metal solutions at elevated temperatures. The Journal of Chemical Thermodynamics, 131, 219-224.

Konings, R. J. M. 2001a. Thermochemical and thermophysical properties of curium and its oxides. J. Nucl. Mater., 298 255-268.

Konings, R. J. M. 2001b. Estimation of the standard entropies of some Am (III) and Cm (III) compounds. Journal of nuclear materials, 295(1), 57-63

Langmuir, D. 1978. Uranium solution-mineral equilibria at low temperatures with applications to sedimentary ore deposits. Geochimica et Cosmochimica Acta, 42(6), 547-569.

Langmuir, D. 1979. Techniques of estimating thermodynamic properties for some aqueous complexes of geochemical interest, in: Chemical Modeling in Aqueous Systems: Speciation, sorption, solubility, and kinetics (Jenne, E.A., ed.), ACS Symp. Ser. 93, American Chemical Society, Washington D.C., pp. 353-387.

Langmuir, D. and Herman, J. S. 1980. The mobility of thorium in natural waters at low temperatures. Geochimica et Cosmochimica Acta, 44(11), 1753-1766.

Langmuir, D. and Riese, A. C. 1985. The thermodynamic properties of radium. Geochimica et cosmochimica acta, 49(7), 1593-1601.

Latimer, W. M. 1951. Methods of estimating the entropies of solid compounds. Journal of the American Chemical Society, 73(4), 1480-1482.

Latimer, W. M. 1952. The oxidation states of the elements and their potentials in aqueous solutions. 2nd ed. New York, Prentice Hall Inc. 392p.

Lemire, R. J., Fuger, J., Nitsche, H., Potter, P., Rand, M. H., Rydberg, J., Spahiu, K., Sullivan, J. C., Ullman, W. J., Vitorge, P. and Wanner, H. 2001. Chemical thermodynamics vol. 4: Chemical thermodynamics of neptunium and plutonium, NEA North Holland Elsevier Science Publishers B. V., Amsterdam, The Netherlands.

Luo, Y. R. R. and Byrne, R. H. 2001. Yttrium and rare earth element complexation by chloride ions at 25ºC. J. Solution. Chem., 30 837-845.

Maiwald, M. M., Sittel, T., Fellhauer, D., Skerencak-Frech, A., and Panak, P. J. 2018. Thermodynamics of neptunium (V) complexation with sulphate in aqueous solution. The Journal of Chemical Thermodynamics, 116, 309-315.

Naumov, G. B., Ryzhenko, B. N., Khodakovsky, I. L., Handbook of thermodynamic data, Atomizdat, Moscow, (1971), in Russian; Engl. transl.: Report USGS-WRD-74-001.

Neck, V., Altmaier, M., Lutzenkirchen, J., Korthaus, E. and FanghäneL, T. 2007. A comprehensive thermodynamic model for the solubility and hydrolysis of Nd (III) and Am (III) in dilute to concentrated NaCl, MgCl2 and CaCl2 solutions. Conference Migration 07.

Neck, V., Altmaier, M., Rabung, T. and Fanghänel, T. 2009. Thermodynamics of trivalent actinides and neodymium in NaCl. MgCl2 and CaCl2 solutions: Solubility, hydrolysis and ternary Ca-M(III)-OH complexes. Pure Appl. Chem., 81, 1555-1568.

Neck, V., Kim, J. I. and Kanellakopulos, B. 1994. Thermodynamisches verhalten von Neptunium(V) in konzentrierten NaCl- und NaClO4- Losungen Kernforscuhngszentrum Karlsruhe.

Powell, R. E. and Latimer, W. M. 1951. The entropy of aqueous solutes. Journal of Chemical Physics, 19, 1139-1141.

Rand, M., Fuger, J., Grenthe, I., Neck, V. and Rai, D. 2009. Chemical thermodynamics 11: Chemical thermodynamics of thorium, NEA North Holland Elsevier Science Publishers B. V., Amsterdam, The Netherlands.

Rand, M.H. and Fuger, J. 2000. The thermodynamic properties of the transuranium halides. Part I: Neptunium and Plutonium Halides. European Commission Joint Research Centre – Institute for Transuranium Elements, Report EUR 17332 EN.

Robie, R. A., Hemingway, B. S. and Fisher, J. R. 1979. Thermodynamic properties of minerals and related substances at 298.15 K and 1 bar and at higher temperatures. Geol. Sur.

Shock, E. L., and Helgeson, H. C. 1988. Calculation of the thermodynamic and transport properties of aqueous species at high pressures and temperatures: Correlation algorithms for ionic species and equation of state predictions to 5 kb and 1000 C. Geochimica et Cosmochimica Acta, 52(8), 2009-2036.

Shock, E. L., Sassani, D. C., Willis, M. and Sverjensky, D. A. 1997. Inorganic species in geologic fluids: correlations among standard molal thermodynamic properties of aqueous ions and hydroxide complexes. Geochimica et Cosmochimica Acta, 61(5), 907-950.

Skerencak-Frech, A., Fröhlich, D. R., Rothe, J., Dardenne, K., and Panak, P. J. 2014. Combined time-resolved laser fluorescence spectroscopy and extended X-ray absorption fine structure spectroscopy study on the complexation of trivalent actinides with chloride at T= 25–200°C. Inorganic chemistry, 53(2), 1062-1069.

Spahiu, K. and Bruno, J. 1995. A selected thermodynamic database for REE to be used in HLNW performance assessment exercises SKB.

Sverjensky D. A. 1987. Calculation of the thermodynamic properties of aqueous species and the solubilities of minerals in supercritical electrolyte solutions. In Thermodynamics of Earth

Materials: Rev. Mineral (ed. I. S. E. Carmichael and H. P. Eugster), Vol. 17, pp 177 209. Amer. Mineral. Soc.

Sverjensky, D. A.; Shock, E. L. and Helgeson, H. C. 1997. Prediction of the thermodynamic properties of aqueous metal complexes to 1000ºC and 5 kb. Geochimica et Cosmochimica Acta 61(7), 1359-1412.

Wagman, D. D., Evans, W. H., Parker, V. B., Schumm, R. H., Halow, I., BAlley, S. M., Churney, K. L. and Nuttal, R. L. 1982. NBS Tables of Chemical Thermodynamic Properties: Selected Values for Inorganic and C1 and C2 Organic Substances in SI Units. Journal of Physical and Chemical Reference Data, 11, 1-392.Baes Jr, C. F. and Mesmer, R. E. 1981. Thermodynamics of cation hydrolysis. Am. J. Sci. 281(7), 935-962.

Xia, Y., Friese, J. I., Moore, D. A., & Rao, L. 2006. Stability constants of Np (V) complexes with fluoride and sulphate at variable temperatures. Journal of radioanalytical and nuclear chemistry, 268(3), 445-451.

6 Appendix A: Literature estimation methods

This Appendix provides information on relevant estimation methods identified in the literature, summarized in the form of tables.

6.1 Powell and Latimer (1951)

Table 6-1. *Technical data sheet for estimation methods: Powell and Latimer (1951).*

Reference
Powell, R. E. and Latimer, W. M. 1951. The entropy of aqueous solutes. Journal of Chemical Physics, 19, 1139-1141.
Related references
N.A.
Basis of method
Standard partial molal entropies of monoatomic ions and of non-electrolytes in aqueous solution are represented by empirical expressions that include the charge of the ion, the effective radius and/or the molal volume.
Applicability
Aqueous complexes: Monoatomic ions and non-electrolytes in aqueous solution.
Estimated parameters
Partial molal entropy.
Main equations
Monoatomic ions $S = (3/2)R\cdot \ln(M) + 37 - 270Z/r^2$ **Non-electrolytes** $S = S^{int} + (3/2)R\cdot \ln(M) + 10 - 0.22V_m$
Comments
Limited applicability in the frame of ThermAc project. The units of the parameters are not clear.

6.2 Latimer (1951)

Table 6-2. *Technical data sheet for estimation methods: Latimer (1951).*

Reference
Latimer, W. M. 1951. Methods of estimating the entropies of solid compounds. Journal of the American Chemical Society, 73(4), 1480-1482.
Related references
Latimer, W. M. 1952. The oxidation states of the elements and their potentials in aqueous solutions. 2nd ed. New York, Prentice Hall Inc. 392p.
Basis of method
The entropy of any salt is estimated by combining the values reported in the paper for negative ions, with the values for the positive ions. The method is then based in adding empirically estimated ionic contributions.
Applicability
Solids: Ionic solid compounds.
Estimated parameters
Entropy of formation, $S_m°$ (cal/mol·°C).
Main equations
$S_m°$ (A_nX_m) (cal/mol·°C) = Contribution [n·(A^{m+})] + Contribution [m·(X^{n-})]

Contribution of the cation (in cal/mol·°C)

Ag	12.8	Dy	14.4	Mn	10.3	Se	(11.6)
Al	8.0	Er	14.5	Mo	12.3	Si	8.1
As	11.45	Eu	14.1	N	5.8	Sm	14.1
Au	15.3	F	(6.9)	Na	7.5	Sn	13.1
B	4.9	Fe	10.4	Nd	13.9	Sr	12.0
Ba	13.7	Ga	11.2	Ni	10.5	Ta	14.9
Be	4.3	Gd	14.3	Os	15.1	Tb	14.3
Bi	15.6	Ge	11.3	Pb	15.5	Te	(13.4)
Br	(11.7)	Hf	14.8	Pd	12.7	Th	15.9
C	5.2	Hg	15.4	Pr	13.8	Ti	9.8
Ca	9.3	Ho	14.5	Pt	15.2	Tl	15.4
Cb	12.2	I	(13.4)	Ra	15.8	Tm	14.6
Cd	12.9	In	13.0	Rb	11.9	U	16.0
Ce	13.8	Ir	15.2	Re	15.0	V	10.1
Cl	(8.8)	K	9.2	Rh	12.5	W	15.0
Co	10.6	La	13.8	Ru	12.5	Y	12.0
Cr	10.2	Li	3.5	S	(8.5)	Yb	14.7
Cs	13.6	Lu	14.8	Sb	13.2	Zn	10.9
Cu	10.8	Mg	7.6	Sc	9.7	Zr	12.1

Contribution of the anion (in cal/mol·°C)

Negative ion	Charge on positive ion +1	+2	+3	+4
F^-	(5.5)	4.7	(4.0)	5.0
Cl^-	9.7	8.1	6.9	8.1
Br^-	13.0	10.9	(9)	(10)
I^-	14.6	13.6	12.5	13.0
CN^-	7.2	(6)		
OH^-	(5.0)	4.5	3.0	
ClO^-	(14)	(10)	(8)	
ClO_2^-	19.2	(17)	(14)	
ClO_3^-	24.9	(20)		
ClO_4^-	26.0	(22)		
BrO_3^-	26.5	22.9	(19)	
IO_3^-	25.5	(22)		
$H_4IO_6^-$	33.9	(30)		
NO_2^-	17.8	(15)		
NO_3^-	21.7	17.7	(15)	(14)
VO_3^-	20.0	(18)		
MnO_4^-	31.8	(28)		
O^{--}	2.4	0.5	0.5	1.0
S^{--}	8.2	5.0	1.3	2.5
Se^{--}	(16)	11.4	(8)	
Te^{--}	(16.5)	12.1	(9)	
CO_3^{--}	15.2	11.4	(8)	
SO_3^{--}	(19)	14.9	(11)	
$C_2O_4^{--}$	(22)	17.7	(14)	
SO_4^{--}	22	17.2	13.7	(12)
CrO_4^{--}	26.2	(21)		
SiO_4^{--}	(19)	13.8	(9)	7.9
SiO_3^{--}	16.8	10.5	(7)	
PO_4^{---}	(24)	17.0	(12)	
HCO_3^-	17.4	(13)	(10)	
$H_2PO_4^-$	22.8	(18)		
$H_2AsO_4^-$	25.1	(21)		

Comments
Besides Latimer (1951, 1952), cation and anion contributions are tabulated in other data sources.

6.3 Cobble (1953)

Table 6-3. *Technical data sheet for estimation methods: Cobble (1953).*

Reference
Cobble, J. W. 1953. Empirical considerations of entropy. II. The entropies of inorganic complex ions. The Journal of Chemical Physics, 21(9), 1446-1450.
Related references
N.A.
Basis of method
Partial molal entropies of aqueous complex ions are correlated with the ratio of their charge to interatomic distance.
Applicability
Aqueous complexes: Inorganic complexes.
Estimated parameters
Partial molal entropy.
Main equations
Relationship between "corrected" entropy S´ and "normal" Sº $S´=S^º - nS^º(H_2O)$ where n is the number of water molecules replaced from the coordinated aquated ion by the complexing agent. **Complexes with monoatomic ions as ligands** $S´=49-99(Z/r_{12})$ $r_{12}=r_1+r_2$, that is the interatomic distance. A value of 1.40Å was considered for OH^-. **Molecularly complexed species** $S´=49-99(Z/r_{12})$ where $r_{12}=(r_1+r_2)/f$. Structural factor f=0.65 **Neutral ions** $S´=132-354/r_{12}$
Comments
The units of the parameters are not clear.

6.4 Helgeson (1978)

Table 6-4. *Technical data sheet for estimation methods: Helgeson (1978).*

Reference
Helgeson, H. C. 1978. Summary and critique of the thermodynamic properties of rock-forming minerals. American Journal of Science, 278, 229.
Related references
N.A.
Basis of method
Estimation of standard molal entropy of a mineral by writing a reaction between the mineral and other minerals of similar structural class, using oxide minerals to balance the reaction.
Applicability
Solids: Non-ferrous silicate minerals.
Estimated parameters
Entropy of formation, $S_m°$ (cal/mol·°C).
Main equations
See the original publication (limited applicability in the context of the present project)
Comments
Limited applicability in the present context (difficult to find minerals to write the reaction for which the entropy is known).

6.5 Langmuir (1978)

Table 6-5. *Technical data sheet for estimation methods: Langmuir (1978).*

Reference
Langmuir, D. 1978. Uranium solution-mineral equilibria at low temperatures with applications to sedimentary ore deposits. Geochimica et Cosmochimica Acta, 42(6), 547-569.
Related references
N.A.
Basis of method
Correlation between the entropies of uranium aqueous complexes and the charge of the complexes, following a 4th degree empirical polynomial equation.
Applicability
Aqueous complexes: Monomeric aqueous uranium complexes.
Estimated parameters
Entropy of formation, $S_m°$ (cal/mol·°C).
Main equations
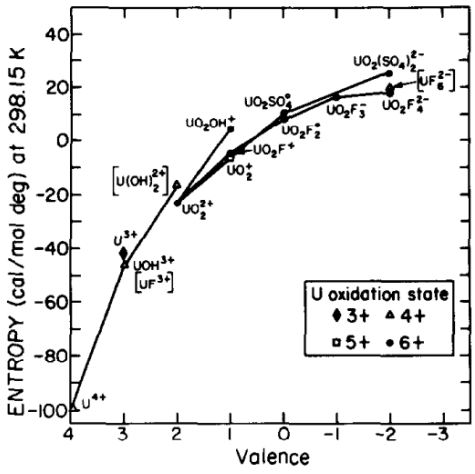 ***Figure 6-1.*** *Entropy vs valence for some uranium ions and complexes. Entropies of bracketed species are estimated. Other values are based on empirical results (See Langmuir (1978) for details).* **Original equation in the publications:** S^o_m (cal·mol^{-1}·$^oC^{-1}$) = 8.3 - 10.55Z - 2.17Z^2 + 0.05Z^3 - 0.13Z^4 Z is the charge of the complex.
Comments
The method was originally developed for monomeric U complexes. It seems to be applicable for polynuclear complexes if the value is divided by the number of uranium atoms in the formula.

6.6 Langmuir (1979)

Table 6-6. *Technical data sheet for estimation methods: Langmuir (1979).*

Reference
Langmuir, D. 1979. Techniques of estimating thermodynamic properties for some aqueous complexes of geochemical interest, in: Chemical Modeling in Aqueous Systems: Speciation, sorption, solubility, and kinetics (Jenne, E.A., ed.), ACS Symp. Ser. 93, American Chemical Society, Washington D.C., pp. 353-387.
Related references
N.A.
Basis of method
Different estimation and correlation techniques are summarized. The electrostatic model and the Fuoss model are based on a correlation between the Gibbs energy of reaction or the entropies of reaction and z_+z_-/d, where z is the charge of the metal or the ligand and d is the distance between the cation and the ligand in the complex.
Applicability
Aqueous fluorides, sulphates and maybe phosphates
Estimated parameters
Gibbs energy of reaction, $\Delta_rG_m^0$. Entropy of reaction, $\Delta_rS_m°$.
Main equations
Simple electrostatic model Δ_rG^0 (kcal·mol^{-1}) = -4.24·10^{-8} (z_+z_-/d) $\Delta_rS^o = \Delta_rG^0$ (-0.0454) **Fuoss model** Δ_rG^0 (cal·mol^{-1}) = -29200 -1364 log d^3 - 4.241·10^{-5} (z_+z_-/d) Δ_rS^o (cal·mol^{-1}·deg^{-1}) = 97.94 + 4.576 log d^3 + 19.26·10^{-8} (z_+z_-/d)
Comments

6.7 Langmuir and Herman (1980)

Table 6-7. *Technical data sheet for estimation methods: Langmuir and Herman (1980).*

Reference
Langmuir, D. and Herman, J. S. 1980. The mobility of thorium in natural waters at low temperatures. Geochimica et Cosmochimica Acta, 44(11), 1753-1766.
Related references
Langmuir, D. 1978. Uranium solution-mineral equilibria at low temperatures with applications to sedimentary ore deposits. Geochimica et Cosmochimica Acta, 42(6), 547-569.
Basis of method
Correlation between the entropies of thorium aqueous complexes and the charge of the complexes, following a 4th degree empirical polynomial equation.
Applicability
Aqueous complexes: Thorium aqueous complexes.
Estimated parameters
Entropy of formation, $S_m°$ (cal/mol·°C).
Main equations

Figure 6-2. *Entropy vs valence for thorium ion and some thorium complexes on a monatomic basis. For polymers: a) Charge of complex (x axes) is the charge of complex / number of thorium atoms in the polymer; b) Entropy of complex (y axes) is the entropy of complex / number of thorium atoms in the polymer.*

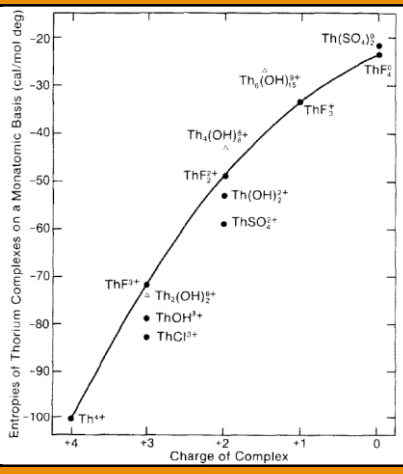

Comments

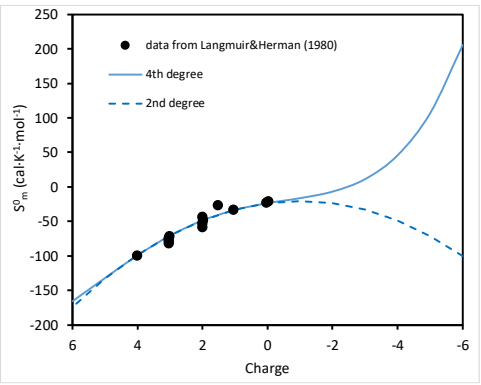

The equation for the fitting of the data is not provided in the original paper. Different fittings result in very different values for the extrapolation to anionic complexes, as seen in the example below.

4th degree: $y = 0.07z^4 – 0.64z^3 – 1.31z^2 - 7.90z - 23.34$

2nd degree: $y = -3.368z^2 - 9.7696z - 4.9269$

Figure 6-3. *Symbols: entropy vs valence for thorium ion and some thorium complexes on a monatomic basis, from Langmuir and Herman (1980). Blue lines: fitting of the data using a 4th degree (solid line) or 2nd degree (dashed line) polynomial. Entropy in cal/mol·K.*

6.8 Baes and Mesmer (1981)

Table 6-8. *Technical data sheet for estimation methods: Baes and Mesmer (1981).*

Reference
Baes Jr, C. F. and Mesmer, R. E. 1981. Thermodynamics of cation hydrolysis. Am. J. Sci. 281(7), 935-962.
Related references
Baes, C. F., and Mesmer, R. E. 1976. Hydrolysis of cations. John Wiley & Sons, New York, London.
Basis of method
Dependency on the entropy of the hydrolysis reaction on the log *K* of hydrolysis and z/d.
Applicability
Aqueous complexes: hydroxides.
Estimated parameters
Entropy of reaction, $\Delta_r S_m°$ (cal/mol·K).
Main equations
First hydrolysis constant $xM^{z+} + yH_2O = M_x(OH)_y^{(xz-y)} + yH^+$ $\Delta_r S°_{11} = 1.772 \log K_{11} + 19.12(z/d)$ **Polymerized reaction** $M(OH)^{(z-1)} = (1/y)M_x(OH)_y^{(xz-y)} + (1 – x/y)M^{z+}$ $\Delta_r S°_{xy}/y = -17.5 + 16.2(z/d) + [(1+y-x)/y]R \cdot Ln(55.5)$ **Successive mononuclear hydrolysis steps** $M(OH)_y^{(z-y)} + H_2O = M(OH)_{y+1}^{(z-y-1)} + H^+$ $\Delta_r S° = -17.8 + 12.2(z-y)$
Comments

6.9 Langmuir and Riese (1985)

Table 6-9. *Technical data sheet for estimation methods: Langmuir and Riese (1985).*

Reference
Langmuir, D. and Riese, A. C. 1985. The thermodynamic properties of radium. Geochimica et cosmochimica acta, 49(7), 1593-1601.
Related references
N.A.
Basis of method
Estimation of radium properties using as a basis the analogy between Ra and other alkaline earth elements.
Applicability
Aqueous complexes and solids: Radium.
Estimated parameters
Main equations
Comments
Not used in the present work.

6.10 Shock et al. (1997)

Table 6-10. *Technical data sheet for estimation methods: Shock et al. (1997).*

Reference
Shock, E. L., Sassani, D. C., Willis, M. and Sverjensky, D. A. 1997. Inorganic species in geologic fluids: correlations among standard molal thermodynamic properties of aqueous ions and hydroxide complexes. Geochimica et Cosmochimica Acta, 61(5), 907-950.
Related references
Shock, E. L., and Helgeson, H. C. 1988. Calculation of the thermodynamic and transport properties of aqueous species at high pressures and temperatures: Correlation algorithms for ionic species and equation of state predictions to 5 kb and 1000 C. Geochimica et Cosmochimica Acta, 52(8), 2009-2036.
Basis of method
Correlation between standard molal entropies S^o_m of an aqueous hydroxide complex and the standard molal entropy of the corresponding cation.
Applicability
Aqueous complexes: hydroxide complexes of monovalent, divalent, trivalent and tetravalent cations.
Estimated parameters
Entropy of formation, $S_m°$ (cal/mol·°C).
Main equations
Complexes of monovalent cations (M^+) • First (MOH): $S^o_{complex} = 1.32 \cdot S^o_{cation} - 6$ • Second (MO^-): $S^o_{complex} = 1.42 \cdot S^o_{cation} - 11$ **Complexes of divalent cations (M^{2+})** • First (MOH^+): $S^o_{complex} = 1.32 \cdot S^o_{cation} + 24.5$ • Second (MO): $S^o_{complex} = 1.42 \cdot S^o_{cation} + 20.5$ • Third (HMO_2^-): $S^o_{complex} = 1.52 \cdot S^o_{cation} + 15.5$ • Fourth (MO_2^{2-}): $S^o_{complex} = 1.62 \cdot S^o_{cation} + 11$ **Complexes of trivalent cations (M^{3+})** • First (MOH^{2+}): $S^o_{complex} = 1.32 \cdot S^o_{cation} + 37$ (Ga, In, Tl, Bi); $S^o_{complex} = 1.32 \cdot S^o_{cation} + 62$ (Others) • Second (MO^+): $S^o_{complex} = 1.42 \cdot S^o_{cation} + 83$ • Third (HMO_2): $S^o_{complex} = 1.52 \cdot S^o_{cation} + 123$ • Fourth (MO_2^-): $S^o_{complex} = 1.62 \cdot S^o_{cation} + 118$ **Complexes of tetravalent cations (M^{4+})** • First (MOH^{3+}): $S^o_{complex} = 1.32 \cdot S^o_{cation} + 74$ • Second (MO^{2+}): $S^o_{complex} = 1.42 \cdot S^o_{cation} + 108$ • Third (HMO_2^+): $S^o_{complex} = 1.52 \cdot S^o_{cation} + 140$ • Fourth (MO_2): $S^o_{complex} = 1.62 \cdot S^o_{cation} + 135$ • Fifth (HMO_3^-): $S^o_{complex} = 1.72 \cdot S^o_{cation} + 130$
Comments
It is not clear if it is applicable to the estimation of trivalent REE and actinides, as those elements were not included among the elements used to construct the calibration curves.

6.11 Sverjensky et al. (1997)

Table 6-11. *Technical data sheet for estimation methods: Sverjensky et al. (1997).*

Reference
Sverjensky, D. A.; Shock, E. L. and Helgeson, H. C. 1997. Prediction of the thermodynamic properties of aqueous metal complexes to 1000ºC and 5 kb. Geochimica et Cosmochimica Acta 61(7), 1359-1412.
Related references
Sverjensky D. A. 1987. Calculation of the thermodynamic properties of aqueous species and the solubilities of minerals in supercritical electrolyte solutions. In Thermodynamics of Earth Materials: Rev. Mineral (ed. I. S. E. Carmichael and H. P. Eugster), Vol. 17, pp 177 209. Amer. Mineral. Soc. Haas, J. R., Shock, E. L., & Sassani, D. C. 1995. Rare earth elements in hydrothermal systems: estimates of standard partial molal thermodynamic properties of aqueous complexes of the rare earth elements at high pressures and temperatures. Geochimica et Cosmochimica Acta, 59(21), 4329-4350.
Basis of method
Correlation between entropy of reaction, ΔS_r, and standard molal entropies S^o_m of the cation + ligand.
Applicability
Aqueous complexes: metal halide, sulphate and carbonate complexes.
Estimated parameters
Entropy of reaction, $\Delta_r S_m°$ (cal/mol·K).
Main equations
Halides (with monovalent and some divalent cations) • $\Delta_r S^0 = (a_Z \cdot S^o_L + a'_Z) \cdot S^o_{ML(y-1)} + b_Z \cdot S^o_L + b'_Z$ • $a_Z = 0.016241Z-0.000479$ • $a'_Z = -0.36097Z+0.3209$ • $b_Z = 0.32102Z-0.05996$ • $b'_Z = 8.2198Z-1.557$ **Sulphates (with monovalent, divalent and trivalent cations)** • $\Delta_r S^o = \alpha_{Z,SO4} \cdot S^o_M + \beta_{Z,SO4}$ • $\alpha_{Z,SO4} = -0.055Z + 0.055$ • $\beta_{Z,SO4} = 13.84Z+18.16$ **Carbonates (limited to some monovalent and divalent cations)** • $\Delta_r S^o = \gamma_{Z,CO3} \cdot S^o_M + \delta_{Z,CO3}$ • $\gamma_{Z,CO3} = -1.617Z+0.213$ • $\delta_{Z,CO3} = 66.82Z+28.67$
Comments
May be possible to extend the equation for halides to OH^- complexes.

6.12 Rand and Fuger (2000)

Table 6-12. *Technical data sheet for estimation methods: Rand and Fuger (2000).*

Reference
Rand, M.H. and Fuger, J. 2000. The thermodynamic properties of the transuranium halides. Part I: Neptunium and Plutonium Halides. European Commission Joint Research Centre – Institute for Transuranium Elements, Report EUR 17332 EN.
Related references
N.A.
Basis of method
Relationship of the enthalpy or entropy of formation with the values for analogous actinides.
Applicability
Solids: An(III), An(IV), An(V) and An(VI) halides.
Estimated parameters
Enthalpy and entropy of formation: $\Delta_f H_m°$ (kJ/mol) and $S_m°$ (J/mol·K).
Main equations
Enthalpy of formation Correlation between [$\Delta_f H_m°(AnX_n(cr)$ – $\Delta_f H_m°(An^{n+}(aq)]$ with the ionic radii of the aqueous An^{n+} ion. **Entropy of formation** • Direct average of different analogous actinide solids. • Direct analogy with analogous actinide solids.
Comments
May be applied to other actinides/systems.

6.13 Konings (2001)

Table 6-13. *Technical data sheet for estimation methods: Konings (2001).*

Reference
Konings, R. J. M. 2001. Estimation of the standard entropies of some Am (III) and Cm (III) compounds. Journal of nuclear materials, 295(1), 57-63.
Related references
N.A.
Basis of method
Estimation of standard entropies as the sum of lattice entropy S_{lat} and excess entropy S_{exs}.
Applicability
Solids: Isoelectric trivalent lanthanide and actinide solid compounds (An_2O_3, $An(OH)_3$, AnF_3, $AnCl_3$).
Estimated parameters
Entropy of formation: $S_m°$ (J/mol·K).
Main equations
$S^o = S_{lat} + S_{exs}$
Comments
Limited range of applicability as available S_{lat} and S_{exs} are limited.

6.14 Duro et al. (2012)

Table 6-14. *Technical data sheet for estimation methods: Duro et al. (2012).*

Reference
Duro, L., Grivé, M., Colàs, E., Gaona, X. and Richard, L. 2012. TDB for elevated temperature conditions using entropy estimations. In: Proceedings of the International Workshops ABC-Salt (II) and HiTAC 2011. Altmaier, M., Bube, C., Kienzler, B., Metz, V., Reed, D.T. (Eds.). KIT Scientific reports Nr. KIT-SR 7625.
Related references
N.A.
Basis of method
The entropy of An and Ln aqueous complexes is related to the charge of the complex by a 4th polynomial function. Boundaries including all data provide uncertainty of ±126 J/mol·K in estimations.
Applicability
Aqueous complexes: An and Ln aqueous complexes.
Estimated parameters
Entropy of formation: $S_m°$ (J/mol·K).
Main equations
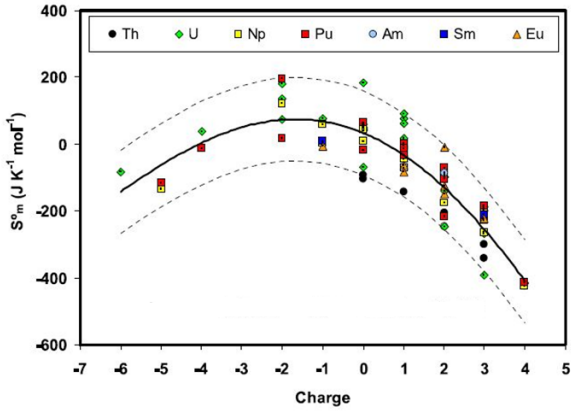 ***Figure 6-4.*** *Experimental data available for some actinide and lanthanide aqueous complexes (symbols) and fitting of the available experimental data to 4th degree polynomial (curve).* **Fitting function:** $S^o = 0.0511x^4 – 0.0785x^3 – 15.588x^2 – 50.38x + 33.193$ where x is the charge of the complex
Comments
Empirical correlation obtained using An and Ln data from experimental studies.

7 Appendix B: Estimated values

The present section contains tables including the estimated data (mainly entropy data). Besides estimated values, other data of interest such as stability constants and internally calculated enthalpy values are also provided.

7.1 Estimations for Nd(III) system

Table 7-1: *Summary of parameters for Nd (III) system at T=25ºC.*

Species	Reaction	$Log_{10}K^0$	Ref.	ESTIMATED $S_m°$ (J/mol·K)	$\Delta_rH_m°$ (KJ/mol) (3)	Method
$Nd(OH)^{2+}$	$Nd^{3+} + H_2O = Nd(OH)^{2+} + H^+$	-7.40 ± 0.40	Neck et al. (2009)	**-129.729 ± 126**	44.333	Duro et al. (2012) (1)
				-68.225 (4)	62.670 ± 37.339	Baes and Mesmer (1981) (2)
				-13.436 ± 20.900	79.005	Shock et al. (1997)
$Nd(OH)_2^+$	$Nd^{3+} + 2H_2O = Nd(OH)_2^+ + 2H^+$	-15.70 ± 0.70	Neck et al. (2009)	**-32.802 ± 126**	99.752	Duro et al. (2012) (1)
				22.498 (4)	116.240 ± 37.482	Baes and Mesmer (1981) (2)
				123.708 ± 20.900	146.416	Shock et al. (1997)
$Nd(OH)_3$	$Nd^{3+} + 3H_2O = Nd(OH)_3 + 3H^+$	-26.20 ± 0.50	Neck et al. (2009)	**33.193 ± 126**	158.507	Duro et al. (2012) (1)
				65.469 (4)	168.130 ± 37.378	Baes and Mesmer (1981) (2)
				270.398 ± 20.900	229.230	Shock et al. (1997)
$Nd(OH)_4^-$	$Nd^{3+} + 4H_2O = Nd(OH)_4^- + 4H^+$	-40.70 ± 0.70	Neck et al. (2009)	**68.114 ± 126**	230.829	Duro et al. (2012) (1)
				60.688 (4)	228.615 ± 37.482	Baes and Mesmer (1981) (2)
				298.758 ± 20.900	299.596	Shock et al. (1997)
$NdCl^{2+}$	$Nd^{3+} + Cl^- = NdCl^{2+}$	0.24 ± 0.03	Neck et al. (2009)	**-129.729 ± 126**	4.704	Duro et al. (2012) (1)
				-61.471 (4)	25.055 ± 6.234	Sverjensky et al. (1997)
$NdCl_2^+$	$Nd^{3+} + 2Cl^- = NdCl_2^+$	-0.74 ± 0.05	Neck et al. (2009)	**-32.802 ± 126**	22.321	Duro et al. (2012) (1)
				27.139 (4)	40.192 ± 6.238	Sverjensky et al. (1997)
$Nd(OH)_3(cr)$	$Nd(OH)_3(cr) + 3H^+ = Nd^{3+} + 3H_2O$	17.68 ± 0.26	(5)	**95.814**	-128.545	Latimer (1951)
				131.620	-139.221	Konings (2001b)

(1) Enlarged Langmuir (1978) method as reported in Duro et al. (2012).
(2) Re-evaluated Baes and Mesmer (1981) method applied in present work.
(3) Internally calculated from Log K^o and S_m^o.
(4) Internally calculated from Log K^o and $\Delta_rS_m^o$.
(5) Data from KIT solubility results (Endrizzi et al. 2018, data not published)

7.2 Estimations for Cm(III) system

Table 7-2: *Summary of parameters for Cm(III)-H_2O system at T=25ºC.*

Species	Reaction	$Log_{10}K^0$	Ref.	ESTIMATED $S_m°$ (J/mol·K)	$\Delta_rH_m°$ (KJ/mol) (3)	Method
$Cm(OH)^{2+}$	$Cm^{3+} + H_2O = Cm(OH)^{2+} + H^+$	-7.20 ± 0.50	Guillaumont et al. (2003)	**-129.729 ± 126**	38.510 ± 37.793	Duro et al. (2012) (1)
				-52.525 ± 125 (4)	61.528 ± 37.378	Baes and Mesmer (1981) (2)
				7.288 ± 20.900	79.362 ± 7.474	Shock et al. (1997)
$Cm(OH)_2^+$	$Cm^{3+} + 2H_2O = Cm(OH)_2^+ + 2H^+$	-15.10 ± 0.70	Guillaumont et al. (2003)	**-32.802 ± 126**	91.646 ± 37.896	Duro et al. (2012) (1)
				38.198 ± 125 (4)	112.815 ± 37.482	Baes and Mesmer (1981) (2)
				146.002 ± 20.900	144.956 ± 7.980	Shock et al. (1997)
$Cm(OH)_3$	$Cm^{3+} + 3H_2O = Cm(OH)_3 + 3H^+$	-26.20 ± 0.50	Guillaumont et al. (2003)	**33.193 ± 126**	153.826 ± 37.793	Duro et al. (2012) (1)
				81.169 ± 125 (4)	168.130 ± 37.378	Baes and Mesmer (1981) (2)
				294.262 ± 20.900	231.664 ± 7.474	Shock et al. (1997)
$Cm(OH)_4^-$	$Cm^{3+} + 4H_2O = Cm(OH)_4^- + 4H^+$	-40.70 ± 0.70	Guillaumont et al. (2003)	**68.114 ± 126**	226.148 ± 37.896	Duro et al. (2012) (1)
				76.388 ± 125 (4)	228.615 ± 37.482	Baes and Mesmer (1981) (2)
				324.192 ± 20.900	302.498 ± 7.980	Shock et al. (1997)
$Cm(OH)_3(am)$	$Cm(OH)_3(am) + 3H^+ = Cm^{3+} + 3H_2O$	-16.90 ± 0.80	Neck et al. (2009)	**96.232**	119.537	Latimer (1951)

(1) Enlarged Langmuir (1978) method as reported in Duro et al. (2012).
(2) Re-evaluated Baes and Mesmer (1981) method applied in present work.
(3) Internally calculated from Log K^o and S_m^o.
(4) Internally calculated from Log K^o and $\Delta_rS_m^o$.

Table 7-3: *Summary of parameters for Cm(III)-Cl-H_2O system at T=25ºC.*

Species	Reaction	$Log_{10}K^0$	Ref.	$S_m°$ (J/mol·K)	$\Delta_rH_m°$ (KJ/mol)	Method
$CmCl^{2+}$	$Cm^{3+} + Cl^- = CmCl^{2+}$	0.24 ± 0.03	Guillaumont et al. (2003)	**-129.729 ± 126**	0.023 ± 37.685 (3)	Duro et al. (2012) (1)
				-45.281 ± 23.170 (2)	25.195 ± 6.234 (3)	Sverjensky et al. (1997)
$CmCl_2^+$	$Cm^{3+} + 2Cl^- = CmCl_2^+$	-0.74 ± 0.05	Guillaumont et al. (2003)	**-32.802 ± 126**	17.640 ± 37.686 (3)	Duro et al. (2012) (1)
				46.100 ± 25.267 (2)	41.165 ± 6.923 (3)	Sverjensky et al. (1997)
		-0.81 ± 0.35 (4)	Skerencak-Frech et al. (2014)	**-32.802 ± 126**	18.040 ± 37.738	Duro et al. (2012) (1)
				90.827 ± 34.665 (5)	54.9 ± 4.5	Skerencak-Frech et al. (2014), experimental
		-1.16 ± 0.10 (4)	Koke et al. (2019)	102.909 ± 30.950 (5)	60.5 ± 1.5	Koke et al. (2019), experimental

(1) Enlarged Langmuir (1978) method as reported in Duro et al. (2012).
(2) Internally calculated from Log K^o and $\Delta_rS_m^o$.
(3) Internally calculated from Log K^o and S_m^o.
(4) Internally calculated from $\Delta_rH_m^o$ and $\Delta_rS_m^o$.
(5) Internally calculated from $\Delta_rS_m^o$.

Table 7-4: *Summary of parameters for Cm(III)-PO_4 system at T=25ºC.*

Species	Reaction	ESTIMATED $\Delta_rG_m°$ (kJ/mol)	ESTIMATED $\Delta_rS_m°$ (J/mol·K)	$Log_{10}K^0$	$\Delta_rH_m°$ (KJ/mol) (4)	Method
$Cm(H_2PO_4)^{2+}$	$Cm^{3+} + H_2PO_4^- = Cm(H_2PO_4)^{2+}$	**-15.887**	**72.126**	2.78	5.618	Electrostatic model (1)
		-10.085	**52.599**	1.77	5.597	Fuoss model (2)

(1) Electrostatic model from Langmuir (1979).
(2) Fuoss model from Langmuir (1979).
(3) Internally calculated from $\Delta_rG_m°$.
(4) Internally calculated from $\Delta_rG_m°$ and $\Delta_rS_m^o$.

7.3 Estimations for Eu(III) system

Table 7-5: *Summary of parameters for Eu(III)-Cl-H_2O system at T=25ºC.*

Species	Reaction	$Log_{10}K^0$	Ref.	ESTIMATED $S_m°$ (J/mol·K)	$\Delta_rH_m°$ (KJ/mol) (3)	Method
$Eu(OH)^{2+}$	$Eu^{3+} + H_2O = Eu(OH)^{2+} + H^+$	-7.80 ± 0.40	Spahiu and Bruno (1995)	**-129.729 ± 126**	51.104 ± 37.676	Duro et al. (2012) (1)
				-83.277 ± 125 (4)	64.953 ± 37.339	Baes and Mesmer (1981) (2)
				33.305 ± 20.900	79.852 ± 6.858	Shock et al. (1997)
$Eu(OH)_2^+$	$Eu^{3+} + 2H_2O = Eu(OH)_2^+ + 2H^+$	-15.70 ± 0.70	Neck et al (2007)	**-32.802 ± 126**	104.240 ± 37.818	Duro et al. (2012) (1)
				7.446 ± 125 (4)	116.240 ± 37.482	Baes and Mesmer (1981) (2)
				102.334 ± 20.900	144.531 ± 7.602	Shock et al. (1997)
$Eu(OH)_3$	$Eu^{3+} + 3H_2O = Eu(OH)_3 + 3H^+$	-26.20 ± 0.50	Neck et al (2007)	**33.193 ± 126**	162.995 ± 37.715	Duro et al. (2012) (1)
				50.417 ± 125 (4)	168.130 ± 37.378	Baes and Mesmer (1981) (2)
				247.519 ± 20.900	226.896 ± 7.069	Shock et al. (1997)
$Eu(OH)_4^-$	$Eu^{3+} + 4H_2O = Eu(OH)_4^- + 4H^+$	-40.70 ± 0.70	Neck et al (2007)	**68.114 ± 126**	235.317 ± 37.818	Duro et al. (2012) (1)
				45.636 ± 125 (4)	228.615 ± 37.482	Baes and Mesmer (1981) (2)
				274.374 ± 20.900	296.814 ± 7.602	Shock et al. (1997)
$EuCl^{2+}$	$Eu^{3+} + Cl^- = EuCl^{2+}$	0.76 ± 0.40	Luo and Byrne (2001)	**-129.729 ± 126**	6.223 ± 37.676	Duro et al. (2012) (1)
				-77.003 ± 21.691 (4)	21.944 ± 6.636	Sverjensky et al. (1997)
$EuCl_2^+$	$Eu^{3+} + 2Cl^- = EuCl_2^+$	-0.05 ± 1.00	Spahiu and Bruno (1995)	**-32.802 ± 126**	22.870 ± 38.038	Duro et al. (2012) (1)
				8.918 ± 21.694 (4)	35.309 ± 8.450	Sverjensky et al. (1997)
$Eu(OH)_3(am)$	$Eu(OH)_3(am) + 3H^+ = Eu^{3+} + 3H_2O$	-17.60 ± 0.84	Diakonov et al (1998)	**96.650**	132.826	Latimer (1951)
				120.060	139.805	Konings (2001b)

1) Enlarged Langmuir (1978) method as reported in Duro et al. (2012). (2) Re-evaluated Baes and Mesmer (1981) method applied in p.w. (3) Internally calc. from Log K^o and S_m^o. (4) Internally calc. from Log K^o and $\Delta_rS_m^o$.

Table 7-6: *Summary of parameters for Eu(III)-PO_4 system at T=25ºC.*

Species	Reaction	ESTIMATED $\Delta_r G_m°$ (kJ/mol)	ESTIMATED $\Delta_r S_m°$ (J/mol·K)	$Log_{10}K^0$	$\Delta_r H_m°$ (KJ/mol) (4)	Method
$Eu(H_2PO_4)^{2+}$	$Eu^{3+} + H_2PO_4^- = Eu(H_2PO_4)^{2+}$	**-15.471**	**70.239**	2.71	5.471	Electrostatic model (1)
		-9.866	**51.373**	1.73	5.450	Fuoss model (2)

(1) Electrostatic model from Langmuir (1979).
(2) Fuoss model from Langmuir (1979).
(3) Internally calculated from $\Delta_r G_m°$.
(4) Internally calculated from $\Delta_r G_m°$ and $\Delta_r S_m°$.

7.4 Estimations for Np(V) system

Table 7-7: *Summary of parameters for Np (V) system at T=25ºC.*

Species	Reaction	$Log_{10}K^0$	Ref.	ESTIMATED $S_m°$ (J/mol·K)	$\Delta_rH_m°$ (KJ/mol) (3)	Method
$NpO_2(OH)$	$NpO_2^+ + H_2O = NpO_2(OH) + H^+$	-11.3 ± 0.70	Lemire et al. (2001)	**38.126 ± 100**	68.698 ± 30.250	Langmuir (1978) (1)
				-2.954 ± 125 (4)	56.450 ± 37.482	Baes and Mesmer (1981) (2)
$NpO_2(OH)_2^-$	$NpO_2^+ + 2H_2O = NpO2(OH)_2^- + 2H^+$	-23.6 ± 0.50	Lemire et al. (2001)	**71.141 ± 100**	127.895 ± 30.121	Langmuir (1978) (1)
				-7.704 ± 125 (4)	104.387 ± 37.378	Baes and Mesmer (1981) (2)
NpO_2Cl	$NpO_2^+ + Cl^- = NpO_2Cl$	-0.93 ± 0.06	Neck et al. (1994)	**38.126 ± 100**	13.487 ± 29.987	Langmuir (1978) (1)
				-13.604 ± 23.483 (4)	-1.937 ± 6.241	Sverjensky et al. (1997)
$NpO_2(SO_4)^-$	$NpO_2^+ + SO_4^- = NpO_2(SO_4)^-$	0.44 ± 0.60	Lemire et al. (2001)	**71.141 ± 100**	26.870 ± 30.181	Langmuir (1978) (1)
				-30.504 ± 23.486 (4)	-3.436 ± 7.110	Sverjensky et al. (1997)

(1) Enlarged Langmuir (1978) method developed in present work.
(2) Re-evaluated Baes and Mesmer (1981) method applied in present work.
(3) Internally calculated from Log K^o and S_m^o.
(4) Internally calculated from Log K^o and $\Delta_rS_m^o$.

7.5 Estimations for U(VI) system

Table 7-8: *Summary of parameters for U(VI) system at T=25ºC.*

Species	Reaction	$Log_{10}K^0$	Ref.	ESTIMATED $S_m°$ (J/mol·K)	$\Delta_r H_m°$ (KJ/mol) (2)	Method
$UO_2(OH)_2$	$UO_2^{2+} + 2H_2O = UO_2(OH)_2 + 2H^+$	-12.15 ± 0.07	Guillaumont et al. (2003)	**66.749 ± 130**	76.821 ± 38.772	Langmuir (1978) (1)
$UO_2(OH)_3^-$	$UO_2^{2+} + 3H_2O = UO_2(OH)_3^- + 3H^+$	-20.70 ± 0.4	Altmaier et al. (2017)	**105.513 ± 130**	116.326 ± 38.837	Langmuir (1978) (1)
$UO_2(OH)_4^{2-}$	$UO_2^{2+} + 4H_2O = UO_2(OH)_4^{2-} + 4H^+$	-31.90 ± 0.2	Altmaier et al. (2017)	**111.879 ± 130**	161.298 ± 38.787	Langmuir (1978) (1)
$(UO_2)_3(OH)_4^{2+}$	$3UO_2^{2+} + 4H_2O = (UO_2)_3(OH)_4^{2+} + 4H^+$	-11.90 ± 0.30	Grenthe et al. (1992)	**-346.191 ± 130**	-30.879 ± 38.890	Langmuir (1978) (1)
$(UO_2)_4(OH)_7^+$	$4UO_2^{2+} + 7H_2O = (UO_2)_3(OH)_4^{2+} + 7H^+$	-21.90 ± 1.00	Grenthe et al. (1992)	**-26.745 ± 130**	88.156 ± 39.341	Langmuir (1978) (1)
$UO_3{:}2H_2O$	$UO_3{:}2H_2O + 2H^+ = UO_2^{2+} + 3H_2O$	5.35 ± 0.13	Altmaier et al. (2004)	**-186.600 ± 1.940**	-52.884 ± 1.298	Latimer (1951)

(1) Enlarged Langmuir (1978) method developed in present work.
(2) Internally calculated from Log K^o and S_m^o.

7.6 Estimations for Th(IV) system

Table 7-9: **Summary of parameters for Th (IV) system at T=25ºC.**

Species	Reaction	$Log_{10}K^0$	Ref.	ESTIMATED $S_m°$ (J/mol·K)	$\Delta_r H_m°$ [2] (KJ/mol)	Method
$Th(CO_3)_5^{6-}$	$Th^{4+} + 5CO_3^{2-} = Th(CO_3)_5^{6-}$	31.00±0.70	Rand et al. (2009)	-141.433± 126.000	-18.432± 38.108	Duro et al. (2012) [1]
$Th(OH)(CO_3)_4^{5-}$	$Th^{4+} + 4CO_3^{2-} + H_2O = Th(OH)(CO_3)_4^{5-} + H^+$	21.60±0.50	Rand et al. (2009)	-62.107± 126.000	23.112± 37.995	Duro et al. (2012) [1]
$Th(OH)_2(CO_3)_2^{2-}$	$Th^{4+} + 2CO_3^{2-} + 2H_2O = Th(OH)_2(CO_3)_2^{2-} + 2H^+$	8.80±0.50	Rand et al. (2009)	73.167± 126.000	85.835± 37.981	Duro et al. (2012) [1]
$Th(OH)_2(CO_3)(aq)$	$Th^{4+} + CO_3^{2-} + 2H_2O = Th(OH)_2(CO_3)(aq) + 2H^+$	2.50±0.60	Rand et al. (2009)	33.193± 126.000	94.970± 38.024	Duro et al. (2012) [1]
$Th(OH)_3(CO_3)^-$	$Th^{4+} + CO_3^{2-} + 3H_2O = Th(OH)_3(CO_3)^- + 3H^+$	-3.70±0.70	Rand et al. (2009)	68.145± 126.000	119.925± 38.080	Duro et al. (2012) [1]
$Th(OH)_4(CO_3)^{2-}$	$Th^{4+} + CO_3^{2-} + 4H_2O = Th(OH)_4(CO_3)^{2-} + 4H^+$	-15.60±0.60	Rand et al. (2009)	73.167± 126.000	168.492± 38.024	Duro et al. (2012) [1]
$Th(OH)_4(aq)$	$Th^{4+} + 4H_2O = Th(OH)_4(aq) + 4H^+$	-17.40±0.70	Rand et al. (2009)	33.193± 126.000	151.941± 38.079	Duro et al. (2012) [1]

[1] Enlarged Langmuir (1978) method as reported in Duro et al. (2012).
[2] Internally calculated from Log K^o and S_m^o.

Table 7-10: *Summary of parameters and estimated values for different Th solids. Using different formulas for the same solid allows to estimate the uncertainty associated to the calculations.*

Solid	Reaction	*Log K°*	Ref.	ESTIMATED $S_m°$ (J/mol·K)	$\Delta_r H_m°$ [2] (KJ/mol)	Method
$Th(OH)_4(s)$	$Th^{4+} + 4OH^- = Th(OH)_4(s)$	50.30±1.00	[3]	143.326±75.000	-105.267± 23.566	Latimer (1951) [1]
$ThO_2{:}2H_2O$	$Th^{4+} + 4OH^- = ThO_2{:}2H_2O$	50.30±1.00	[3]	158.526±75.000	-100.735± 23.566	Latimer (1951) [1]
$ThO_2{:}H_2O$	$Th^{4+} + 4OH^- = ThO_2{:}H_2O + H_2O$	50.30±1.00	[3]	113.826±75.000	-93.207± 23.566	Latimer (1951) [1]
$ThO_2(s)$	$Th^{4+} + 4OH^- = ThO_2(s) + 2H_2O$	50.30±1.00	[3]	69.126±75.000	-85.678± 23.566	Latimer (1951) [1]

[1] Latimer approach (see text).
[2] Internally calculated from Log K^o and S_m^o.
[3] Preliminary value from KIT; to be updated after new experiments are completed.

8 Appendix C: Other relevant data

Thermodynamic data for reference states and master species used in the calculations.

Table 8-1: *Summary of thermodynamic parameters for reference states.*

Species	$\Delta_f G_m°$ (KJ/mol)	$\Delta_r H_m°$ (KJ/mol)	$S_m°$ (J/mol·K)	Reference
Nd(cr)	0.000 ± 0.000	0.000 ± 0.000	71.090 ± 4.180	Robie et al. (1979)
Cm(cr)	0.000 ± 0.000	0.000 ± 0.000	70.800 ± 3.000	Konings (2001a)
Eu(cr)	0.000 ± 0.000	0.000 ± 0.000	77.780 ± 3.010	Wagman et al. (1982)
Th(cr)	0.000 ± 0.000	0.000 ± 0.000	52.640 ± 0.500	Rand et al. (2009)
Np(cr)	0.000 ± 0.000	0.000 ± 0.000	50.460 ± 0.800	Lemire et al. (2001)
U(cr)	0.000 ± 0.000	0.000 ± 0.000	50.200 ± 0.200	Guillaumont et al. (2003)

Table 8-2: *Summary of thermodynamic parameters for master species.*

Species	$\Delta_f G_m°$ (KJ/mol) [(1)]	$\Delta_r H_m°$ (KJ/mol)	$S_m°$ (J/mol·K)	Reference
Nd^{3+}	-671.82	-696.200	-206.700	Cox et al. (1989)
Cm^{3+}	-595.388 ± 6.759	-615.000 ± 6.000	-191.000 ± 10.000	Konings (2001a)
Eu^{3+}	-574.463 ± 1.600	-605.325 ± 2.521	-221.752 ± 5.800	Johnson et al. (1992)
Th^{4+}	-704.783 ± 5.298	-768.700 ± 2.300	-423.100 ± 16.000	Rand et al. (2009)
NpO_2^+	-907.765 ± 5.628	-978.181 ± 4.629	-45.904 ± 10.706	Lemire et al. (2001)
UO_2^{2+}	-952.551 ± 1.747	-1019.000 ± 1.500	-98.200 ± 3.000	Grenthe et al. (1992)

(1) Internally calculated

INE Scientific Working Documents
ISSN 2701-262X

www.kit.edu